

*H. Bloomfield*

NASA CR-72875  
AVSD-0429-71-RR

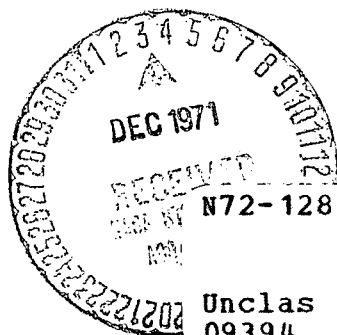


HEAT SOURCE REENTRY VEHICLE DESIGN STUDY

Prepared for  
NATIONAL AERONAUTICS AND SPACE ADMINISTRATION

Contract NAS 3-14937

AVCO CORPORATION  
AVCO SYSTEMS DIVISION  
201 Lowell Street  
Wilmington, Massachusetts 01887



(NASA-CR-72875) HEAT SOURCE REENTRY  
VEHICLE DESIGN STUDY R.L. Ryan (Avco  
Corp.) Oct. 1971 336 p CSCL 22B

Unclas  
09394

G3/31

*88-66482e*

1. Report No. NASA CR-72875		2. Government Accession No.		3. Recipient's Catalog No.	
4. Title and Subtitle HEAT SOURCE REENTRY VEHICLE DESIGN STUDY				5. Report Date Oct. 1971	
				6. Performing Organization Code	
7. Author(s) R. L. Ryan, et al				8. Performing Organization Report No. AVSD-0429-71-RR	
				10. Work Unit No.	
9. Performing Organization Name and Address AVCO Corporation AVCO Systems Division 201 Lowell Street Wilmington, Mass. 01887				11. Contract or Grant No. NAS 3-14397	
				13. Type of Report and Period Covered Contract Report	
12. Sponsoring Agency Name and Address National Aeronautics and Space Administration Washington, D. C. 20546				14. Sponsoring Agency Code	
15. Supplementary Notes Project Manager, Harvey S. Bloomfield, Space Power Systems Division NASA Lewis Research Center, Cleveland, Ohio					
16. Abstract The study provided the detail design of a flight-type Heat Source Reentry Vehicle and Heat Exchanger compatible with the Isotope Brayton Power Conversion System under development at the NASA Lewis Research Center. Specific objectives of the study that were met were:  <div style="margin-left: 40px;"> (1) Modification of the reference reentry vehicle and heat exchanger developed in contract NAS 3-10938 and reported in NASA CR-72555   (2) Assessment of orbital and superorbital capability   (3) Complete set of detail design layout drawings were provided </div>					
17. Key Words (Suggested by Author(s)) Isotope Brayton Reentry			18. Distribution Statement  Unclassified - unlimited		
19. Security Classif. (of this report) Unclassified		20. Security Classif. (of this page) Unclassified		21. No. of Pages 323	
				22. Price* \$6.00	

\* For sale by the National Technical Information Service, Springfield, Virginia 22151

PRECEDING PAGE BLANK NOT FILMED

### ACKNOWLEDGEMENT

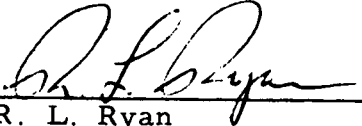
This report, "Heat Source Reentry Vehicle Design Study", was prepared by the Avco Systems Division, Wilmington, Mass., under NASA Contract NAS 3-14397. The study was performed for the Space Power Systems Division of the NASA Lewis Research Center, Cleveland, Ohio. Mr. Harvey Bloomfield, the NASA Lewis Project Manager, provided valuable assistance and guidance in developing the study.

Mr. R. L. Ryan, of the Space Systems Directorate, was the Avco Project Manager. Various technical specialists from the Systems Division line engineering department participated in the program effort. Principal contributors and their specialties areas were:

J. Graham	- Associate Program Manager, Thermal Analyses
R. Billings	- Materials
B. Laub	- Thermal Analysis, ACHX Design
H. Steinle	- Thermal Control
K. Stewart	- Design
M. Miani	- Design
R. Wray	- Structures
O. Zappa	- Aerothermo

The Garrett Airesearch Corporation, Los Angeles Division, developed the Heat Source Heat Exchanger design under subcontract to Avco. Mr. Murray Coombs was the Garrett Project Engineer.

The Avco report number is AVSD-0429-71-RR.

Approved: 

R. L. Ryan  
HSRV Program Manager

## CONTENTS

1.0	INTRODUCTION .....	1
2.0	SUMMARY .....	5
2.1	Task I - Preliminary Modification .....	5
2.2	Task II - Design.....	15
2.3	Task III - Detail Design.....	26
2.4	Conclusions & Recommendations .....	31
2.5	References .....	38
3.0	HEAT SOURCE REENTRY VEHICLES .....	39
3.1	Systems Analysis.....	39
3.2	Reentry Performance Analysis.....	43
3.2.1	Heating & Loads Summary.....	48
3.2.2	Analysis & Results .....	53
3.2.2.1	Aerodynamic Characteristics .....	53
3.2.2.2	Reentry Dynamics .....	60
3.2.2.3	Reentry Heating Environments .....	73
3.3	Heat Source Unit (HSU) Design .....	87
3.3.1	Summary Description .....	87
3.3.2	Thermal Analysis .....	93
3.3.2.1	HSU Thermal Model Description .....	94
3.3.2.2	Thermal Performance .....	97
3.3.3	Auxiliary Coolant Heat Exchanger (ACHX).....	113
3.3.3.1	Mechanical Description .....	118
3.3.3.2	Thermal Analysis .....	118
3.3.3.3	Hydraulic Analysis .....	121
3.3.3.4	Alternate Design .....	130



## CONTENTS (Cont'd)

3.3.4	Heat Source Unit Structural Design .....	130
3.3.4.1	Design Requirements & Criteria .....	136
3.3.4.2	Earth-Orbital-HSU Structure Design....	136
3.3.4.3	Super-Orbital HSU Structure .....	146
3.4	Heat Source Reentry Vehicle (HSRV) Design .....	147
3.4.1	Earth-Orbital Reentry Vehicle .....	148
3.4.1.1	Heat Shield .....	148
3.4.1.2	Aeroshell Structure.....	154
3.4.1.3	Thermal Control .....	161
3.4.1.4	HSRV Design .....	171
3.4.2	Super-Orbital Reentry Vehicle .....	180
3.4.2.1	Heat Shield .....	180
3.4.2.2	Thermal Control (Super-Orbital) .....	184
3.4.2.3	Super-Orbital Reference Design Structural Performance .....	189
3.4.2.4	Design Description .....	191
3.4.3	Aeroshell Thermal Simulation .....	197
3.4.3.1	Design Considerations .....	197
3.5	References .....	201
4.0	HEAT SOURCE HEAT EXCHANGER .....	203
4.1	HSHX-Super Alloy Evaluation.....	203
4.2	Design Description .....	215
4.2.1	Thermal Analysis .....	217
4.2.2	Structural Design .....	239
4.3	Fabrication .....	246
4.4	Drawings .....	256
4.5	References .....	256

## CONTENTS (Concluded)

APPENDIX A	Analysis of ACHX Transient for the Emergency Case of Cooldown from Steady-State .....	A-1
APPENDIX B	Orifice Computations - Auxiliary Coolant Heat Exchanger (ACHX) .....	B-1
APPENDIX C	HS Support Plate Analysis - Earth Orbit .....	C-1

## ILLUSTRATIONS

Figure 1.0-1	Heat Source Reentry Vehicle Assembly .....	2
1.0-2	Spiral Heat Source Heat Exchanger .....	4
2.1-1	Isotope Reentry Vehicle Reference Design (NAS 3-10938)...	8
2.1-2	Reference Heat Source .....	9
2.1-3	HSRV Assembly Drawing .....	11
2.1-4	Reentry Conditions .....	12
2.1-5	Stagnation Point - Integrated Heat Load .....	13
2.1-6	Aerodynamic Load .....	14
2.1-7	Spiral Heat Source Heat Exchanger (NAS 3-10938 Design...	16
2.2-1	Heat Shield Requirements Avcoat 5026-39/HC-G .....	20
2.2-2	HSRV-Earth Orbital (INT-21) Design .....	21
2.2-3	HSRV Steady-State Temperature Distribution (Normal Operation in Earth Orbit).....	22
2.3-1	2-D HSU & HSHX Thermal Model .....	27
2.3-2	Steady-State-Brayton Cycle Operating 2-D Heat Source Model .....	28
2.3-3	Heat Source Heat Exchanger Steady-State Performance ....	29
2.3-4	HSU Transient Response-Heatup from ACHX Cooled Equilibrium Launch with Insulation Doors Open .....	30
2.3-5	HSU Transient Response - Engine Startup, Insulation Doors Closed .....	32
2.3-6	Heat Source Temperature History - Orbital Decay Entry, $\gamma_e = 0.0^\circ$ Tumbling .....	33

## ILLUSTRATIONS (Cont'd)

Figure	2.3-7	Heat Source Temperature History - Lunar Return Entry, $\gamma_e = -15^\circ$ , Tumbling .....	34
	2.3-8	Thermal Simulation Aeroshell .....	35
	2.3-9	HSRV Steady-State Temperature Distribution SPF Test, Coldwall @ $0^\circ\text{F}$ .....	36
	3.1-1	Reentry Conditions .....	40
	3.1-2	Aerodynamic Load .....	42
	3.1-3	Aerodynamic Shear.....	44
	3.1-4	Maximum Convective Heating Rates .....	45
	3.1-5	Stagnation Point (Integrated Heat Load) .....	46
	3.2-1	HSRV Design - Aerodynamic Heating Stations .....	51
	3.2-2	Alternate Fence Geometries.....	55
	3.2-3	Correlation of Fence Effectiveness Cylindro - Conical Fence .....	57
	3.2-4	Variation of Normal Force Coefficient With Angle of Attack .....	58
	3.2-5	Variation of Axial Force Coefficient .....	59
	3.2-6	Variation of Pitching Moment With Angle of Attack .....	61
	3.2-7	Damping in Pitch Derivative ( $M = 1.1$ ) .....	62
	3.2-8	Damping in Pitch Derivative (Mach No. Dependence).....	63
	3.2-9	Early Angle of Attack Histories (Rearward Entry) .....	65
	3.2-10	Angle of Attack Histories (Worst Case Tumble) .....	66

## ILLUSTRATIONS (Cont'd)

Figure	3.2-11	Angle of Attack Envelope History (Orbit Injection Tumble).....	67
	3.2-12	Terminal Stability Limits .....	69
	3.2-13	Ablation Phenomena Variation -Lunar Return Skip Limit ....	71
	3.2-14	Effect of Ablation Induced Asymmetries on Aerodynamics - Lunar Return Skip Tumble.....	72
	3.2-15	Terminal Performance with Wind Shear & Gusts Orbit Injection Tumble .....	74
	3.2-16	Shock Standoff Distance .....	75
	3.2-17	Fuel Capsule Heating (Rearward Entry Lunar Return Skip)...	77
	3.2-18	Fuel Capsule Heating (Lunar Return Skip Limit Tumble).....	78
	3.2-19	Fuel Capsule Heating (Lunar Return, $\gamma = -15^\circ$ ) Rearward Entry .....	79
	3.2-20	Capsule Heating (Lunar Reentry $\gamma_E = -15^\circ$ Tumble).....	80
	3.2-21	Capsule Heating (Orbit Injection $\gamma_E = -20^\circ$ Tumble) .....	81
	3.2-22	Fuel Capsule Heating (Rearward Entry Orbit Injection) .....	82
	3.2-23	Capsule Heating (Orbit Decay Tumble) .....	83
	3.2-24	Stagnation Point Heating Comparison (Orbit Decay).....	84
	3.2-25	Stagnation Point Heating Comparison (Orbit Decay).....	85
	3.2-26	Drag Coefficient Dependence on Dynamic Motion .....	86
	3.2-27	Aeroshell Heating (Orbit Decay) .....	88
	3.2-28	Aeroshell Heating (Orbit Decay) .....	89
	3.2-29	Aeroshell Heating (Orbital Decay Tumble) .....	90

## ILLUSTRATIONS (Cont'd)

Figure	3.2-30	Aeroshell Heating (Lunar Skip Limit Return).....	91
	3.2-31	Aeroshell Heating (Lunar Skip Limit Return Tumble).....	92
	3.3-1	Two-Dimensional Model of HSRV Heat Source.....	96
	3.3-2	HSHX Surface Temperature .....	100
	3.3-3	Steady State-Brayton Cycle Operating 2-D Heat Source Model .....	101
	3.3-4	Heat Source Temperature History Deployed to Space.....	103
	3.3-5	Steady State - Deployed to Space 2-D Heat Source Model .....	104
	3.3-6	HSU Transient Response Heatup from ACHX Cooled Equilibrium Launch with Insulation Doors Open.....	106
	3.3-7	HSU Transient Response to Equilibrium Heatup from ACHX Cooled Equilibrium Launch with Insulation Doors Open .....	107
	3.3-8	HSU Transient Response (Four Hours After Launch) .....	108
	3.3-9	HSU Transient Response Startup from Equilibrium Engine Fails to Start - Insulation Door Closed .....	110
	3.3-10	HSU Transient Response - Engine Failure Insulation Doors Closed .....	111
	3.3-11	Heat Source Temperature History Orbit Injection Abort $\gamma = -20^\circ$ Tumbling .....	112
	3.3-12	Heat Source Temperature History Orbital Decay Reentry $\gamma_e = 0.0^\circ$ Tumbling .....	114
	3.3-13	Heat Source Temperature History Lunar Return Entry $\gamma_e = -5.4^\circ$ Tumbling .....	115
	3.3-14	Heat Source Temperature History Lunar Return Entry $\gamma_e = -15^\circ$ Tumbling .....	116

## ILLUSTRATIONS (Cont'd)

Figure	3.3-15A	ACHX Channel Cross-Section View .....	117
	3.3-15B	ACHX Channel/HSU Cross-Section View .....	117
	3.3-16	S. S. Temp. vs. Nusselt Number ACHX Operating With Nitrogen Coolant - 2-D CINDA Results Design Channel.....	121
	3.3-17	Steady-State ACHX Operation - 2-D Heat Source Model ...	123
	3.3-18	ACHX Mass Flow Rates Design Channel.....	125
	3.3-19	Inlet Tube Mach Number - Design Channel .....	126
	3.3-20	Header Mach Number - Design Channel .....	128
	3.3-21	Finned Channel.....	131
	3.3-22	S. S. Temp. vs. Nusselt Number ACHX Operating with Nitrogen Coolant-2-D CINDA Results - Finned Channel.....	132
	3.3-23	ACHX Mass Flow Rates - Finned Channel .....	133
	3.3-24	Inlet Tube Mach Number - Finned Channel .....	134
	3.3-25	Header Mach Number - Finned Channel .....	135
	3.3-26	Maximum ACHX Working Pressure vs. Temperature. ....	142
	3.3-27	Distribution of HSU Loads at Strut/Ring Attachments .....	144
	3.4-1	AVCOAT 5026-39/HC-G Requirements-Orbital Decay Entry (Stagnation & Midcone Points) .....	151
	3.4-2	AVCOAT 5026-39/HC-G Requirements-Orbital Decay Entry (Shoulder, Base, Cylinder Points) .....	152
	3.4-3	Fence & Bolt Temperature Histories - Orbital Decay Return-Tumbling.....	155

## ILLUSTRATIONS (Cont'd)

Figure	3.4-4	Variation of Aeroshell Facesheet Thickness Earth Orbit Design and INT-21 Reentry Loads .....	157
	3.4-5	Fence Pressures - INT-21 Peak N/W .....	160
	3.4-6	Temperature Profiles in 2-D Fence- Orbit Decay - Tumble Case .....	162
	3.4-7	Thermal Stress in Fence at Peak Loads .....	163
	3.4-8	Thermal Stress in Fence -Worst Temperature Differential	164
	3.4-9	INT-21 Reference Design, Normal Operations In Orbit...	165
	3.4-10	HSRV Steady-State Temperature Distribution and Heat Loss Summary, Earth Orbital Vehicle, Normal Operation in Orbit (INT-21).....	169
	3.4-11	HSRV Steady-State Temperature Distribution and Heat Loss Summary, SPF Test @ 0°F.....	170
	3.4-12	HSRV - Earth Orbital (INT-21) .....	172
	3.4-13	HSRV (INT-21) Reference Design Detail Layout-Sheet 1. .	175
	3.4-14	HSRV (INT-21)Reference Design Detail Layout-Sheet 2..	176
	3.4-15	HSRV (INT-21) Reference Design Detail Layout-Sheet 3..	177/178
	3.4-16	AVCOAT 5026-39/HC-G Requirements, Skip Limit Lunar Return-Stagnation and Midcone Point .....	182
	3.4-17	AVCOAT 5026-39/HC-G Requirements, Skip Limit Lunar Return- Shoulder & Cylinder Base .....	183
	3.4-18	Fence & Bolt Temperature Histories - Lunar Return - Skip Limit Tumbling .....	185
	3.4-19	Super-Orbital Reentry Vehicle Reference Design, Normal Operation in Orbit .....	186
	3.4-20	Super-Orbital (Increased Strut Area) HSRV Steady-State Temperature Distribution, Normal Operation in Earth Orbit .....	187



## ILLUSTRATIONS (Cont'd)

Figure	3.4-21	Steady-State Temperature Distribution, Super-Orbital Reentry Vehicle, Crushup Design, Normal Operation in Orbit .....	188
	3.4-22	HSRV Super-Orbital .....	192
	3.4-23	Super-Orbital System Weights .....	193
	3.4-24	Super-Orbital Layout (-15°) LA13244 .....	196
	3.4-25	Aeroshell Thermal Simulation.....	202
	4.0-1	Spiral Heat Source Heat Exchanger .....	204
	4.1-1	Evaporation Rates of Some Elements Under Vacuum.....	208
	4.1-2	Comparative Stress Rupture Properties of Sheet Material	209
	4.1-3	Comparative Tensile Data, Sheet Material Solution Heat Treated Condition.....	210
	4.1-4	Effect of Ageing for 3000 hr. on Room Temperature Bend Ductility .....	212
	4.1-5	Evaporation Problem of Materials in Vacuum Using an Evaporation Dequence for Thin Specimens of Type 316 Stainless Steel Exposed to High Vacuum Between 1475° and 1835°F as an Example .....	214
	4.2-1	Spiral Heat Source Heat Exchanger .....	216
	4.2-2	Model Used for Heat Transfer Analysis .....	220
	4.2-3	Heat Source Heat Exchanger Steady State Performance...	222
	4.2-4	Change of Flow Rate During Startup .....	223
	4.2-5	Gas Inlet Temperature to HSHX During Startup .....	224
	4.2-6	Gas Outlet Temperature During Startup .....	226
	4.2-7	Response of the Maximum Effective Source Temperature During Startup .....	228

## ILLUSTRATIONS (Cont'd)

Figure	4.2-8	Tube Temperature During Startup (Mid Point Along Tube Length) .....	229
	4.2-9	Inlet Manifold Temperature During Startup .....	230
	4.2-10	Outlet Manifold Temperature During Startup .....	231
	4.2-11	Heat Source Deployed .....	233
	4.2-12	Response of Average Tube Temperature During Shutdown	234
	4.2-13	Inlet Manifold Temperature During Shutdown .....	235
	4.2-14	Outlet Manifold Temperature During Shutdown .....	236
	4.2-15	Insulation Deployed .....	237
	4.2-16	Average Temperature of HSHX Tubes During Shutdown...	238
	4.2-17	Inlet Manifold Temperature During Shutdown .....	240
	4.2-18	Outlet Manifold Temperature During Shutdown .....	241
	4.2-19	Effective Heat Source Temperature Distribution After 2 hrs. of Cooling During Shutdown .....	242
	4.3-1	Spiral Heat Source Heat Exchanger .....	248
	4.3-2	Fabrication of Heat Exchanger Tubes .....	249
	4.3-3	Fabrication of "U" Tube Section .....	250
	4.3-4	Fabrication of Tube Set (9 Required) .....	251
	4.3-5	Fabrication, Ring Manifolds .....	252
	4.3-6	Fabrication, Ring Manifolds (Continued) .....	253
	4.3-7	HSHX - Assembly .....	254
	4.3-8	HSHX - Assembly - 2 .....	255

## TABLES

Table	2.0-I	Baseline Design Criteria .....	6
	2.0-II	Steady-State Heat Source Heat Exchanger Specification ..	7
	2.2-I	Loads Summary .....	18
	2.2-II	Heating Summary.....	19
	2.2-III	HSRV (Earth Orbital) Performance Summary .....	23
	2.2-IV	HSRV (Super-Orbital Design) Performance Summary ....	25
	2.4-I	Conclusions .....	37
	3.2-I	Trajectory Entry Data Summary .....	47
	3.2-II	Influence of Initial Tumble Rate (Orbit Injection) .....	49
	3.2-III	Entry Loads Summary .....	50
	3.2-IV	Heating Summary.....	52
	3.2-V	HSRV Mass Characteristics .....	64
	3.2-VI	Ablation Dependent Characteristics and Total Change (Lunar Return - Skip Limit) .....	70
	3.3-I	Heat Source Thermal Design Criteria .....	93
	3.3-II	ACHX Cooling Requirements for Ground Operation .....	98
	3.3-III	ACHX Heat Source Interface Boundary Condition Variations .....	119
	3.3-IV	ACHX Performance Summary.....	120
	3.3-V	Summary of Structural Design Requirements.....	137
	3.3-VI	Structural Design Criteria .....	138
	3.3-VII	Summary of HSU Stress Analysis .....	139

# TABLES (Concluded)

Table	3.4-I	HSRV Heat Shield Requirements AVCOAT 5026 -39/HC-G .....	153
	3.4-II	Mass Properties Summary, HSRV-Earth Orbital, 84.0 Dia. 25 KW <sub>t</sub> (Ref. LA 13235) .....	179
	3.4-III	Mass Properties Summary, HSRV Super-Orbital, at -15 <sup>0</sup> , 84.0 Dia., 25 KW <sub>t</sub> , (Ref. LA 13244) .....	194
	3.4-IV	Mass Properties Summary, HSRV-Super-Orbital at -25 <sup>0</sup> , 88.0 Dia., 25 KW <sub>t</sub> .....	195
	3.4-V	Mass Properties Summary, HSRV, Super-Orbital at -38 <sup>0</sup> , 92.0 Dia., 25 KW <sub>t</sub> .....	196
	3.4-VI	Aeroshell Concepts for Thermal Similitude Tests.....	198
	3.4-VII	Aeroshell Costs for Thermal Similitude Tests .....	199
	4.1-I	Mechanical Properties of Candidate Superalloys.....	206
	4.1-II	Physical Properties of Candidate Alloys .....	213
	4.2-I	Pressure Drop Summary .....	218
	4.2-II	Haynes 188 Pressure Containment Summary.....	244

## 1.0 INTRODUCTION

This report summarizes the results of the Heat Source Reentry Vehicle (HSRV) Design Study. The study has been performed for the NASA Lewis Research Center under Contract NAS 3-14397. Overall objectives of the study were:

- modification of the reference Isotope Reentry Vehicle (IRV) design developed under NAS 3-10938 to incorporate a revised fuel capsule design.
- assessment of the revised reentry vehicle design capability for surviving super-orbital reentry.
- development of layout drawings incorporating the design revisions
- modification of the NAS 3-10938 Heat Source Heat Exchanger (HSHX) design to allow specification of a super-alloy as the fabrication material.

The design of the HSRV and the HSHX is to be compatible with both flight requirements and the Brayton Engine presently being investigated at the NASA Lewis Research Center.

Aerodynamic data used to establish the performance of the turn-around fence shown in Figure 1.0-1 are based on the fence test program conducted at the NASA Ames Research Center.

The HSHX design has been developed by the Garrett AiResearch, Los Angeles Division, under a subcontract from Avco. Results of the subcontract effort are summarized in this report.

Figure 1.0-1 shows an exploded perspective view of the HSRV design developed during this study. The isotope Heat Source Unit (HSU) consists of a circular planar array of graphite encased refractory isotope fuel capsule (Heat Sources) containing  $\text{PuO}_2$  fuel. Approximately 66 capsules are required to achieve a net thermal output power of 25 KW. The HSU is comprised of the Heat Source array mounted on a refractory support plate which also serves as an Auxiliary Coolant Heat Exchanger (ACHX) duct network during launch pad operations. A refractory truss is used to attach the HSU to the aluminum honeycomb aeroshell. Low conductivity vacuum multi-foil insulation is placed around the HSU and HSHX to minimize heat loss to the reentry vehicle and temperature sensitive subsystems.

## HEAT SOURCE REENTRY VEHICLE ASSEMBLY

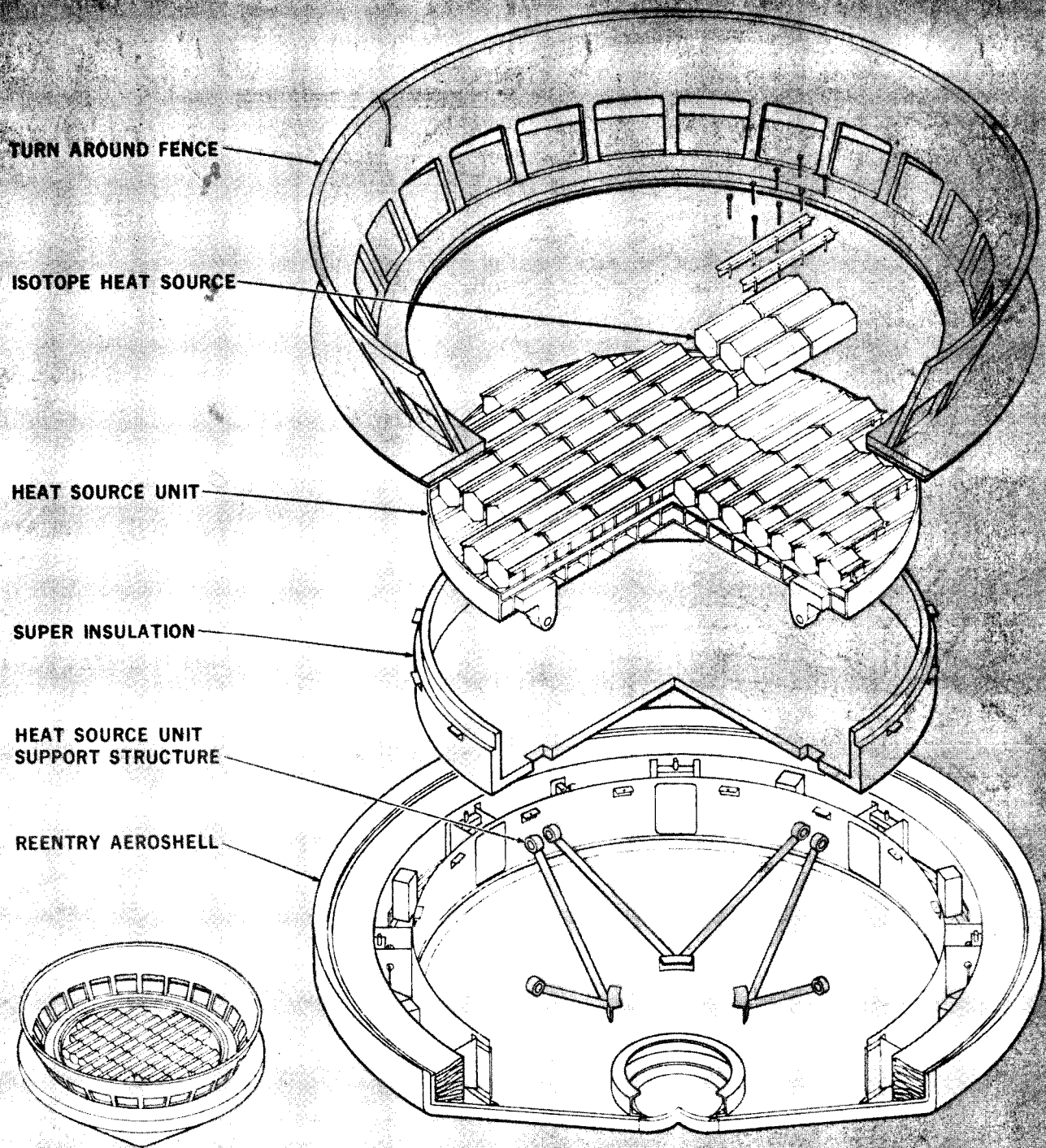


FIGURE 1.0-1

Transfer of heat from the HSU to the HSHX is accomplished solely by radiation.

The HSHX (Figure 1.0-2) is one element in the closed gas loop of the Brayton engine. Major elements of the Brayton engine gas loop are similar to those described in the NAS 3-10938 final report.

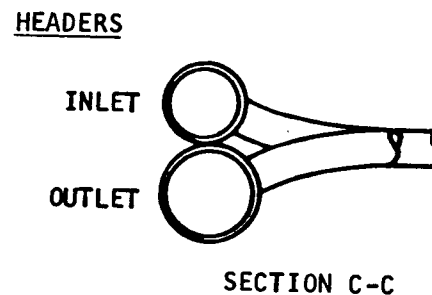
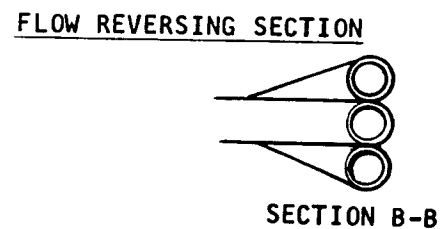
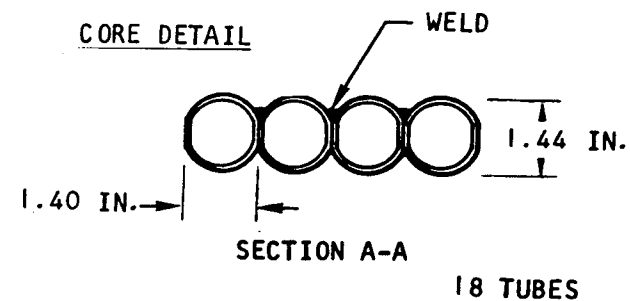
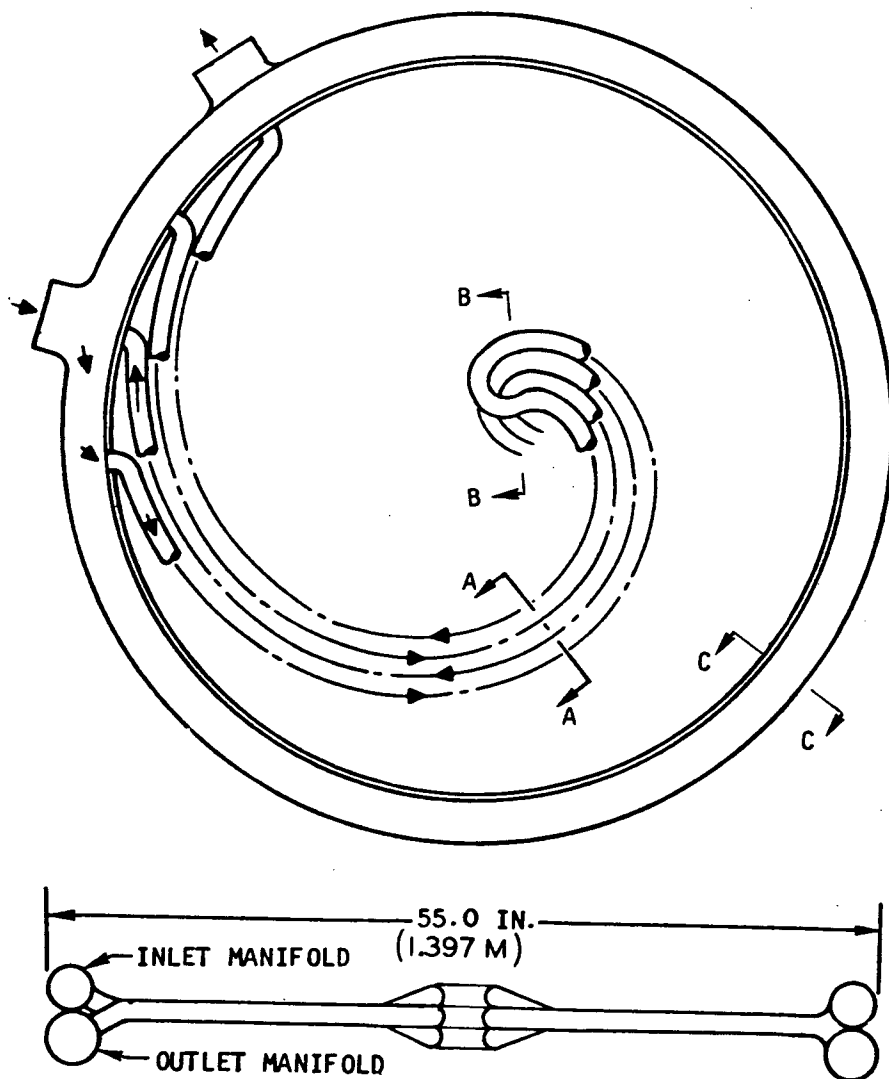


Figure 1.0-2 SPIRAL HEAT SOURCE HEAT EXCHANGER



## 2.0 SUMMARY

This study consisted of the following three separate elements:

- Task I - Preliminary Modification
- Task II - Design
- Task III - Detail Design

The summary contains a brief review of the task efforts, significant results, and study conclusions and recommendations.

Baseline design criteria established by NASA at the outset of the study are presented for the Heat Source Reentry Vehicle in Table 2.0-I and for the Heat Source Heat Exchanger in Table 2.0-II.

To avoid confusion in terminology the following definitions will apply throughout this report:

- Capsule: A capsule is a metallic closed receptacle encasing radio-isotope fuel; the receptacle, with or without venting, may be a structural member protected by inner and outer cladding.
- Heat Source: A heat source (HS) is a capsule with reentry protection added to meet specific mission environments.
- Heat Source Unit: A heat source unit (HSU) is an assembly of heat sources.
- Heat Source Reentry Vehicle: A heat source reentry vehicle (HSRV) consists of an aerodynamic thermal protection and support structure enclosing a heat source unit.
- Heat Source Heat Exchanger: The heat source heat exchanger (HSHX) is the Brayton cycle gas heat exchanger which receives its heat by radiation from the isotope heat sources.

### 2.1 TASK I - PRELIMINARY MODIFICATION

Under this task the reference Isotope Reentry Vehicle (IRV) design developed under NAS 3-10938 (Figure 2.1-1) was modified to incorporate the revised isotope fuel capsule and thermal protection casing (heat source) shown in Figure 2.1-2. The basic reentry vehicle and HSU support scheme remained

TABLE 2.0-I

BASELINE DESIGN CRITERIA

Thermal Loading - Heat Source Array	25 kWt
- Individual Heat Source	400 W
Maximum Heat Source Operating Temperature	<2000°F
Maximum Heat Source Transient (Instantaneous) Temperature at the Capsule Strength Member	<3000°F
Maximum Refractory Structure Temperature with Auxiliary Cooling Operation	<350°F
Heat Sink Material	BeO or C
Minimum Heat Sink Capability	700° F/hr @ 2000°F
Heat Leak Design Goal	2 KW
Temperature Limitations Goal within Aeroshell	Table 3-10, NASA CR-72555

TABLE 2.0-II

STEADY STATE HEAT SOURCE HEAT EXCHANGER SPECIFICATIONS

FLUID	He-Xe, 83.8 MW
FLOW RATE	0.85 lb/sec
$\Delta P/P$	$\leq 3.3\%$
TEMPERATURE IN	1600°R
TEMPERATURE OUT	2060°R
PRESSURE IN	31.8 psia
HEAT INPUT	23.0 kWt

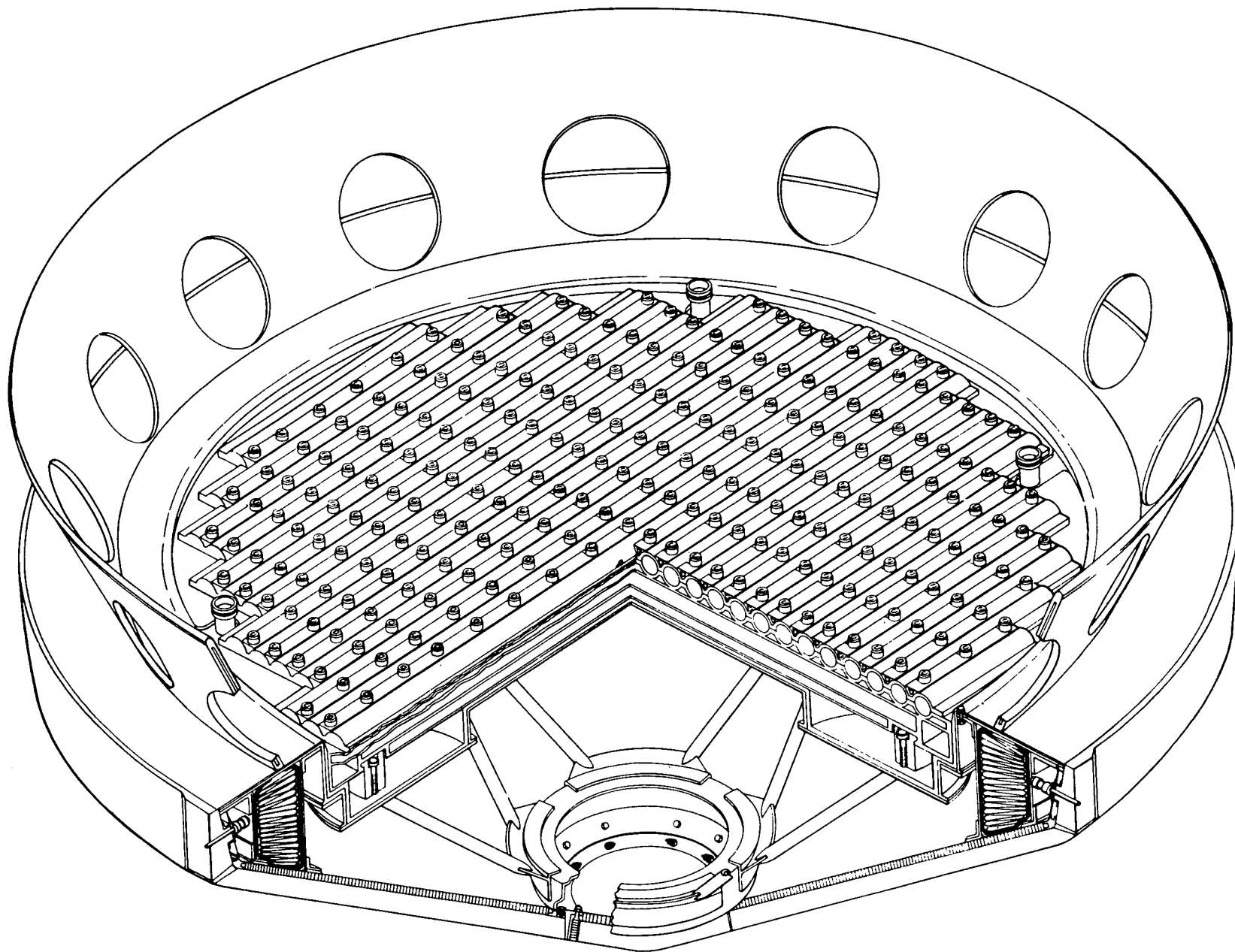
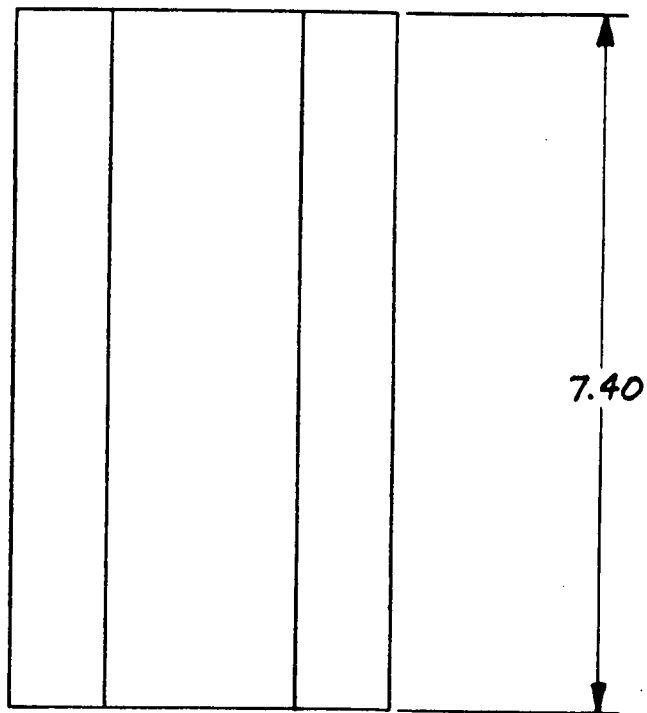
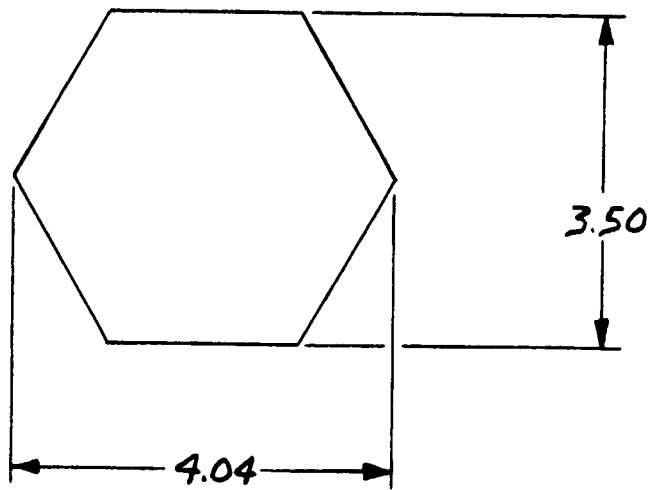


Figure 2.1-1 ISOTOPE REENTRY VEHICLE REFERENCE DESIGN (NAS 3-10938)



MATERIAL: POCO Graphite

Figure 2.1-2 REFERENCE HEAT SOURCE

essentially unchanged, however, the HSU design required extensive modification reflecting the new heat source dimensions and number. A cross section view of the revised HSRV is shown in Figure 2.1-3. Several significant design revisions can be noted when comparing this layout with the reference NAS 3-10938 IRV design (Figure 3-127, reference 2-1-1). Most noteworthy, is an overall vehicle diameter increase from 68" to 84". This change is attributable to the:

- HSU array growth from 49" to 56.5"
- Allowance of up to 1.5" for multi-foil insulation surrounding the HSU.
- HSU depth (stack-height) increase due to heat source dimension growth.

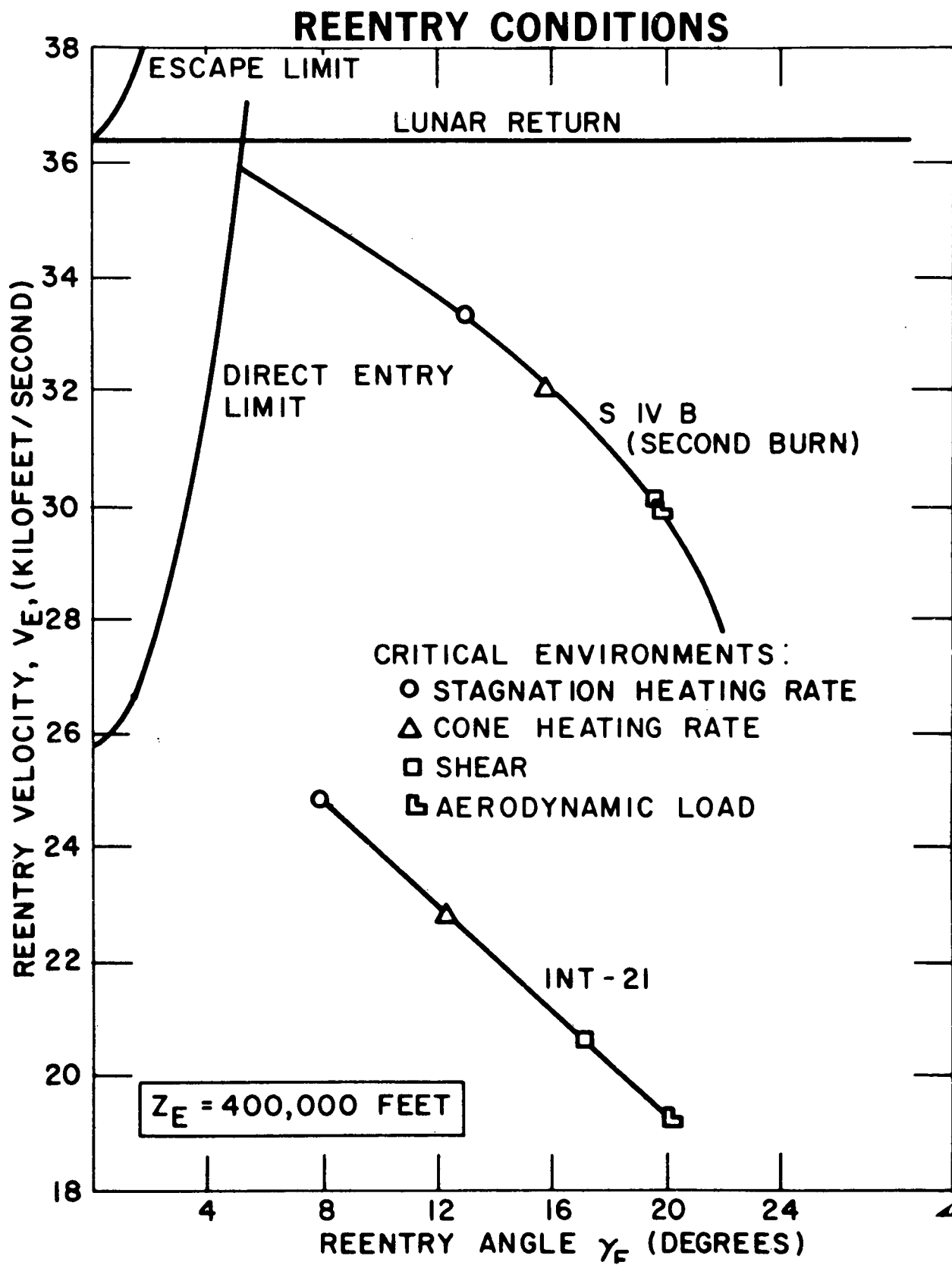
The method of attachment of the support strut to the HSU was also modified to ease the assembly procedure for the insulation foils. Addition of the graphitic thermal protection sleeves to the individual fuel capsules increased the thermal capacitance of the HSU enough to negate the need for the Beryllium oxide heat sink provided in the NAS 3-10938 design. Finally, the turn-around fence design was modified to reflect the performance data developed in the aerodynamic test program recently completed at NASA-Ames Research Center.

A brief systems analysis of possible launch and injection vehicle failures was conducted to establish the reentry vehicle (RV) design performance requirements. This review included possible earth orbital, lunar injection, and lunar return failure modes so as to assess the capability of the reference HSRV to perform under lunar mission reentry conditions. Resultant initial reentry conditions at an altitude of 400,000 feet are summarized in Figure 2.1-4.

Based on these initial conditions loads were computed for an assumed vehicle base diameter of 84", a weight at entry of 2900 pounds, and an  $\alpha$  (angle of attack) of zero at entry. The integrated heat loads are well within the capability of the specified Avco 5026-39 heat shield for the design envelope shown on Figure 2.1-5. However, the aerodynamic loads environment for the three classes of reentry do effect the structural design of the HSRV as the maximum structural loading encountered during an abort from an earth orbital injection trajectory is approximately 20% greater for the INT-21 launch vehicle than for the Saturn I-B ascent trajectories evaluated during the NAS 3-10938 study. This load increase coupled with the growth in HSU array diameter substantially increased the structural weight of the HSU and support struts.

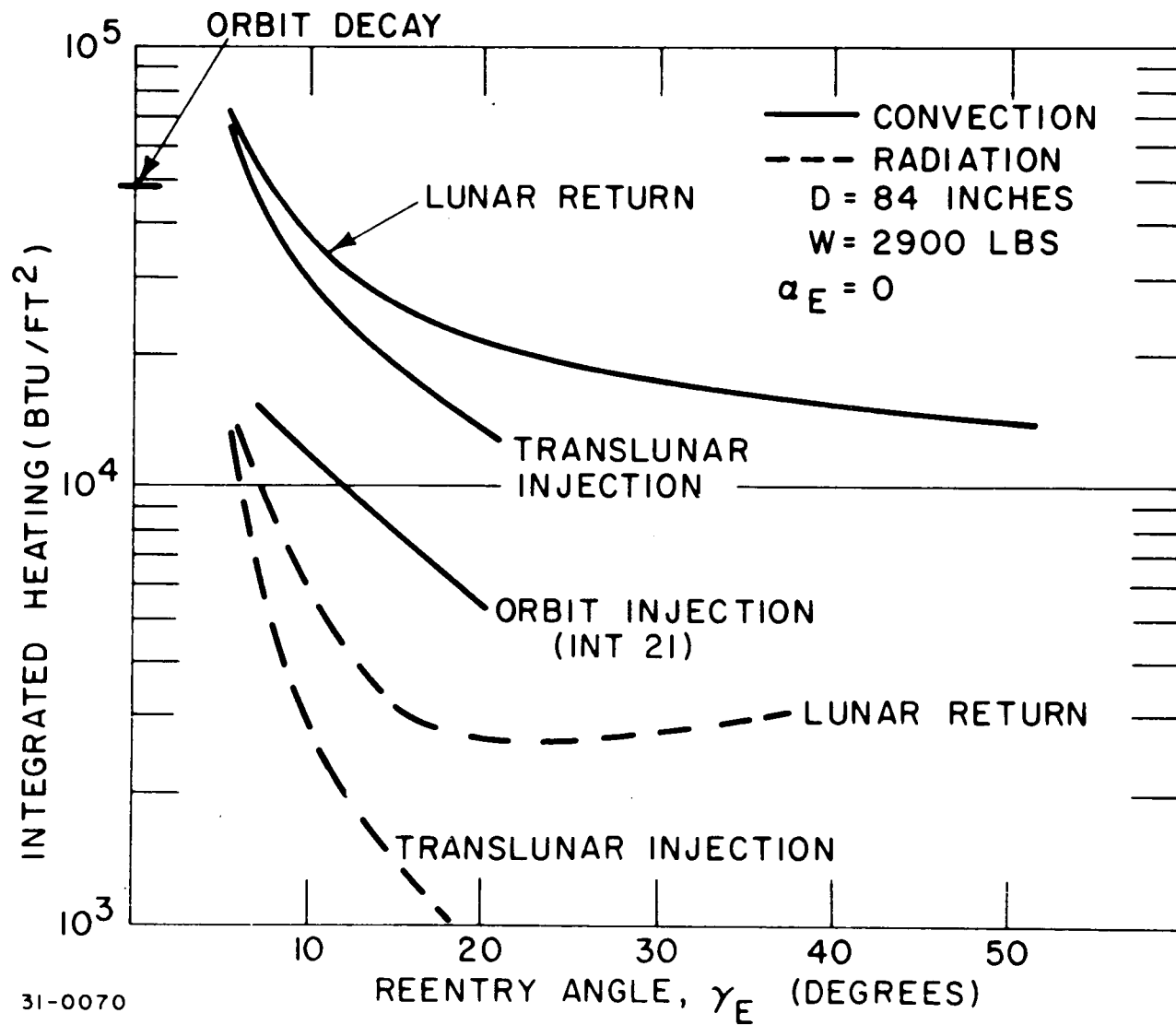
Possible loads resulting from translunar abort and lunar return reentries can be substantially greater than those achieved from earth orbit injection trajectories (Figure 2.1-6). Ideally, the reference HSRV design, (Figure 2.1-3) requires some modification to efficiently react the type of structural loads







# STAGNATION POINT INTEGRATED HEAT LOAD

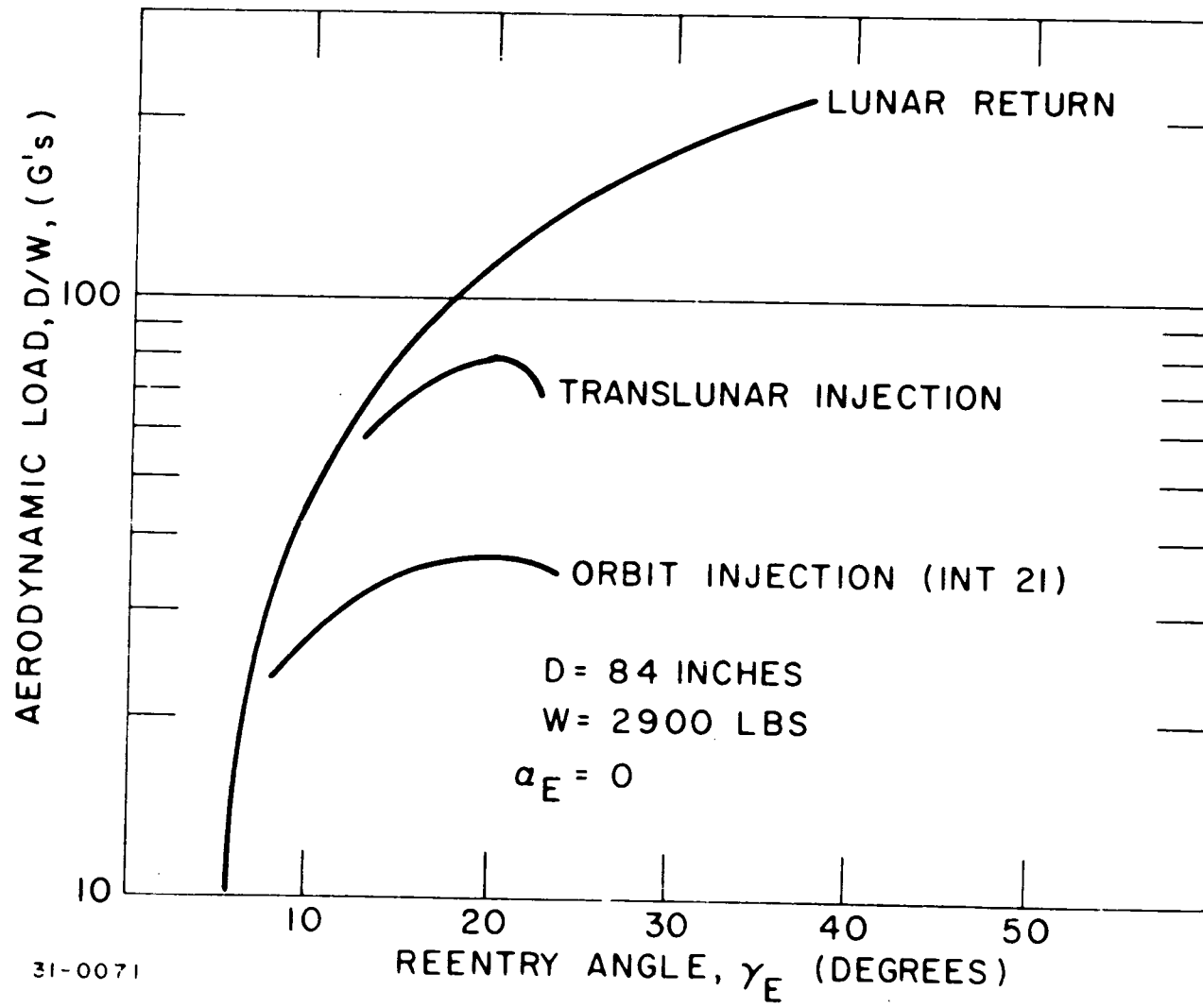


31-0070



FIGURE 2.1-6

## AERODYNAMIC LOAD



environment that can be encountered in parabolic reentry situations. Such a modification is defined in section 2.2.

The basic heat source heat exchanger developed in the previous study is illustrated in Figure 2.1-7. The spiral heat exchanger consists of 18 tubes which spiral out from a center manifold and terminate at two tubular ring headers which form the circumference of the heat exchanger. The Brayton cycle gas is distributed to nine of the spiral tubes through the upper ring header. The gas is collected in the central reversing manifold and enters the nine return tubes which makes the return pass across the heat exchanger core to the bottom outlet ring header. The use of this type of heat exchanger results in an almost flat temperature distribution across the isotope heat source as well as across the HSHX during normal operation.

During this task the heat source heat exchanger design was modified to accommodate the larger isotope heat source array. This was done by slightly increasing the length of the spiral tubes to obtain a 55-in. diameter heat exchanger. Also in Task I, the use of a superalloy for the HSHX for a ground test system was contrasted with the columbium design. After reviewing the Task I results, NASA selected Haynes-188 as the HSHX material for the ground test unit superalloy option.

## 2.2 TASK II - DESIGN

A detailed dynamic reentry analysis was performed to establish design requirements for the HSRV. Maximum aerodynamic loads environment from the selected design trajectories are summarized in Table 2.2-I for the two classes of reentry - earth orbital and lunar return. Initial HSRV attitude conditions assumed for the structural and heating loads analysis were:

- HSRV tumbling at a rate of 6 RPM
- HSRV stabilized rearward ( $\alpha = 180^\circ$ ), no spin
- HSRV stabilized forward ( $\alpha = 0^\circ$ ), no spin,

where  $\alpha$  is defined as angle of attack of the HSRV.

In the first two cases the resultant dynamic loads history have been determined as encountered by the HSRV while it achieves a "stable", normal reentry mode - i. e., the vehicle stops tumbling or rights itself ( $\alpha = 0^\circ$ ) prior to encountering peak reentry heating or load conditions.

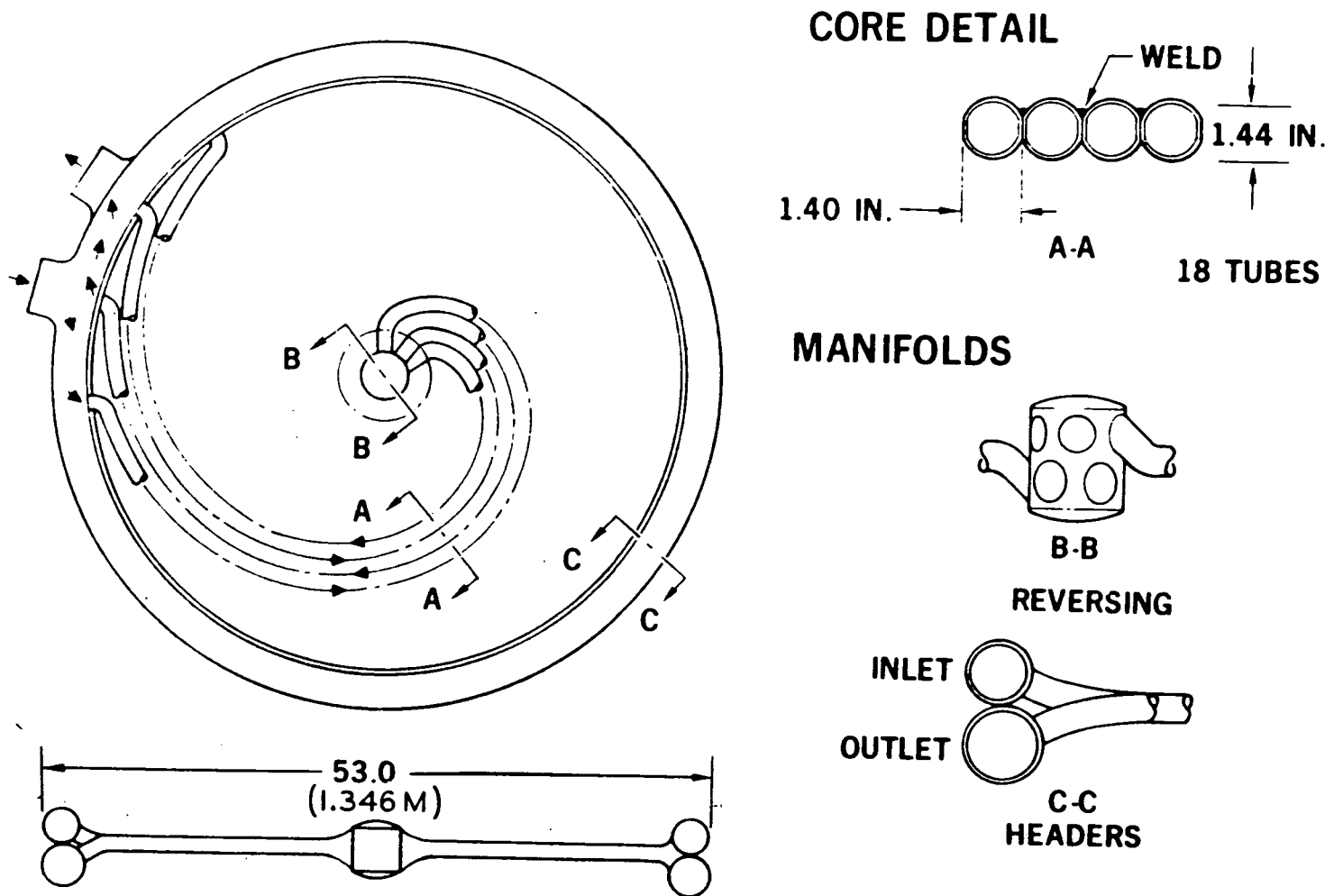


Figure 2.1-7 SPIRAL HEAT SOURCE HEAT EXCHANGER (NAS 3-10938 DESIGN)

Maximum dynamic heating environments for several points on the HSRV are summarized in Table 2.2-II for the two classes of reentry. The resultant heat shield thicknesses for an earth entry thermal protection system are shown in Figure 2.2-1. Avcoat 5026-39 (the Apollo heat shield), a well characterized, lightweight low density ablator is the specified thermal protection material for both earth orbital and super orbital reentries. Design thickness at all points on the reentry vehicle (RV) were dictated by the orbital decay heating loads.

Figure 2.2-2 shows a partial cross-section view of the reference earth orbital (INT-21 launch trajectory) HSRV design. In this concept 66 heat sources in a circular planar array on a Cb-1%Zr support structure comprise the Heat Source Unit (HSU). Launch pad cooling of the HSU is achieved by passing nitrogen through the trapezoidal auxiliary coolant heat exchange (ACHX) passages located below the heat sources. HSU reentry loads are reacted into the aluminum honeycomb aeroshell through a series of T-111 struts that act as a support truss. Resultant "kick" loads dictate a need for Cb-1%Zr fittings at the HSU/strut reaction points. The fitting configuration is also controlled by assembly requirements for the multifoil insulation subsystem.

Multifoil insulation with an effective conductivity of .002 BTU/ft-hr-<sup>°</sup>F surrounds the HSU-HSHX cavity. It is also placed around the T-111 struts to maintain the desired heat balance and temperature distribution throughout the HSRV. The resultant heat leak through the HSU "half" of the insulation system is 657 watts. A temperature distribution for the HSRV during normal operation in earth orbit is shown in Figure 2.2-3. These temperatures are well within the capability of the specified materials. Achievement of the desired heat leak and temperature distribution in the aeroshell has been attained by using heavy Al face sheets on the honeycomb shell and a solid Al section mating with the Ti attachment ring.

Performance characteristics of the earth orbital HSRV design are summarized in Table 2.2-III.

The 25 KW<sub>t</sub> super orbital HSRV configuration, as shown in Figure 2.2-4 is identical to the 25 KW<sub>t</sub> earth orbital configuration described previously, except in the areas where design changes were necessary to increase the structural capability in order to survive the higher inertia loading of super-orbital reentry.

The aeroshell face sheet thickness has been increased as has the 2D graphite fence thickness. Structural capability of the heat source plate was increased by the combined effects of increasing the face sheet thicknesses and by spacing them further apart thus increasing the total plate depth.

TABLE 2.2-I

**LOADS SUMMARY**

MISSION PHASE (ENTRY MODE)	DYNAMIC PRESSURE (ATM.)	(D/W) <sub>MAX</sub>	(N/W) <sub>MAX</sub>	(X/W) <sub>N</sub>	FREQUENCY (CPS)
ORBIT INJECTION					
A) FORWARD	.592	35.5			
B) REARWARD	.698	42.0	4.3	32.0	3.5
C) TUMBLE *	.706	42.7	4.6	31.0	3.5
ORBIT DECAY					
A) FORWARD	.130	7.8			
B) REARWARD	.131	7.9	.1	7.8	1.5
C) TUMBLE *	.135	8.1	.5	6.0	1.6
LUNAR RETURN (SKIP LIMIT)					
A) FORWARD	.0861	5.2			
B) REARWARD	.0888	7.0	.8	4.0	1.2
C) TUMBLE *	.0903	7.5	1.2	3.3	1.3
LUNAR RETURN ( $\gamma_E = -15^\circ$ )					
A) FORWARD	1.27	77.0			
B) REARWARD	1.48	89.0	9.0	70.6	5.1
C) TUMBLE *	1.54	93.3	11.2	65.5	5.2

\*6 RPM



TABLE 2.2-II

**HEATING SUMMARY**

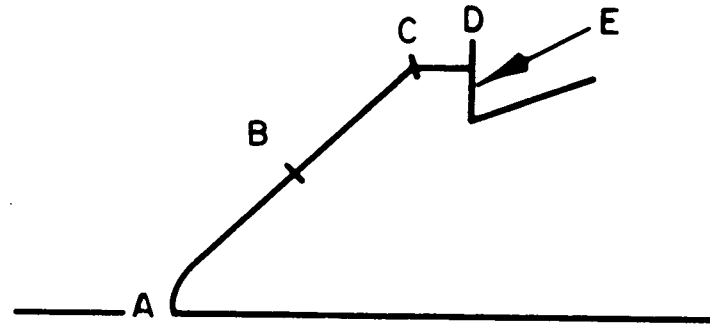
	ORBITAL		LUNAR RETURN	
	MAXIMUM RATE <sup>1</sup> W/CM <sup>2</sup>	INTEGRATED LOAD <sup>2</sup> W SEC/CM <sup>2</sup>	MAXIMUM RATE <sup>3</sup> W/CM <sup>2</sup>	INTEGRATED LOAD <sup>4</sup> W SEC/CM <sup>2</sup>
STAGNATION POINT	355	43700	2010	71600
CONE	117	17300	663	20700
SHOULDER	502	24260	2910	47000
FENCE				
INSIDE	50	5200	470	4380
OUTSIDE	188	17010	1160	30680
CAPSULE	80	11500	660/220 <sup>5</sup>	6100/1350

1. ORBIT INJECTION, PEAK CYCLE RATE FOR TUMBLE
2. ORBIT DECAY
3.  $\gamma_E = -15^\circ$ , PEAK CYCLE RATE FOR TUMBLE
4. SKIP LIMIT
5. CONVECTIVE/RADIATIVE



FIGURE 2.2-1

# HEAT SHIELD REQUIREMENTS AVCOAT 5026-39/HC-G



LOCATION	HEAT SHIELD THICKNESS		DESIGN TRAJECTORY	INTEGRATED HEATING (JOULES/CM <sup>2</sup> )
	(CM.)	(IN.)		
A	4.03	1.59	ORBITAL DECAY- ZERO ANGLE OF ATTACK	43700
B	3.55	1.40	"	17300
C	3.20	1.26	ORBITAL DECAY- TUMBLING	24260
D	2.97	1.17	"	10030
E	2.89	1.14	"	6970



FIGURE 2.2-2

## EARTH ORBITAL (INT-21)

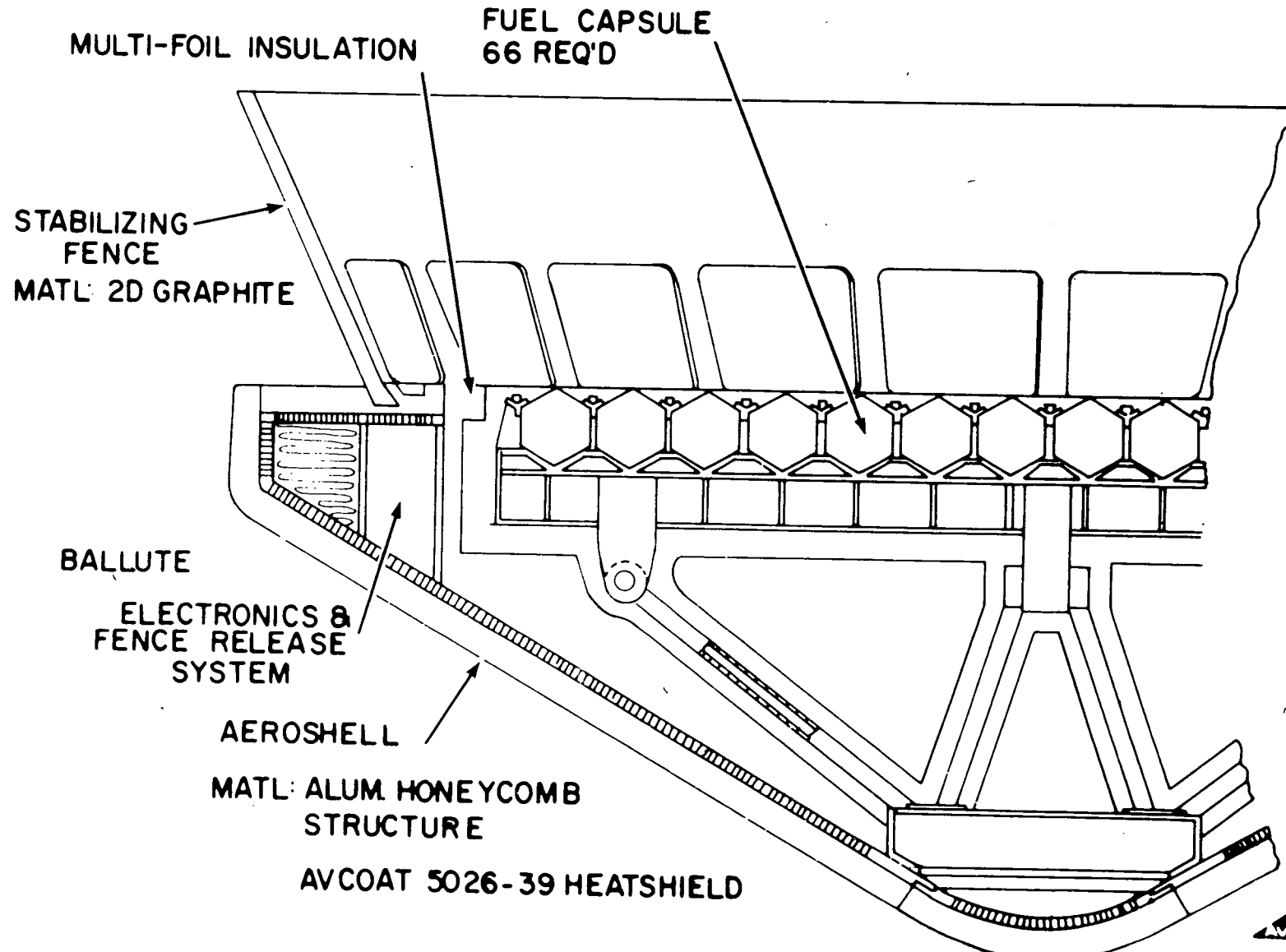


FIGURE 2. 2-3

# HSRV STEADY-STATE TEMPERATURE DISTRIBUTION NORMAL OPERATION IN EARTH ORBIT

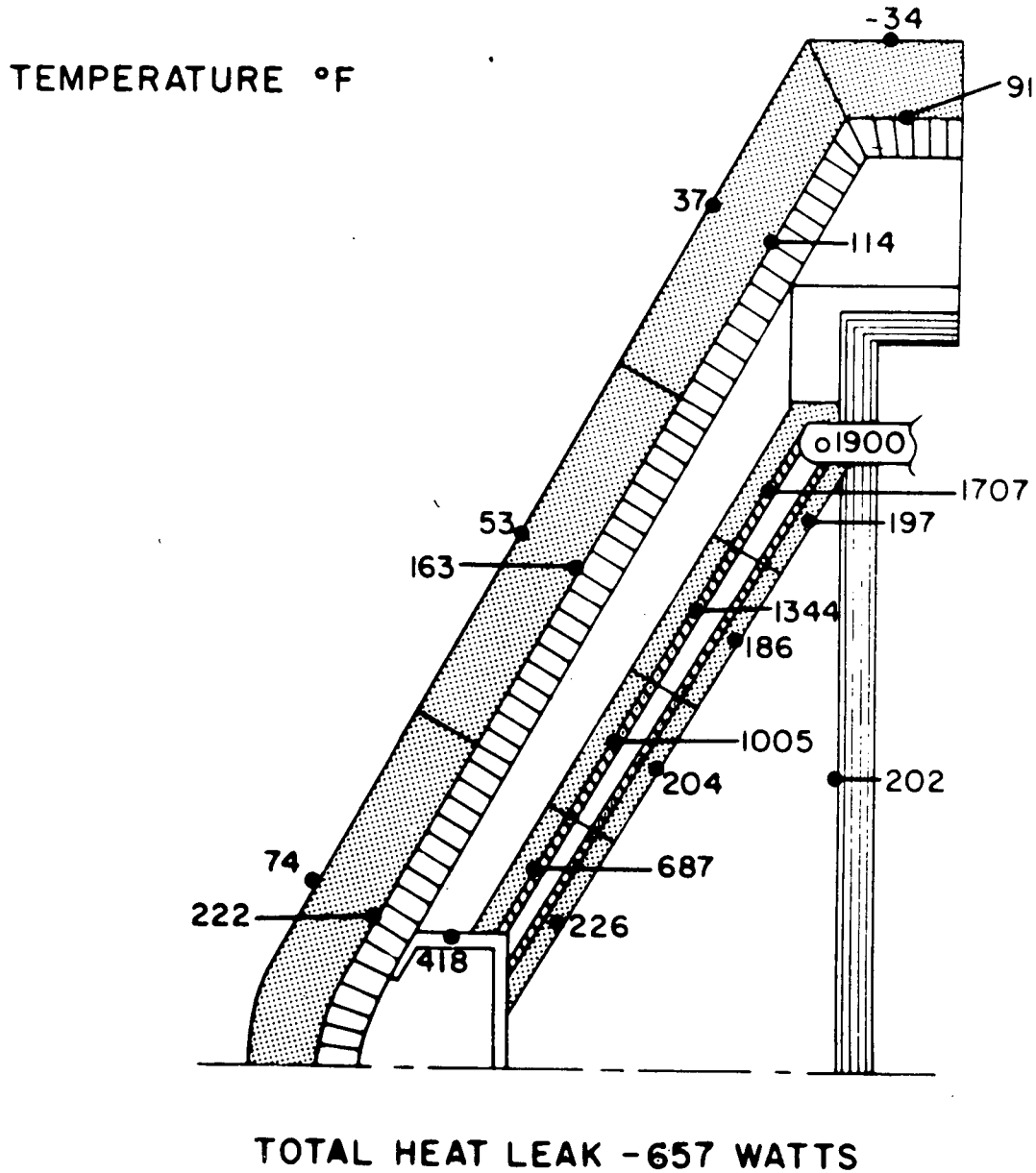


TABLE 2.2-III

HSRV (EARTH ORBITAL) PERFORMANCE SUMMARY

• CONFIGURATION	60° BLUNTED CONE	
• DIAMETER	84.0 "	(2.1336m)
• $X_{CG}/D_B$	0.291	
• $W/C_D A$ (HYPERSONIC)	37.5 lbs/ft <sup>2</sup>	(1795.5 N/m <sup>2</sup> )
• ENTRY WEIGHT	2297 lbs	(1042 kg)
• MOMENTS OF INERTIA		
I <sub>xx</sub> (ROLL)	319 sl-ft <sup>2</sup>	(432 kg-meter <sup>2</sup> )
I <sub>yy, zz</sub> (PITCH, YAW)	177 sl-ft <sup>2</sup>	(240 kg-meter <sup>2</sup> )
• TERMINAL VELOCITY(NO BALLUTE)	225 ft/sec	(68.58 m/s)

The heat leak analysis revealed that an increase in the structural capability of the struts would result in an increase in the overall heat leak beyond the  $1 \text{ KW}_t$  maximum for this "half" of the HSRV/HSHX system. Therefore, an alternate design approach was chosen. The loads experienced in the struts were limited by installing crushable honeycomb between the rings at the base of the truss support system. This honeycomb pad is designed to crush during reentry, (at 35 g's) thus allowing the heat source plate to move forward 1.0 inch and bear directly on the aeroshell mounted load reaction pads located under each heat source plate fitting. With this approach, the strut cross sectional area does not have to be increased, and the heat leak then remains below  $1 \text{ KW}_t$  as during the earth orbital mission. The resultant design is capable of surviving superorbital reentries at reentry angles up to  $-15^\circ$ , at lunar return velocity ( $\sim 36,000 \text{ fps}$ ). Performance characteristics are summarized in Table 2.2-IV.

Selection of Haynes-188 alloy dictated a modification in the HSHX design. The revised HSHX design has been shown schematically in Figure 1.0-2. The major modification introduced in this study was the design of the center of the spiral where the gas flow reversal takes place. Previously (Figure 2.1-7) this flow reversal was accomplished in a cylindrical manifold located at the hub of the spiral. In the current design this is accomplished by connecting every third tube together with a short "U" tube type piece. In order to fill the core of the spiral as much as possible with tubes, two of the three tube pieces are fabricated with a compound bend which allows them to go over or under the adjacent tubes to connect with the appropriate return tube. Thus the maximum height of the hub of the spiral is approximately three times the diameter of the tube (i. e., 4.32 in.). The eighteen tubes which make up the heat exchanger core are approximately 70 in. long and are constructed from 0.045-in. sheet stock. The inlet ring manifold is 2.40 in. in diameter while the exit ring manifold is 3.30 in. in diameter. The overall weight of the HSHX is 195 lb. All external surfaces of the heat exchanger are coated to provide a high emittance surface (effective emissivity = 0.8).

The fabrication of the modified HSHX would be similar to the sequence described in NASA CR-72555. The deletion of the central reversing manifold presents a slightly easier final assembly procedure. It is envisioned that the two tubes which comprise one of the nine sets would be joined with the "U" tubes prior to final assembly. With this exception the assembly sequence would be as described in the cited reference.

TABLE 2.2-IV

HSRV (SUPERORBITAL DESIGN) PERFORMANCE SUMMARY

• CONFIGURATION	60° BLUNTED CONE	
• DIAMETER (IN)	84.0"	(2.1336m)
• $X_{CG/D_B}$	0.285	
• W/CDA (HYPERSONIC)	45.0 lbs/ft <sup>2</sup>	(2154.6 N/m <sup>2</sup> )
• ENTRY WEIGHT	2743 lbs.	(1244 kg)
• MOMENTS OF INERTIA		
I <sub>xx</sub> (ROLL)	376 sl-ft <sup>2</sup>	(510 kg-m <sup>2</sup> )
I <sub>yy</sub> , I <sub>zz</sub> (PITCH, YAW)	211 sl-ft <sup>2</sup>	(286 kg-m <sup>2</sup> )
• TERMINAL VELOCITY (NO BALLUTE)	270 ft/sec	(82.30 m/s)

### 2.3 TASK III - DETAIL DESIGN

A transient thermal performance analysis of the HSRV and the HSU/HSHX was performed to determine component temperature histories and compatibility with the thermal criteria listed in Table 2.0-I during normal operation, startups and shutdowns, and reentry. Figure 2.3-1 shows the thermal model used in the analysis.

The model was developed in sufficient detail to provide the capability to analyze the following performance states:

- Steady-state capsule temperature distribution during ACHX operation.
- Temperature history of heat source, support structure and HSHX immediately after ACHX disconnect.
- Steady-state temperature distribution of heat source in space with:
  - HS facing HSHX during normal operation
  - HS facing space in deployed position
- Temperature history of heat source during HSHX startup.
- Temperature history of heat source immediately after HSHX shutdown but prior to deployment of the HS.
- Temperature history of heat source immediately after deployment to space.
- Temperature history of heat source during HSRV reentry while exposed to both orbital and superorbital reentry environments.

The normal operational temperature distribution in the HSU is shown in Figure 2.3-2. Concurrent temperatures in the HSHX are depicted in Figure 2.3-3. Startup and shutdown thermal performance of the HSU/HSHX system was also established. Figure 2.3-4 shows the temperature history of significant component locations for a normal launch subsequent to ACHX shutoff. It is assumed that there is no gas flow in the HSHX in this case.

FIGURE 2.3-1

## 2-D HSU & HSHX THERMAL MODEL

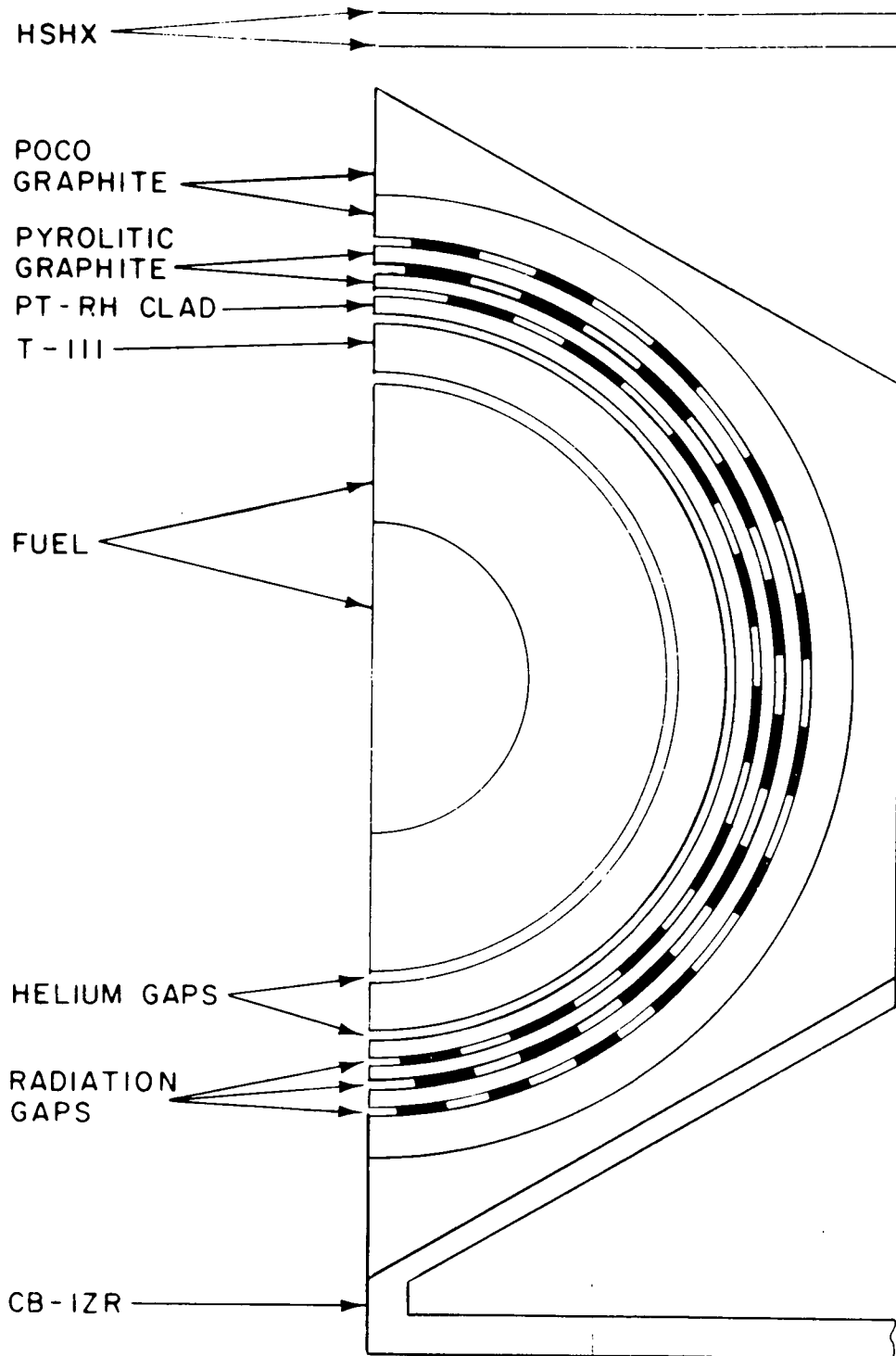
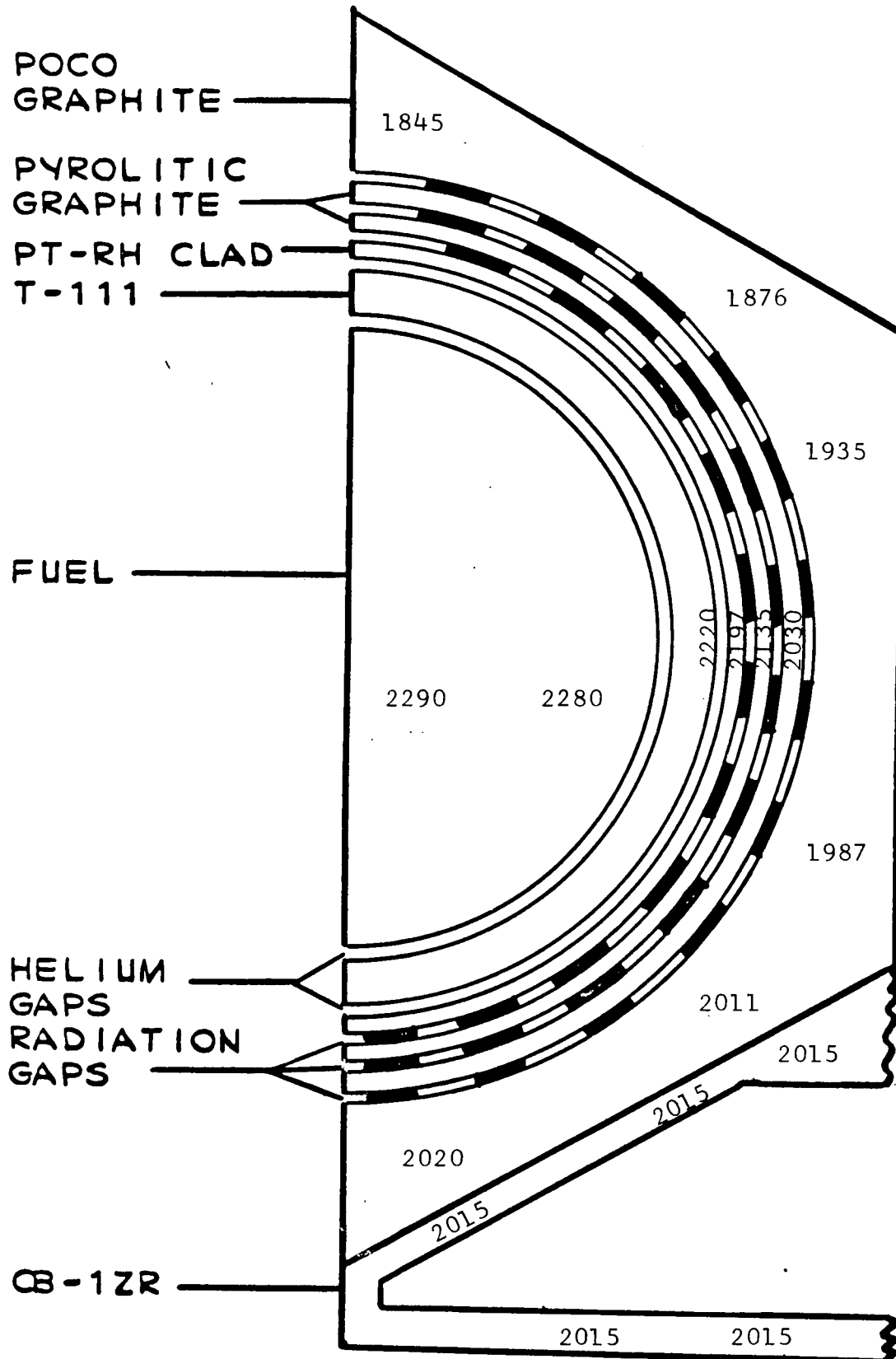
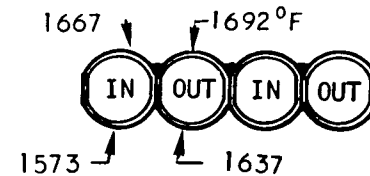
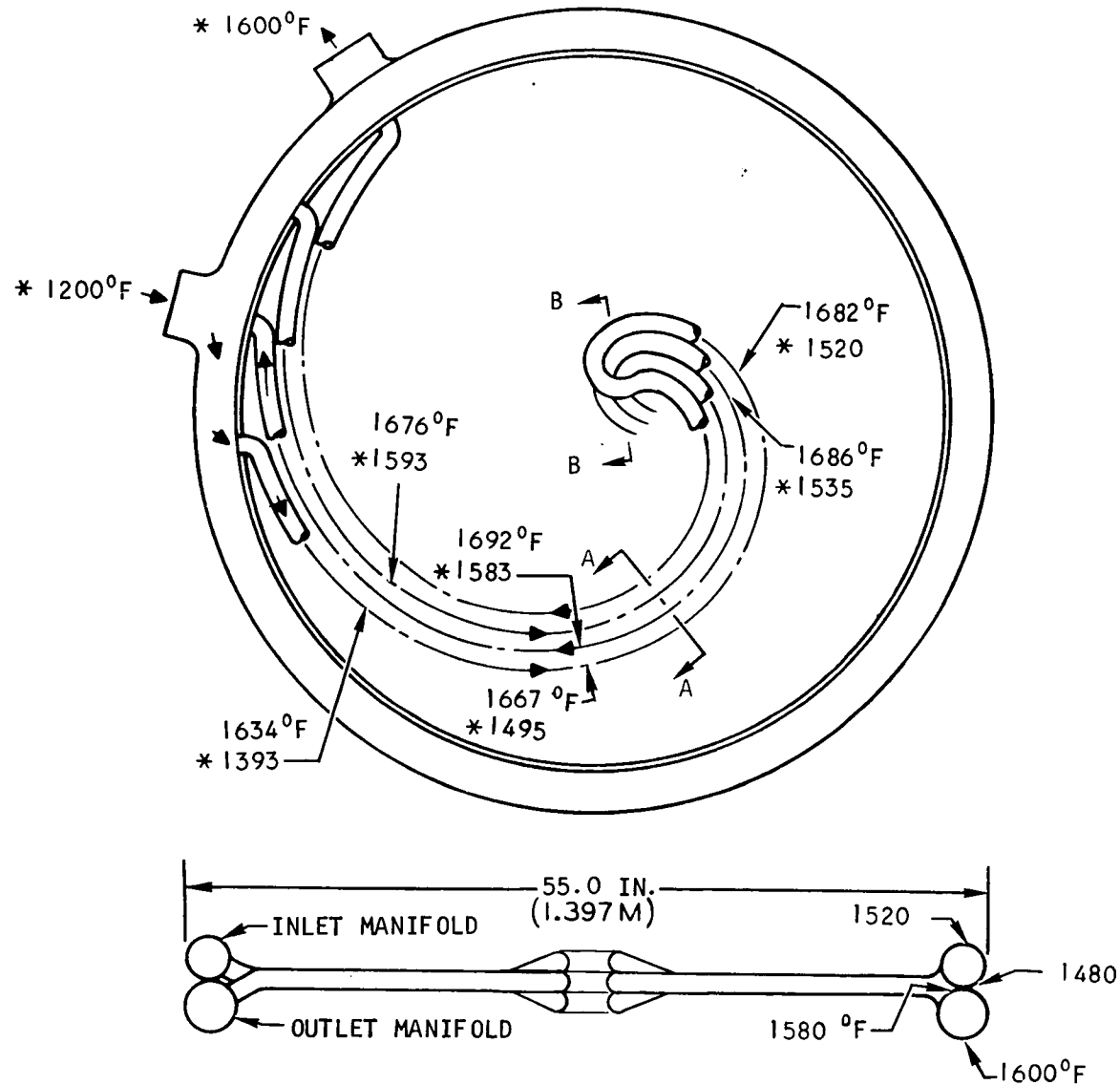


FIGURE 2.3-2

STEADY STATE-BRAYTON CYCLE OPERATING  
1-1689  
2-D HEAT SOURCE MODEL

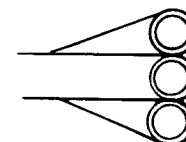






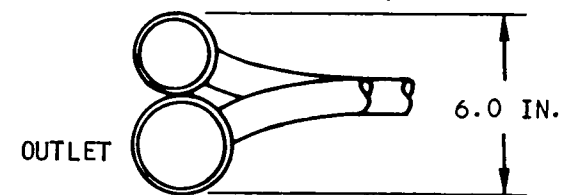
SECTION A-A

CORE DETAIL



SECTION B-B

FLOW REVERSING SECTION



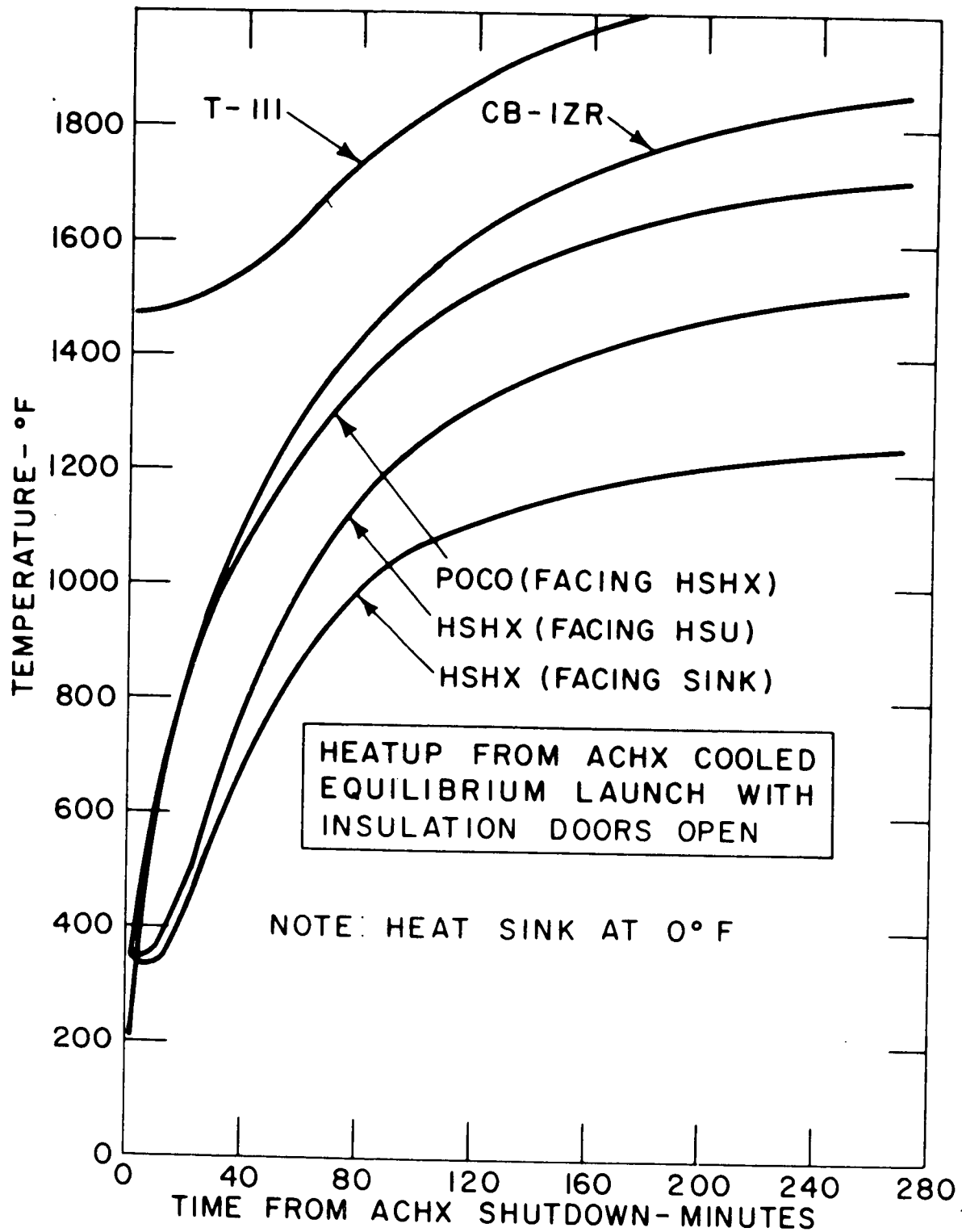
HEADERS

\* FLUID TEMPERATURE

Figure 2.3-3 HEAT SOURCE HEAT EXCHANGER STEADY-STATE PERFORMANCE

Figure 2.3-4 HSU TRANSIENT RESPONSE

HEATUP FROM ACHX COOLED EQUILIBRIUM-LAUNCH WITH INSULATION DOORS OPEN



It takes approximately four hours for the HSHX to reach the desired start-up temperature of 1500°F under these conditions. The transient response of the system with gas flowing after closing the insulation doors is shown in Figure 2.3-5. It takes more than three hours for the system to approach steady state operating temperatures.

The temperature history of key points on the HSU during reentry has also been investigated. Figure 2.3-6 illustrates the resultant temperatures for one of the more severe entry situations, i. e., for a vehicle initially tumbling at 6 RPM in an orbital decay reentry ( $\gamma_E \approx 0^\circ$ ). The resultant temperatures in the POCO heat source thermal protection, the isotope fuel capsule T-111 strength member and the Cb-1%Zr structure are clearly well below allowables. Similarly, in the case of a tumbling steep angle lunar return reentry component hot spot temperatures are still acceptable (Figure 2.3-7).

Design activity in this task in the areas of: designation of an adequate fabrication sequence for the HSRV and HSHX; development of final layouts; and, definition of a thermal simulation mockup of the HSRV aeroshell for use in the NASA-Space Power Facility (SPF) at Plum Brook. Figure 2.3-8 depicts the thermal simulation mockup. Substantial cost savings are incurred by the substitution of Al monocoque type structure for the flight version Al honeycomb. Thermal analysis of the HSRV under simulated SPF test conditions show a resultant temperature profile quite similar to that encountered under normal operating conditions in low earth orbit (Figure 2.3-9).

## 2.4 CONCLUSIONS AND RECOMMENDATIONS

Basic conclusions reached during this design study are summarized in Table 2.4-I. The analysis and design activity completed demonstrates that the HSRV offers significant potential for improving the already substantial safety margins built into this class of space isotope power supply. With comparatively small weight penalties the HSRV can be modified to withstand super-orbital reentries.

It should be noted that the diameter of the reference HSRV design developed in this study can be significantly reduced if packaging constraints limit available volume. Diameter reductions of 10-12 inches are achievable by altering the strut angles and attachment points; reducing the ballute stowage volume; and, changing the HSU outer corner design.

In addition to the basic conclusions, a series of recommendations pursuant to ultimate hardware test and development have resulted from the study. They are as follows:

Figure 2.3-5

HSU TRANSIENT RESPONSE

ENGINE STARTUP, INSULATION DOORS CLOSED

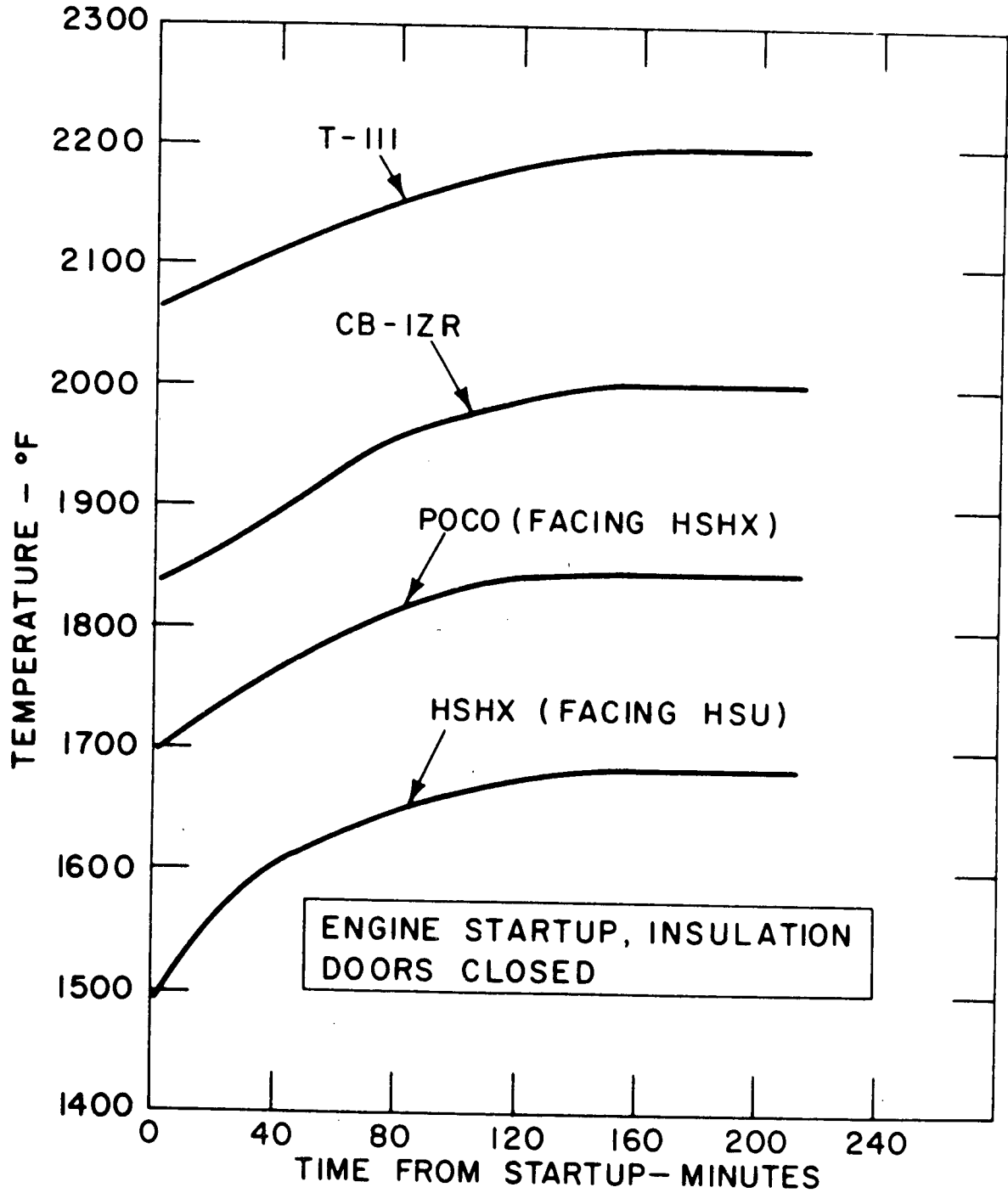


Figure 4.3-6 HEAT SOURCE TEMPERATURE HISTORY

ORBITAL DECAY ENTRY,  $\gamma_e = 0.0^\circ$ , TUMBLING

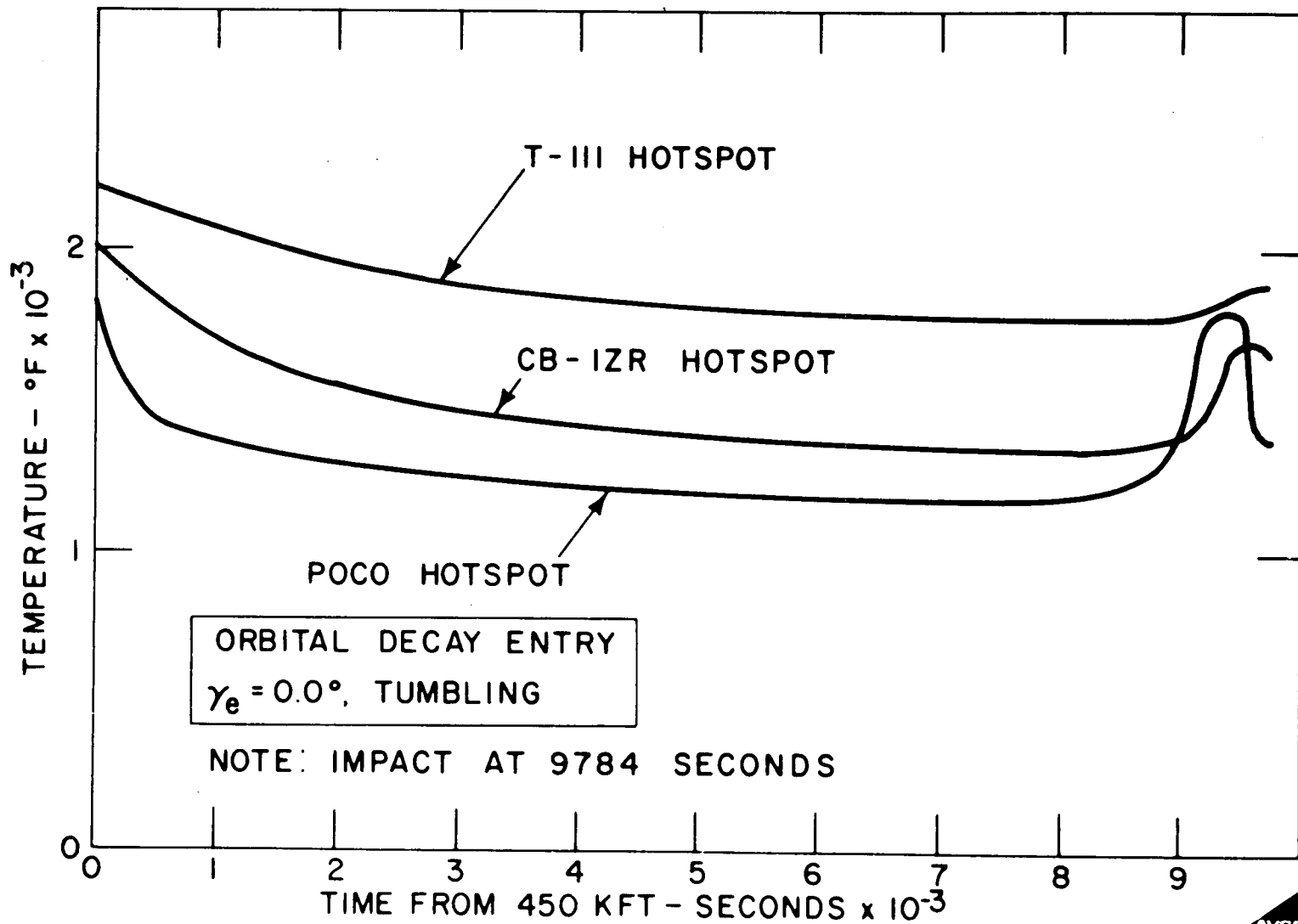


Figure 2.3-7 HEAT SOURCE TEMPERATURE HISTORY  
ORBITAL DECAY ENTRY,  $\gamma_e = -15^\circ$ , TUMBLING

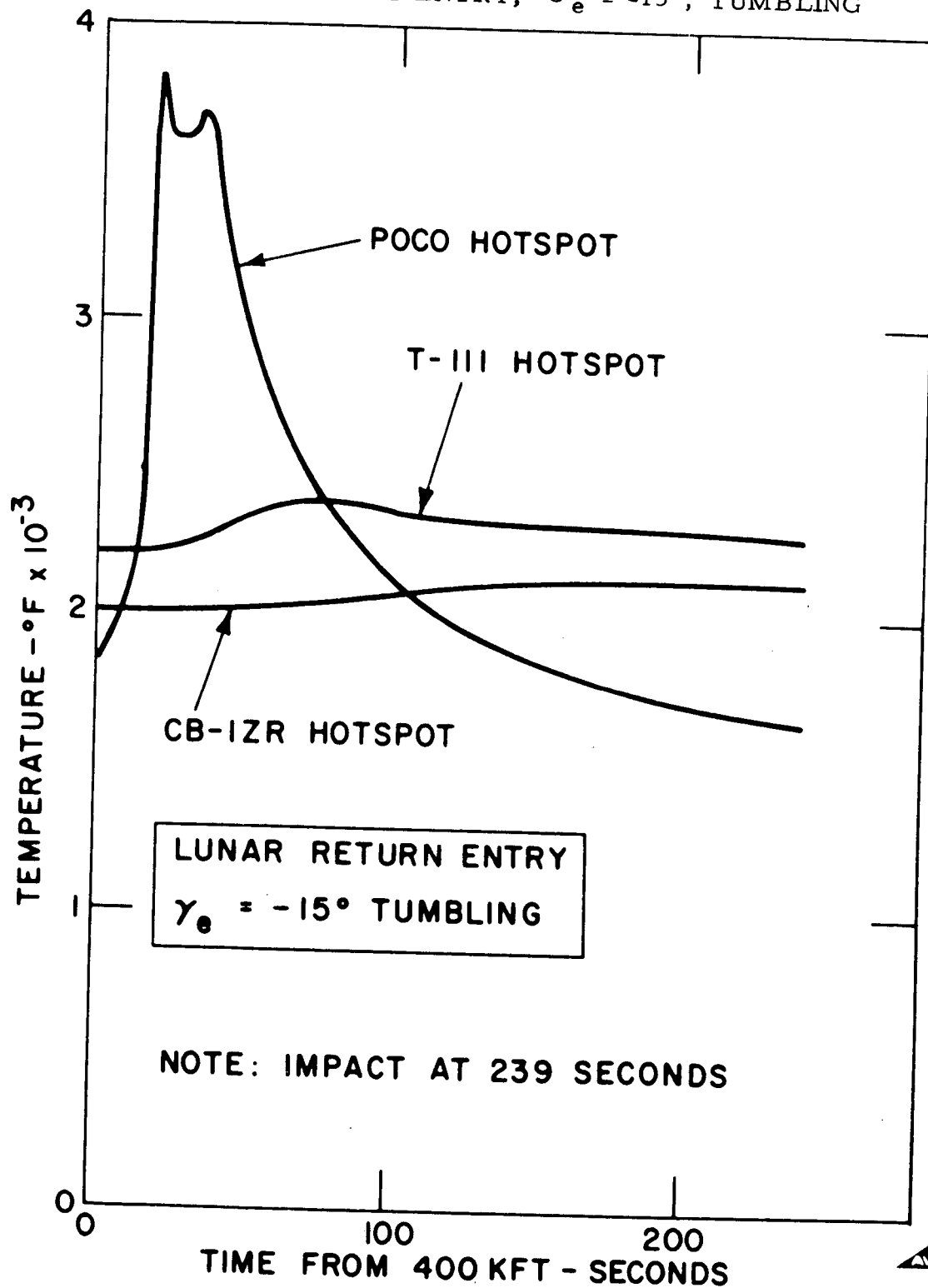


FIGURE 2.3-3

# THERMAL SIMULATION AEROSHELL

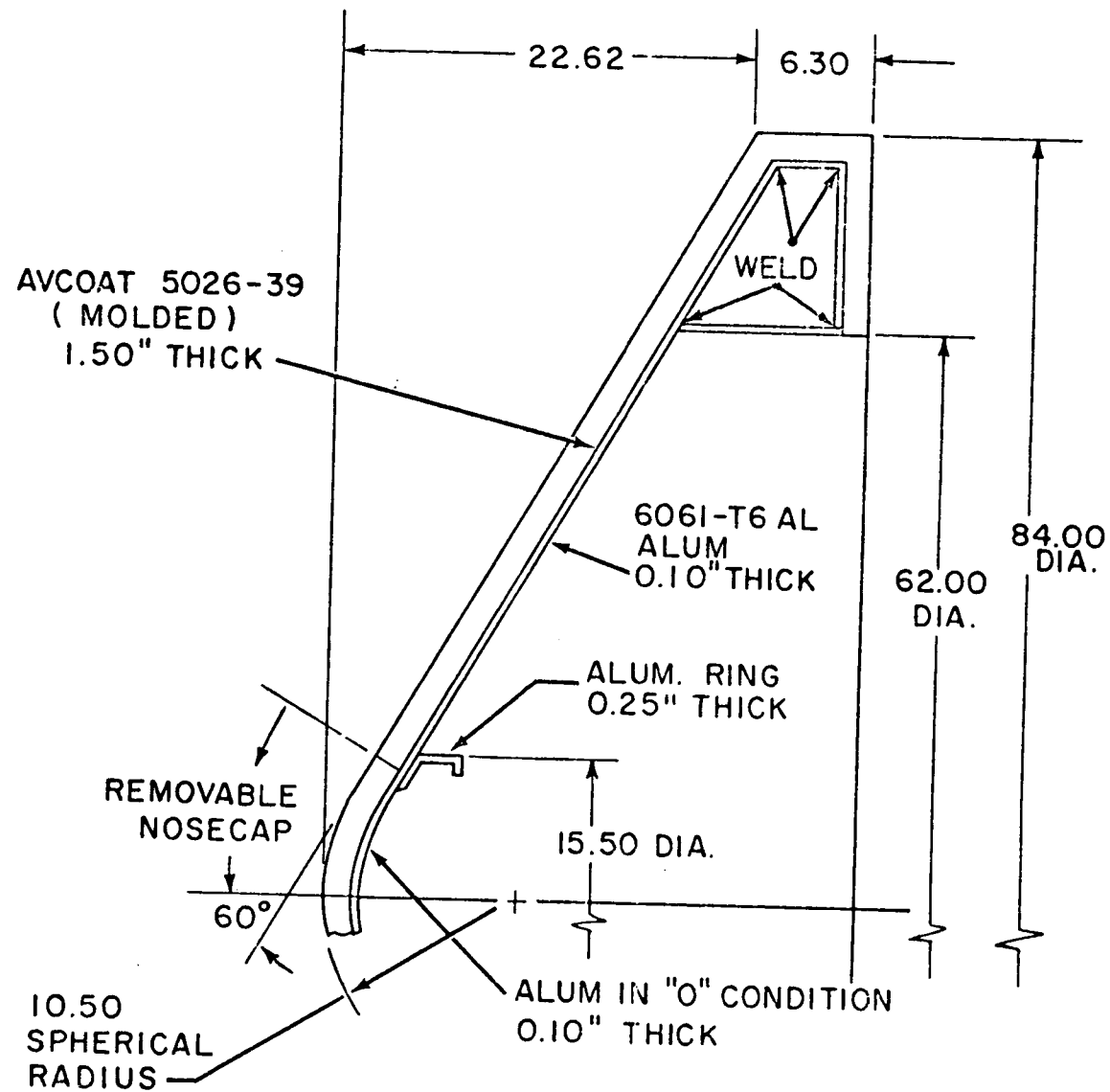
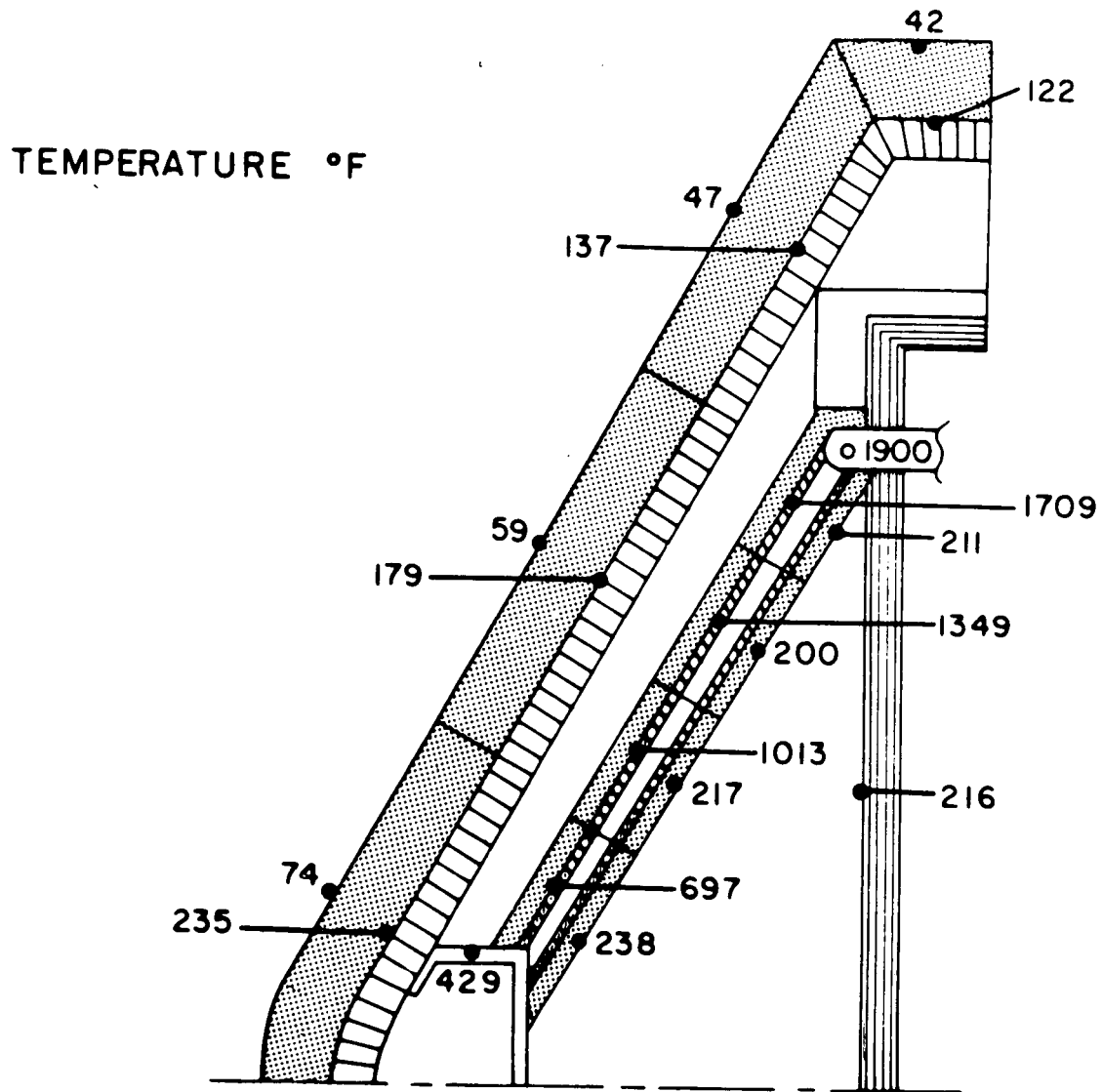


FIGURE 2.3-9

# HSRV STEADY-STATE TEMPERATURE DISTRIBUTION SPF TEST, COLDWALL @ 0°F



TOTAL HEAT LEAK - 654 WATTS





TABLE 2.4-I

CONCLUSIONS

- HSRV CAN ACCOMMODATE A WIDE VARIETY OF HEAT SOURCE GEOMETRIES
- HSRV CAN SURVIVE SUPER-ORBITAL REENTRY WITH MINOR MODIFICATION
- HSRV DESIGN WITH A GRAPHITIC HEAT SOURCE DOES NOT REQUIRE ADDED HEAT SINK CAPACITY
- LOW DENSITY ABLATOR IS A FEASIBLE HEAT SHIELD CHOICE
- HSHX FLOW REVERSING CONCEPT SHOULD BE MODIFIED TO EASE THERMAL STRESS LEVELS

- Utility and feasibility of advanced thermal protection systems (graphite, diborides) should be evaluated.
- Further testing of the aerodynamic turnaround device is required in gas environments (such as freon) which more closely simulate predicted operating environments.
- Impact testing should be initiated to evaluate HSRV utility in limiting impact damage to heat sources.
- Test effort should be initiated to determine the effect of long term space exposure to the HSRV operating environment on materials, components and subsystems, e. g. , low density ablator, thermal control coatings, pyrotechnics, thermal batteries, solid propellants.
- Insulation system development to characterize fabrication techniques, penetration effects, edge effects, and performance in the various operating modes (including dynamic environment) is required.
- Continued investigation of ballutes and parachutes should be conducted to firmly establish feasibility and utility.
- Materials testing is required to evaluate the HS/HSU structure and HS/retention system interface compatibility.

## 2.5 REFERENCES

- 2.1-1 Ryan, R. L., Graham, J. W., IRV Design Study Preliminary Design Study - Phase II - Final Report, NASA CR-72555 - AVSD-0306-69-RR, August, 1969.

### 3.0 HEAT SOURCE REENTRY VEHICLE

The Heat Source Reentry Vehicle design and study results are summarized in this section. A brief system analysis was first accomplished to establish the envelope of HSRV design requirements. These requirements were based on a review of the various possible launch and orbital failure modes. Results of this analysis are summarized in Section 3.1.

Final performance requirements for the HSRV are based on aerodynamic analysis described in Section 3.2. This analysis determined aerodynamic heating and load requirements as well as defining vehicle stability margins.

The analysis and design of the Heat Source Unit (HSU) component of the HSRV system is reported in Section 3.3. Results for both the earth orbital reference and the super orbital modified designs are presented. The thermal analysis discussion treats steady state, operational transient, and reentry performance of the HSU and HSU/HSRV/HSHX systems. Requirements for the ground auxiliary coolant heat exchanger (ACHX) are established, with consideration having been given to the Plum Brook SPF test interface.

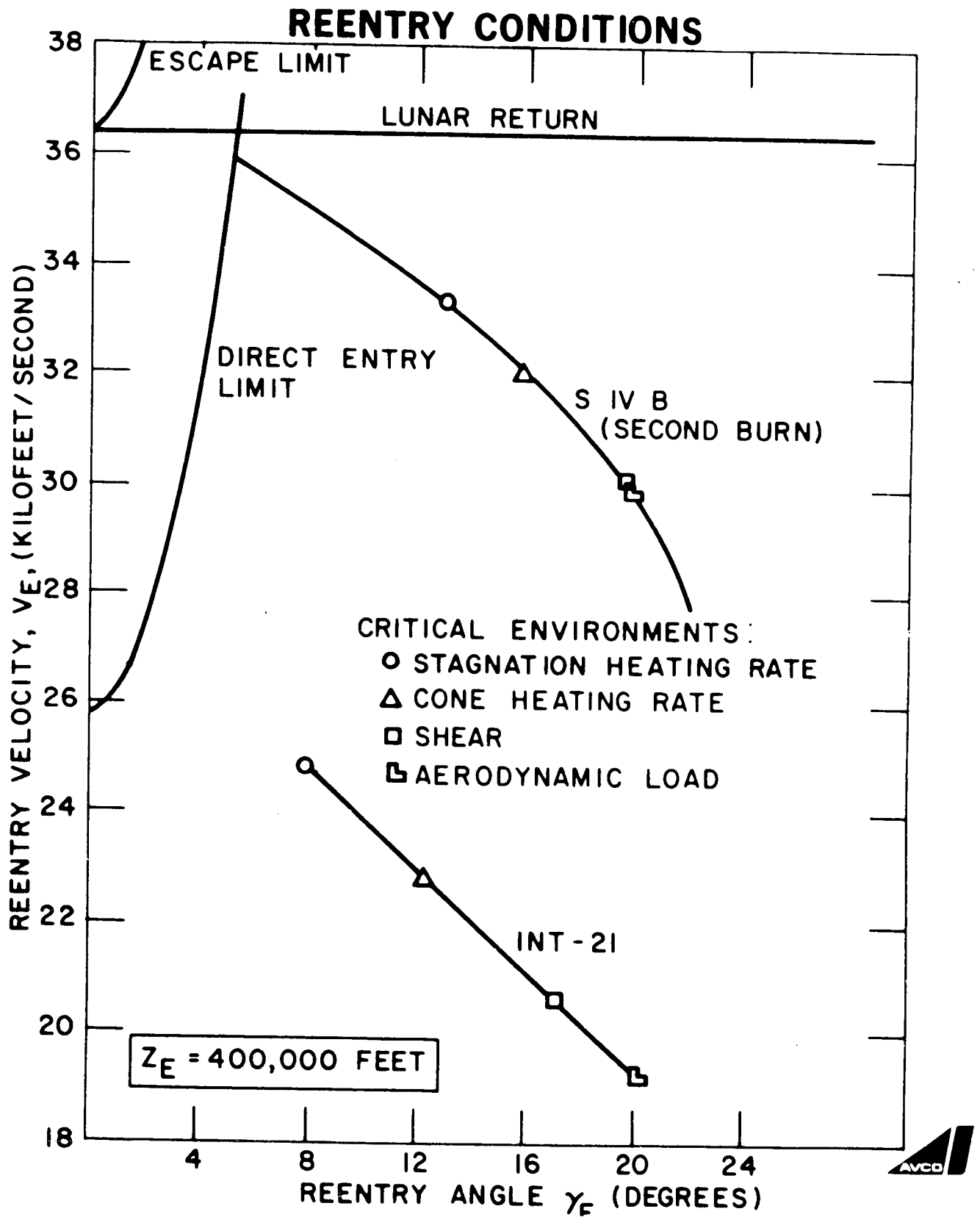
The reference HSRV design that meets the requirements established in Sections 3.1 and 3.2 is defined in Section 3.4. Primary emphasis is on the earth orbital HSRV. Concept modification required to meet super orbital reentry conditions are described. Weight estimates have been developed for vehicles capable of surviving super orbital reentry at angles up to  $-38^{\circ}$  at lunar return velocity. Temperature profile and heat leak estimates for the HSRV are presented in this section for the earth orbital reference, the super orbital design, and, for the SPF thermal simulation HSRV.

#### 3.1 SYSTEMS ANALYSIS

The first phase of the study was a brief review of possible launch and orbital failure modes to establish initial design requirements for the HSRV. This analysis also provided the initial conditions necessary to the accomplishment of the aerodynamic loads analysis.

The orbital mission analysis utilized the INT-21 orbit insertion trajectory; consideration was given to the maximum aerodynamic load case for this trajectory and orbital decay. The Lunar return analyses considered entry at the skip limit as well as at an entry angle for which the aerodynamic loads are no worse than those associated with translunar injection. These entry conditions are summarized in Figure 3.1-1.

FIGURE 3.1-1



Maximum aerodynamic loads and shears, aerodynamic heating rates and heating integrals were obtained by means of particle trajectories. The missions and/or phases considered included orbit injection, orbit decay, translunar injection and lunar return.

The reentry conditions were obtained by considering a twenty second delay between malfunction and abort initiation, these conditions were shown in Figure 3.1-1 for the orbit injection (INT-21). In contrast, the translunar injection (SIVB, second burn) considered the misapplication of the entire remaining fuel at any instant of time, these results are also presented in the figure. The lunar return conditions have considered parabolic velocities. The consideration of a twenty second delay for an abort from the translunar injection will result in significant reductions in the critical environs particularly the aerodynamic loads.

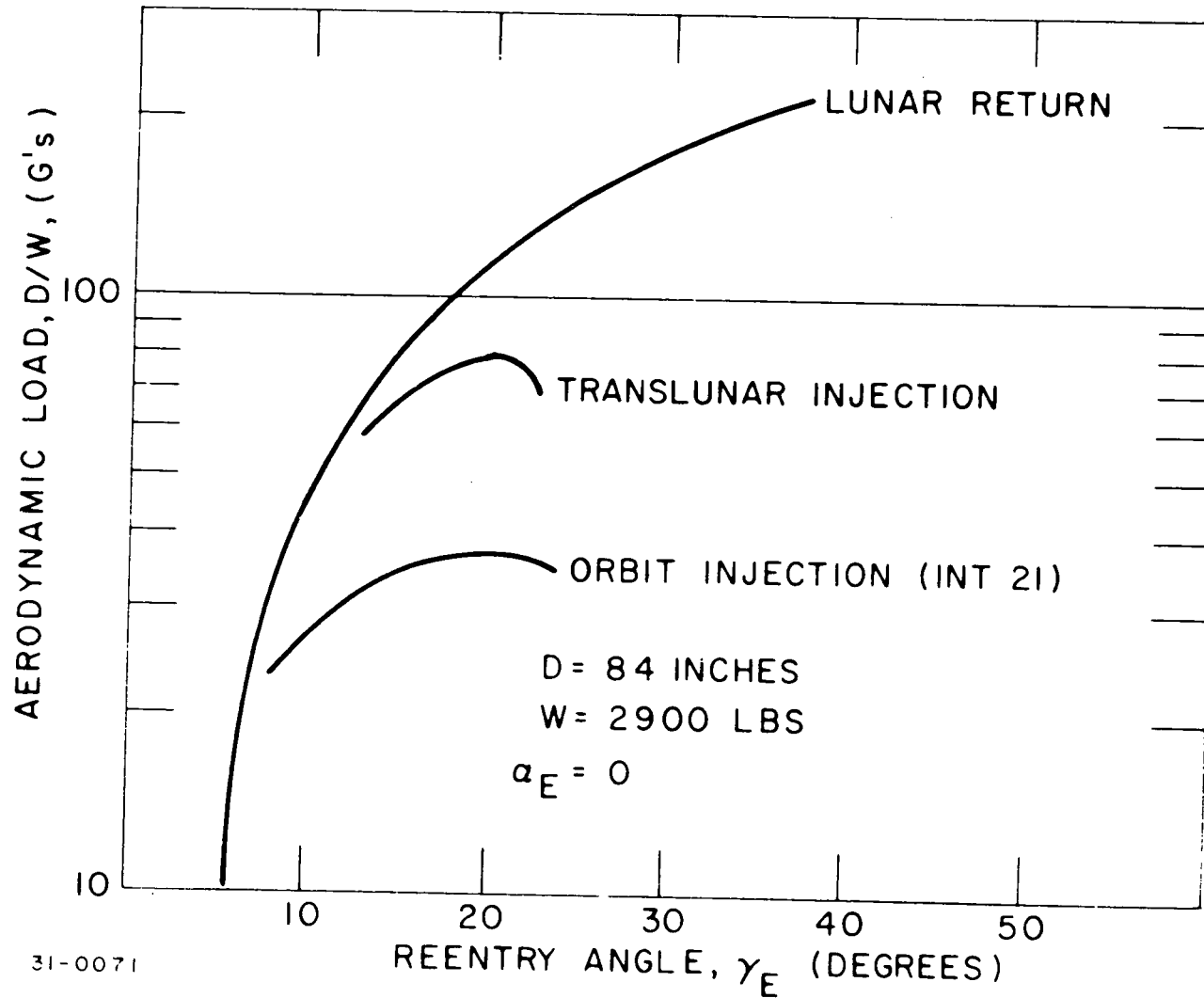
Indicated on the envelopes presented are the reentry conditions which result in a possible design criteria. These were established analytically assuming a straight line trajectory into an isothermal atmosphere. These reentry conditions are independent of the vehicle ballistic coefficient, however, vehicle dynamics as well as inapplicability of the above assumptions particularly near the skip limit will alter these results.

Assumed vehicle size and weight were 2.13 meters (84 inches) diameter and 1,316 kilograms (2900 pounds) respectively. All analyses were done for particle trajectories.

The variation of the aerodynamic load with reentry angle (the corresponding reentry velocity is given in Figure 3.1-1) for the three missions considered are presented in Figure 3.1-2. The translunar injection abort (conservative case) and lunar return result in significant increases in the axial load. At steep entry angles, the lunar return continues to result in high loads since the reentry velocity has been fixed at the parabolic return velocity.

Preliminary evaluation indicates that a twenty second delay for the translunar injection, results in loads which are substantially less than those for the total  $\Delta V$  application (the worst aerodynamic load is associated with assuming the total SIV B second burn normal to the orbit at ignition.) The twenty second delay results in loads for which the orbital design should be more than adequate. In the figures presented, the translunar injection curves can be deleted if a twenty second delay is considered for the abort model.

FIGURE 3.1-2  
**AERODYNAMIC LOAD**



31-0071



The results presented for the aerodynamic shear at the zero angle-of-attack sonic point (at the cone/cylinder junction) are similar in form (see Figure 3.1-3) to those for the aerodynamic load. These results agree reasonably with the straight line approximations as does the maximum rates (Figures 3.1-4 which presents both the stagnation and sonic point convective heating rates).

Figure 3.1-5 illustrates the effect of shallow reentry angles and parabolic velocities on the heating load at the stagnation point. Included in the figure is an indication of the radiative environment (approximate method used). At shallow entry angles the radiative rates are low, however, the pulse duration is long. At steep entry angles the high rates more than compensate for the short pulse durations, with the result that the integrated radiative heating again increases as the entry angle is made steeper.

The skip limit is that entry, for which an altitude increase does not occur. The entry conditions (i. e., entry angle) were established by means of particle trajectories analysis. As would be expected, dynamic motion results in a steepening of the entry angle for the HSRV shape. The skip limit was not reestablished for these conditions as the extent of altitude increase was nominal.

### 3.2 REENTRY PERFORMANCE ANALYSIS

Aerodynamic analyses were conducted in order to define the environments for the HSRV for both an orbital and lunar return mission. The aeroshell and heat source capsule heating and loads as well as the dynamic behavior of the HSRV have been determined through entry.

The dynamic behavior analyses considered a nominal entry mode with the HSRV stabilized in a forward attitude, initial rearward attitude and tumble entry. Initial entry conditions are summarized in Table 3.2-I. The two latter modes, particularly the tumble mode, are critical for the heat source and aft aeroshell environment, whereas the nominal mode is critical for the forebody heating. The tumble mode is severe since it can result in the deepest persistence of high angles of attack, however, the initial vehicle attitude (consistent with the reentry condition, i. e., velocity entry angle and altitude) for which this applies must be determined, since tumble may also result in less severe environments. The variation in initial attitude which gives a more severe entry for tumble in comparison to rearward entry is limited to a narrow range of entry angle-of-attack making it difficult to establish the critical entry attitude. The

FIGURE 3.1-3 - AERODYNAMIC SHEAR

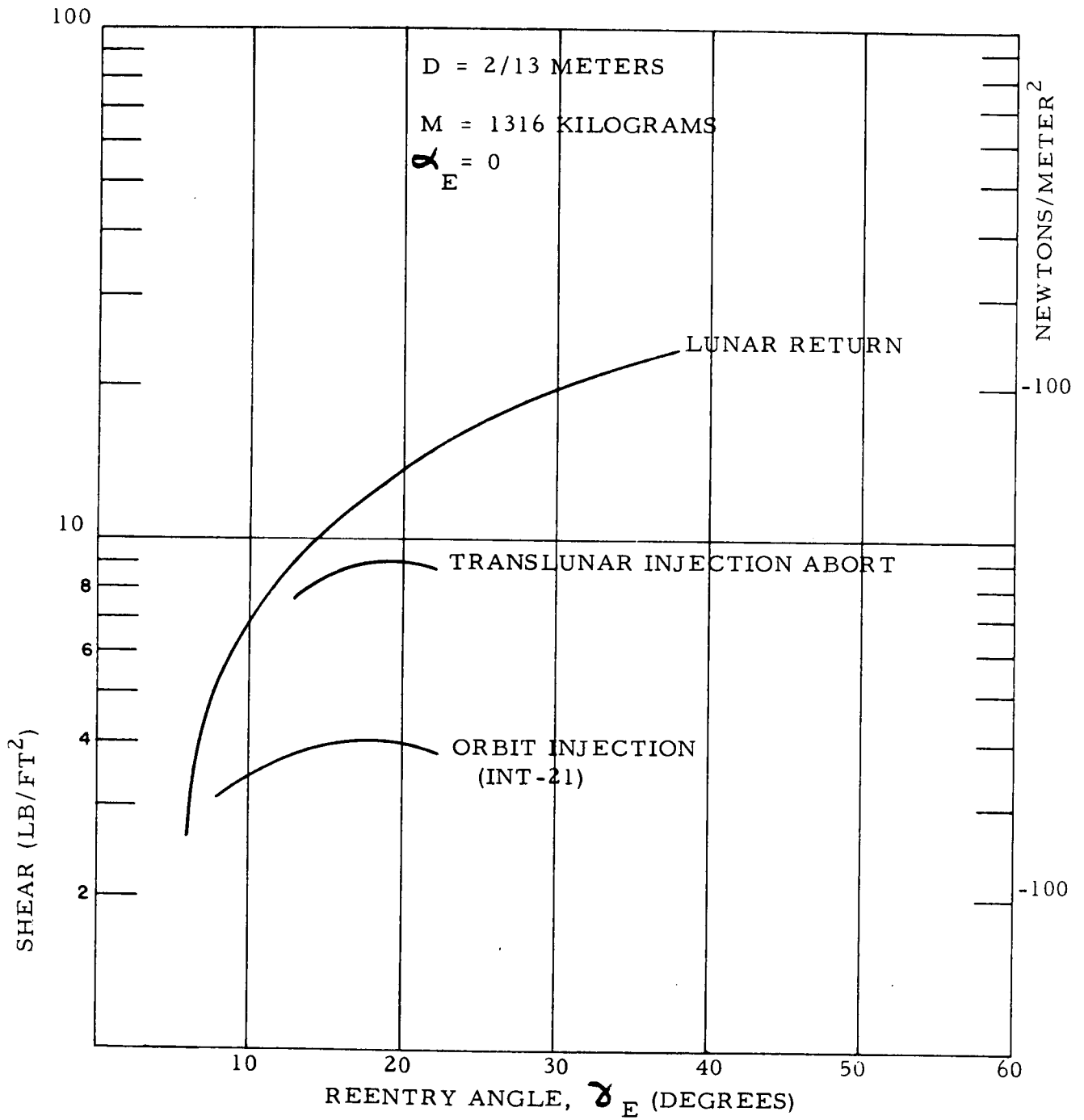




FIGURE 3.1-4  
MAXIMUM CONVECTIVE HEATING RATES  
HSRV

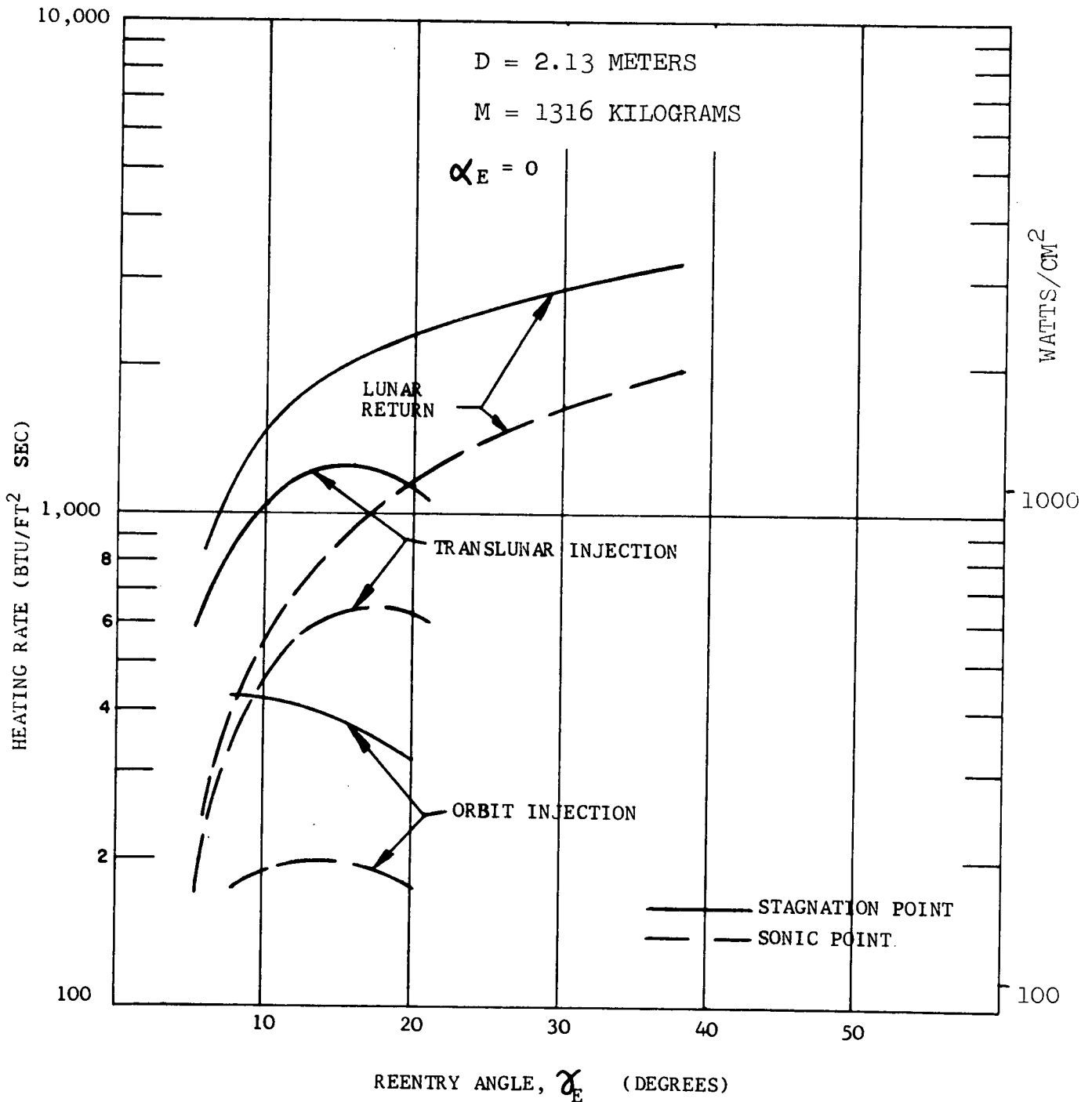
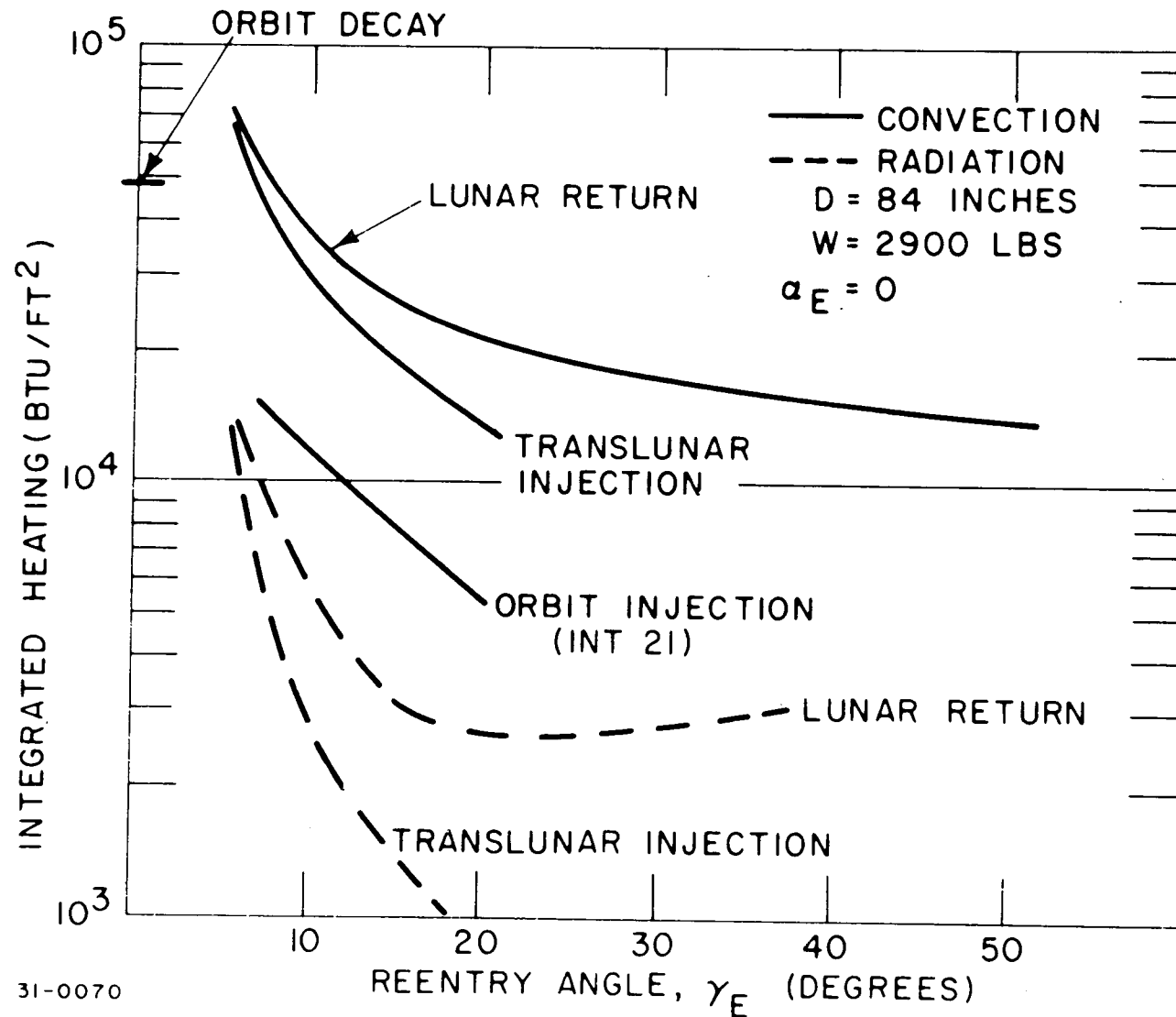


FIGURE 3.1-5

# STAGNATION POINT INTEGRATED HEAT LOAD



-46-

31-0070



TABLE 3.2-I

TRAJECTORY ENTRY DATA SUMMARY

MISSION	LUNAR RETURN		ORBITAL	
PHASE			DEORBIT	INJECTION
	SKIP LIMIT	MAX TRANS INJ	ORBITAL DECAY	MAX AERO LOADS
ENTRY ALTITUDE (Km)	122	122	137	122
VELOCITY (Km/SEC)	11.07	11.07	7.83	5.86
ANGLE (DEG)	- 5.4	-15	-.01	-20
ALTITUDE <sup>1</sup> (DEG)	-130.4	173.6	*	-64.6
PROBABILITY <sup>2</sup> (PERCENT)	12	.53	100	.56

<sup>1</sup> VEHICLE ORIENTATION (MEASURED FROM LOCAL HORIZONTAL) WITH TUMBLE (6 RPM) WHICH RESULTS IN MAXIMUM ANGLE OF ATTACK ENVELOPES.

<sup>2</sup> PROBABILITY OF EXCEEDING RANDOM ENTRY ANGLE OF ATTACK ENVELOPES WITH A TUMBLE RATE OF 6 RPM.

\* ORBITAL DECAY CASE - INITIAL ATTITUDE IS NOT CRITICAL

procedure followed in establishing the critical entry conditions was to vary the initial attitude parametrically with the maximizing of the amplitude of the first oscillation after arresting tumble being the criteria for the critical entry attitude. Table 3.2-II presents the variation of critical design requirements for the design tumble rate of .628 rad/sec and also for 1.256 rad/sec with initial attitude. The sensitivity to tumble rate is indicated, for the higher initial tumble rate, a lower altitude is achieved with large amplitude resulting in higher capsule and aeroshell heating and loads.

### 3.2.1 Heating and Loads Summary

The trajectory conditions utilized for the heating and loads analyses were summarized in Table 3.2-I for the orbital and Lunar mission. The entry altitude of 137 km (450,000 feet) was used for orbital decay. The initial aeroshell and capsule temperatures are based on steady state conditions in the absence of aerodynamic heating, requiring the evaluation of the free molecular and high altitude heating above 122 km (400,000 feet) to provide accurate temperature rise calculations for the heat source capsules and aeroshell. This higher entry altitude was only necessary for the orbital decay mode since for the steeper entry modes the time spent and heating levels between these altitudes were insignificant.

The critical heating environment for the capsules is associated with those conditions which result in high heating rates. High rates for the capsules can only be realized at large angles of attack. Therefore, those conditions which result in maximum angle of attack envelopes through entry are critical. The initial vehicle attitude associated with the tumble rate considered for design is presented in the table for each of the entry conditions. Also presented is the range of entry attitude (i. e., probability) which results in loads and heating which exceed rearward entry. It can be seen that those trajectories which result in maximum loads and heating rates have lower probabilities for tumble environments exceeding the rearward entry mode.

Tables 3.2-III and 3.2-IV summarize the aerodynamic loads and heating respectively, for the design trajectories. The maximum aerodynamic heating rates are experienced for the maximum aerodynamic load trajectories (steep entry angles). The random entry with tumble mode resulted in the most severe heating rates and aerodynamic loads. However, the integrated heat load, while being most severe for the tumble mode for the heat source capsules, the fence and shoulder, was a maximum on the forebody for the forward attitude (zero angle of attack) throughout entry. The location of the typical vehicle stations considered are presented in Figure 3.2-1. All orbital decay integrated heating load figures include the high altitude heating from 137 km.

TABLE 3.2-II  
INFLUENCE OF INITIAL TUMBLE RATE  
(ORBIT INJECTION)

TUMBLE RATE, $Q_E$ (RAD/SEC)	0.628	1.256
INITIAL ANGLE OF ATTACK (DEG)	-44.6	-145.0
MAXIMUM AXIAL LOAD, D/W (g-s)	42.7	44.8
MAXIMUM NORMAL LOAD N/W, (g's)	4.6	6.7
MAXIMUM CAPSULE HEATING RATE (WATT/CM <sup>2</sup> )	80	98
MAXIMUM STAGNATION HEATING RATE (WATT/CM <sup>2</sup> )	355	368

The radiative heating for the capsules occurs at the rearward attitude when, because of the fence, the gas cap thickness is large.

Although the Lunar return skip limit entry mode is at a much higher velocity the peak aerodynamic loads occur at a high altitude and as such are less than the orbital decay loads. The frequency of the oscillation is indicated in Table 3.2-III. The axial load varies between  $(D/W)_{\max}$  and  $(X/W)_N$  whereas the normal acceleration varies between positive and negative  $(N/W)_{\max}$  values at the frequency indicated.

TABLE 3.2-III  
ENTRY LOADS SUMMARY

MISSION PHASE (ENTRY MODE)	DYNAMIC PRESSURE (ATM)	$(D/W)_{\max}$	$(N/W)_{\max}$	$(X/W)_N$	FREQUENCY (CPS)
ORBIT INJECTION					
a) FORWARD	.592	35.5			
b) REARWARD	.698	42.0	4.3	32.0	3.5
c) TUMBLE	.706	42.7	4.6	31.0	3.5
ORBIT DECAY					
a) FORWARD	.130	7.8			
b) REARWARD	.131	7.9	.1	7.8	1.5
c) TUMBLE	.135	8.1	.5	6.0	1.6
LUNAR RETURN (SKIP LIMIT)					
a) FORWARD	.0861	5.2			
b) REARWARD	.0888	7.0	.8	4.0	1.2
c) TUMBLE	.0903	7.5	1.2	3.3	1.3
LUNAR RETURN ( $\gamma_E = -15^\circ$ )					
a) FORWARD	1.27	77.0			
b) REARWARD	1.48	89.0	9.0	70.6	5.1
c) TUMBLE	1.54	93.3	11.2	65.5	5.2

Figure 3.2-1 HSRV DESIGN  
AERODYNAMIC HEATING STATIONS

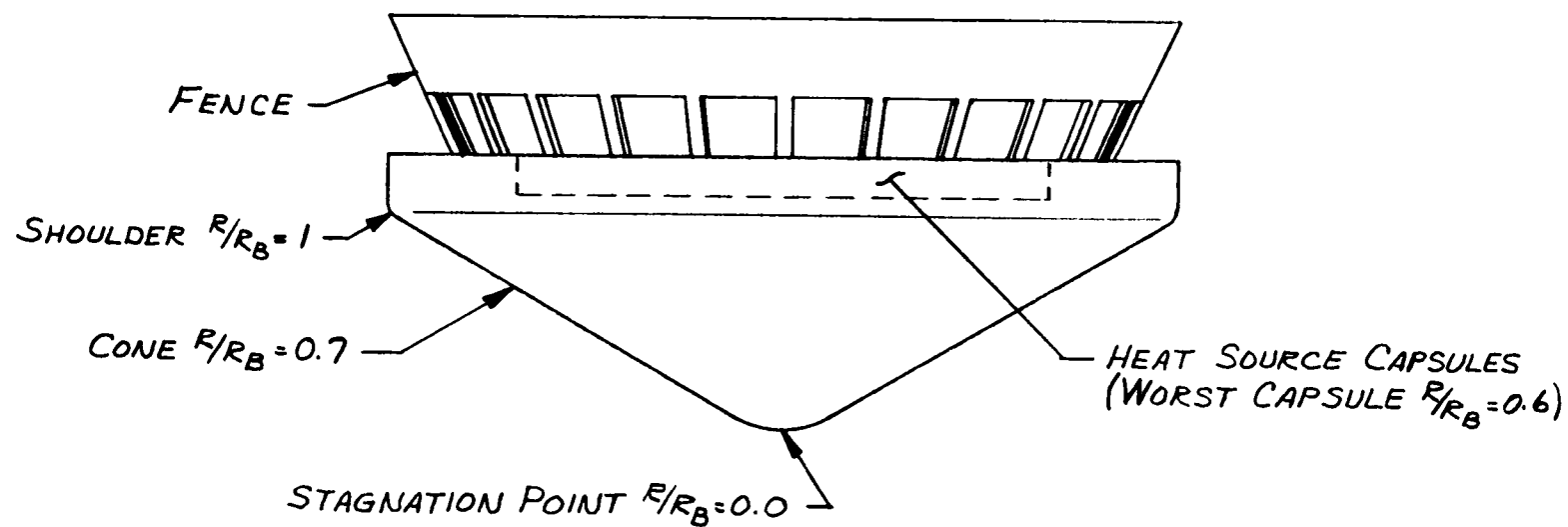


TABLE 3.2-IV  
HEATING SUMMARY

	ORBITAL		LUNAR RETURN	
	MAXIMUM RATE <sup>1</sup> W/Cm <sup>2</sup>	INTEGRATED LOAD <sup>2</sup> W SEC/Cm <sup>2</sup>	MAXIMUM RATE <sup>3</sup> W/Cm <sup>2</sup>	INTEGRATED LOAD <sup>4</sup> W SEC/m <sup>2</sup>
STAGNATION POINT	355	43700	2010	71600
CONE	117	17300	663	20700
SHOULDER	502	24260	2910	47000
FENCE				
INSIDE	50	5200	470	4380
OUTSIDE	188	17010	1160	30680
CAPSULE	80	11500	660/220 <sup>5</sup>	6100/1350

<sup>1</sup> ORBIT INJECTION, PEAK CYCLE RATE FOR TUMBLE

<sup>2</sup> ORBIT DECAY

<sup>3</sup>  $\gamma_E = -15^\circ$ , PEAK CYCLE RATE FOR TUMBLE

<sup>4</sup> SKIP LIMIT

<sup>5</sup> CONVECTIVE/RADIATIVE



The loads associated with a Lunar return mission with the imposed limitation (i. e.,  $\gamma_E = -15^\circ$ ) are twice those of an orbital mission (INT-21 injection trajectory) for both axial and normal loads.

The integrated heat load is greater for the Lunar return mission with high rates, however, the orbit decay mode may be critical because of the long pulse duration.

### 3.2.2 Analysis and Results

#### 3.2.2.1 Aerodynamic Characteristics

Aerodynamic coefficients were established for the reference HSRV fence. The results of the analysis dictated the need for increasing the vent area from sixteen to an area equivalent to 24 holes of diameter  $0.2 R_B$ . In addition to establishing the aerodynamic coefficients in the continuum flow region (subsonic to hypersonic) those for the free molecular regime were also established. Analyses determined that the C. G. be no further aft than .305D from the stagnation point for the reference vehicle.

Considerable test data have been developed for the blunted sixty-degree cone with a cylindrical section and various fence devices by NASA Ames Research Center. (Ref. 3.2-1) In addition, previously obtained data (references 3.2-2, -3, -4, -5) can be utilized in evolving the desired coefficients where data is lacking and extrapolations are necessary. Further analyses and tests are required since all fence test data has been obtained with fences that are larger than that presently considered.

The necessary analyses involve the determination of the effectiveness of the fence and its variation with relevant correlation parameters which are also to be determined. The fence effectiveness depends upon the shock interaction extent; in addition the fence perturbs the base pressure distribution, this factor must also be considered in assessing the fence turn around capability.

Determination of the aerodynamic coefficients, particularly those associated with a complex shape such as that under consideration, requires, in addition to the Mach number simulations, representative shock density ratios. The shock density ratio will be indicative of shock locations and in addition, will be important in establishing the extent of venting. The Ames data were analyzed for equilibrium, normal shock density ratios of approximately six and eleven. (However, frozen flow chemistry can result in normal shock density ratios of only 7.2 in the shock tunnel (Ref. 3.2-1). This equilibrium flow assumption results in a conservative evaluation of the pitching moment characteristics. In addition, the fence standoff was varied for the cylindrical-conical configurations.

The correlation parameter which was evolved in the course of this study was the effective area parameter, which is the ratio of the fence venting area to the base area modified by the ratio of the sonic flow rates after a normal shock to the free stream flow rates and angle of attack, i. e. :

$$K_A = \left( \frac{4 A^*}{\pi D^2} \right) \left( \frac{G^*}{G_\infty} \right) / \cos \alpha$$

where:

$K_A$  effective venting area parameter

$A^*$  venting area

$D$  fence maximum diameter

$G^*$  sonic flow computed after a normal shock, and

$G_\infty$  free stream flow rate

The flow rates  $G^*$  and  $G$  given by the expressions

$$G^* = \left( \frac{\rho_s}{\rho_\infty} \right) \left( \frac{\rho^*}{\rho_s} \right) \left( \frac{u^*}{V_\infty} \right) \pi r_o^2 V_\infty$$

and

$$G_\infty = \rho_\infty V_\infty$$

where

$\rho_s$  is the normal shock density ratio,

$\frac{\rho^*}{\rho_s}$  is the sonic to stagnation density ratio,

$\frac{u^*}{V_\infty}$  is the ratio of sonic velocity after a normal shock to the free stream velocity, and

$\rho_\infty$  is the free stream density.

The effective area parameter is significant with respect to both the fence effectiveness and the base interaction since the internal shock structure and flow characteristics will be strongly influenced by the extent of mass swallowing as represented by this parameter. The venting area was varied from zero to a maximum (fence height of .7  $R_B$ ) for the cylindro-conical configuration, in addition test conditions provide two values of shock density ratio. These combined variations result in test data for four values of  $K_A$ , assuming that the effects of fence mounting (see Figure 3.2-2) can be factored out.

Figure 3.2-2 ALTERNATE FENCE GEOMETRIES

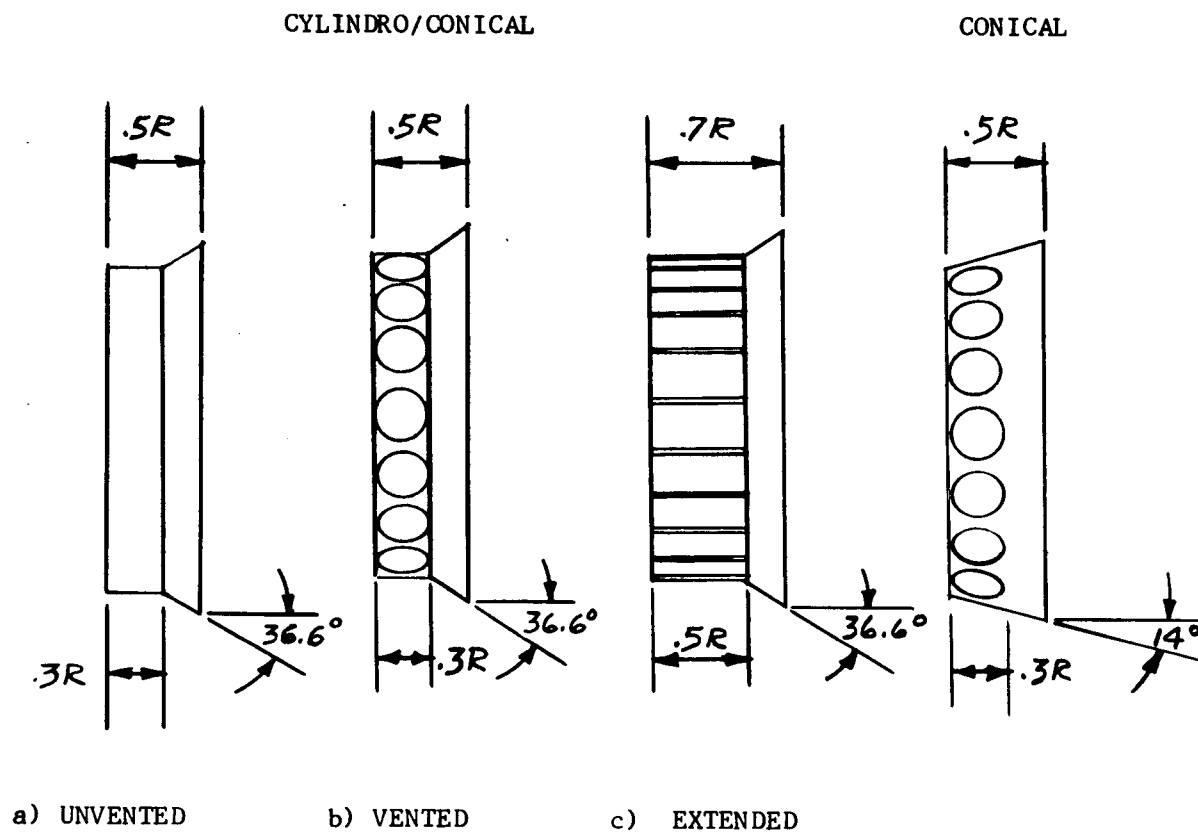


FIGURE 3-3

The conical fence and the cylindro/conical fence for a one half base radius height should have the same performance (analytically determined). This is reflected in the data for the sting mounted models, where the moment contributions of the fences are equal near the rearward angles of attack. The free flight data, involving an indirect measure of the moment coefficient reflects greater scatter. The results of these tests have been averaged for the cylindro-conical and conical fences.

The effectiveness of a fence device is defined as the ratio of its measured moment contribution to that predicted analytically, i. e.

$$K_E = \frac{\Delta C_{m_F}}{C_{n_{\alpha_F}} \propto (X_{c.g.} - X_{c.p.})/D}$$

where:

$\Delta C_{m_F}$  change in moment coefficient due to fence,

$C_{n_{\alpha_F}}$  fence normal force coefficient slope,

$\propto$  angle of attack,

$X_{c.p.}$  center of pressure measured from nose, and

$X_{c.g.}$  center of gravity measured from nose.

The correlation of the fence effectiveness with venting parameter is shown in Figure 3.2-3. The effectiveness with no venting is zero since no fence contribution was discernable from the data. As the venting approaches the condition of "swallowing" (i. e.,  $K_A = 1.0$ ) the effectiveness increases rapidly. The effectiveness does not appear to improve significantly beyond the "swallowed" conditions. The increase in moment at values of  $K_A$  greater than one, would be primarily that associated with the increased moment of the fence which results from providing the venting area.

The performance of the reference design fence was predicted utilizing the above correlation. The analysis indicates that the 16 hole fence is not adequate. The necessary fence characteristics (only one stable trim point at  $\alpha = 0$ ) can be obtained by increasing the vent area to that equivalent to 24 holes of diameter  $0.2 R_B$ . Figures 3.2-4 and 3.2-5 present the normal and axial force coefficients, respectively, and are the result of correcting the data for the reduced fence area. The present results for the moment coefficients are comparable to the nominal variation which were utilized in the previous IRV study. Since the HSRV will experience significant periods of flight at free

FIGURE 3.2-3 CORRELATION OF FENCE EFFECTIVENESS  
(CYLINDRO - CONICAL FENCE)

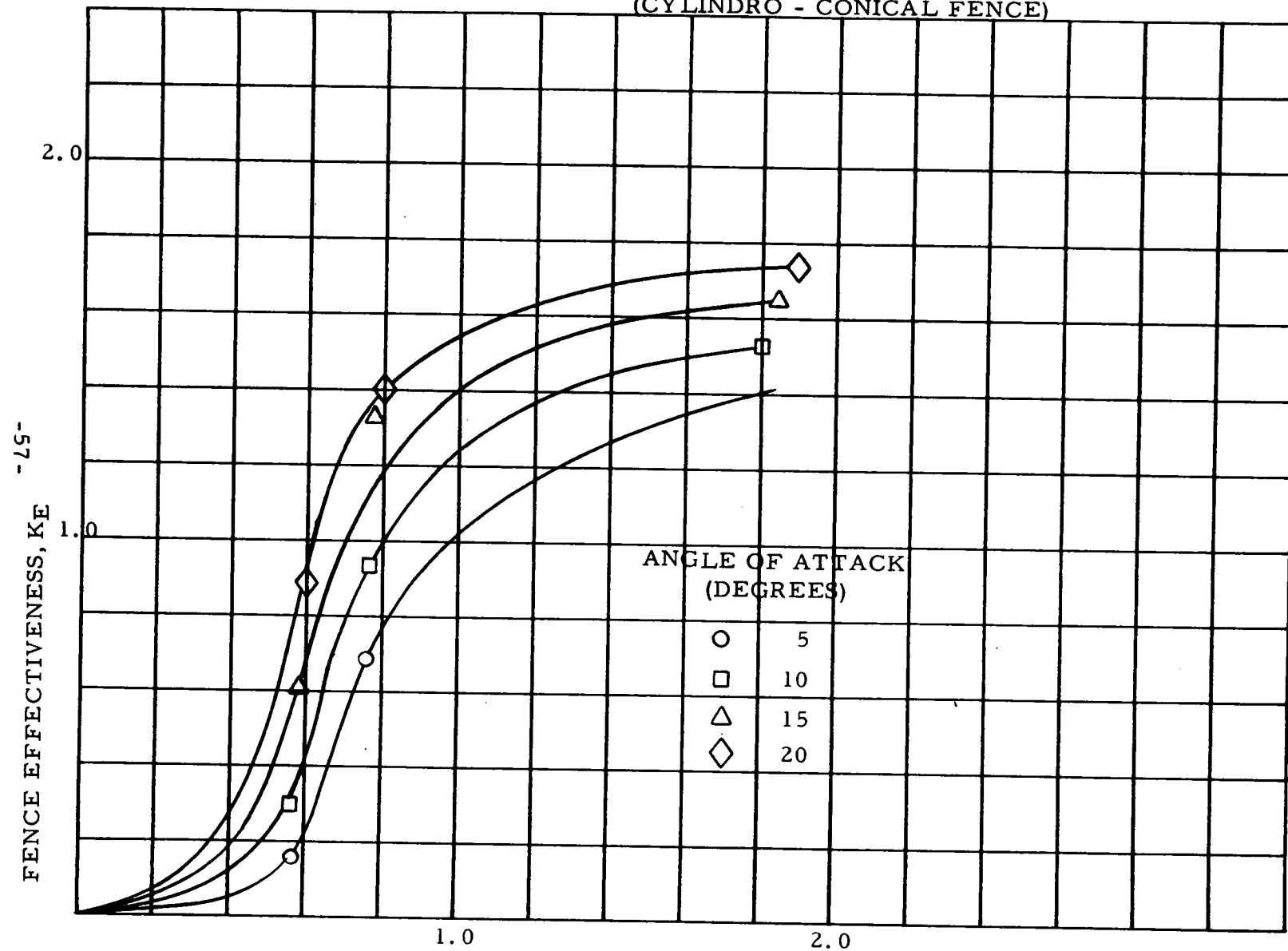


Figure 3.2-4

VARIATION OF NORMAL FORCE COEFFICIENT WITH ANGLE OF ATTACK

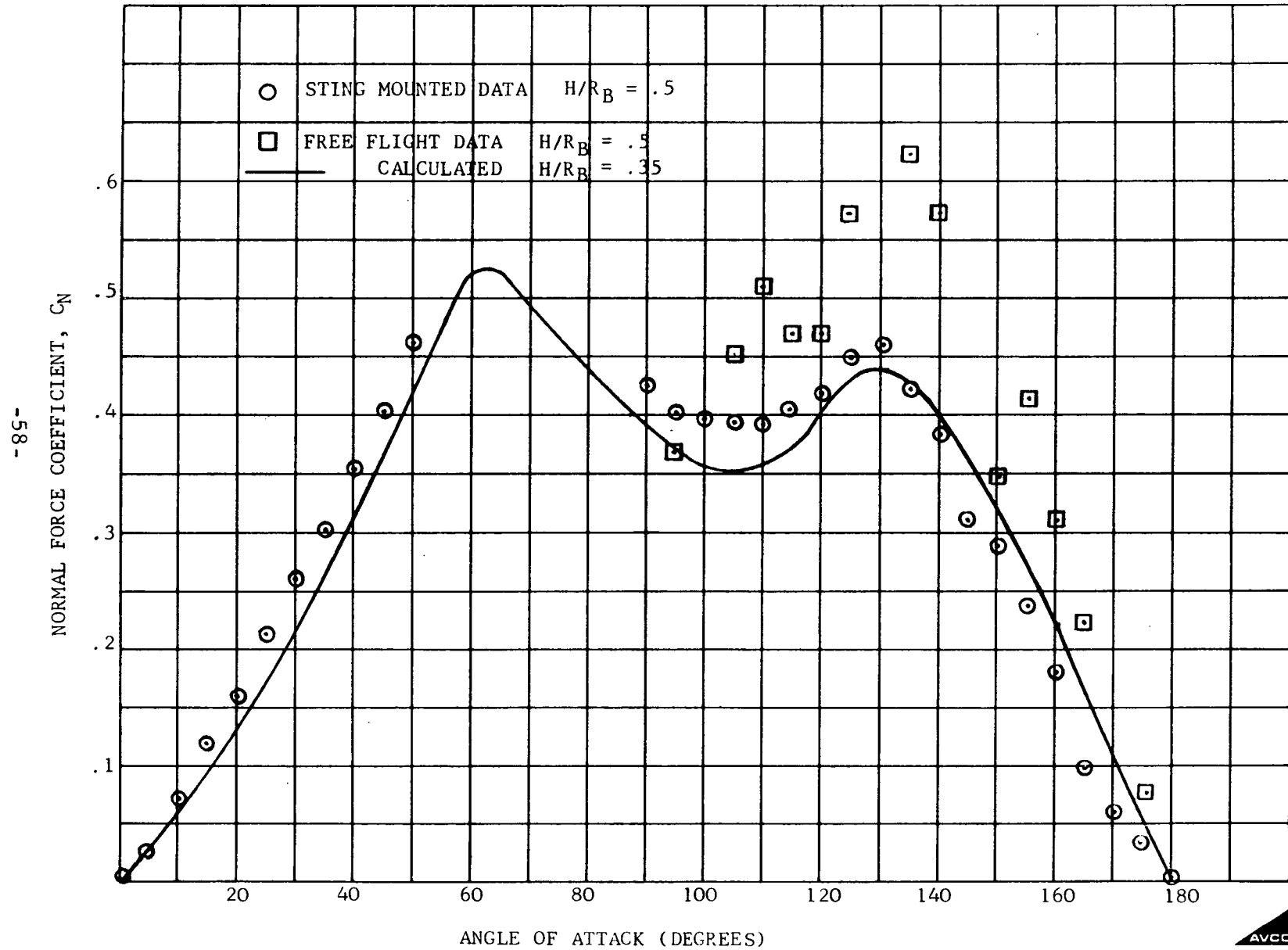
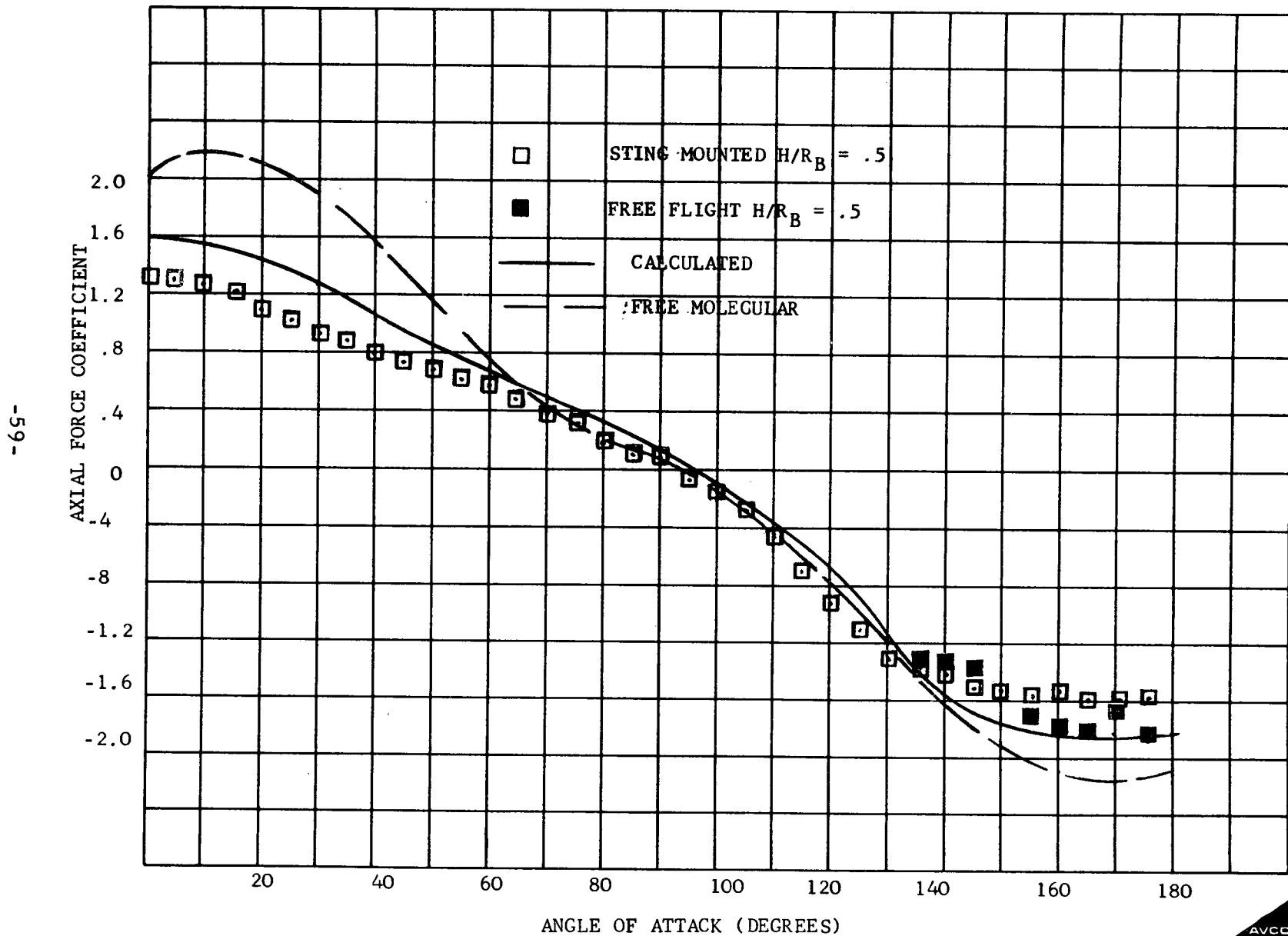


Figure 3.2-5

VARIATION OF AXIAL FORCE COEFFICIENT



molecular conditions, the coefficients for this regime have been evaluated and the results presented in Figure 3.2-6. Although the area under the moment coefficient curves are comparable, which would result in similar arrestment of tumble, the free molecular results indicate superior performance for rearward entry conditions. Test data obtained from Reference 3.2-1 support this improved performance assumption.

The damping in pitch coefficients ( $C_{mq} + C_{m\dot{\alpha}}$ ) obtained in the study reported in Reference 3.2.1-5). The significant parameter is the center of gravity, for which the present data provide an extension. Figure 3.2-7 indicates that little effect on the damping results transonically as a consequence of introducing the fence. The envelope of the data is consistent with the previous results. Since the data reflects the average damping over a cycle, the damping derivative evaluation at a specific angle of attack requires the assumption of this variation. An eighth order polynomial was assumed, the integral of this variation was equated to the test data variation with the result indicated in the figure for the "actual" damping variation with angle of attack. Similar results were obtained at other Mach nos. (see Figure 3.2-8) for the damping derivative.

The coefficients at other Mach nos. were obtained by modifying the variations presented with angle of attack by the appropriate derivative variation with Mach no. obtained in the tests at small angles of attack.

The center of gravity location for the data presented is located at a station which is 30.5% of the diameter aft of the stagnation point. Since the rearward stability at 180 degrees angle of attack is small, further movement of the center of gravity aft of this location is unacceptable.

#### 3.2.2.2 Reentry Dynamics

The trajectory analysis was performed with the aerodynamic coefficients evolved (see Section 3.2.2.1). The mass characteristics utilized are presented in Table 3.2-V.



Figure 3.2-6

VARIATION OF PITCHING MOMENT, WITH ANGLE OF ATTACK

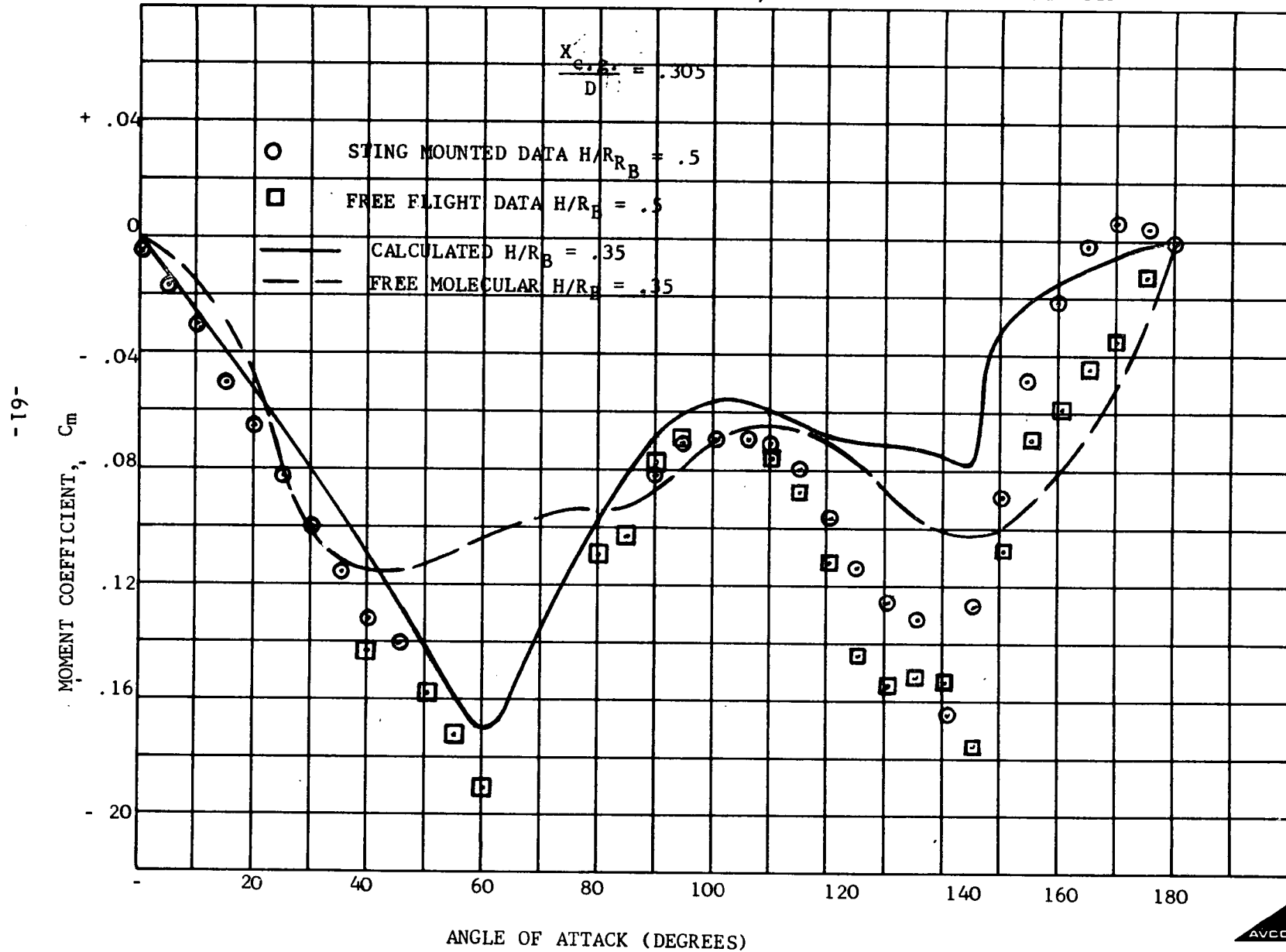


Figure 3.2-7  
DAMPING IN PITCH DERIVATIVE  
M = 1.1

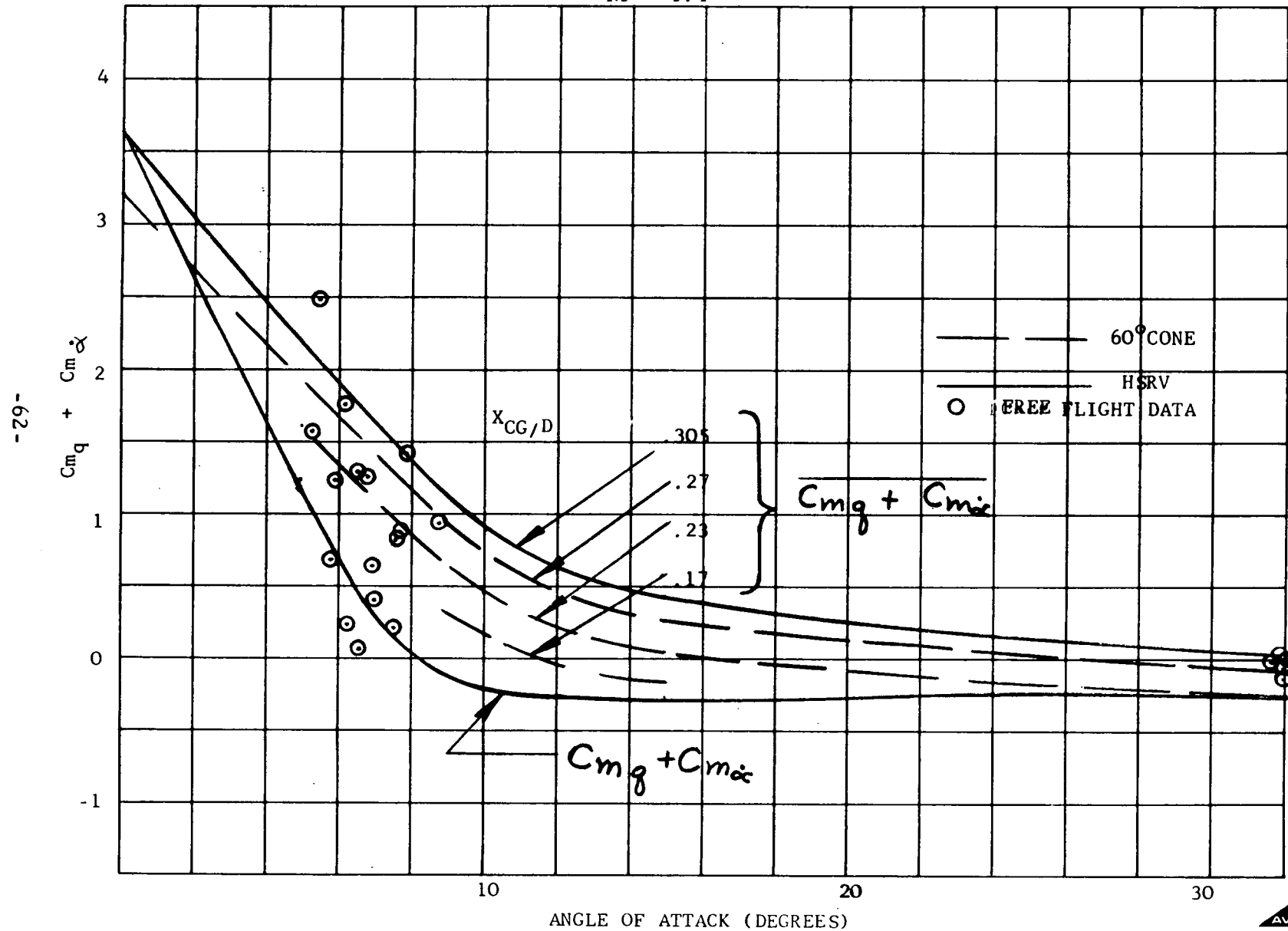


Figure 3.2-8  
DAMPING IN PITCH DERIVATIVE (MACH NO. DEPENDENCE)

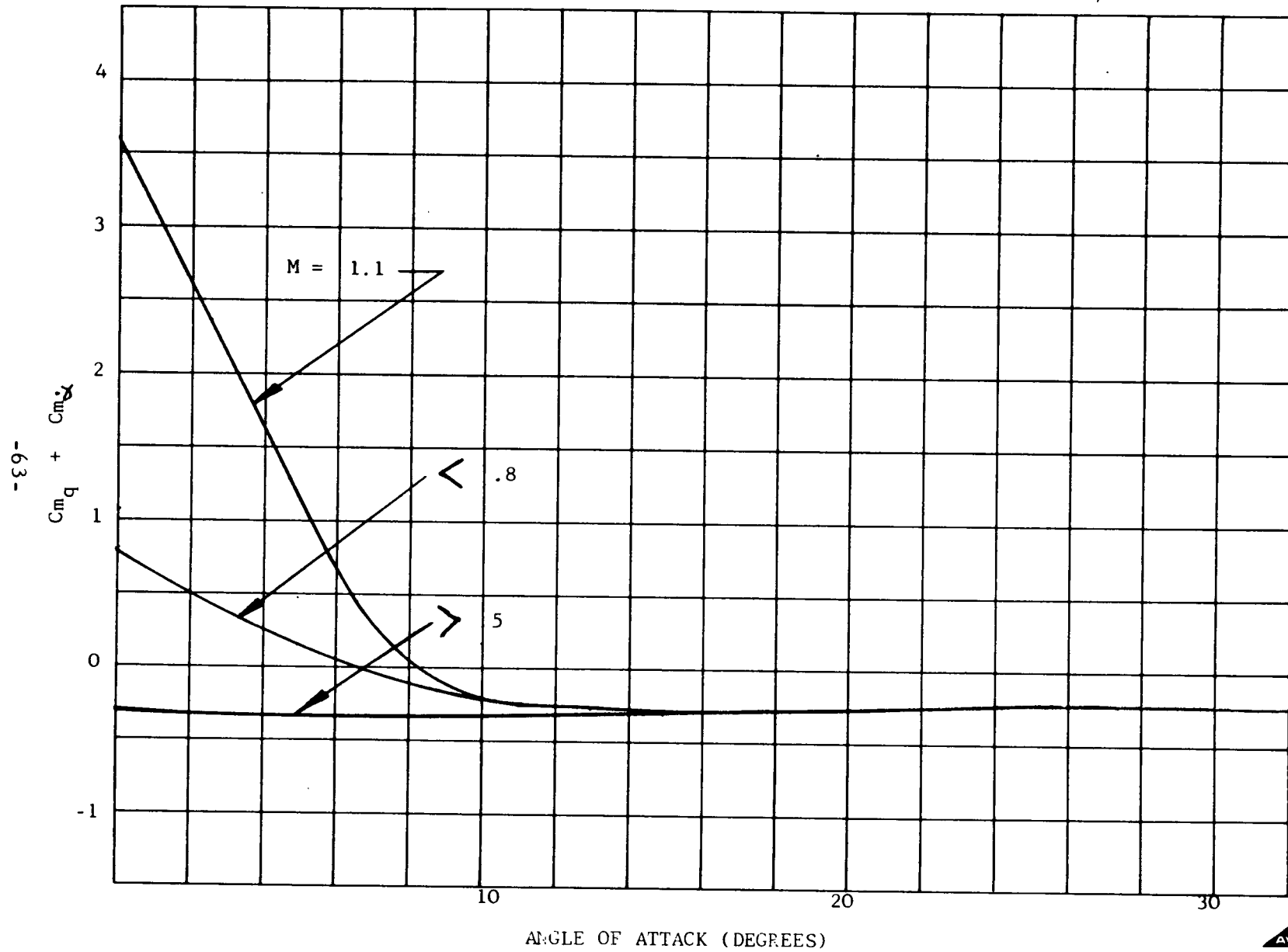


TABLE 3.2-V

HSRV Mass Characteristics

Diameter (m)	2.134
Mass (kg)	987
Center of Gravity ( $\frac{X_{c.g.}}{D}$ )	.287
Spin Radius of Gyration $\delta_{xx} / D$	.292
Pitch Radius of Gyration $\delta_{yy} / D$	.216

All entry conditions resulted in terminal descent at twenty kilometers altitude with the maximum angle of attack envelope associated with the orbit injection maximum loads trajectory (  $\gamma = -20^\circ$  ), with tumble. The early entry angle of attack envelopes are presented in Figure 3.2-9 for the rearward entry mode and in Figure 3.2-10 for the tumble mode. The significance of the entry attitude is indicated in the latter figure, comparison of the two figures illustrates the effect of tumble on the dynamics. The rearward attitude is present at a later time in the trajectory for the tumble mode, as a consequence the angle of attack envelopes are greater. These higher angles of attack result in higher capsule and aeroshell heating. In addition, the lower drag coefficient at angle of attack results in further aggravation as higher velocities are realized at specified altitudes.

The first quarter of a cycle for the orbit decay requires 188 seconds with the entire oscillation taking 586 seconds. The tumble for orbit decay does not cease until 100 kilometers altitude.

A typical angle of attack envelope history is presented in Figure 3.2-11 for the orbit injection tumble mode entry. The early angle of attack variation is that shown in Figure 3.2-10. The angle of attack envelope,  $\alpha$ , converges to the terminal limit cycle. The effect of a wind profile shear was minimal, (the instant of maximum wind shear is indicated in Figure 3.2-11 as are the times at which other significant events occur). These results will be altered if there is a spin build up (due to asymmetries either

Figure 3.2-9 - EARLY ANGLE OF ATTACK HISTORIES  
REARWARD ENTRY

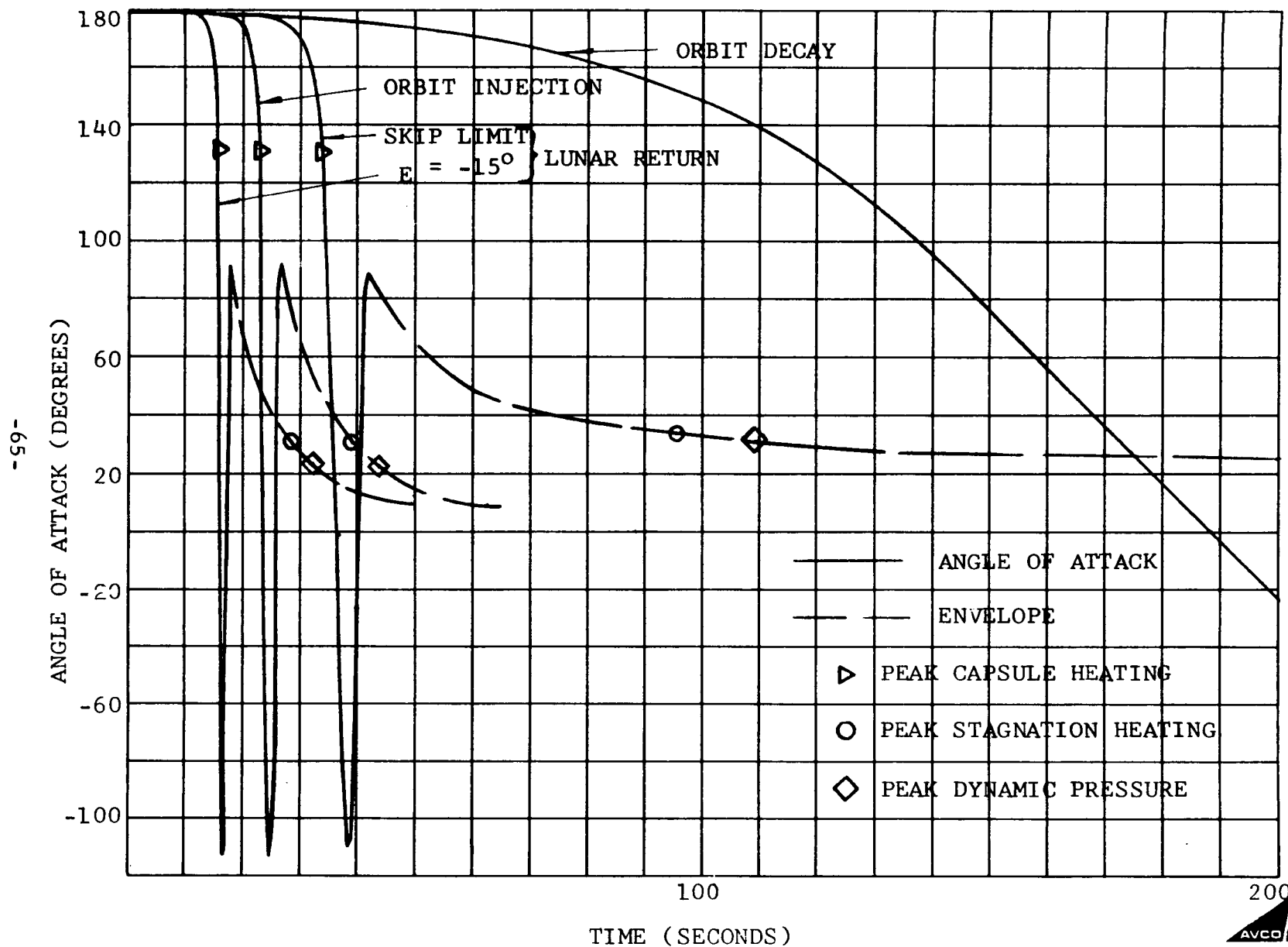


FIGURE 3.2-10  
 ANGLE OF ATTACK HISTORIES  
 WORST CASE TUMBLE

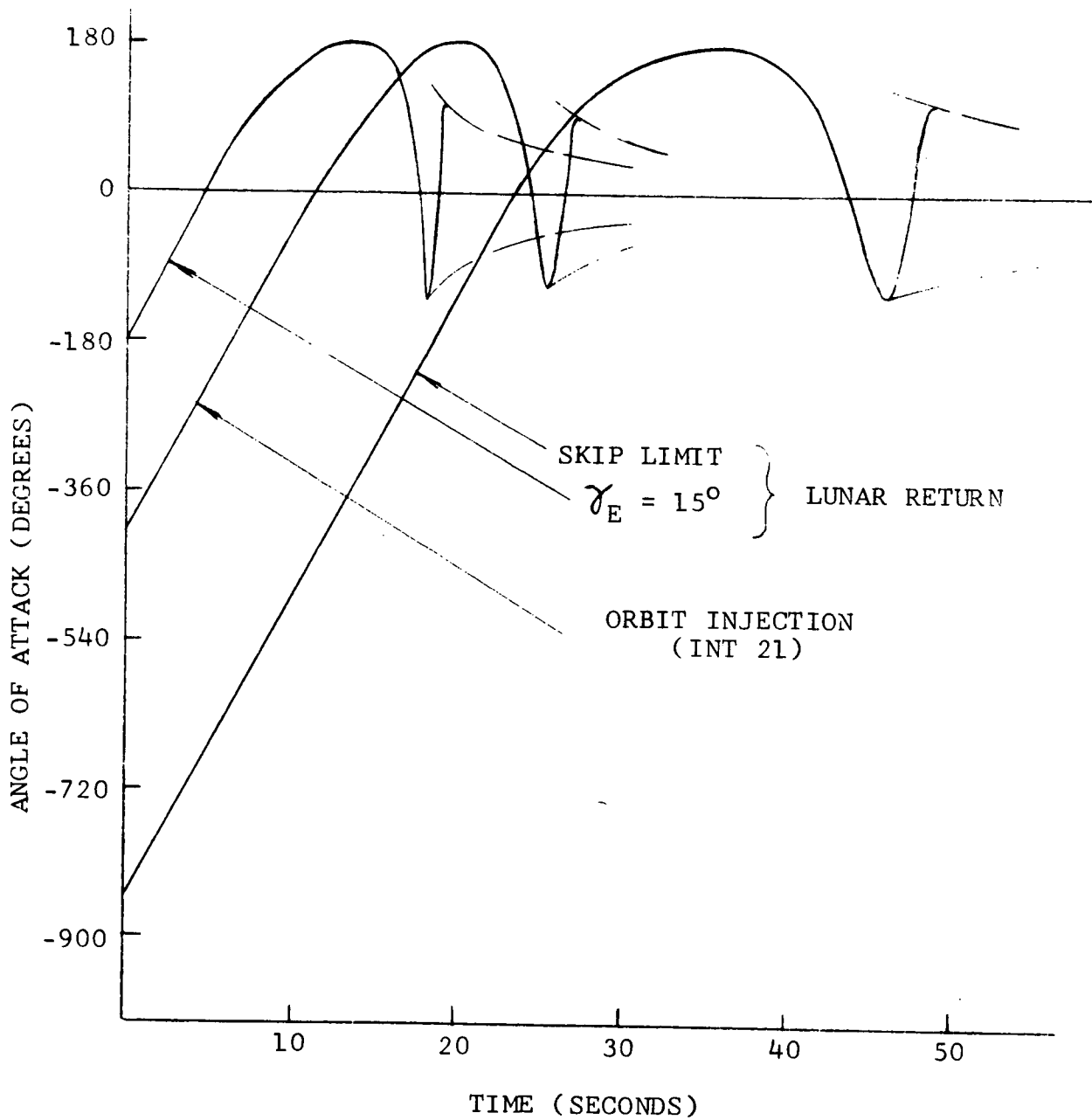
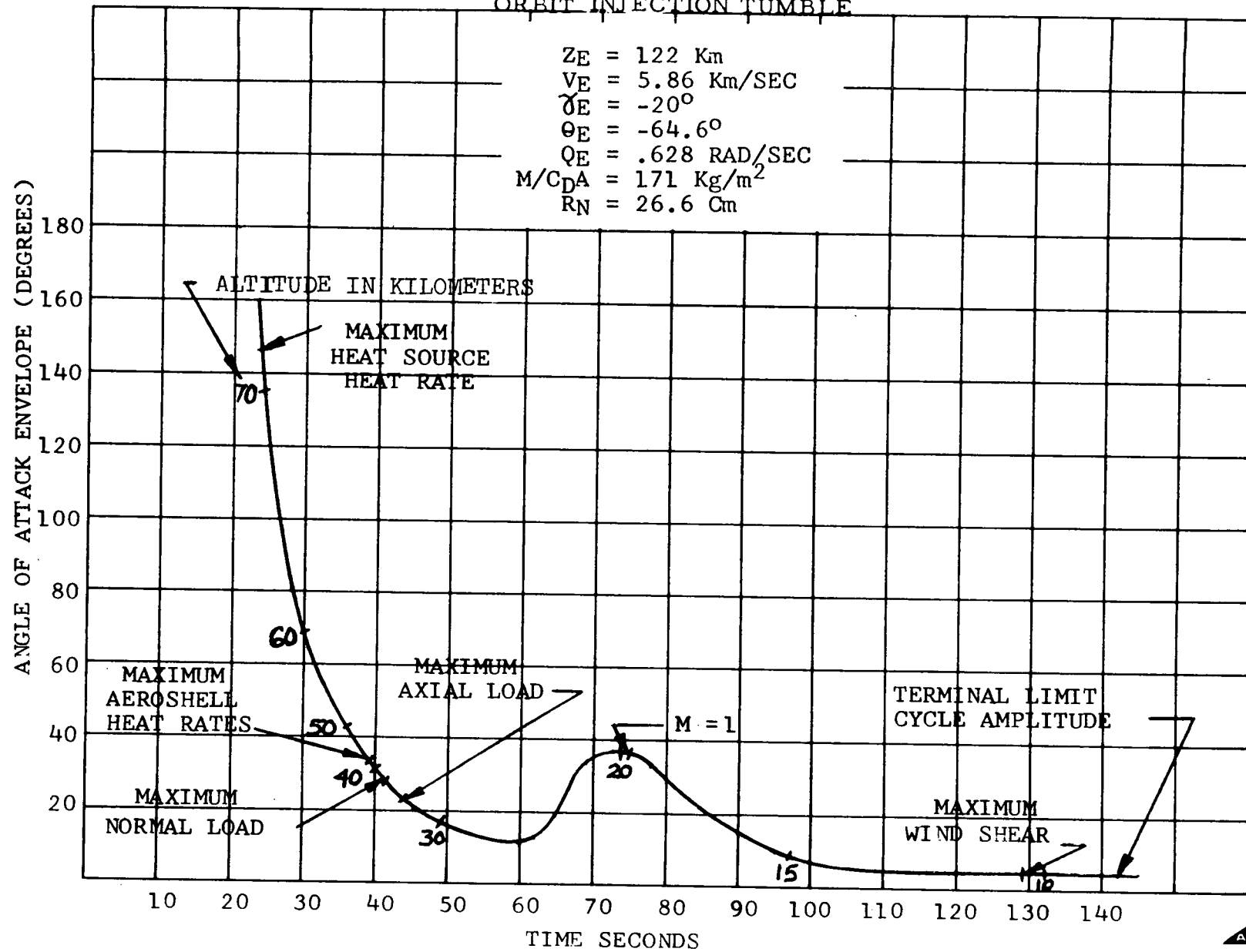


Figure 3.2-11  
 ANGLE OF ATTACK ENVELOPE HISTORY  
 ORBIT INJECTION TUMBLE



inherent or as a consequence of ablation) or if there are wind gusts (these topics will be discussed below). A small amount of spin appears desirable in that the transonic characteristics should improve (due to nonlinearity of the aerodynamic coefficients for the HSRV shape) however, the spin build up must be less than that which is critical for terminal descent. The determination of the critical spin rate is complicated by the fact that the coefficients are nonlinear. Figure 3.2-12 presents the variation of the critical spin rate (Reference 3.2-6) considering the average aerodynamic coefficient derivatives ( $C_{m\alpha}$ ,  $C_{N\alpha}$  and  $C_{m\dot{q}}$ ) within the indicated angle of attack envelopes. The curve is indicative of the limit cycle variation to be expected with a given spin rate.

The spin rates anticipated at entry are low (of the same order as tumble) however, high spin rates can result as the consequence of the mass characteristic variations and entry dynamics. The spin buildup can arise either through a roll moment or a center of gravity offset in combination with an angle of attack. The roll moment is primarily the result of surface irregularities at entry or incurred as a result of ablation. The center of gravity offset, at entry or as a result of ablation, in combination with the angle of attack motion usually is self compensating except in the case where a surface asymmetry results in a trim normal to the offset, in which case a continuous roll torque is generated. Since all trajectories investigated attained terminal conditions at high altitudes, attention was focused on the maximum ablation trajectory, i. e., the Lunar return skip limit. This trajectory in addition, experiences a large integral of dynamic pressure. This combination (i. e., maximum ablation and high integrated dynamic pressure) results in the potential for large spin buildup.

Maximum asymmetries associated with ablation were determined assuming lunar type motion. Table 3.2-VI summarizes the total mass characteristics variations, with Figure 3.2-13 presenting the time variation. The two curves presented in the figure reflect the variations associated either with mass variation or surface characteristics. The mass variation parameters include center of gravity location and moments and products of inertia. The surface characteristics dependent parameters considered are the roll moment and the trim moment at zero angle of attack ( $C_{m\alpha_t}$ ).

The implications on the HSRV dynamic behavior due to these variations were analyzed by means of a six degree of freedom computer code. The spin buildup associated with these extensive variations was 54 RPM which is well below the indicated critical spin rate of 150 RPM (see Figure 3.2-12). The angle of attack history with ablation induced asymmetries are compared with the unperturbed behavior in Figure 3.2-14, included the roll rate history. The primary source of roll buildup is that associated with the roll moment ( $C_{l_p}$ ). An improvement in the terminal characteristics (limit cycle amplitude) is experienced with spin since in contrast to planar oscillations which rotate past zero angle of attack, where there is dynamic instability, the coning motion with spin always experiences some damping. In this respect it has been assumed that the experimental data is



FIGURE 3.2-12  
TERMINAL STABILITY LIMITS

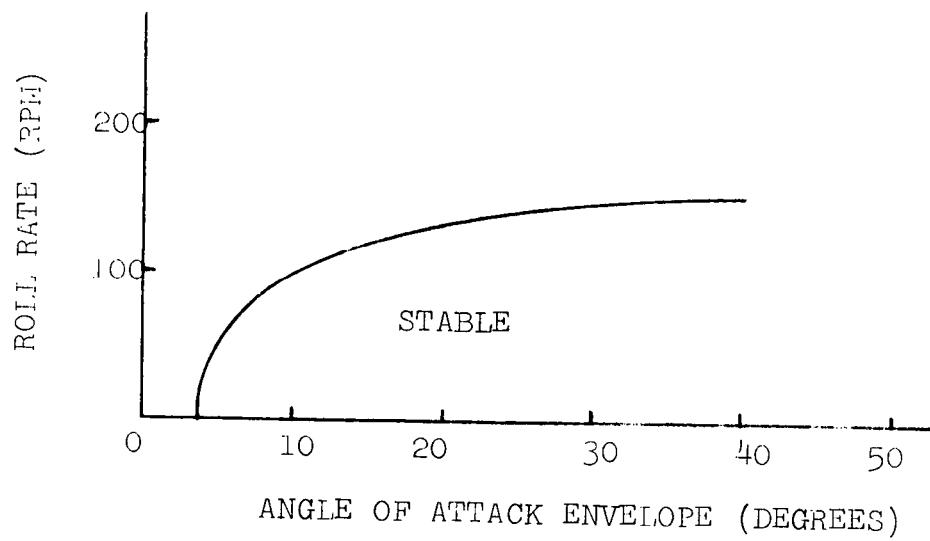


TABLE 3.2-VI

ABLATION DEPENDENT CHARACTERISTICS AND TOTAL CHANGE  
(LUNAR RETURN SKIP-LIMIT)

MASS PROPERTIES CHANGE ( )

ORIGINAL

$$M = 987 \text{ Kg}$$

$$I_{xx} = 380 \text{ Kg-m}^2$$

$$I_{yy} = I_{zzo} = 209 \text{ Kg-m}^2$$

$$X_{c.g./D} = .287$$

CHANGE

$$\Delta M = 14.4 \text{ Kg}$$

$$\Delta I_{zz} = -22.8 \text{ Kg-m}^2$$

$$\Delta I_{xy} = -1.1 \text{ Kg-m}^2$$

$$\Delta I_{yy} = -5.5 \text{ Kg-m}^2$$

$$\Delta I_{xx} = -8.4 \text{ Kg-m}^2$$

$$\Delta X_{c.g./D} = .0026$$

$$\Delta Y_{c.g./D} = .0056$$

AERODYNAMIC COEFFICIENT CHANGE

$$C_{lp} = .001$$

$$C_{m_t} = .00018$$

Figure 3.2-13  
ABLATION PHENOMENA VARIATION  
LUNAR RETURN SKIP LIMIT

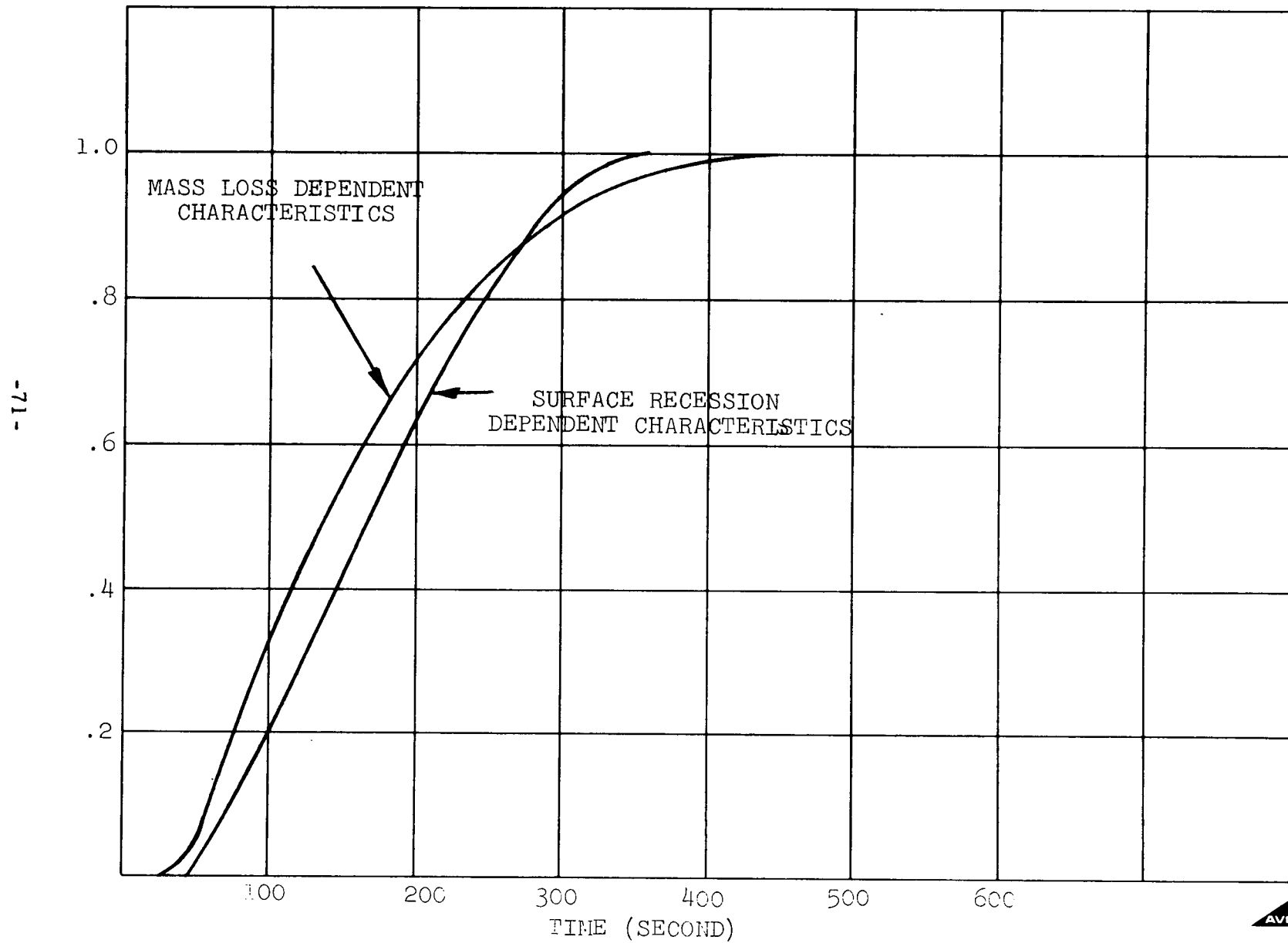
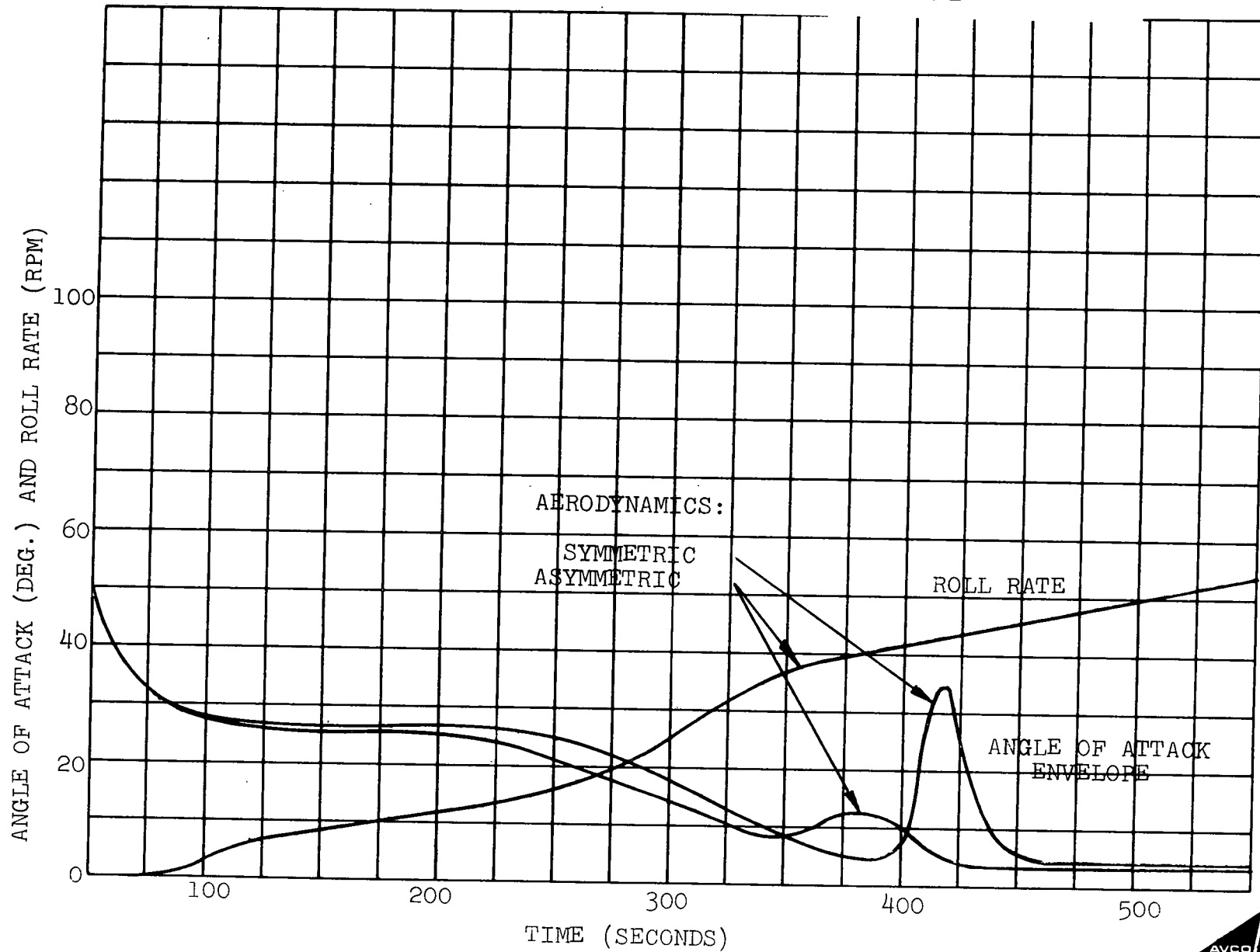


Figure 3.2-14  
EFFECT OF ABLATION INDUCED ASYMMETRIES ON AERODYNAMICS  
LUNAR RETURN SKIP LIMIT TUMBLE



applicable to both planar and coning oscillations, no data is available to refute or substantiate this assumption. In addition, the transonic divergence is inhibited because of spin stabilization. No deleterious effects were found to be associated with the predictable asymmetries introduced by ablation.

A wind gust of 15.2 m/sec was introduced with a duration of .5 second (see reference 3.2-7) at terminal conditions near impact. The effect of this gust is presented illustratively in Figure 3.2-15. Although there was no appreciable effect due to shear, the angle of attack amplitude opened up to approximately eighteen degrees, the corresponding angle between the local vertical and the vehicle axis is thirty degrees. Both the angle of attack and vehicle axis attitude relative to the vertical would be reduced by spin (Reference 2.1-1).

### 3.2.2.3 Reentry Heating Environments

In providing the necessary stability characteristics, the fence introduces flow interactions which aggravate the local heating particularly for the heat source capsules. Although the velocities are considerably higher for the Lunar return, the relevant shock shapes and pressure distributions are similar to those associated with orbital velocities. (The methods of Reference 2.1-1 have been utilized where applicable.)

The gas temperatures are significantly higher for Lunar return resulting in high radiative intensities and high radiative heating over sections of the aeroshell where large shock layer thicknesses exist.

The evaluation of the radiative heating for the stagnation region was relatively straightforward. The appropriate shock shape and the incident radiant energy was determined (References 3.2-7, -8, -9). The evaluation of the Heat Source Unit radiation environment was more complex. Since the flow is not completely swallowed by the fence (insufficient venting area, see Section 3.2.2.1) large shock standoffs are possible. The location of the bow shock for the rearward attitude is shown in Figure 3.2-16. As the shock density ratio increases relatively more flow is vented through the apertures, thereby reducing the shock standoff distance from the fence. (The shock would be swallowed for the reference fence at a shock density ratio of approximately thirty). The total shock layer thickness evident and the geometry require further analyses than those considered on the forebody. Corrections are necessary to account for absorption and decay (Reference 3.2-10) for large shock thicknesses, in addition a correction was evaluated for the truncation associated with the presence of the fence.

#### a. Heat Sources

Preliminary analysis indicated that the tumble mode would result in maximum Heat Source heating. This is due to the combined effect of the heating aggravation at angle of attack and the alteration of the reentry trajectory due to the effectively increased ballistic coefficient.

Figure 3.2-15  
 TERMINAL PERFORMANCE WITH WIND SHEAR AND GUSTS  
 ORBIT INJECTION TUMBLE

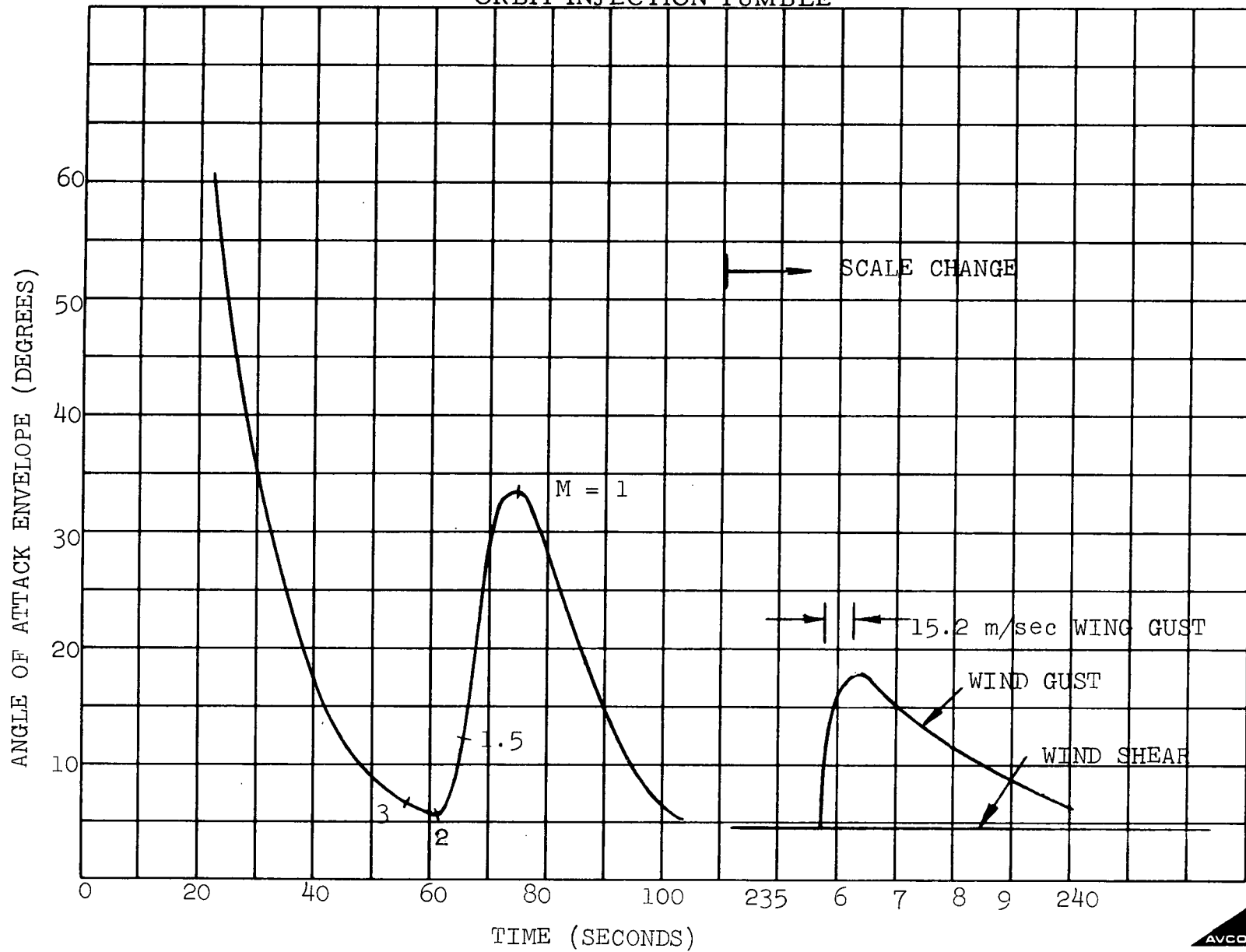
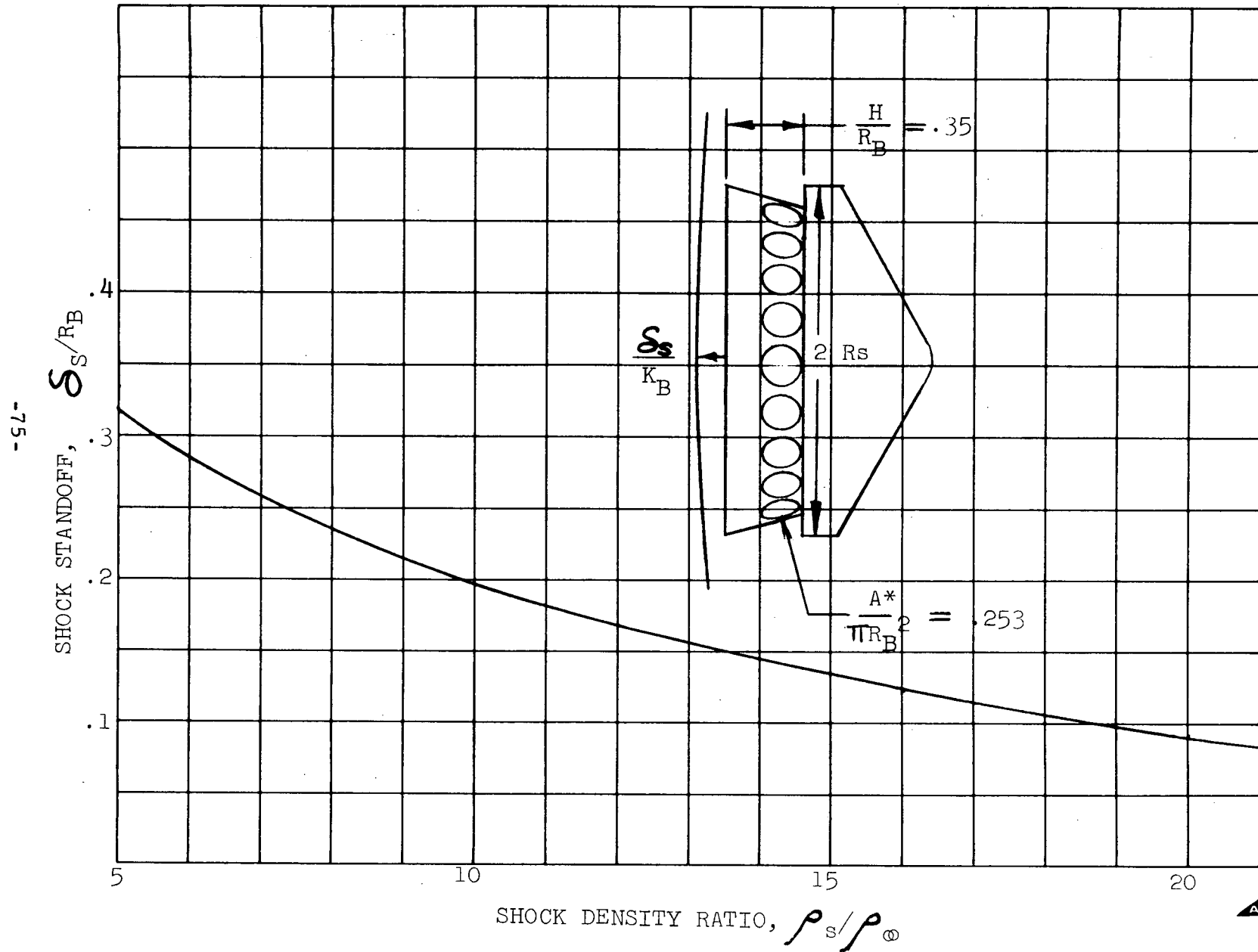


Figure 3.2-16  
SHOCK STANDOFF DISTANCE



The Heat Source heating histories are presented in Figures 3.2-17 through 3.2-23, for both rearward and tumble entry modes. The initial heating variation during tumble and rearward entry is presented as evaluated (the calculated cyclic variation). After arrestment of tumble or after the first oscillation in the case of rearward entry, only the average heating during a cycle is presented. Only one substantial radiative pulse occurred for the tumble mode. Steep entry conditions resulted in turbulent heating over a significant portion of the heat pulse (see Figures 3.2-19 through 3.2-22). Although the integrated heat load was largest for orbit decay entry, the heating rates were relatively low (see Figure 3.2-23).

Considerable differences exist among the various entry modes for orbital decay (i. e., rearward and forward entry and tumble). The interplay between the dynamic motion and the trajectory (altitude/time histories) was significant for this entry resulting in variations in thousands of seconds in reentry time. In all orbit decay analyses the entry altitude considered is 137 kilometers, which is consistent with utilizing steady state temperature conditions associated with a space environment (no aerodynamic heating). Further comparisons for the orbit decay conditions are presented below.

#### b. Aeroshell and Fence

The critical or design heating for the heat shield on the aeroshell and fence were evolved from investigating the orbit decay and Lunar return skip limit. A comparison was made of the mode of entry (i. e., forward, rearward or tumble) and its effect on the aerodynamic heating. This is particularly important for the orbit decay since the trajectory is very sensitive to the angle of attack history, which in turn depends upon the trajectory. In addition, the local heating depends upon the angle of attack.

The heating history for the zero angle of attack stagnation point on the aeroshell is shown in Figures 3.2-24 and 3.2-25. Figure 3.2-24 presents the early entry history (high altitude).

Since the tumble mode results in the highest angle of attack histories (at a given altitude) it would be anticipated prima facie that its descent time would be greatest. However, the tumble average drag is greater than the oscillatory average over a wide range of angle of attack (Figure 3.2-26 presents this variation for the continuum regime). The reduced flight times for tumble entry as opposed to rearward entry is directly associated with the higher drag during the early entry phase prior to arrestment of tumble.

The maximum heating rate for the three conditions were almost identical (see Figure 3.2-24 and 3.2-25), the early entry heating associated with the forward attitude, resulting in the maximum heat load for that entry mode. The early entry heating with tumble is applicable to all body stations up to the time of tumble arrestment which occurs at 9110 seconds.



Figure 3.2-17  
FUEL CAPSULE HEATING  
REARWARD ENTRY LUNAR RETURN SKIP

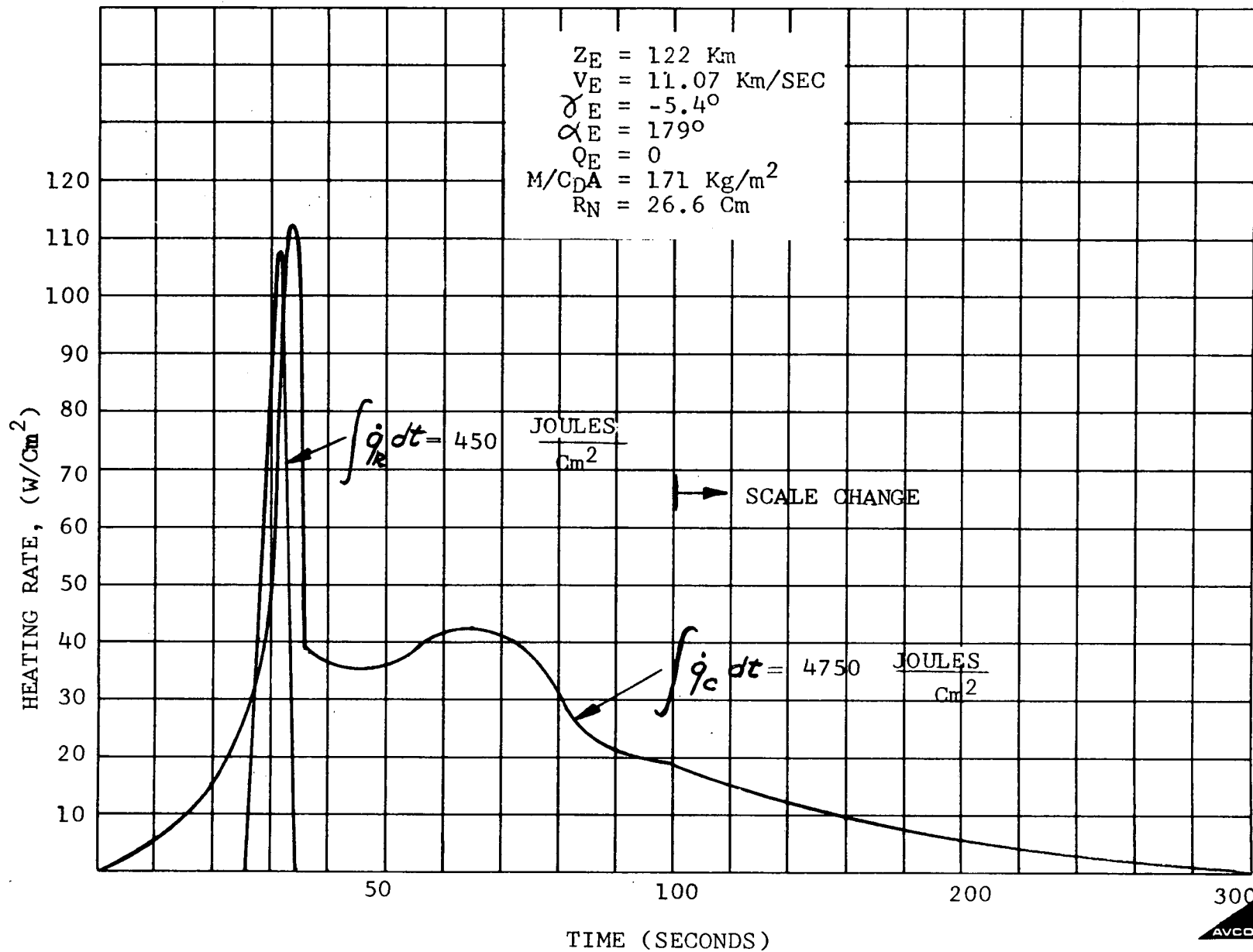


Figure 3.2-18  
FUEL CAPSULE HEATING  
LUNAR RETURN SKIP LIMIT TUMBLE

-78-

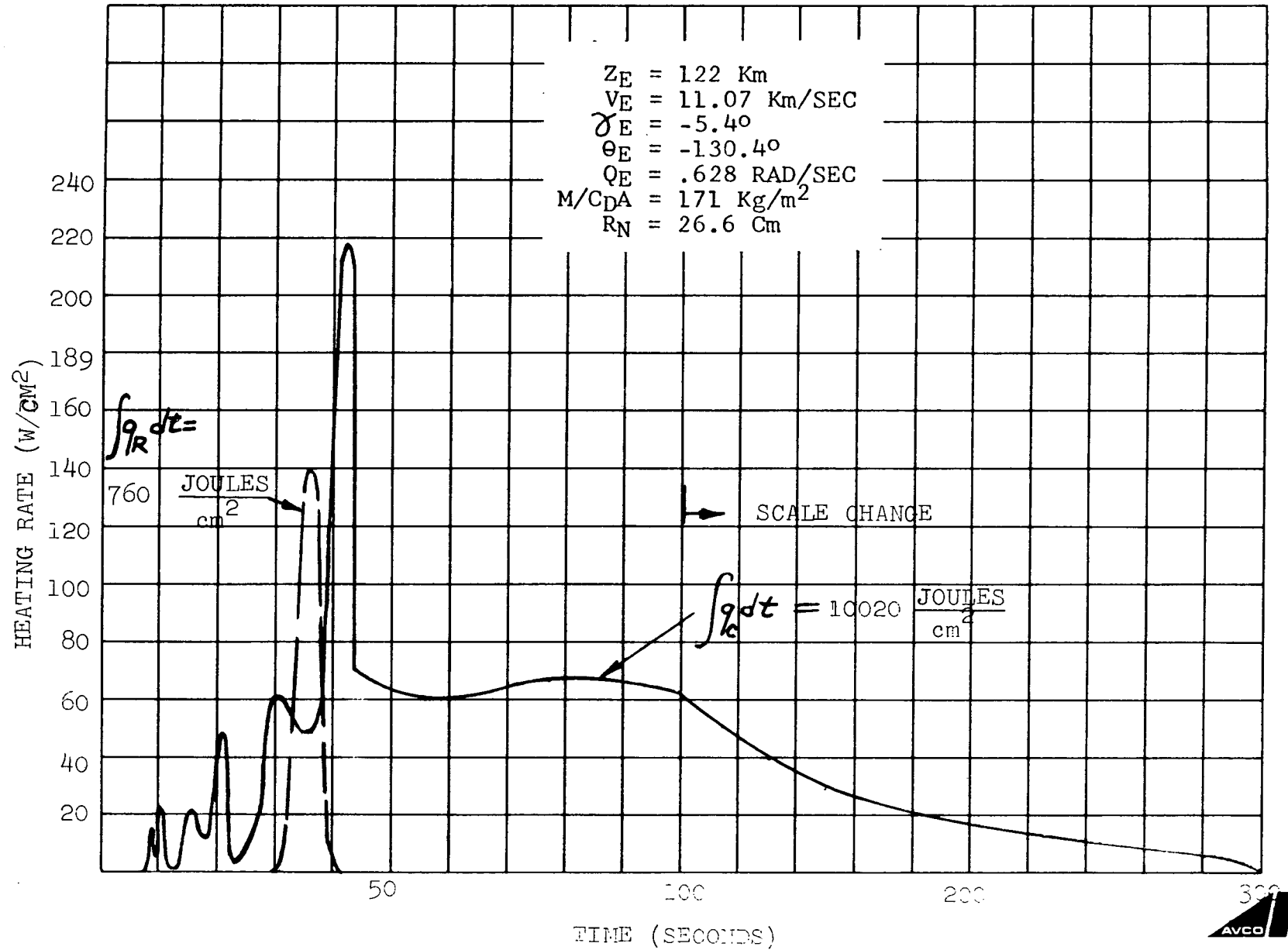
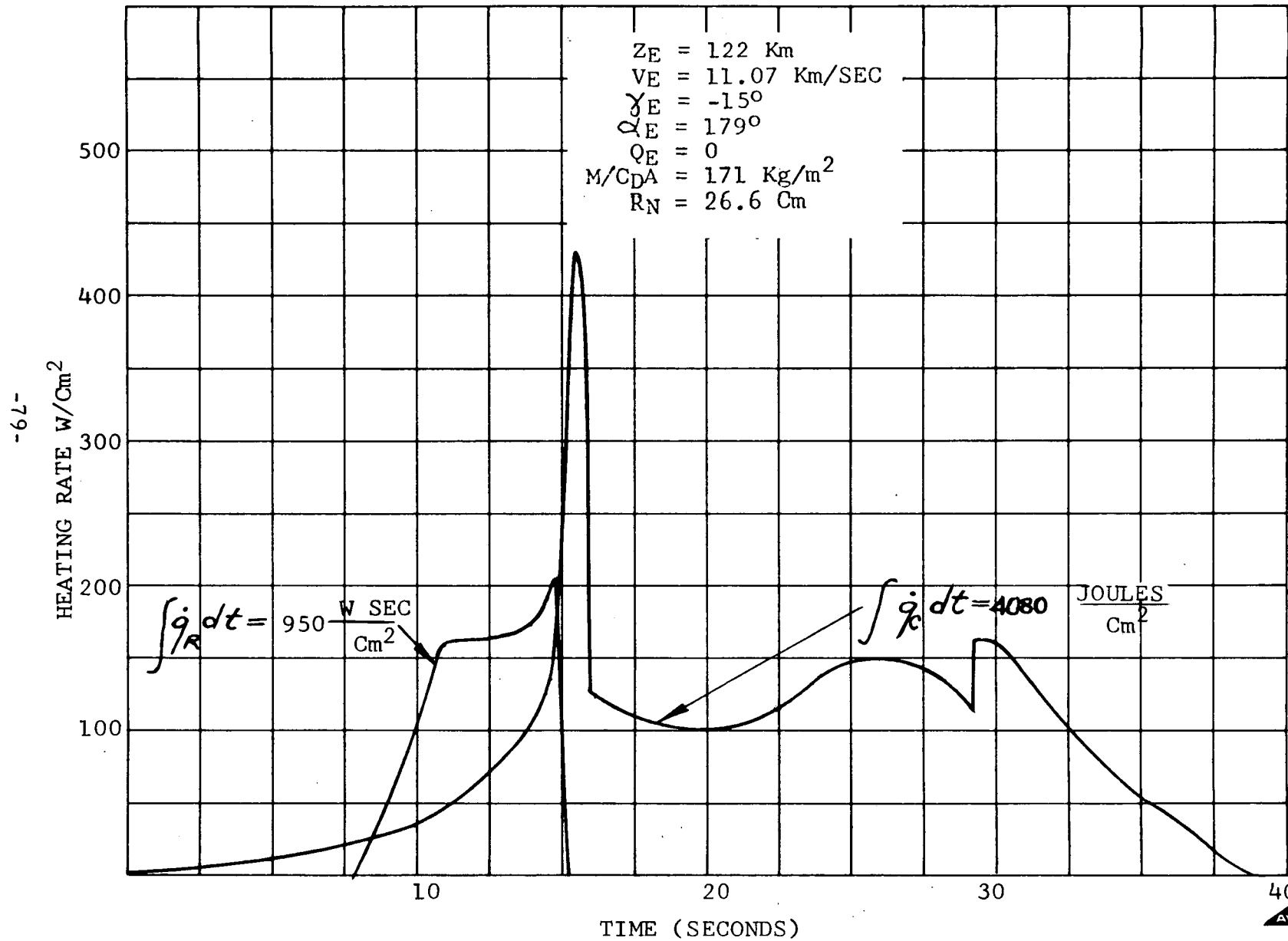


Figure 3.2-19

FUEL CAPSULE HEATING  
LUNAR RETURN,  $\gamma = -15^\circ$   
REARWARD ENTRY

$Z_E = 122 \text{ Km}$   
 $V_E = 11.07 \text{ Km/SEC}$   
 $\gamma_E = -15^\circ$   
 $\alpha_E = 179^\circ$   
 $Q_E = 0$   
 $M/C_{DA} = 171 \text{ Kg/m}^2$   
 $R_N = 26.6 \text{ Cm}$



CAPSULE HEATING  
Figure 3.2-20 LUNAR ENTRY  $\gamma_E = -15^\circ$  TUMBLE

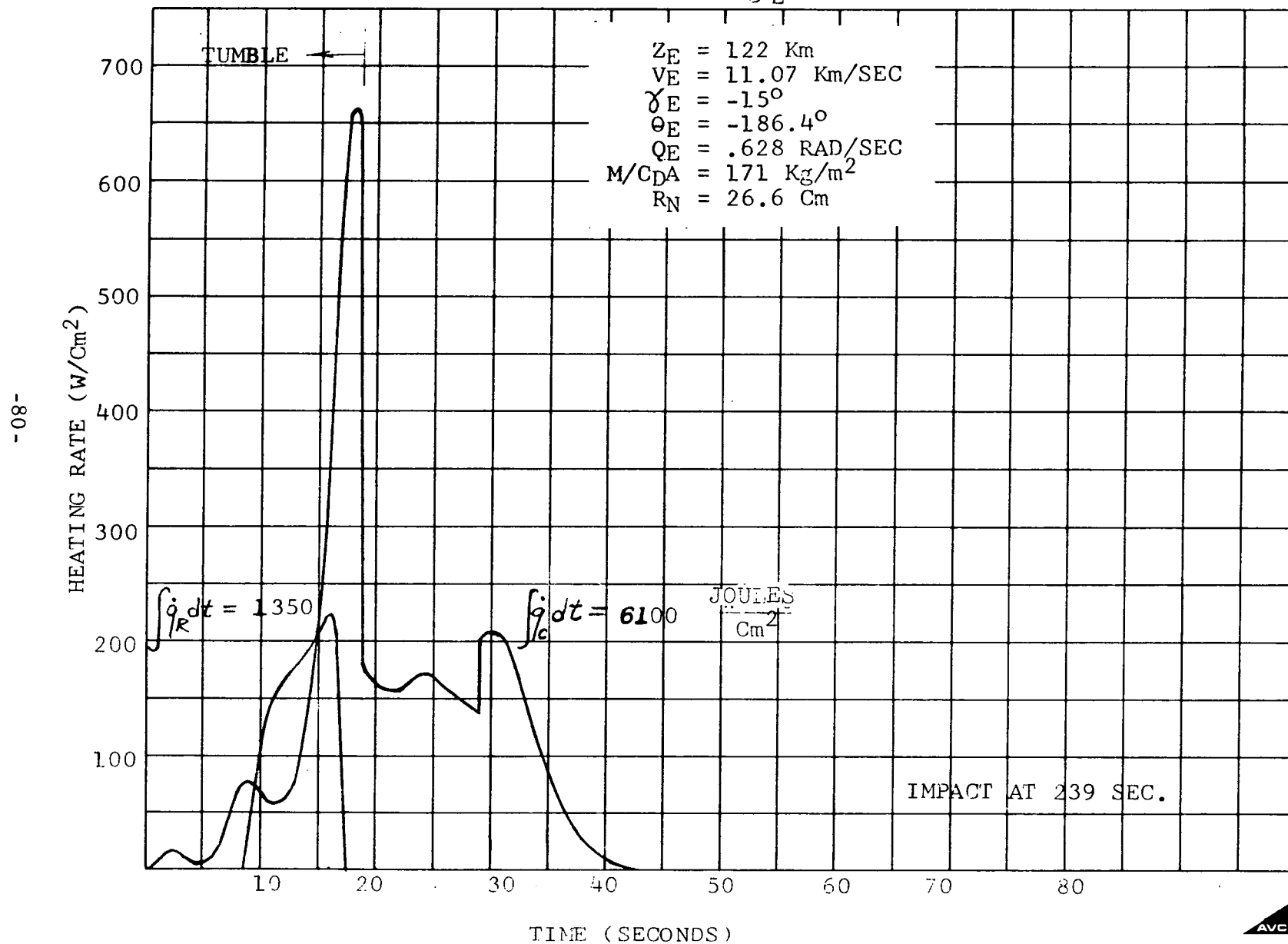


Figure 3.2-21

CAPSULE HEATING  
ORBIT INJECTION  $\gamma_E = -20^\circ$  TUMBLE

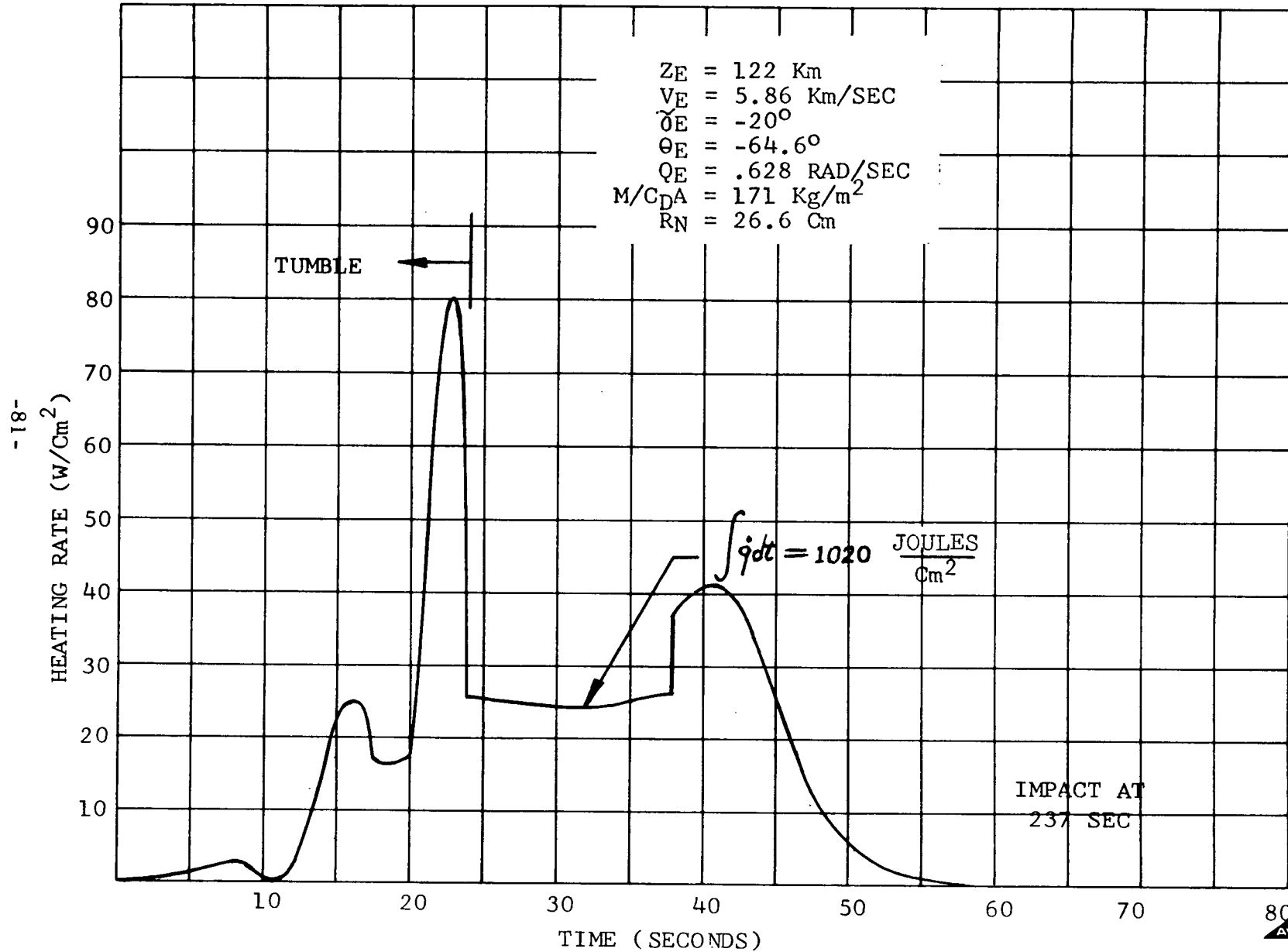


Figure 3.2-22 - FUEL CAPSULE HEATING  
REARWARD ENTRY ORBIT INJECTION

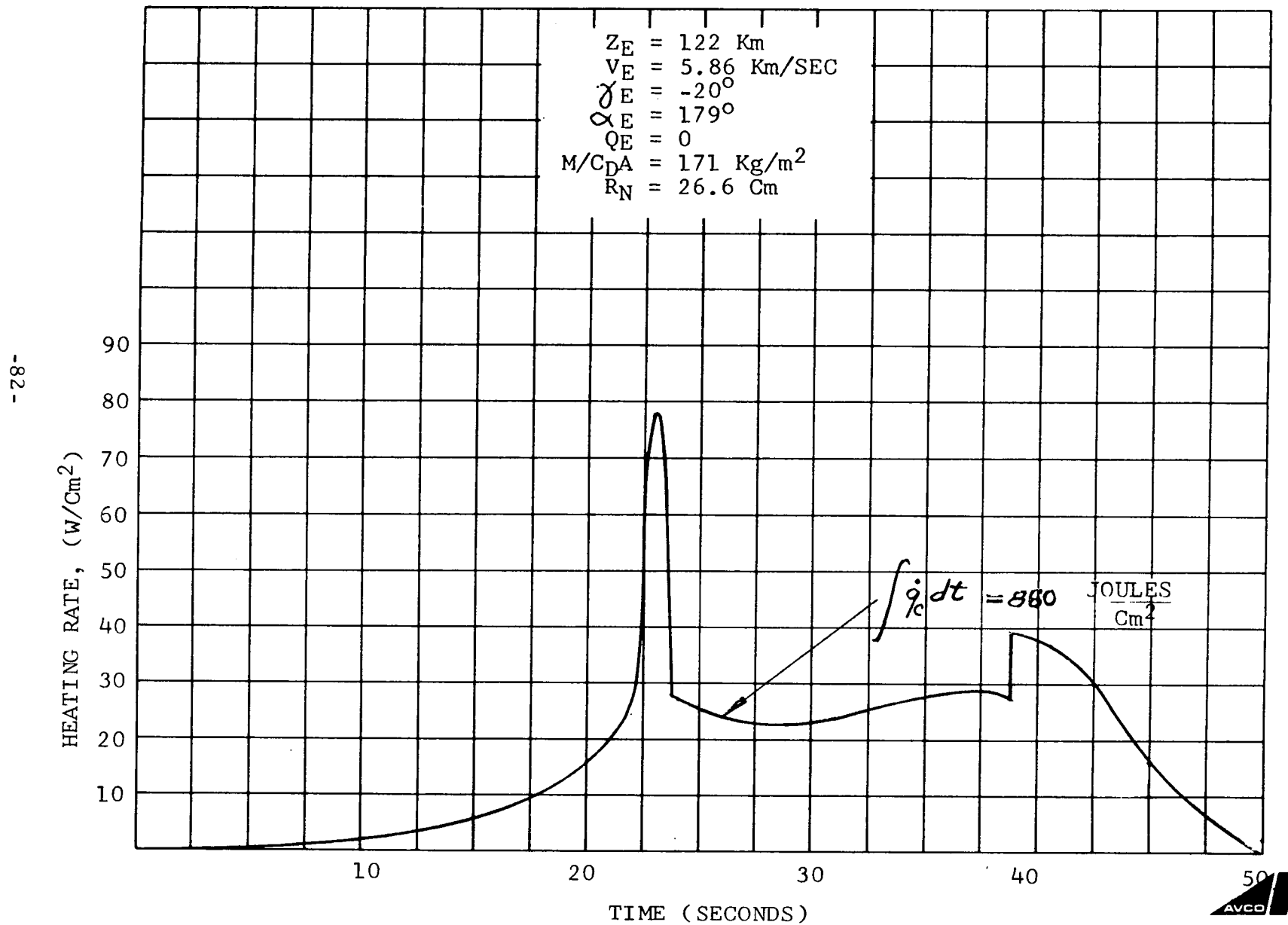


Figure 3.2-23 CAPSULE HEATING  
ORBIT DECAY TUMBLE

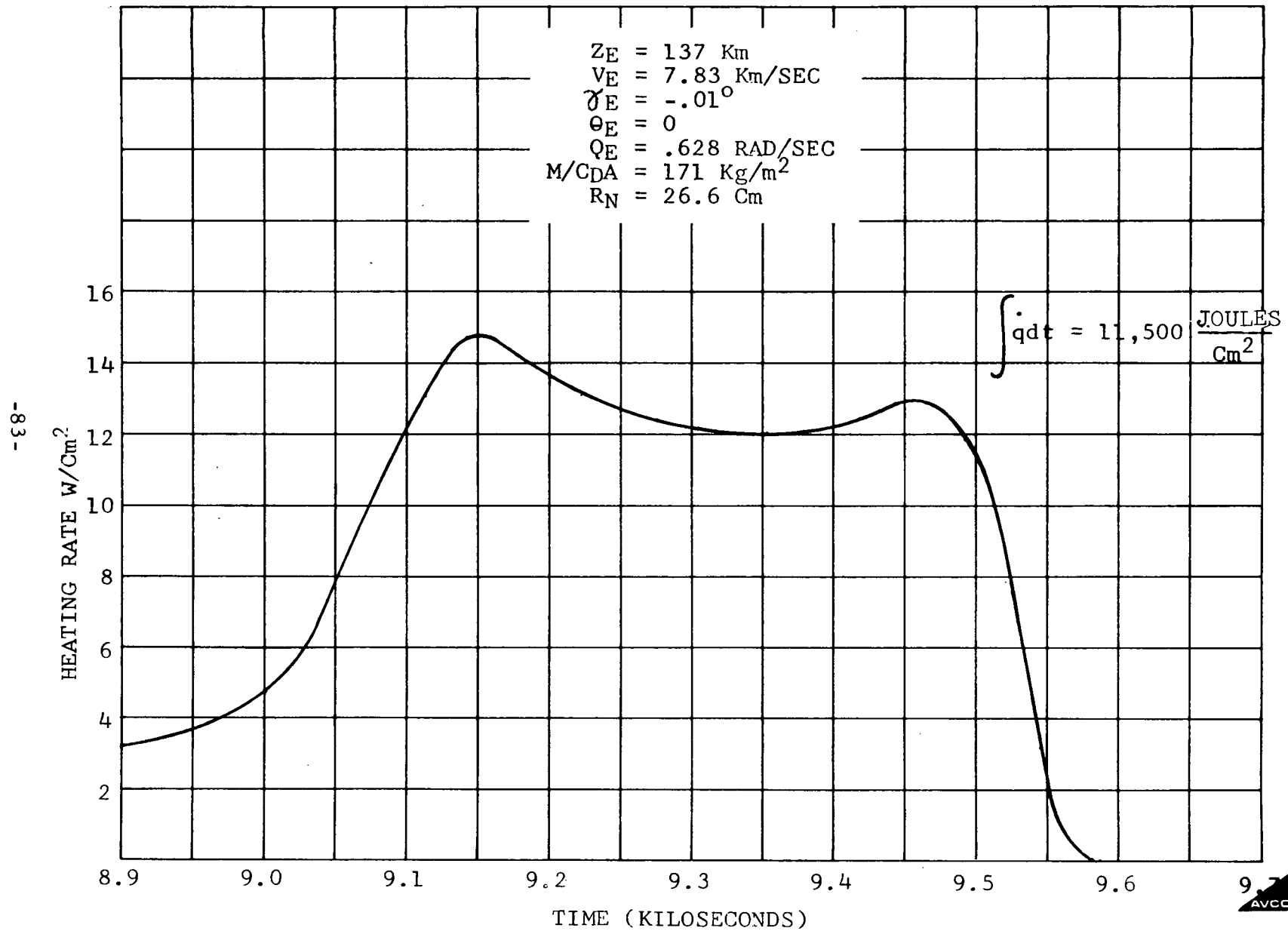


Figure 3.2-24  
STAGNATION POINT HEATING COMPARISON  
ORBIT DECAY

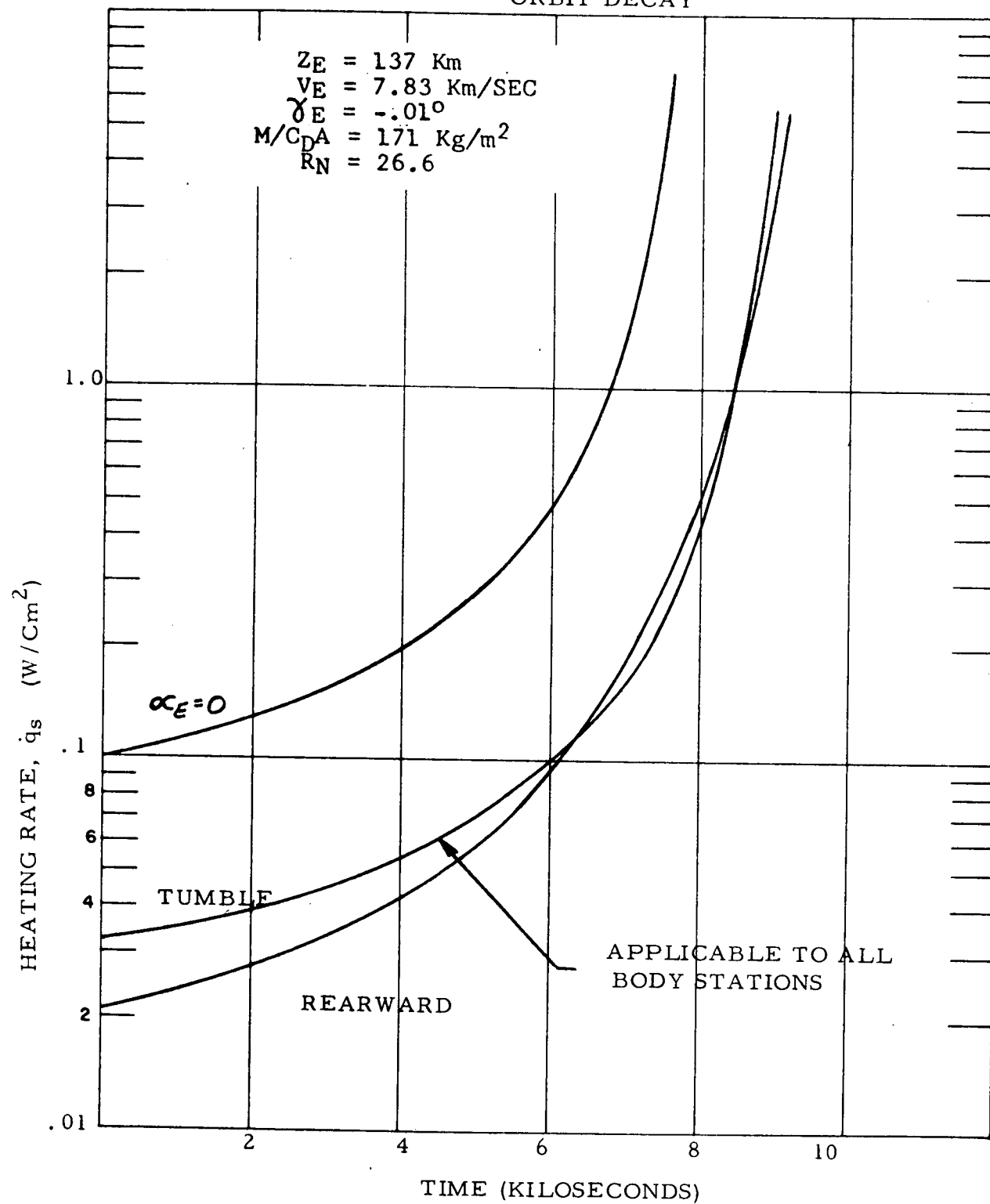




FIGURE 3.2-25  
STAGNATION POINT HEATING COMPARISON  
ORBIT DECAY

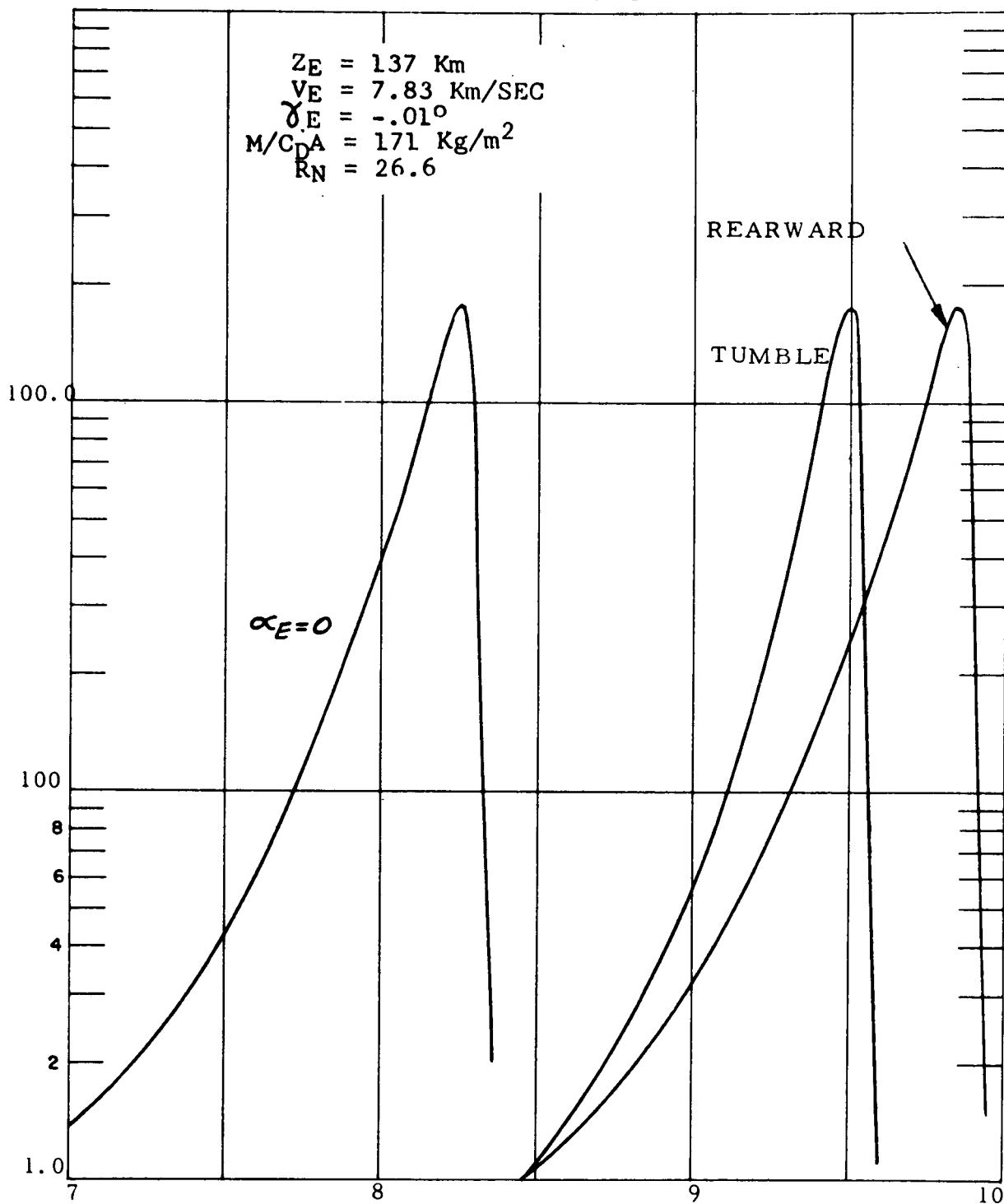
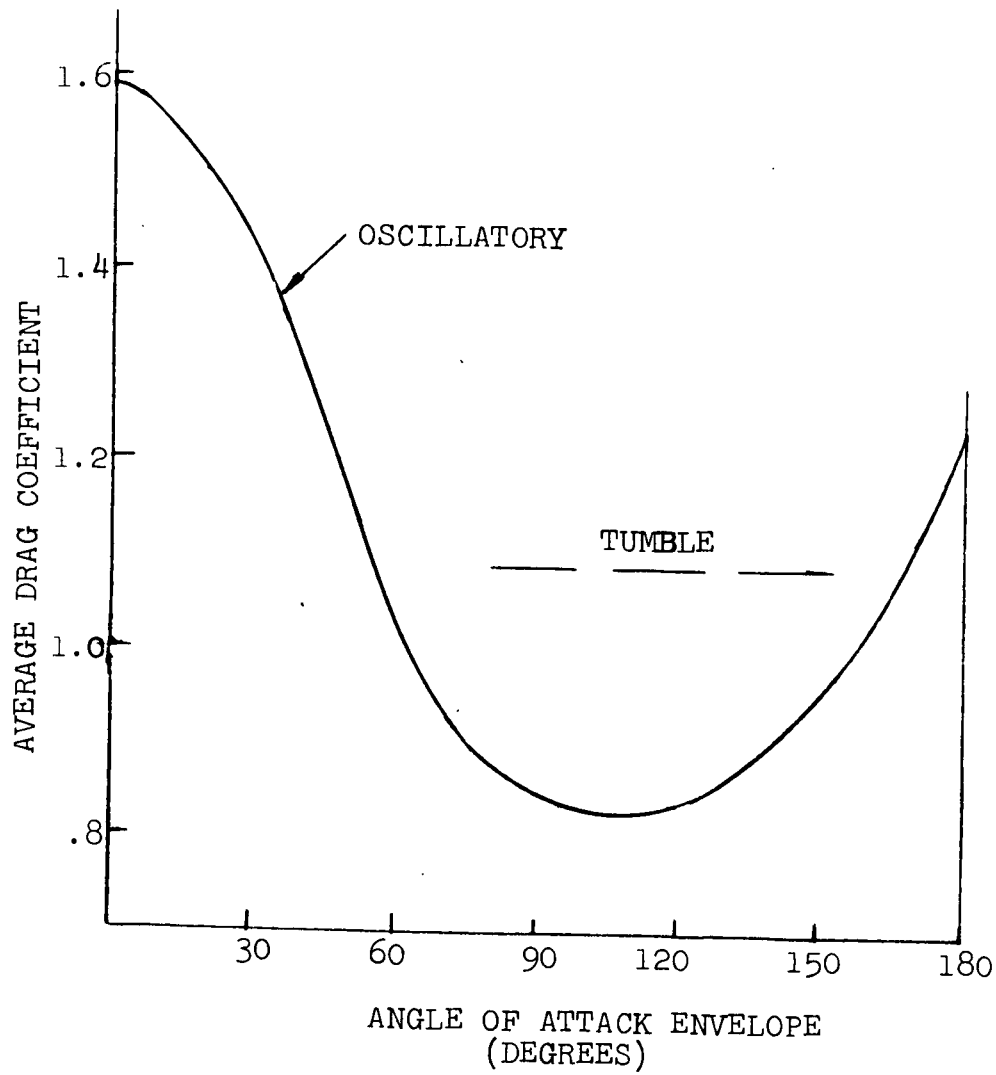


Figure 3.2-26

DRAG COEFFICIENT DEPENDENCE ON DYNAMIC MOTION



The heating at other forebody stations is presented in Figures 3.2-27 through 3.2-29.

Heating for body stations other than those on the forebody are sensitive to the angle of attack variations. Again, as in the case of the heat source capsules, the critical entry mode is that which exhibits maximum angle of attack envelopes through the heating phase. The combination of entry angle of attack with the design tumble rate which results in the lowest altitude of arrestment was used to determine the critical heating environment for the shoulder, cylinder, base and fence (outside and inside surfaces). The orbit decay tumble results were presented illustratively in Figure 3.2-27, the early entry heating has been previously presented in Figure 3.2-24. The histories presented are the tumble or oscillatory average heating during a cycle. Comparison with Figures 3.2-25 and 3.2-26 illustrate that for orbit decay forebody stations experience the maximum heat load for forward entry. In contrast the Lunar skip limit return results presented in Figures 3.2-30 and 3.2-31 indicate that were it not for the radiative heating pulse the stagnation point would also incur maximum heat load for forward entry. Although the heating rates for Lunar skip are considerably higher, the heat load for the two design conditions (orbit decay and Lunar return skip limit) are comparable. The effects of the dynamics on the heating is manifested in terms of an extension in the pulse duration; for some body stations the angle of attack dependence compensates for the trajectory effect.

### 3.3 HEAT SOURCE UNIT (HSU) DESIGN

This section summarizes the results of the HSU design analyses. Results of both steady state and transient thermal analysis are presented in section 3.3.2 for the HSU. The transient performance of the coupled HSU/HSRV/HSHX is also described. Section 3.3.3 contains a discussion of the ACHX design analyses. Finally, section 3.3.4 treats the HSU mechanical design for both earth-orbital and super-orbital loadings.

#### 3.3.1 Summary Description

The heat source unit (HSU) consists of a circular, planar array of heat sources (HS) each of which contains isotope fuel. The HSU radiates thermal energy to the heat source heat exchanger (HSHX). The entire HSU is an integral part of a reentry vehicle (HSRV). Should atmospheric reentry ever occur, the HSRV is designed to ensure safe, intact reentry of the HSU. In addition, should an individual HS ever become separated from the HSU and HSRV it is provided with the capability of safe reentry by its own individual reentry protection material. Within the reentry materials, each HS contains a refractory metal capsule into which the isotope fuel is loaded.

Figure 3.2-27  
AEROSHELL HEATING (ORBIT DECAY)

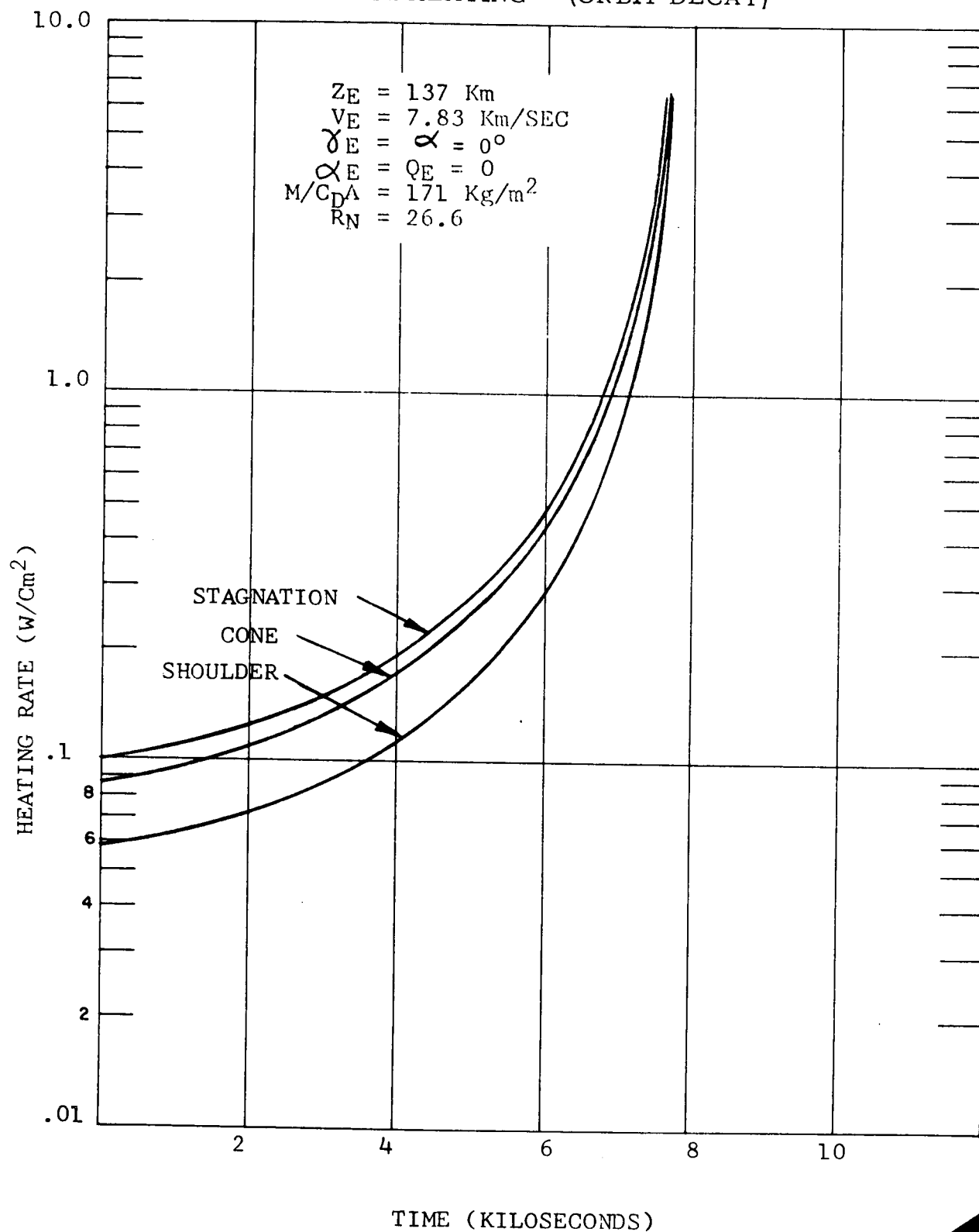
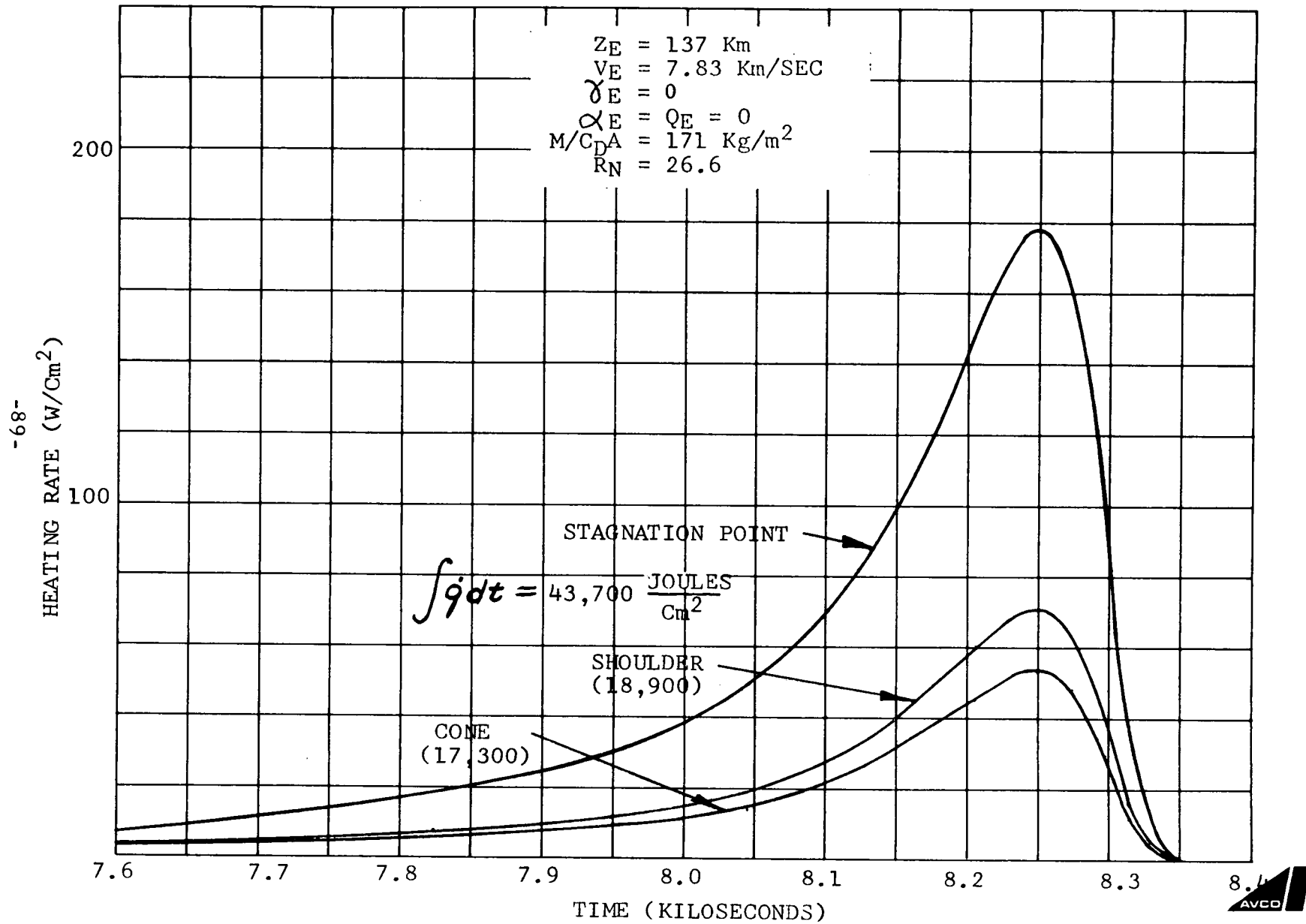


Figure 3.2-28 AEROSHELL HEATING  
ORBIT DECAY



AEROSHELL HEATING  
Figure 3.2-29 - ORBITAL DECAY TUMBLE

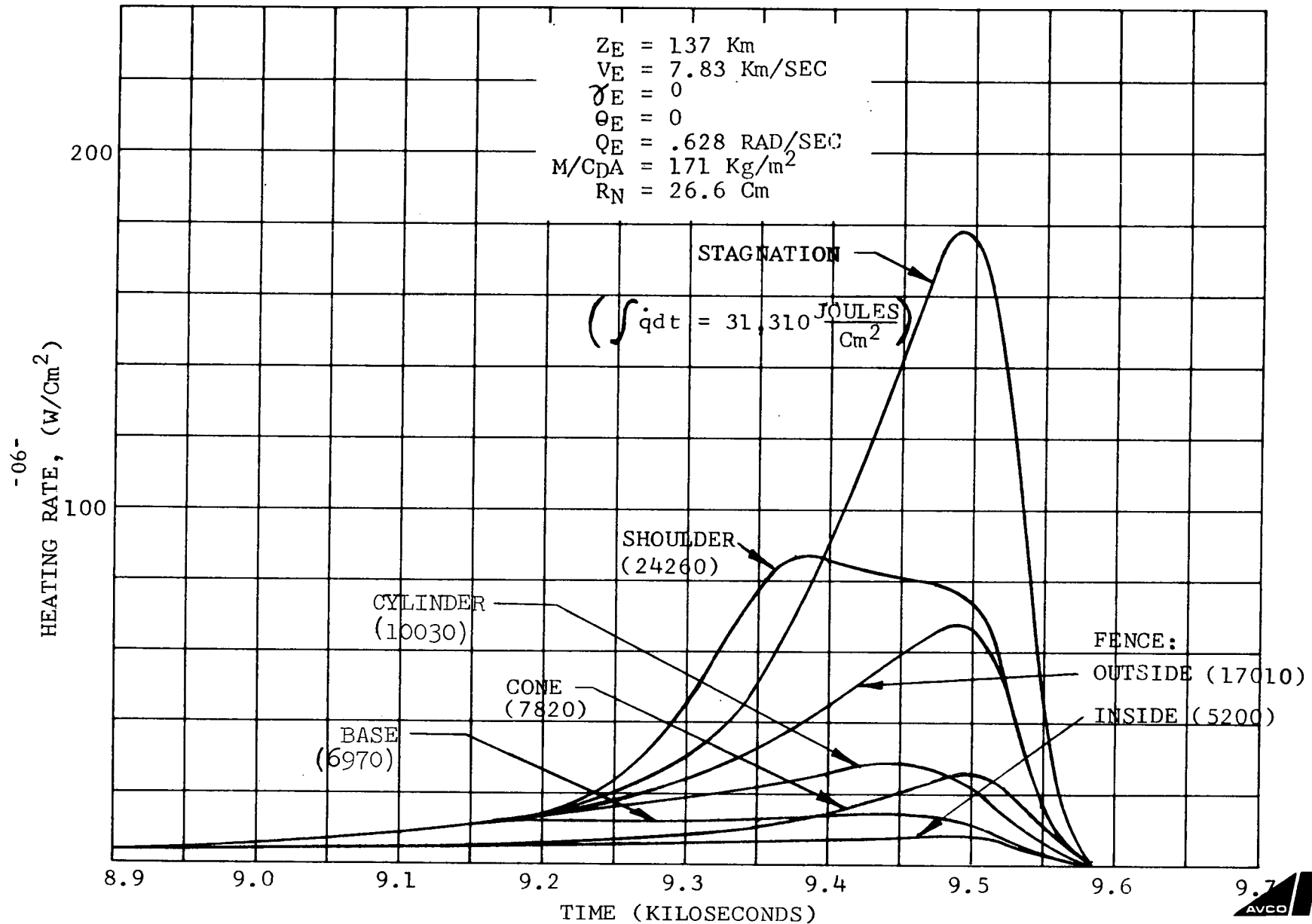


Figure 3.2-30

AEROSHELL HEATING  
LUNAR SKIP LIMIT RETURN

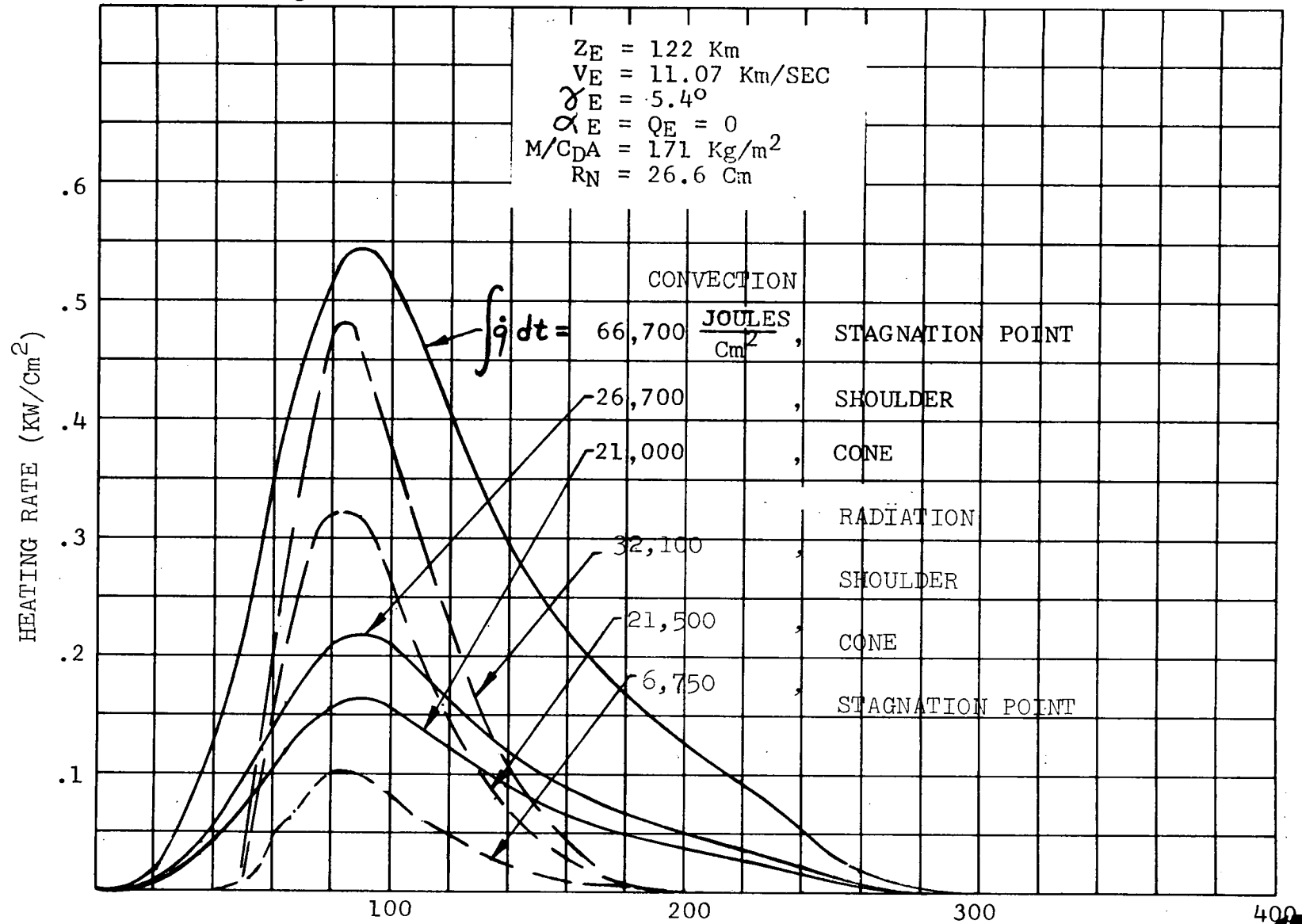
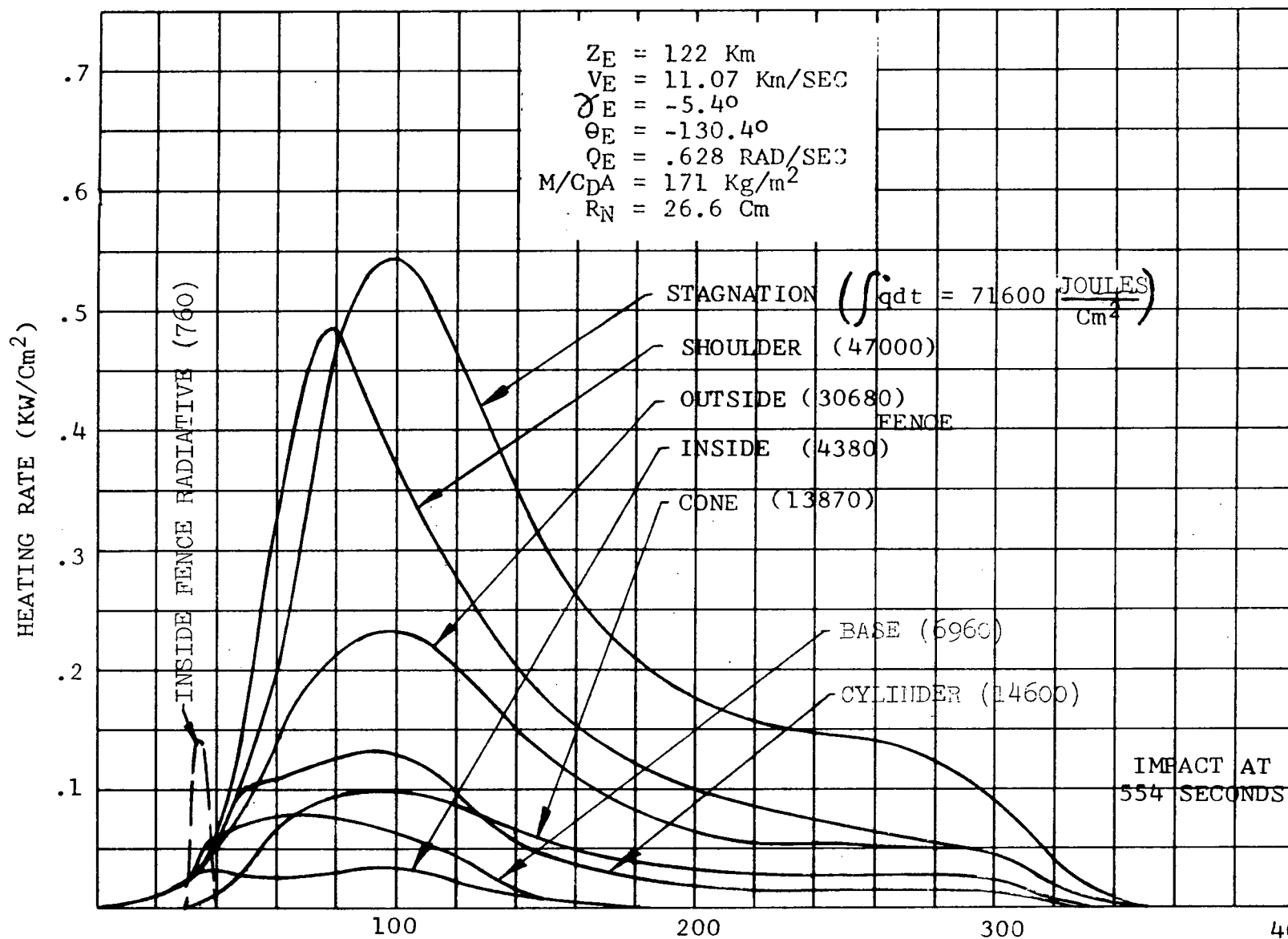


Figure 3.2-31 AEROSHELL HEATING  
LUNAR SKIP LIMIT RETURN TUMBLE





In the Brayton application each HS contains 400 watts thermal of fuel and heat is transferred from only one side of the HS planar array to a sink temperature (HSHX surface) above 870°C (1600°F). Since the heat generated in the fuel must be transferred through the HS reentry protection, the presence of this material increases the capsule temperatures during power system operation. Since increased reentry protection results in increased steady state operating temperatures, these materials must be chosen to simultaneously satisfy both reentry and steady state thermal requirements. In the present application the fuel capsule is surrounded by a hexagonal prism of POCO graphite reentry protection material. Between the capsule and the POCO, two 0.169 cm (0.066 in.) thick sleeves of pyrolytic graphite insulating material completely surround the cylindrical portion of the capsule.

### 3.3.2 Thermal Analysis

The heat source thermal design requires that the source be maintained at safe temperatures during ground handling, space operation, and reentry, yet provide the capability to deliver heat to a Brayton cycle system during steady state operation at an efficient temperature level. The thermal criteria established as a requirement during periods of handling and flight are shown in Table 3.3-I.

TABLE 3.3-I  
HEAT SOURCE THERMAL DESIGN CRITERIA

Maximum Steady-state capsule-surface temperature	1093°C	2000°F
Maximum transient temperature at the capsule structural strength member.	1640°C	3000°F
Maximum capsule strength member temperatures in one hour from 1093°C (2000°F)	371°C	700°F
Maximum steady-state heat source surface temperature in oxygen atmosphere.	177°C	350°F
Maximum operating heat loss	2000 watts	6826 $\frac{\text{BTU}}{\text{hr.}}$

The following operating environments were considered in these studies.

a. Launch pad

1. Steady State - ACHX cooled.
2. Transient - ACHX disconnected

b. Space

1. Steady-state-normal operation - HSHX operating
2. Steady-state - heat source deployed in space
3. Transient - HSHX startup
4. Transient - HSHX shutdown
5. Transient - heat source deployed in space

c. Reentry - Transient

Evaluation of the capability of the HSU design to meet the thermal criteria outlined in Table 3.3-1 constituted the thermal analysis. To perform this evaluation the temperature distribution of capsule and support structure during steady-state conditions and the temperature history of critical elements during transient periods were calculated for the lifetime of the heat source.

### 3.3.2.1 HSU Thermal Model Description

A two-dimensional model of a typical fuel capsule was developed to analyze the thermal performance of the heat source during critical states of flight and handling. The model was developed in sufficient detail to provide the capability to analyze the following performance states:

- Steady-state capsule temperature distribution during ACHX operation.
- Temperature history of heat source, support structure and HSHX immediately after ACHX disconnect.
- Steady-state temperature distribution of heat source in space with:
  - HS facing HSHX during normal operation
  - HS facing space in deployed position
- Temperature history of heat source during HSHX startup.
- Temperature history of heat source immediately after HSHX shutdown but prior to deployment of the HS.

- Temperature history of heat source immediately after deployment to space.
- Temperature history of heat source during HSRV reentry while exposed to both orbital and superorbital reentry environments.

To facilitate this analysis a versatile multidimensional thermal analyzer (CINDA-3G, Ref. 3.3-1) was used. This code can calculate steady-state and/or transient temperature distributions of multidimensional systems that can be mathematically simulated by a lumped parameter representation.

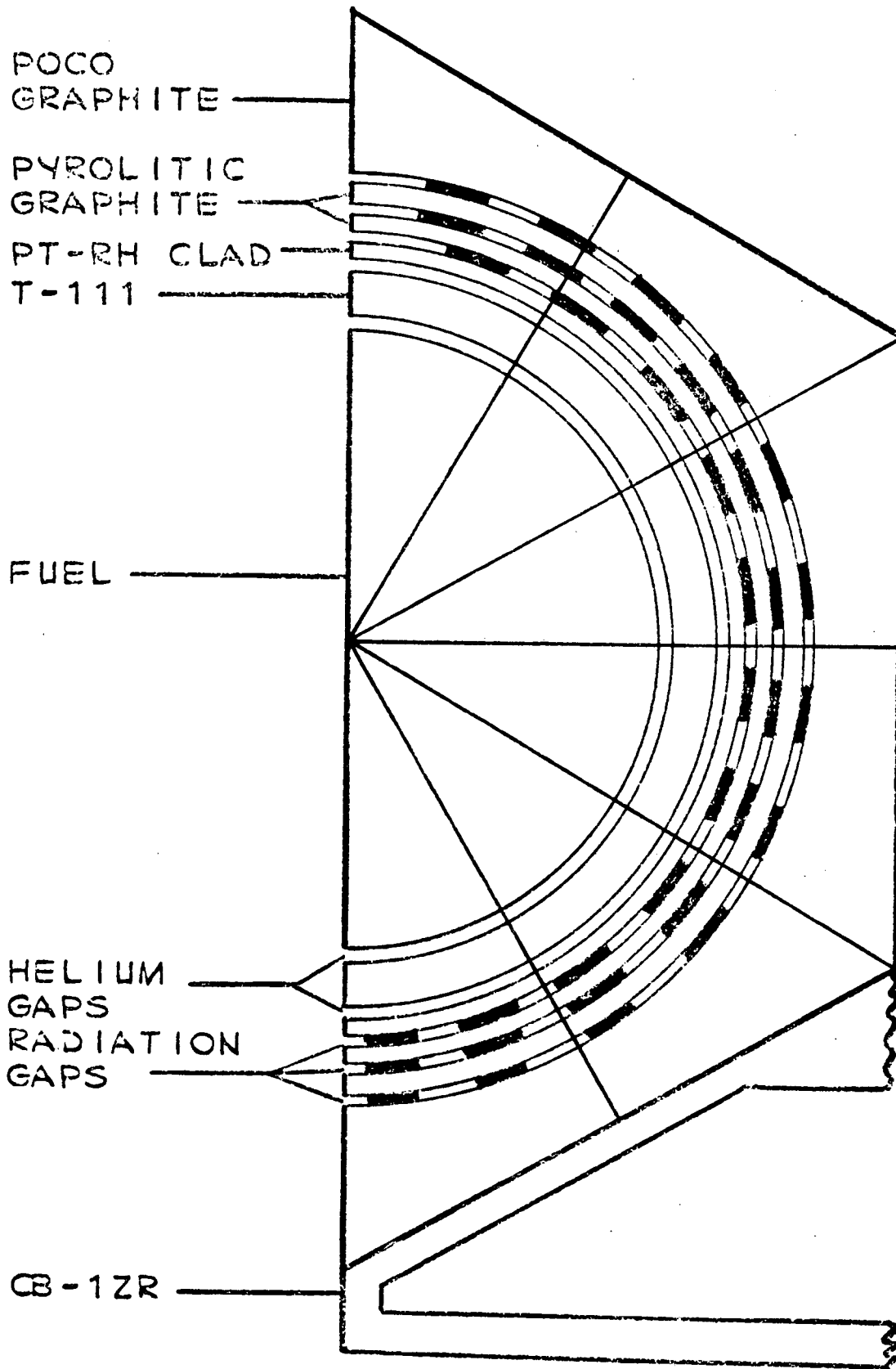
For analysis of the heat source a two-dimensional model of the typical cross-section of the heat source representing one half of a Heat Source was used. This model represented the smallest element over which the heat flow was symmetrical. (Figure 3.3-1 depicts the model geometry.) The network was divided into 65 nodes representing the mass of the constituent elements and 81 nodes representing the nodal interfaces. Heat Source (HS) components included in the model were:

- Fuel capsule
  - PuO<sub>2</sub> fuel
  - Helium gap
  - T-111 structural strength member
  - Helium gap
  - Platinum-rhodium oxidation-resistance clad (Pt - Rh)
- Insulation
  - Radiation gap
  - Pyrolytic graphite reentry insulation (PG)
  - Radiation gap
  - Pyrolytic graphite reentry insulation (PG)
  - Radiation gap
  - Poco graphite reentry insulation
- Cb-1%Zr support plate

The general assumptions incorporated in the model included the following:

- All heat transferred two-dimensionally over the active length of the HS.
- Heat flows between adjacent HS are symmetrical (adiabatic sides).
- Internal heat generation in PuO<sub>2</sub> nodes (Power density =  $1.22 \text{ watts/cm}^3 = 68.26 \text{ BTU/Hr-in}^3$ )

## 2-D HEAT SOURCE MODEL



- Radiation between Pt-Rh clad and pyrolytic graphite insulation ( $\epsilon_{PG} = 0.80$ )
- Radiation between outer layer of pyrolytic graphite and POCO graphite insulations ( $\epsilon_{poco} = 0.80$ )
- Radiation between HS and HSHX accounts for presence of adjacent HS ( $\epsilon_{HSHX} = 0.85$ )
- Radiation across uncoated Cb-1%Zr ACHX channel in all operating modes except ACHX operation ( $\epsilon_{Cb-1\%Zr} = 0.225$ )
- Partial contact maintained between HS and Cb-1%Zr support structure (contact conductance =  $525 \text{ watts/M}^2\text{-}^\circ\text{C} = 300 \text{ BTU/ft}^2\text{-hr-}^\circ\text{F}$ )

Temperature dependent properties, when available, were used for all materials and were obtained from the best available information (Ref. 3.3-2). For each case analyzed, conservative boundary conditions were selected to represent the worst condition.

### 3.3.2.2 Thermal Performance

A two dimensional model simulating one-half of a single heat source located in the close-packed array of the Brayton heat source unit was thermally analyzed. In order that the two-dimensional model simulates the actual HS, an effective power density must be used for the fuel in the thermal model (Ref. 3.3-3). The effective power density was obtained by dividing the HS loading by the effective volume of the fuel. Effective fuel volume for a given capsule diameter is a function of the capsule length and the three-dimensional heat transfer effects at the heat source ends. Two possible approaches are to: (1) take the effective volume as the volume of the cylindrical portion of the fuel cavity, or (2) take the effective volume as the total of the volume of the cylindrical portion and the two hemispherical end regions. The first approach, chosen for this analysis, would be conservative since it does not account for the presence of longitudinal heat transfer. The second approach is probably optimistic since the ends will not be completely filled and the HS ends will be surrounded by low thermal conductivity Ta felt compliance pads.

The HS designed assumed in the analysis is 18.8 cm (7.4 in.) long with an effective power density (as defined above) of  $1.22 \text{ watts/cm}^3$  ( $68.26 \text{ BTU/hr-in}^3$ ). The thermal performance of the HS is discussed in the following paragraphs for the operating conditions of interest.

### 3.3.2.2.a Heat Source Unit

Steady-State-ACHX Operating -- The temperature distribution of the HS and support structure was calculated with the two dimensional model based on the following assumptions specific to the ground cooled case.

- Forced nitrogen cooling in the ACHX
- No heat removed by HSHX operation
- Partial contact between HS and support structure (h - 525)  
watts/meter<sup>2</sup> - °C = 300 Btu/ft<sup>2</sup>-hr. - °F

Because of the sensible heat rise in the coolant, the hottest capsules along any cooling channel would be the capsule adjacent to the channel exit. By orificing each of the channels, the coolant flow rates could be adjusted for each channel such that capsules at the exit of each channel would be maintained at the same peak temperature. The peak HS surface temperature would therefore correspond to the hot spot on the HS adjacent to each of the channel exits. Flow requirements were established to limit the peak HS surface temperature to less than 177°C (350 °F). Details of the analysis and the results are presented in Section 3.3.3. The cooling requirements are summarized in Table 3.3-II.

TABLE 3.3-II

#### ACHX COOLING REQUIREMENTS FOR GROUND OPERATION

Nitrogen Inlet Temperature	16°C	60°F
Nitrogen Outlet Temperature	25°C	77°F
Nitrogen Inlet Pressure	69 newtons/ cm <sup>2</sup>	100 psi
Nitrogen Outlet Pressure	55 newtons/ cm <sup>2</sup>	80 psi
Mass Flow Rate	2.38 Kg/sec	5.26 lbs/sec
Maximum HS surface temperature	177°C	350°F
Mean Channel Exit Temperature	79°C	173.5°F

b. HSU Steady State-Space Operation -- The primary thermal design criterion in the mating of the HSU and HSHX designs is to maintain a peak HS surface temperature below 1090°C (2000°F) during steady state operation of the Brayton system. To aid in the design and to establish the operating condition, steady state temperature profiles of the heat source representing the hottest portion of the heat source unit were calculated. Specific assumptions for this calculation include:

- Conduction around active fueled length of HS.
- Radiation from HS to HSHX with view factors based on HS seeing HSHX and adjoining HS.
- HSHX at 910° C (1670°F)  
(Hot spot temperature predicted in Reference 2.1-1)
- Radiation across ACHX channel
- Partial contact between HS and support structure  
( $h = 525 \text{ watts/meter}^2\text{-}^\circ\text{C} = 300 \text{ Btu/ft}^2\text{-hr. -}^\circ\text{F}$ )

Steady-state temperature distributions were calculated for a range of peak HS surface temperatures from 980°C (1800°F) to 1200°C (2200°F). From these results an effective HS radiating temperature can be defined and is shown in Figure 3.3-2 versus the peak HS surface temperature.

The temperature profile around the heat source at the HSU hot spot is shown in Figure 3.3-3 for full power operation. The peak HS surface temperature of 1103°C (2020°F) exceeds the design criterion by 13°C (20°F). However, the conservatism introduced by the two-dimensional analysis would cause higher temperature predictions than actual. Similarly, the T-111 structural strength member is operating at 1215°C (2220°F) which is in the vicinity of its commonly accepted temperature limit. This temperature could be reduced by either reducing fuel loading or increasing capsule length. The other alternative would be to reduce the amount of reentry insulation, which, of course, would result in decreased reentry capabilities.

c. Deployed to Space --An important safety feature incorporated into the HSRV design is the ability to provide an emergency cooling mode in the event of any accident that would result in a temperature rise in the HSU. By deploying the HSU to space the resulting radiation heat transfer will maintain fuel temperatures below 2500°F transient and below 2000°F steady state.

# PEAK AND EFFECTIVE HEAT SOURCE TEMPERATURE

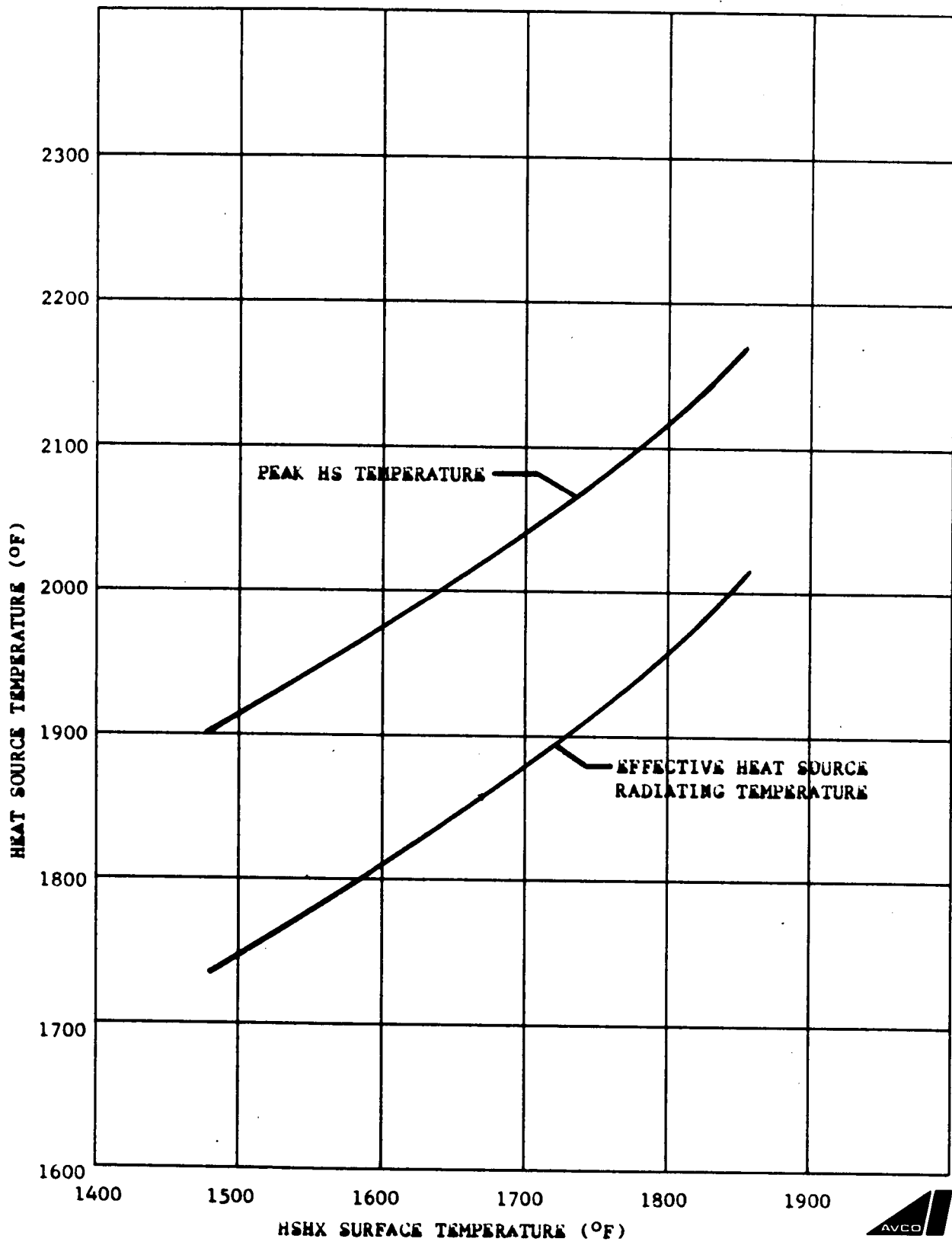
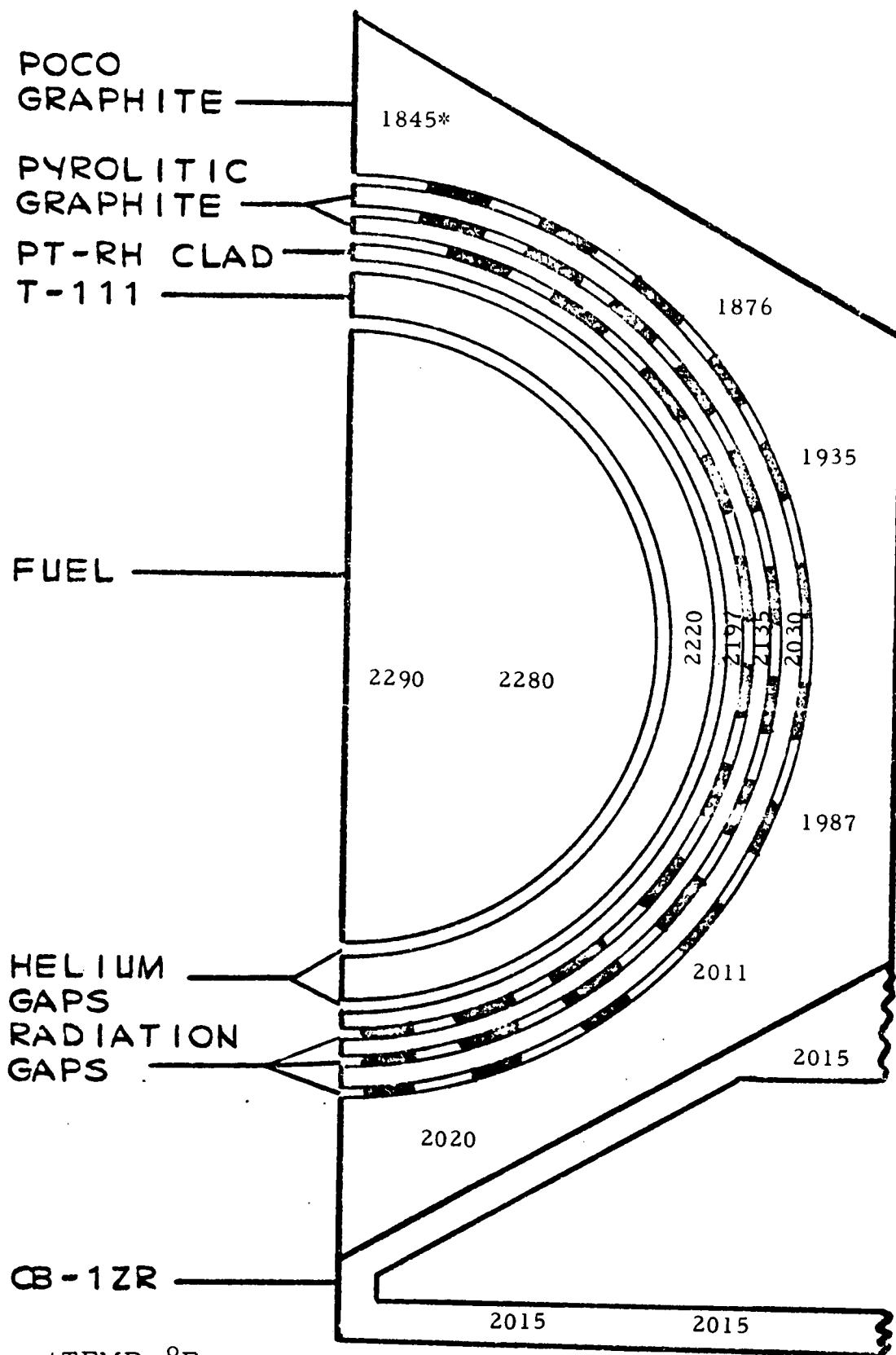


Figure 3.3-2





## 2-D HEAT SOURCE MODEL



\*TEMP. °F

Figure 3.3-3

J



- Radiation from HS to space with view factors based on HS seeing space only.
- Space sink temperature taken as  $-17^{\circ}\text{C}$  ( $0^{\circ}\text{F}$ )
- Radiation across ACHX channel
- Partial contact between HS and support structure.

The temperature history of the hottest HS during the initial period of cooling is shown in Figure 3.3-4. The space exposed POCO surface cools very rapidly at first but more gradually thereafter. The T-111 structural strength member exhibits very gradual cooling due to the presence of the pyrolytic graphite insulation layers which act as effective barriers to heat transfer in either direction. Eventually, in the deployed orientation, the HSU will reach an equilibrium with its environs. The steady state distribution of the space deployed HS is shown in Figure 3.3-5. The  $-17^{\circ}\text{C}$  ( $0^{\circ}\text{F}$ ) space sink temperature utilized in the analysis is meant to compensate for an average earth thermal and reflected solar environment. If the HSU is deployed facing the sun, temperatures will be higher. If facing deep space,  $-273^{\circ}\text{C}$ , temperatures will be appreciably lower.

d. HSU/HSRV/SHSX Transient Response

During a nominal mission profile, the HSU will experience various periods during which it is transiently heated or cooled. Two thermal criteria were established for the design of a heat source that will survive these transients.

- Provide a design that maintains peak structural strength member temperatures less than  $1650^{\circ}\text{C}$  ( $3000^{\circ}\text{F}$ ) during transient periods.
- Provide sufficient thermal capacitance such that the structural strength member temperature rise from  $1093^{\circ}\text{C}$  ( $2000^{\circ}\text{F}$ ) does not exceed  $371^{\circ}\text{C}$  ( $700^{\circ}\text{F}$ ) in one hour.

Several transient conditions were analyzed. The results are summarized below.

e. ACHX Disconnected -- The temperature history of the HS and SHSX immediately after ACHX disconnect was calculated using the following assumptions specific to this transient case:

- No heat removed by ACHX operation
- HSU radiating to SHSX with heat absorbed but not removed by SHSX operation.

## HEAT SOURCE TEMPERATURE HISTORY

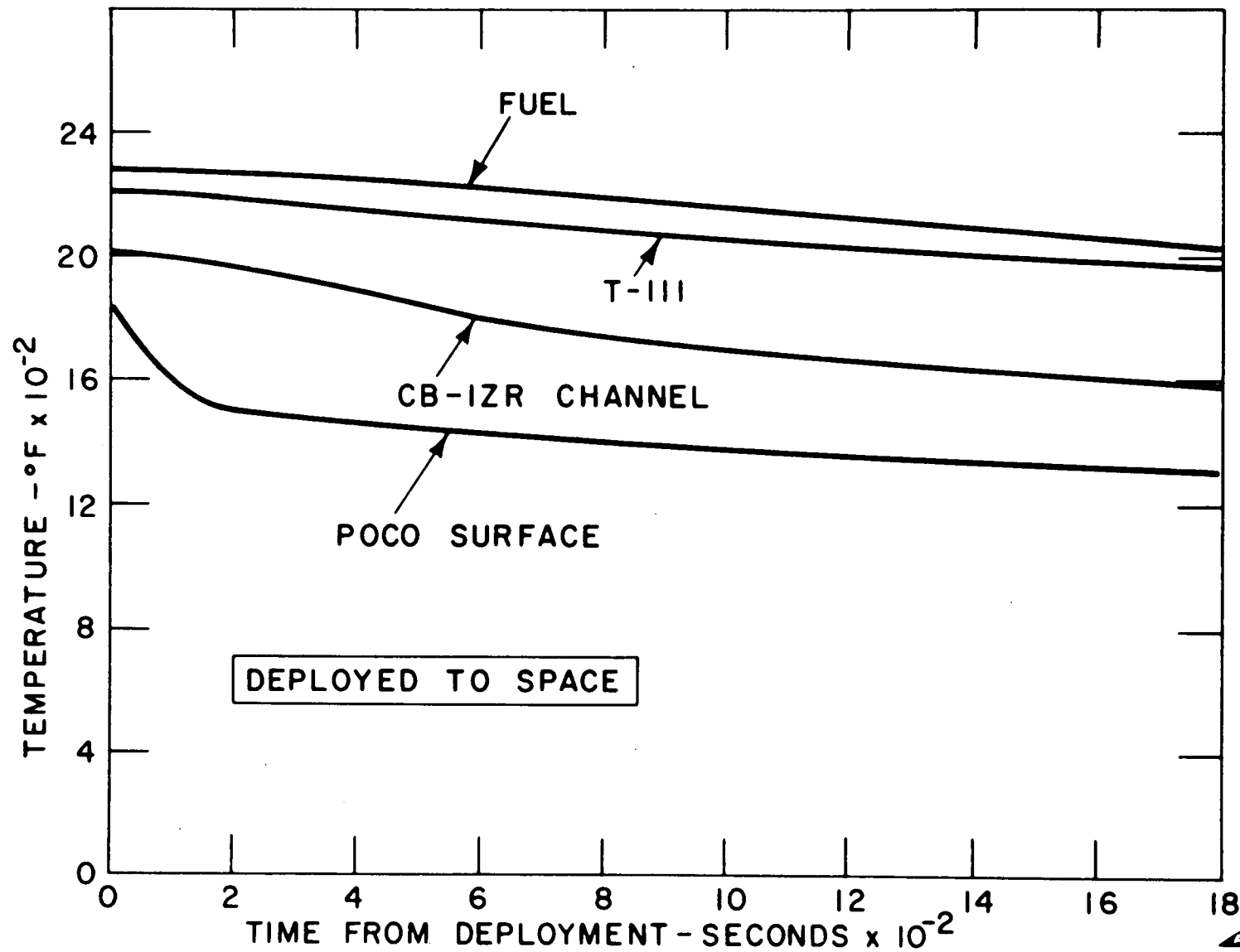


Figure 3.3-4

## 2-D HEAT SOURCE MODEL

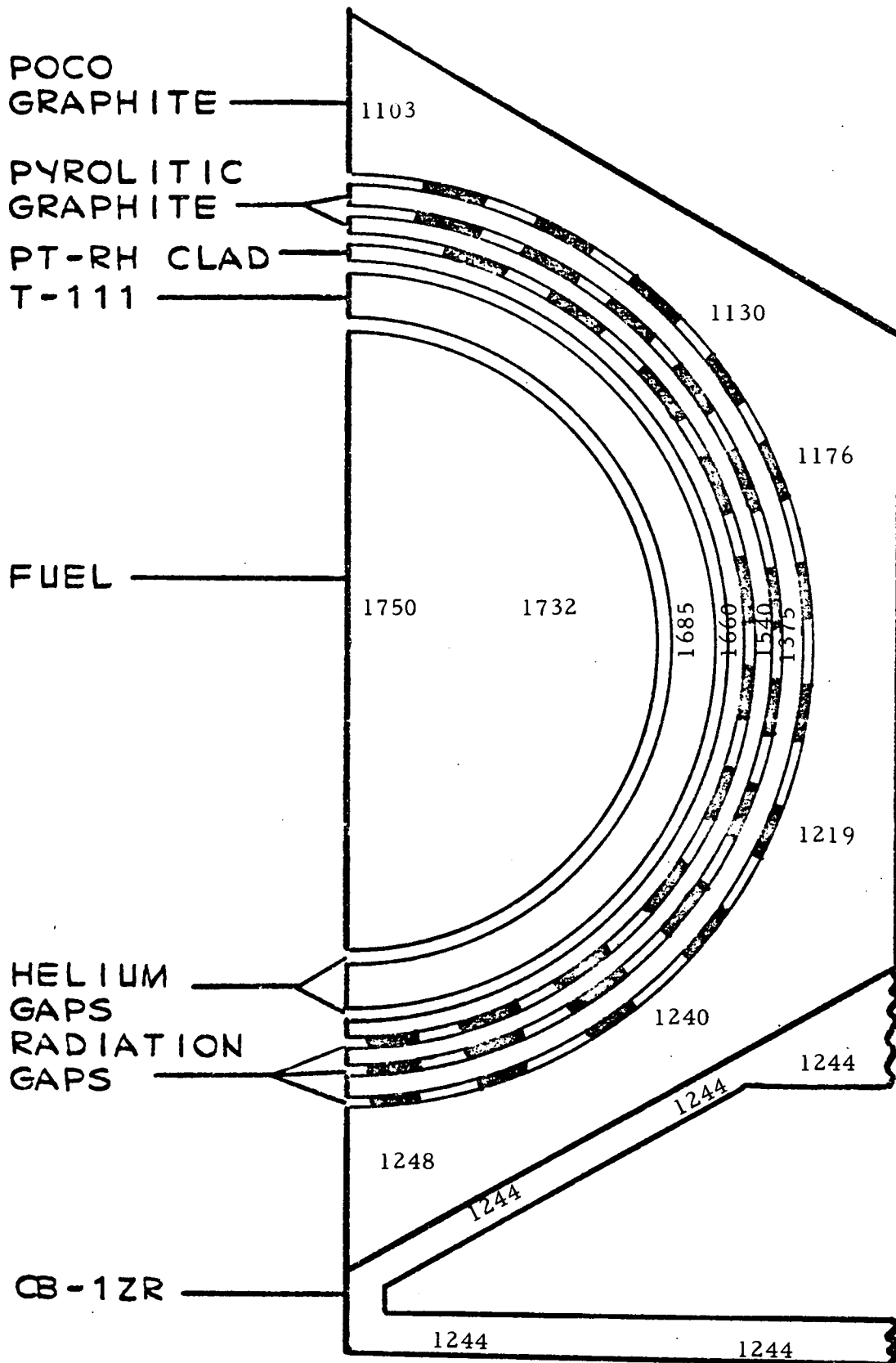


Figure 3.3-5



- HSHX radiating to  $-17^{\circ}\text{C}$  ( $0^{\circ}\text{F}$ ) sink through open insulation doors.

It was desired to determine the time required to reach equilibrium in this mode. However, the temperature rise rates become so small that such a calculation is impractical. The transient response of the front and back of the HSHX as well as the POCO and T-111 at the top of the HS are shown in Figure 3.3-6 for the first 270 minutes. Based on these results it is estimated that more than 10 hours are required to reach equilibrium. The equilibrium temperatures are illustrated in Figure 3.3-7. However, it appears that the HSHX and HSU are at sufficient temperatures to attempt a Brayton Engine startup after 4 hours.

f. Engine Startup -- The temperature history of the HS during engine startup was calculated using the following assumptions specific to this transient case:

- Initial condition requires  $815^{\circ}\text{C}$  ( $1500^{\circ}\text{F}$ ) HSHX temperature
- Initial condition in HS is temperature profile at 240 minutes during launch heatup (Figure 3.3-6)
- Insulation doors closed
- Gas flow - HSHX

The HSHX temperature response was calculated by Garrett AiResearch and was used as the boundary condition for this analysis. As is shown in Figure 3.3-8, the HS responds similarly to the HSHX. The results indicate that full power Brayton output is essentially achieved after two hours.

g. Startup Conditions - Engine Fails to Start -- In the event that the engine fails to start after achieving the minimum temperature conditions for startup, it is of interest to determine the time in which safety measures could be effectively employed. The assumptions utilized for this specific transient case are:

- No heat removed by HSHX operation
- Insulation doors closed
- Initial HS temperature distribution is that existing at 240 minutes during launch heatup (Figure 3.3-6)

## HSU TRANSIENT RESPONSE

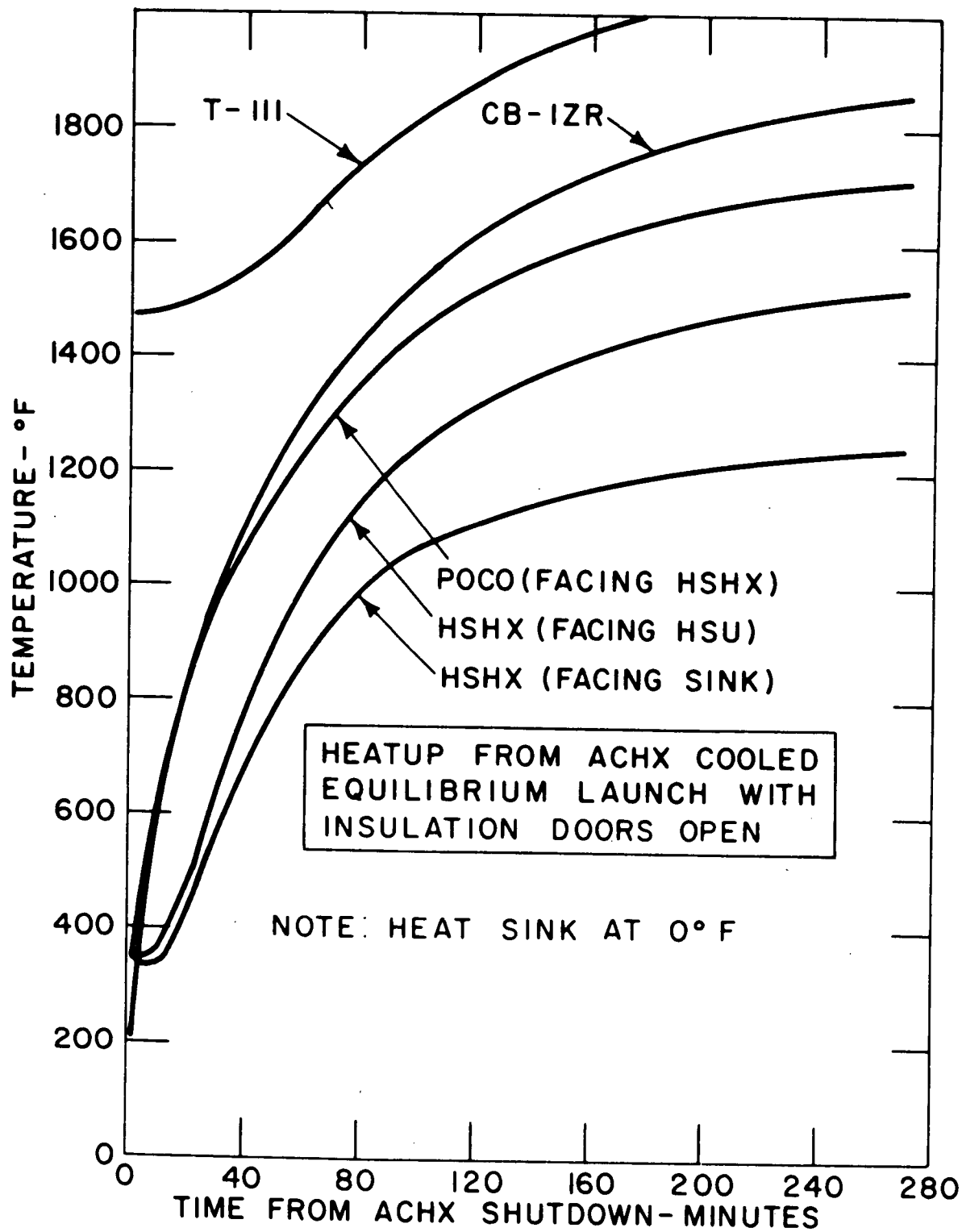
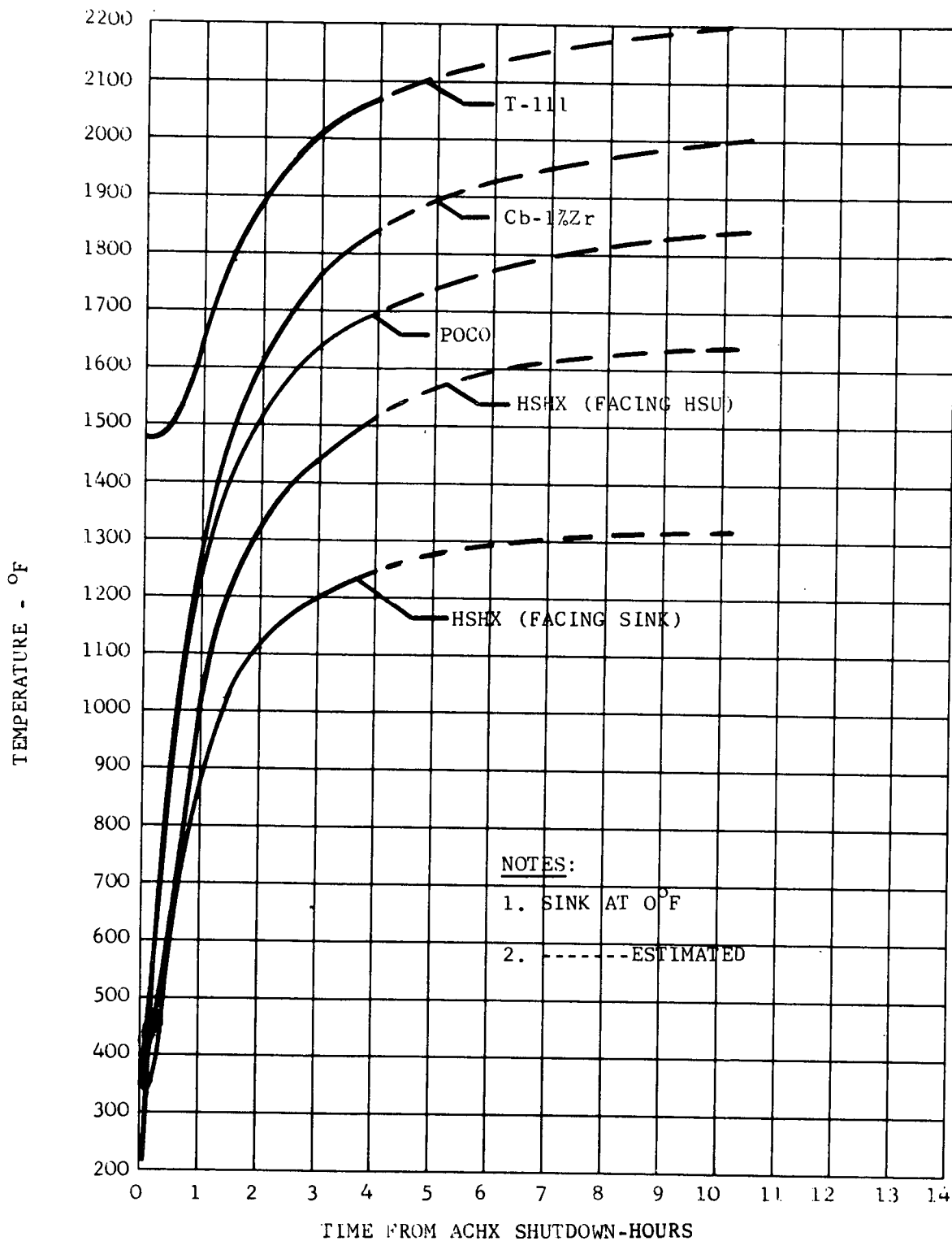


Figure 3.3-6

**Figure 3.3-7 HSU Transient Response to Equilibrium Heatup from ACHX Cooled Equilibrium Launch with Insulation Doors Open**



# HSU TRANSIENT RESPONSE

(Four Hours After Launch (HSHX @ 1500° F)

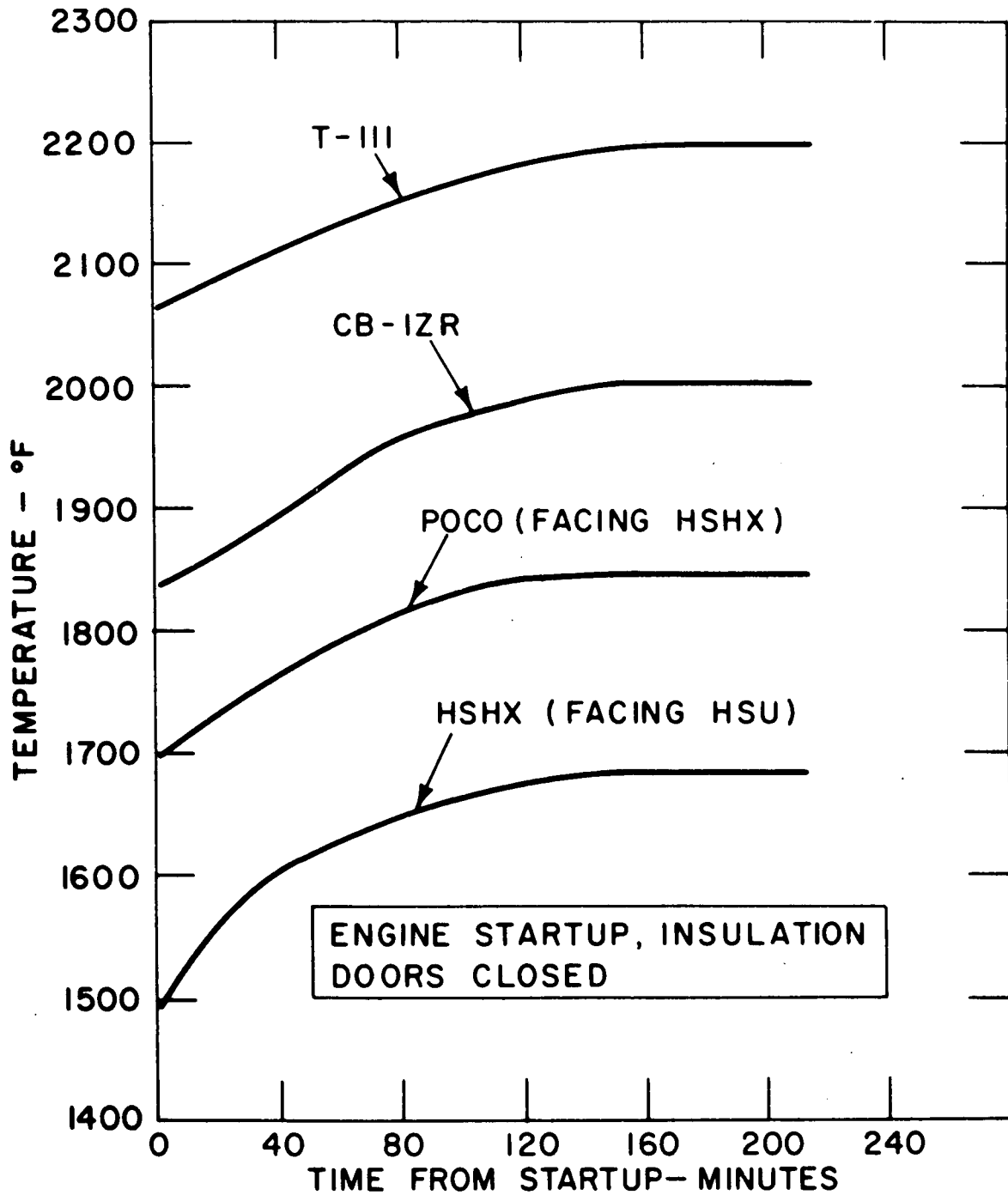


Figure 3.3-8





The results of the analysis are shown in Figure 3.3-9. After the first 15 minutes the temperature rate of all materials appears rather constant. The heatup rate is then tolerable and this condition allows 96 minutes before the T-111 strength member exceeds  $1650^{\circ}\text{C}$  ( $3000^{\circ}\text{F}$ ).

(Appendix A describes the results of an analysis of the potential use of the ACHX in an emergency cooling mode, where during a ground test the Brayton Engine shuts down accidentally and primary and secondary heat dump modes fail. This analysis shows that the ACHX system is an effective emergency cooling system for this extreme failure).

h. Space Operation - Engine Failure--To assess the most severe contingency an analysis was performed to determine the thermal response of a HS if an engine failure occurred and none of the safety features could be immediately utilized (HSU could not be deployed or insulation doors could not open). The assumptions specific to this particular case are:

- Initial condition is the steady state operation temperature profile.
- No heat removed by HSHX operation
- Insulation doors closed

The thermal response is shown in Figure 3.3-10. The object of the analysis is to ascertain whether the HSU has sufficient thermal capacitance to meet the third thermal criteria (see Table 3.3-I).

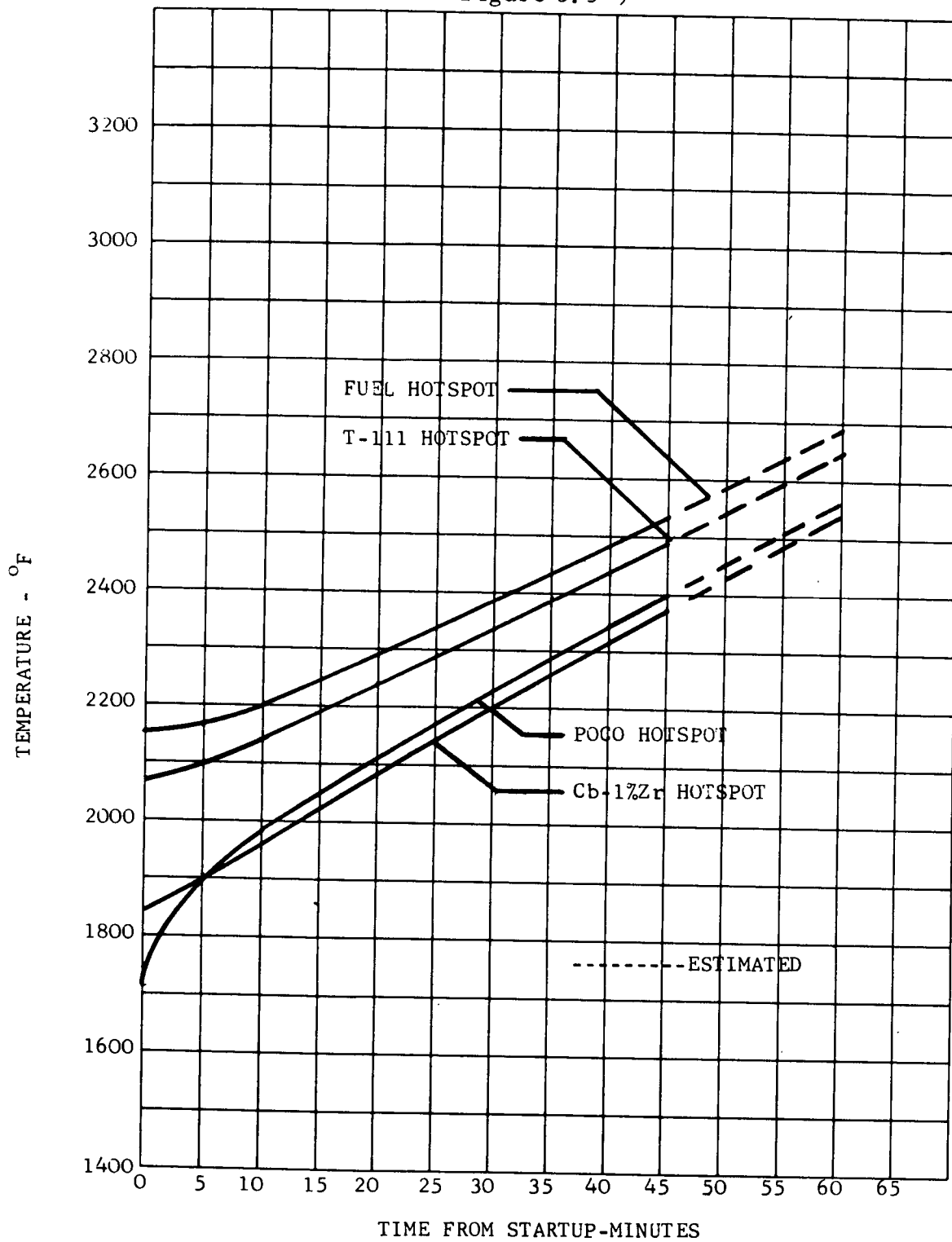
Extrapolating the results, the temperature rise in the first hour after failure is about  $300^{\circ}\text{C}$  ( $570^{\circ}\text{F}$ ) for the T-111 strength member and about  $450^{\circ}\text{C}$  ( $845^{\circ}\text{F}$ ) for the POCO. The criterion is achieved for the T-111 strength member. The steady temperature rise rate increases to  $326^{\circ}\text{C/hr}$  ( $620^{\circ}\text{F/hr}$ ) which, again, satisfies the criterion on thermal capacitance.

It can be concluded that a supplementary heat sink is not required, since the reentry protection material on each HS provides sufficient thermal capacitance to eliminate the requirement for additional BeO.

i. HS Response During Reentry -- Reentry trajectories from sub-orbital to super-orbital reentry velocities were analyzed. The trajectories of interest were selected to cover maximum heat load, maximum heat rate, and maximum dynamic load conditions (i. e., initially tumbling vehicles). The first case analyzed was an orbit injection abort of the INT-21 resulting in an entry at  $-20^{\circ}$ ; tumbling, which results in the maximum dynamic loads for the orbital design. The initial conditions were selected (from Figure 3.3-6) as the temperature distribution existing 1150 seconds after launch which is consistent with the time required to establish these entry conditions. The thermal response is illustrated in Figure 3.3-11. It is seen that the POCO graphite surface responds to the incident convective heating but the T-111 strength member is relatively insensitive. Temperature levels are low enough that the magnitude of the dynamic loads does not present a problem.

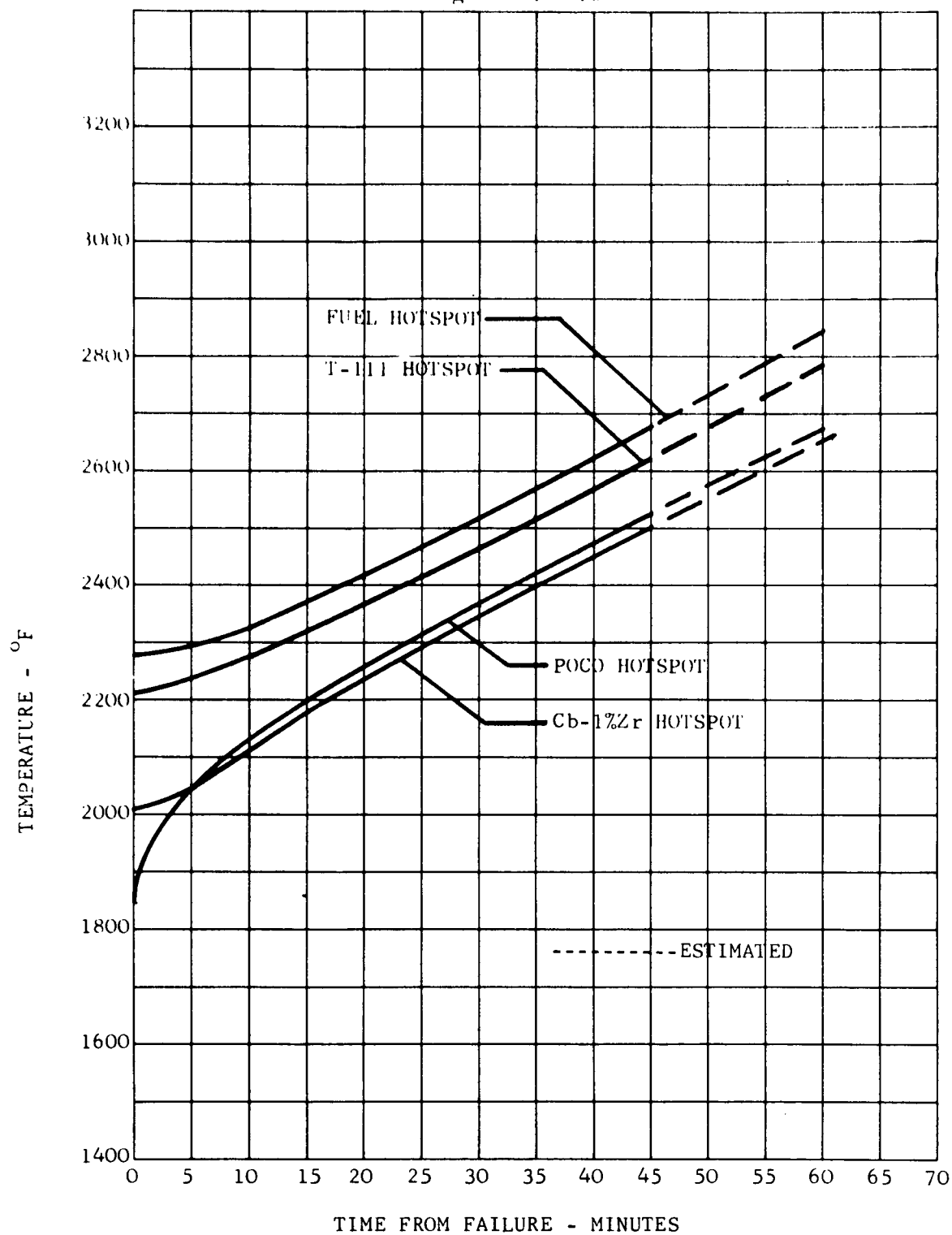
HSU TRANSIENT RESPONSE  
STARTUP FROM EQUILIBRIUM-ENGINE FAILS TO START  
INSULATION DOORS CLOSED

Figure 3.3-9



HSU TRANSIENT RESPONSE  
ENGINE FAILURE-INSULATION DOORS CLOSED

Figure 3.3-10



# HEAT SOURCE TEMPERATURE HISTORY

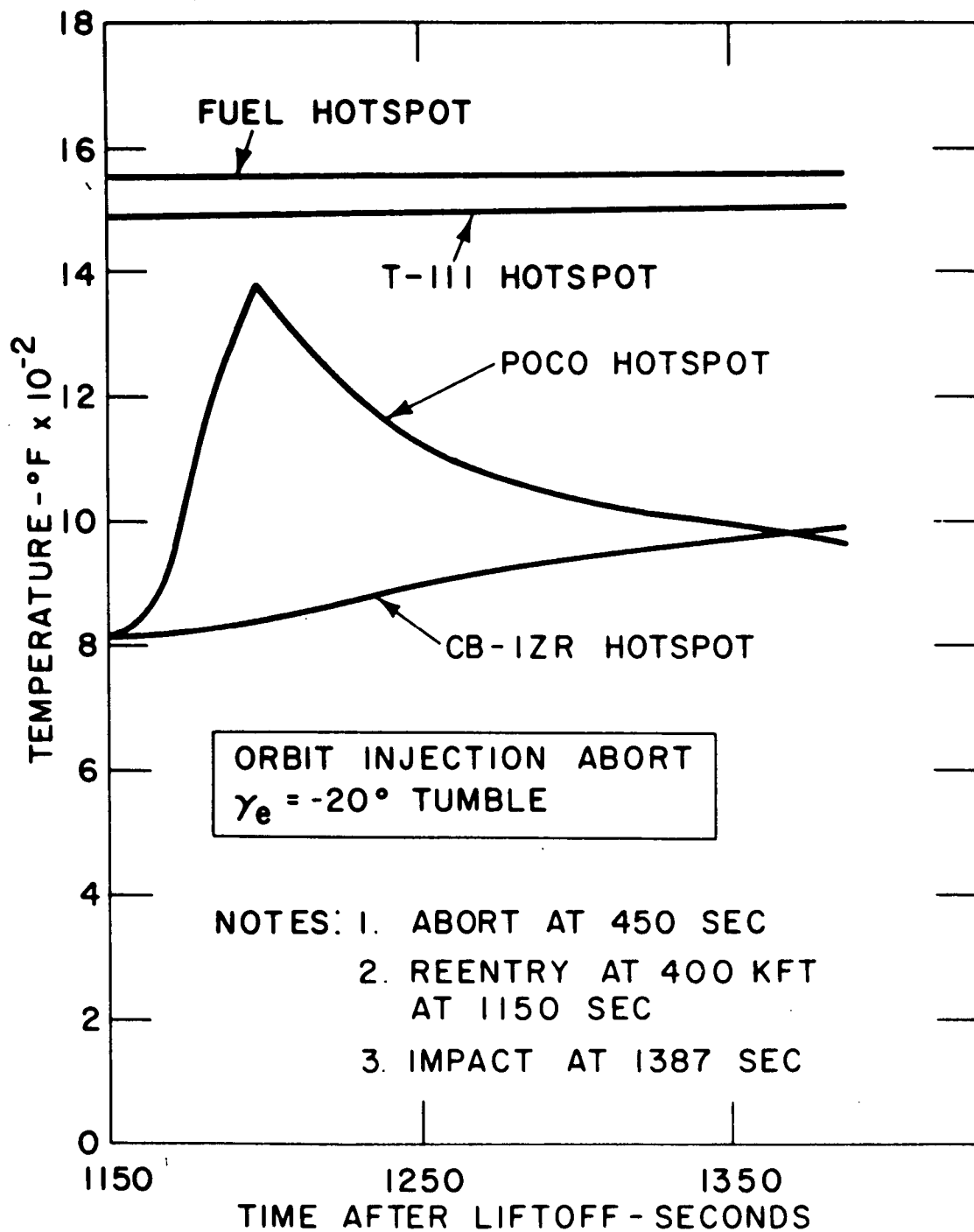


Figure 3.3-11



An orbital decay tumbling entry exposes the HSU to the maximum integrated heat load, but, low to moderate heating rates. The initial condition was the steady-state operation temperature distribution. The thermal response is shown in Figure 3.3-12. The HS cools until the convective heat flux is sufficient to exceed the rate at which the POCO surface is radiating to space. Again the temperature levels and peaks present no problem for the HS and the utilization of pyrolytic graphite reentry protection is sufficient for the orbital entry conditions studied.

HSRV entry at lunar return velocities exposes the HSU and individual HS to relatively high convective and radiative heat fluxes. The third case considered was a lunar skip limit return in a tumbling mode. This case provides the maximum heat load of the super-orbital cases considered. The initial condition, as in the orbital decay analysis, was assumed to be the temperature distribution for space operation. The thermal response is shown in Figure 3.3-13. A maximum T-111 strength member temperature of  $1305^{\circ}\text{C}$  ( $2380^{\circ}\text{F}$ ) is attained which does not represent a significant increase over the steady state operating levels.

The fourth case considered is a tumbling lunar return at an entry angle of  $-15^{\circ}$ . This represents the maximum dynamic loads case. The thermal response is shown in Figure 3.3-14. POCO temperatures in excess of  $2100^{\circ}\text{C}$  ( $3800^{\circ}\text{F}$ ) are attained. Peak T-111 temperature is the same as for the skip limit case considered,  $1305^{\circ}\text{C}$  ( $2380^{\circ}\text{F}$ ). The Cb-1%Zr heat source plate is subjected to a  $50^{\circ}\text{C}$  ( $120^{\circ}\text{F}$ ) temperature rise but the response does not start until well after peak dynamic loads.

It has been shown that the HSU can survive all reentry trajectories considered for intact reentry of the HSRV. None of the thermal design criteria are violated. It is concluded that the design is credible.

### 3.3.3 Auxiliary Coolant Heat Exchanger (ACHX)

The HSU is provided with an integral auxiliary coolant heat exchanger (ACHX) sized to maintain the HSU temperature below  $177^{\circ}\text{C}$  ( $350^{\circ}\text{F}$ ) while in an oxygen atmosphere to minimize the probability of structure oxidation and to facilitate handling.

The ACHX design consists of trapezoidal channels placed in the heat source plate between adjacent HS rows. (Figure 3.3-15A, and 15-B), square inlet and outlet headers at the HSU periphery, one inlet and one outlet connector located on opposite sides of the header baffle in close proximity. Each channel is orificed to insure proper coolant mass flow distribution which, in turn, limits the maximum heat source surface temperature in each channel to  $177^{\circ}\text{C}$  ( $350^{\circ}\text{F}$ ).

# HEAT SOURCE TEMPERATURE HISTORY

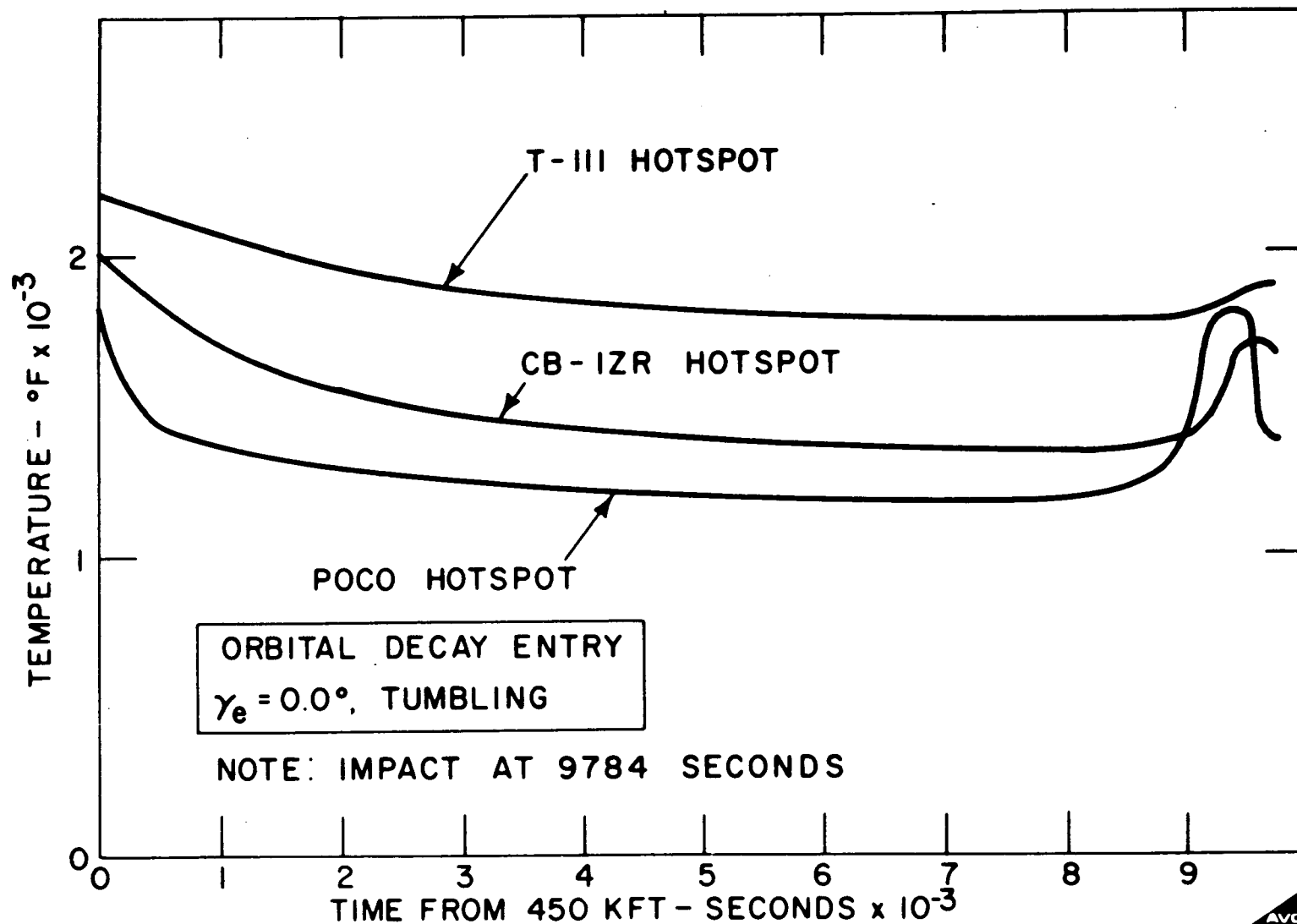


Figure 3.3-12

## HEAT SOURCE TEMPERATURE HISTORY

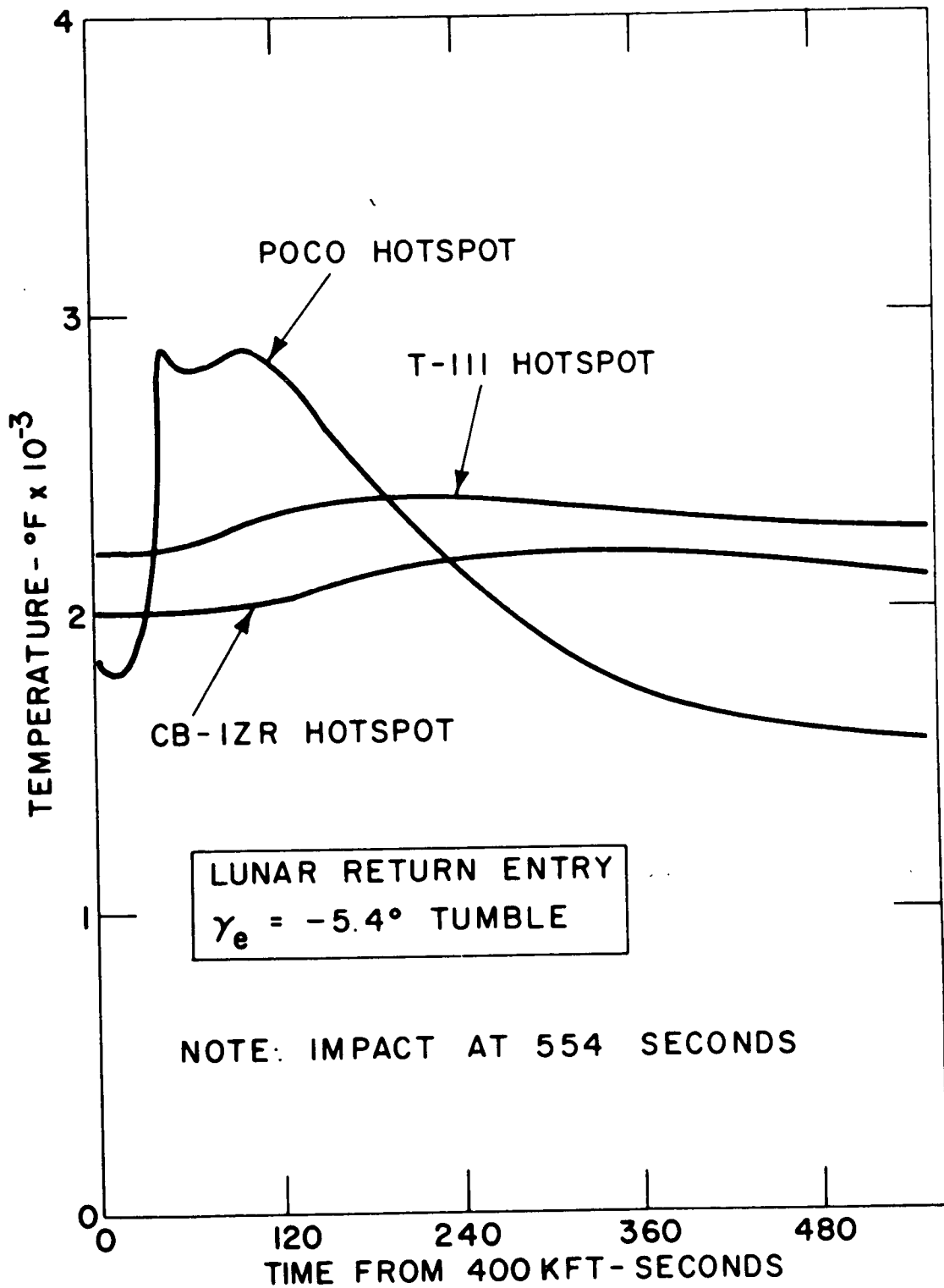


Figure 3.3-13

HEAT SOURCE TEMPERATURE HISTORY  
LUNAR RETURN ENTRY  
 $\gamma_e = -15^\circ$  TUMBLING

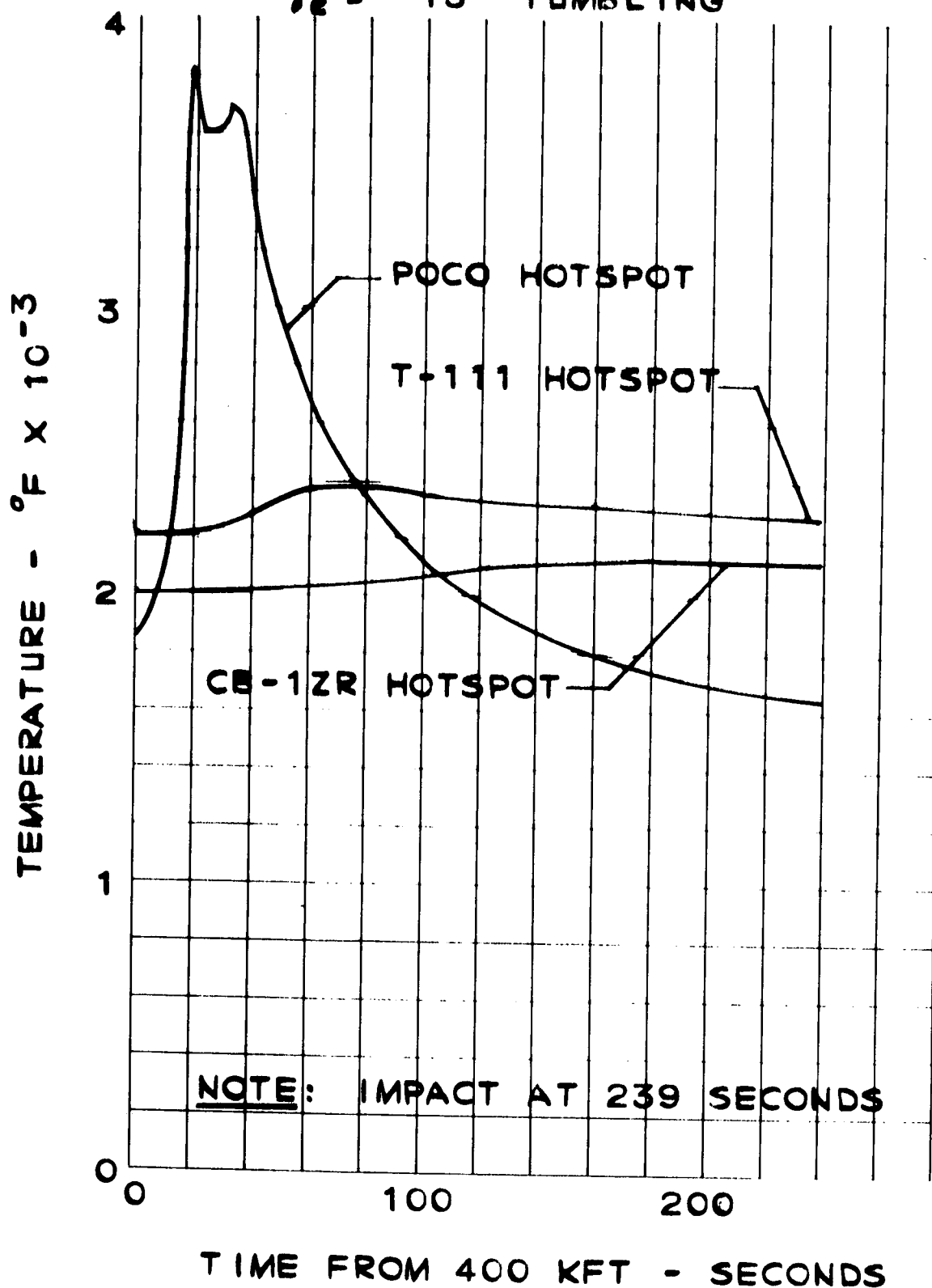


Figure 3.3-14





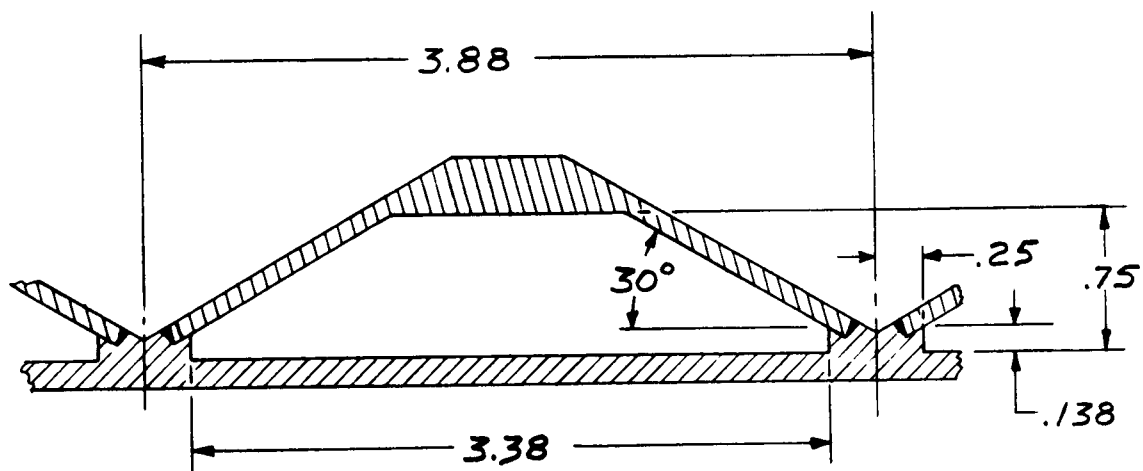


Figure 3.3-15A - ACHX Channel Cross-Section View

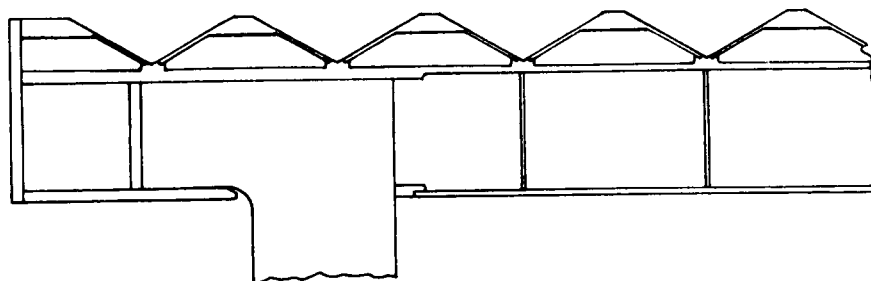


Figure 3.3-15B - ACHX Channel/HSU Cross-Section View

FIGURE 3.3-15

Two-dimensional heat transfer calculations of the steady-state temperature distribution around the HS and channel structure were performed. The effect of the contact between the HS and the channel structure was evaluated for three conditions; a radiation gap, an air gap, and partial contact. The results of these calculations indicated that the peak HS temperature could not be limited to 177° (350°F) with either a radiation gap or an air gap. Partial contact is required and, furthermore, a minimum contact conductance of 525 watts/meter<sup>2</sup>-°C (300 BTU/ft<sup>2</sup>-hr-°F) is necessary to keep ACHX mass flow rates within reasonable limits. The two-dimensional calculations show that a 38° C (100°F) circumferential temperature drop from the POCO graphite hotspot (at the top of the HS) to the POCO graphite in contact with the channel wall exists. The interface boundary condition analysis results are shown in Table 3.3-III.

Nitrogen was selected by NASA as the coolant. The coolant flow rates and flow distribution requirements were calculated parametrically for ranges of inlet temperature and pressure. Based on the results, NASA selected inlet conditions of 16°C (60°F) and 69 newton/cm<sup>2</sup> (100 psi). Orifice sizes were determined to meet performance requirements with the restriction that total ACHX head loss not exceed 13.8 newton/cm<sup>2</sup> (20 psi). (See Appendix B.) The ACHX design conditions for the reference design are summarized in Table 3.3-IV.

#### 3.3.3.1 Mechanical Description

The ACHX system consists of coolant headers, inlet and outlet connectors and coolant channels in the heat source plate. Square headers with approximately 33 cm<sup>2</sup> (5 in<sup>2</sup>) of cross-sectional area are arranged around the periphery of the heat source plate. The flow channels, which are approximately 12 cm<sup>2</sup> (1.88 in<sup>2</sup>), run parallel between and below the rows of HSU heat sources connecting the inlet and outlet headers. Each flow channel is orificed at the return header to maintain a constant channel exit wall temperature across the heat source plate. The ACHX header which surrounds the heat source plate is baffled to separate the inlet and outlet headers. There is one 5.7 cm (2.25 in) diameter connector to each of the inlet and outlet headers for connection of the coolant supply used during assembly, transportation, and launch pad operation.

#### 3.3.3.2 Thermal Analysis

The auxiliary cooling system requirements were established based on nitrogen flowing in parallel through the ACHX channels. Variation in flow rates from channel to channel is required due to the variation of the number of HS in each row. Control of the flow distribution is achieved by orificing the channel exits.

Because of the sensible temperature rise of the coolant, the exit wall temperature at the coolant exit would be the hottest temperature along the channel. The temperature drop around HS from the HS hot spot to the channel wall is fairly constant along a channel since very little heat is transferred axially along a channel. The hottest HS would, therefore, be those adjacent to the

TABLE 3.3-III

ACHX/HEAT SOURCE INTERFACE BOUNDARY CONDITION VARIATIONS

<u>BOUNDARY CONDITION</u>	<u>T<sub>WALL</sub>-°F</u>	<u>T<sub>POCO</sub>-°F</u>	<u>T<sub>HOTSPOT</sub>-°F</u>
RADIATION GAP $\epsilon_{POCO} = 0.8$ $\epsilon_{CB-1ZR} = 0.225$	216	1788	1888
0.002 IN. AIR GAP	216	295	395
PARTIAL CONTACT $H=100 \text{ BTU/FT}^2\text{-HR-°F}$	216	308	408
PARTIAL CONTACT $H=300 \text{ BTU/FT}^2\text{-HR-°F}$	216	246	346

TABLE 3.3-IV

## ACHX PERFORMANCE SUMMARY

FLUID	NITROGEN	NITROGEN
INLET TEMPERATURE	16 °C	60 °F
MEAN COOLANT OUTLET TEMPERATURE	25 °C	77.7 °F
INLET PRESSURE	69 N/METER <sup>2</sup>	100 PSI
OUTLET PRESSURE	55 N/METER <sup>2</sup>	80 PSI
MASS FLOW RATE	2.38 KG/SEC	5.26 LBS/SEC
MEAN CHANNEL EXIT WALL TEMPERATURE	79 °C	173.5 °F
PEAK CHANNEL VELOCITY	20 M/SEC	64 FT/SEC
INLET TUBE VELOCITY	116 M/SEC	330 FT/SEC

channel exits. The two-dimensional steady-state temperature distributions determine the maximum allowable temperature at any exit. The heat transfer from the channel to the coolant is calculated by:

$$Nu_x = 0.021 Re_x^{0.8} Pr_x^{1/3} \left( \frac{T_{b_x}}{T_{w_x}} \right)^{0.575} \quad (\text{Reference 3.3-4})$$

where  $Nu_x$  = local Nusselt numbers

$Re_x$  = local Reynolds number

$Pr_x$  = local Prandtl number

$T_{b_x}$  = local coolant bulk temperature

$T_{w_x}$  = local mean channel wall temperature

The Nusselt number is evaluated at the channel exit. Results of the two-dimensional calculations give the variation of HS hot spot and mean channel wall temperature with Nusselt number. This variation is shown in Figure 3.3-16. These results indicate that to maintain the peak HS temperature below 177°C (350°F) requires a local exit Nusselt number of 380 with a corresponding mean channel wall temperature of 79°C (173.5°F). For comparison, if the peak HS temperature was relaxed to 205°C (400°F) a local exit Nusselt number of 265 is required with an associated mean channel wall temperature of 99°C (209°F). The steady-state temperature distribution in the hottest HS along any channel is illustrated in Figure 3.3-17 for the design constraint which limits the peak POCO graphite temperature to 177°C (350°F). All of these results are based on a contact conductance of 525 watts/meter<sup>2</sup> °C (300 BTU/ft<sup>2</sup>-hr-°F) at the HS channel interface.

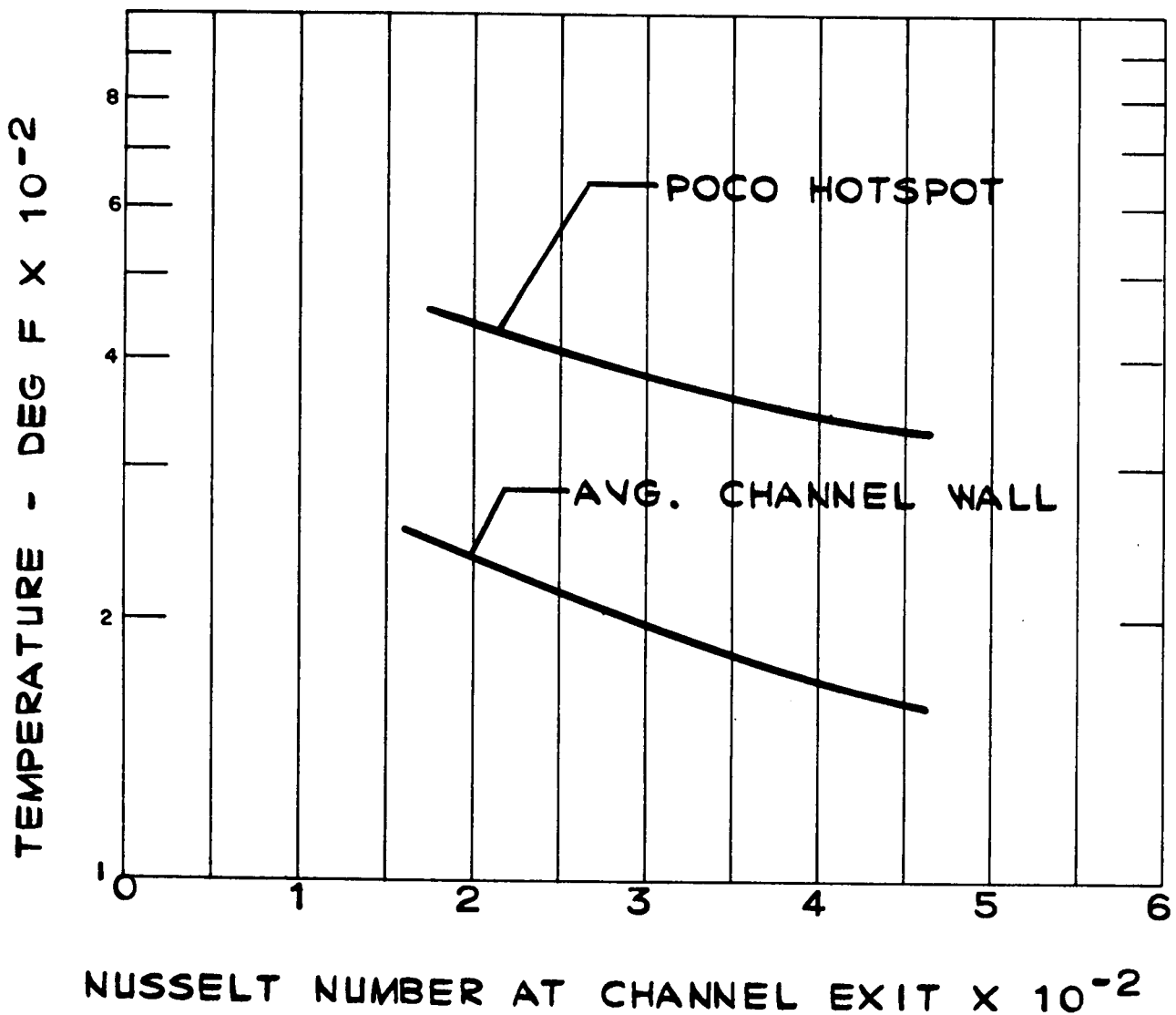
### 3.3.3.3 Hydraulic Analysis

A model was established to calculate the channel mass flow rates to cool the heat source for the heat load distribution corresponding to the 25 KW design. The model was based on the assumption that coolant through each channel picked up one-half of the heat generated from each HSU adjacent to the channel. Flow parameters include the coolant inlet pressure and temperature and the exit wall temperature. All coolant properties were taken as temperature dependent only.

The model calculated the mass flow rates required for each channel having the same exit wall temperature based on the simultaneous solution of the following equations:

Figure 3.3-16

S.S. TEMPERATURE VS. NUSSELT NUMBER  
ACHX OPERATING WITH NITROGEN COOLANT  
2-D CINDA RESULTS  
DESIGN CHANNEL



## 2-D HEAT SOURCE MODEL

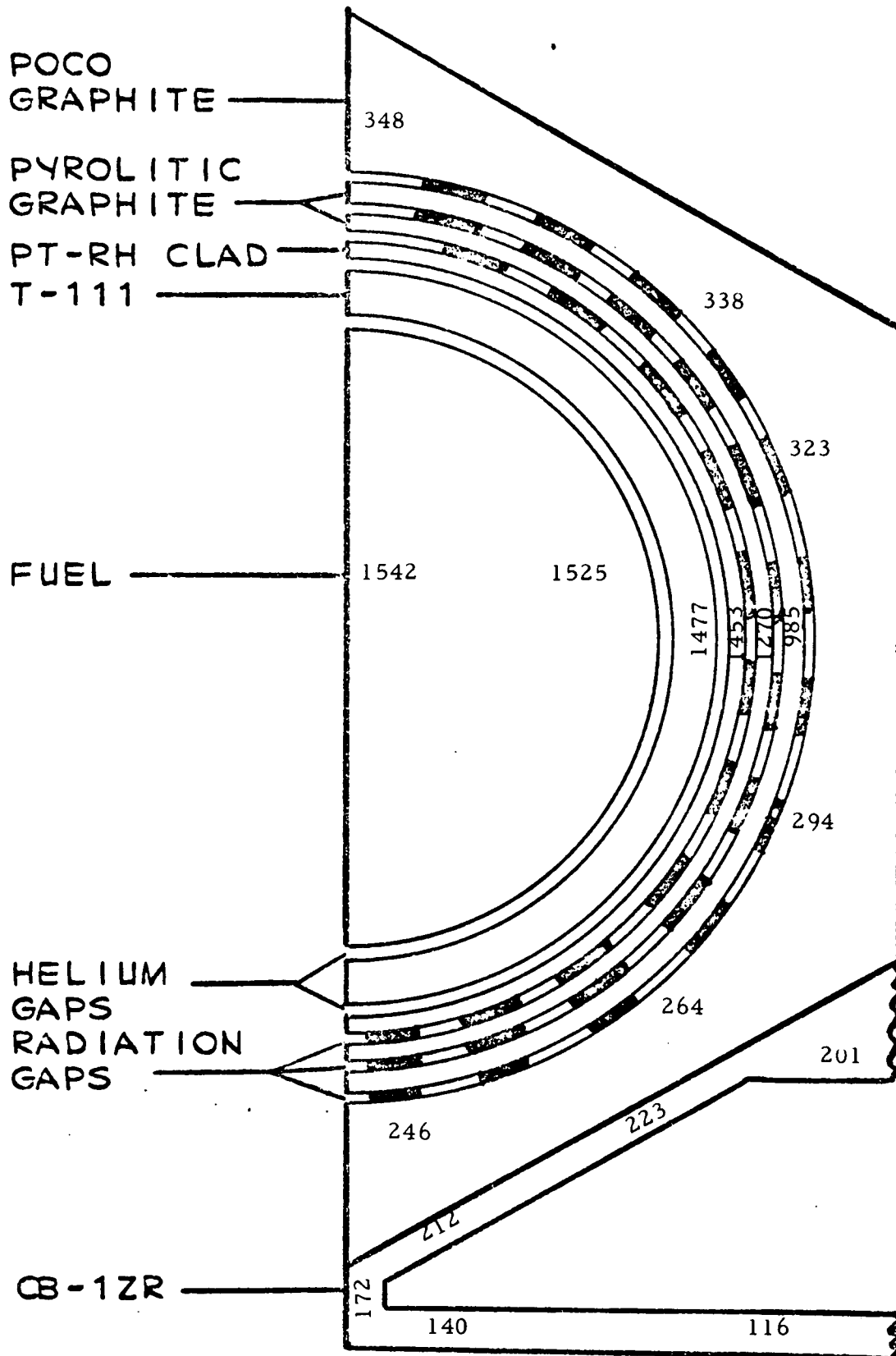


Figure 3.3-17



$$Q_{CH} = \dot{m} \bar{c}_p (T_{be} - T_{bi})$$

$$Q_{CH} = \int_0^L h_x P (T_{w_x} - T_{b_x}) dx$$

where  $Q_{CH}$  = Channel heat load

$\dot{M}$  = Channel mass flow rate

$\bar{c}_p$  = Mean specific heat of coolant

$T_b$  = Bulk coolant temperature

$h$  = Heat transfer coefficient

$P$  = Channel perimeter

$L$  = Channel heated length

$T_w$  = Channel wall temperature

Subscripts:  $x$  = local position in channel

$i$  = channel inlet

$e$  = channel exit

The basic assumption is that heat transfer is uniform along the channel but that the effective length corresponds to the active fuel length times the number of HS per channel. Since the hottest HS is at the channel exit and the hot spot temperature is a function of the channel wall temperature, it is convenient to evaluate all properties at the channel exit. With these assumptions the second equation becomes:

$$Q_{CH} = PL h_e (T_{w_e} - T_{b_e})$$

where all properties for the heat transfer coefficient,  $h_e$ , are evaluated at  $T_{b_e}$ .

Total ACHX mass flow requirements were determined as a function of coolant inlet temperature and channel exit wall temperature. The results are shown in Figure 3.3-18 for channel exit wall temperatures corresponding to POCO hot spot temperatures of 177°C (350°F) and 205°C (400°F).

Due to the large mass flow rate requirements an analysis was performed to determine the maximum Mach number in the inlet tube and headers as a function of inlet temperature and pressure. The inlet tube Mach number is shown in Figure 3.3-19 and the maximum header Mach number (based on



Figure 3.3-18

# ACHX MASS FLOW RATES DESIGN CHANNEL

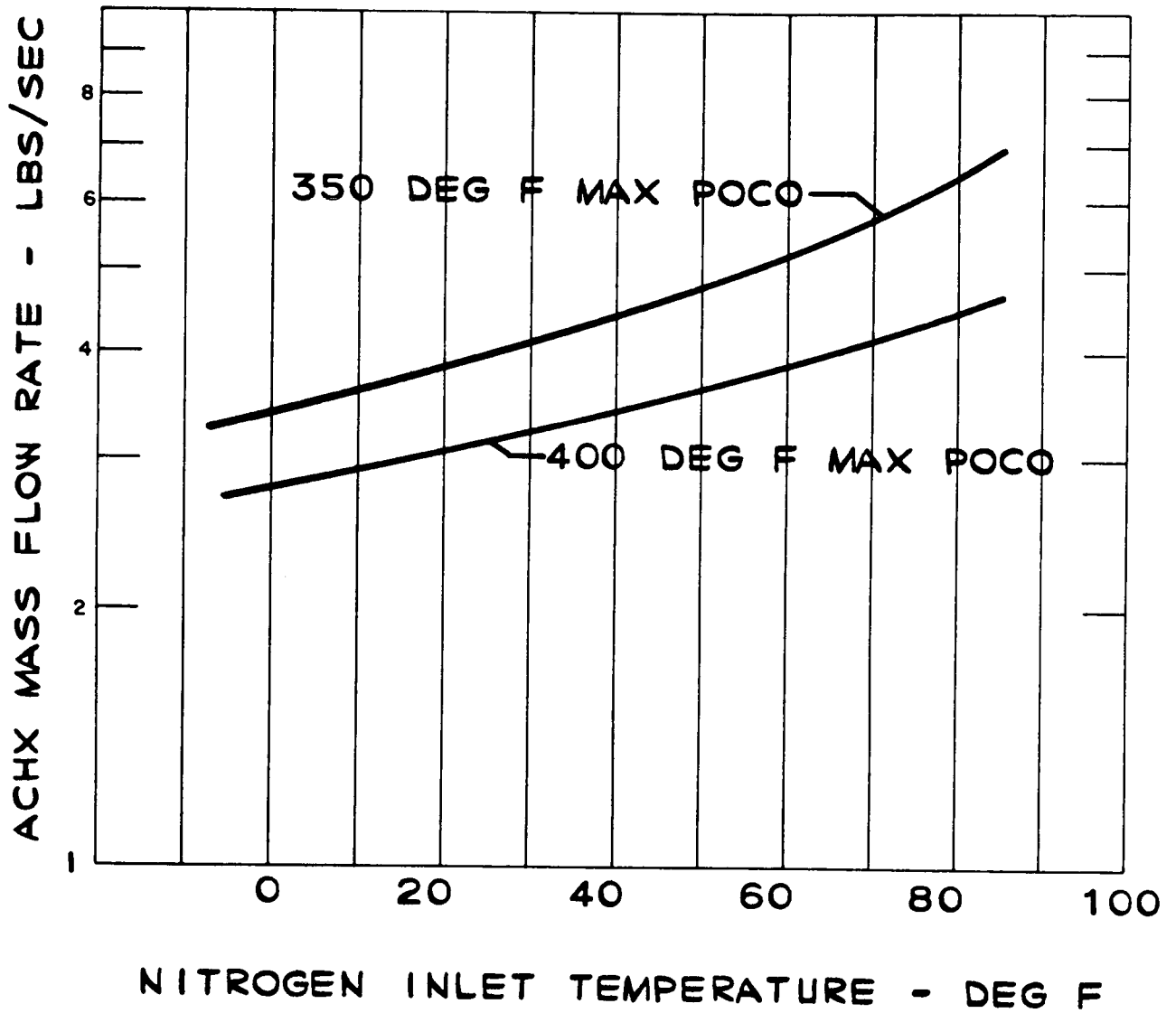
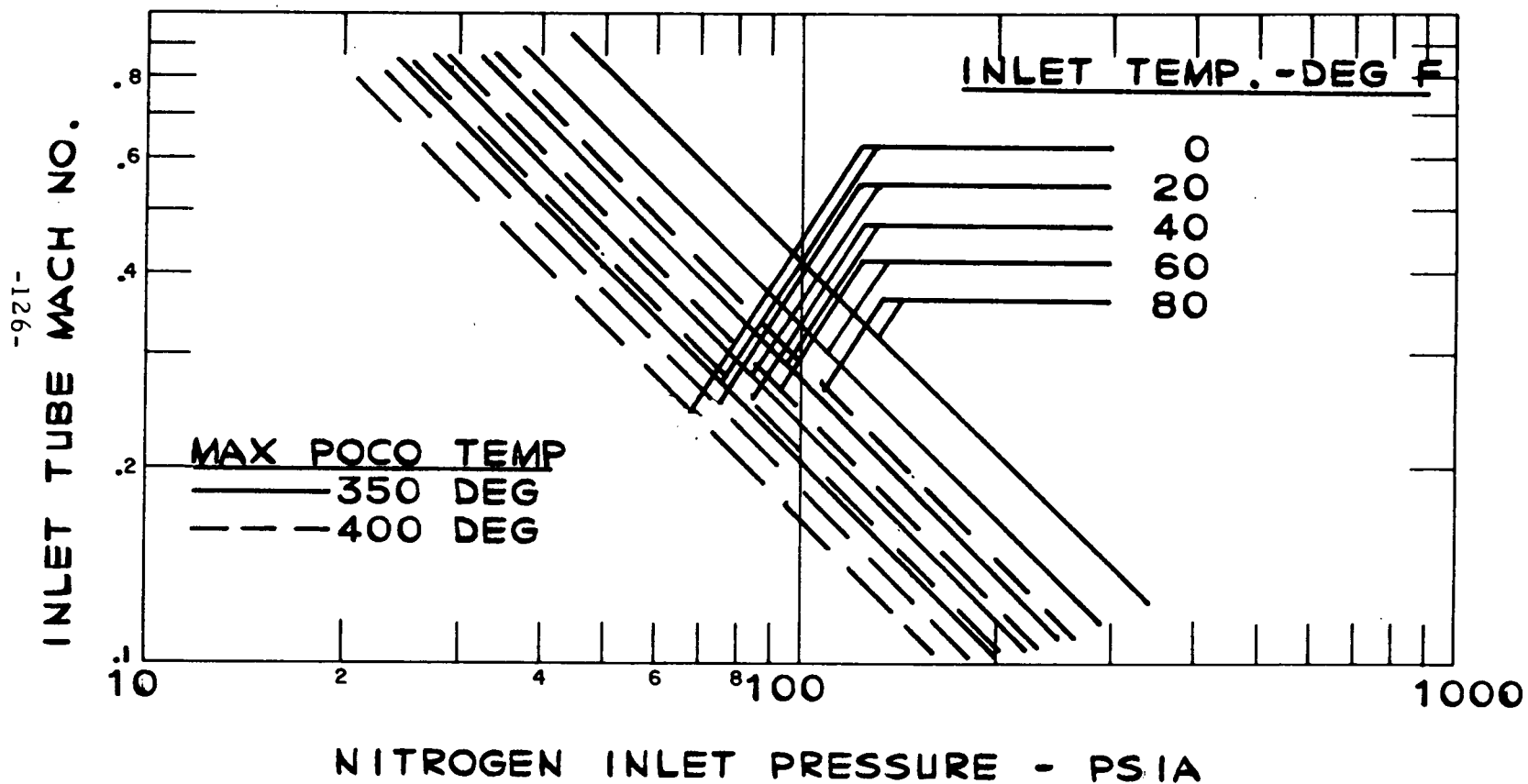


FIGURE 3.3-19 - INLET TUBE MACH NUMBER  
DESIGN CHANNEL



total mass flow) is shown in Figure 3.3-20. For the design condition of 16°C (60°F) inlet temperature and 69 newton/cm<sup>2</sup> (100 psi) inlet pressure specified by NASA, the maximum Mach number in the ACHX system occurs in the inlet tube and is 0.33. This corresponds to a total ACHX mass flow rate of 2.38 Kg/sec (5.26 lb/sec) which would limit the HS hot spot temperature to 177°C (350°F).

To establish the required mass flow distribution each channel was orificed at the exit. To determine the necessary orifice dimensions knowledge of the static pressure distribution throughout the entire ACHX system was needed. Due to the unusual flow distribution, dynamic head losses due to 90° turns, constrictions, etc., are not applicable in the classical sense. The most significant change in static pressure is in the inlet and outlet headers and is associated with the local change of momentum at each channel inlet and exit. The static pressure distribution in the headers was approximated by (Reference 3.3-5)

$$P_{i_x} = P_i + P_{D_i} \left( \frac{\dot{M}_T^2 - M_x^2}{\dot{M}_T^2} \right) - 4 f_{ix} \frac{L_x}{D_H} \left( \frac{\rho_x V_x^2}{2g} \right)_i$$

$$P_{e_x} = P_e + 2 P_{D_e} \left( \frac{\dot{M}_T^2 - M_x^2}{\dot{M}_T^2} \right) + 4 f_{ex} \frac{L_x}{D_H} \left( \frac{\rho_x V_x^2}{2g} \right)_e$$

where  $P$  = static pressure

$P_D$  = dynamic pressure

$M_T$  = total ACHX mass flow rate

$M_x$  = local header mass flow rate

$f_x$  = local coefficient of friction

$L_x$  = flow path length

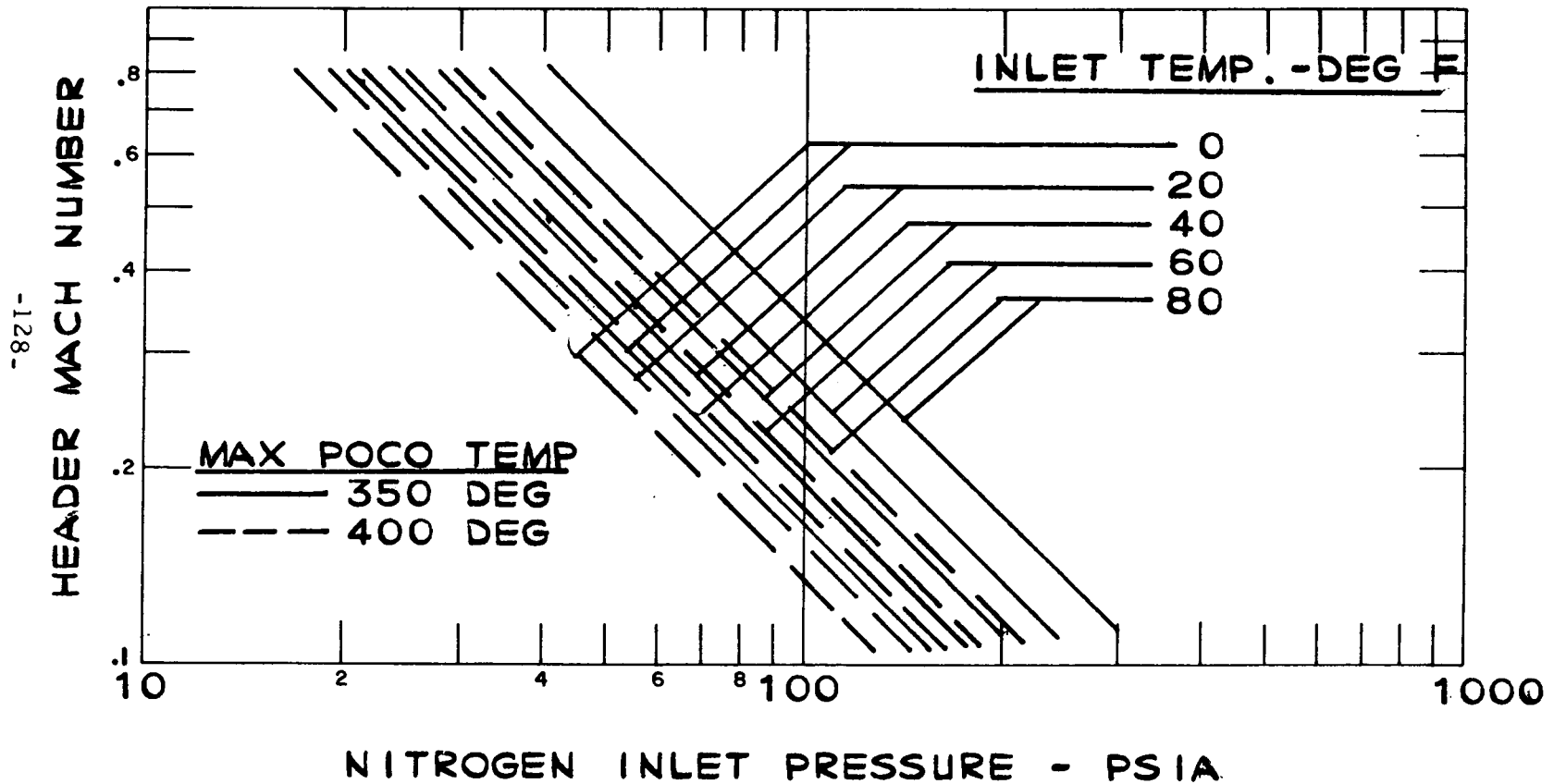
$D_H$  = header hydraulic diameter

$\rho$  = coolant density

$V$  = coolant velocity

$g$  = universal gravitational constant

FIGURE 3.3-20 - HEADER MACH NUMBER  
DESIGN CHANNEL



## Subscripts

X = local header conditions

i = inlet header

e = exit header

and 
$$f_x = \frac{0.046}{Re_x^{0.2}} \left[ Re_x \left( \frac{D_e}{D_H} \right)^2 \right]^{0.05} \quad (\text{Reference 3.3-6})$$

where  $Re_x$  = local header Reynolds number

$D_e$  = diameter of curvature of header

The flow in the inlet header was assumed isothermal at the inlet temperature. Static pressure distributions were calculated for both the inlet and exit headers neglecting all losses other than the momentum and friction head losses. A head loss at the inlet to each channel was accounted for and with knowledge of the static pressure and temperature, both upstream and downstream, at the exit orifices the orifice dimensions were calculated by

$$\Delta P_{OR} = \frac{1}{C^2} \frac{\dot{M}_c^2}{2 \rho_c A_{OR}^2}$$

where  $\Delta P_{OR}$  = pressure drop across the orifice

$\dot{M}_c$  = channel mass flow rate

$\rho_c$  = coolant density at channel exit

$A_{OR}$  = orifice area

C = orifice discharge coefficient  $\approx 0.6$

The expansion factor, Y, normally included in the orifice equation was estimated to be greater than 0.95 and was therefore neglected since the discharge coefficient, C, has a larger bound of uncertainty. Friction losses in the channels were found to be negligible and were neglected. Due to the location of the inlet and outlet connectors, there is no pressure symmetry in the system which is reflected in the unusual orifice diameter distribution attained.

The orifice dimensions are shown in the detail design drawing, (Figure 3.4-15 and Appendix "B"). The analysis was based on the design conditions chosen by NASA with a total ACHX mass flow of 2.38 Kg/sec (5.26 lbs/sec) at an inlet temperature of 16°C (60°F), an inlet pressure of 69 newton/cm<sup>2</sup> (100 psi) and an outlet pressure of 55 newton/cm<sup>2</sup> (80 psi).

If a larger total head loss was allowable it would be advisable to orifice at the inlet side of each channel with slightly rounded critical throat areas which would establish choked flow at each inlet. The only information necessary to accurately distribute the required channel mass flows is the local static pressure and temperature distribution in the inlet header. Again, this information in itself cannot be analytically established with great confidence.

In the existing ACHX design more than 50% of the total head loss is taken across the orifice of each channel. The magnitude of this pressure drop will help stabilize the flow. The ACHX design conditions are summarized in Table 3.3-IV.

#### 3.3.3.4 Alternate Design

As a contingency against establishing mass flow requirements that are difficult or expensive to achieve an analysis was performed to determine the effect of ACHX modifications upon the total mass flow rate. As an example, calculations were performed to determine the mass flow requirements for a channel design wherein a vertical fin is welded to the heat source plate running the entire length of each channel (Figure 3.3-21). Such a design gives an 18% increase in heat transfer area and an associated 18% increase in the heat transfer coefficient. The improved heat transfer characteristics are reflected in Figure 3.3-22 where it is shown that for a maximum hotspot temperature of 177° C (350°F) requires a Nusselt number of 262 compared to 380 for the design channel. The required total mass flow is about 20% less than the design requirements, as illustrated in Figure 3.3-23. The associated inlet tube and header Mach numbers for the finned channel are shown in Figures 3.3-24 and 3.3-25 respectively. It follows that further reduction in mass flow requirements can be achieved through the use of additional fins.

#### 3.3.4 Heat Source Unit Structural Design

Structural design performance requirements for the HSU have been established for both the environments associated with Earth Orbital missions and for the Super-Orbital reentries. The loads and design criteria for both classes of operation are summarized in section 3.3.4.1. Results of the structural analyses for both cases are described in section 3.3.4.2 (Earth Orbital - HSU Structural) and 3.3.4.3 (Super - Orbital - HSU Structure). Detailed structural computations are presented in Appendix "C".

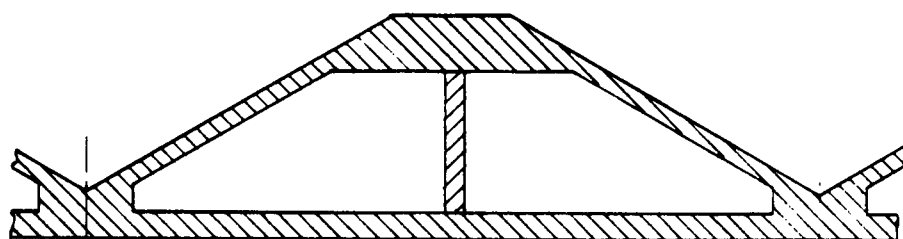


Figure 3.3-21

FINNED CHANNEL

S.S. TEMPERATURE VS. NUSSELT NUMBER  
ACHX OPERATING WITH NITROGEN COOLANT  
2-D CINDA RESULTS  
FINNED CHANNEL

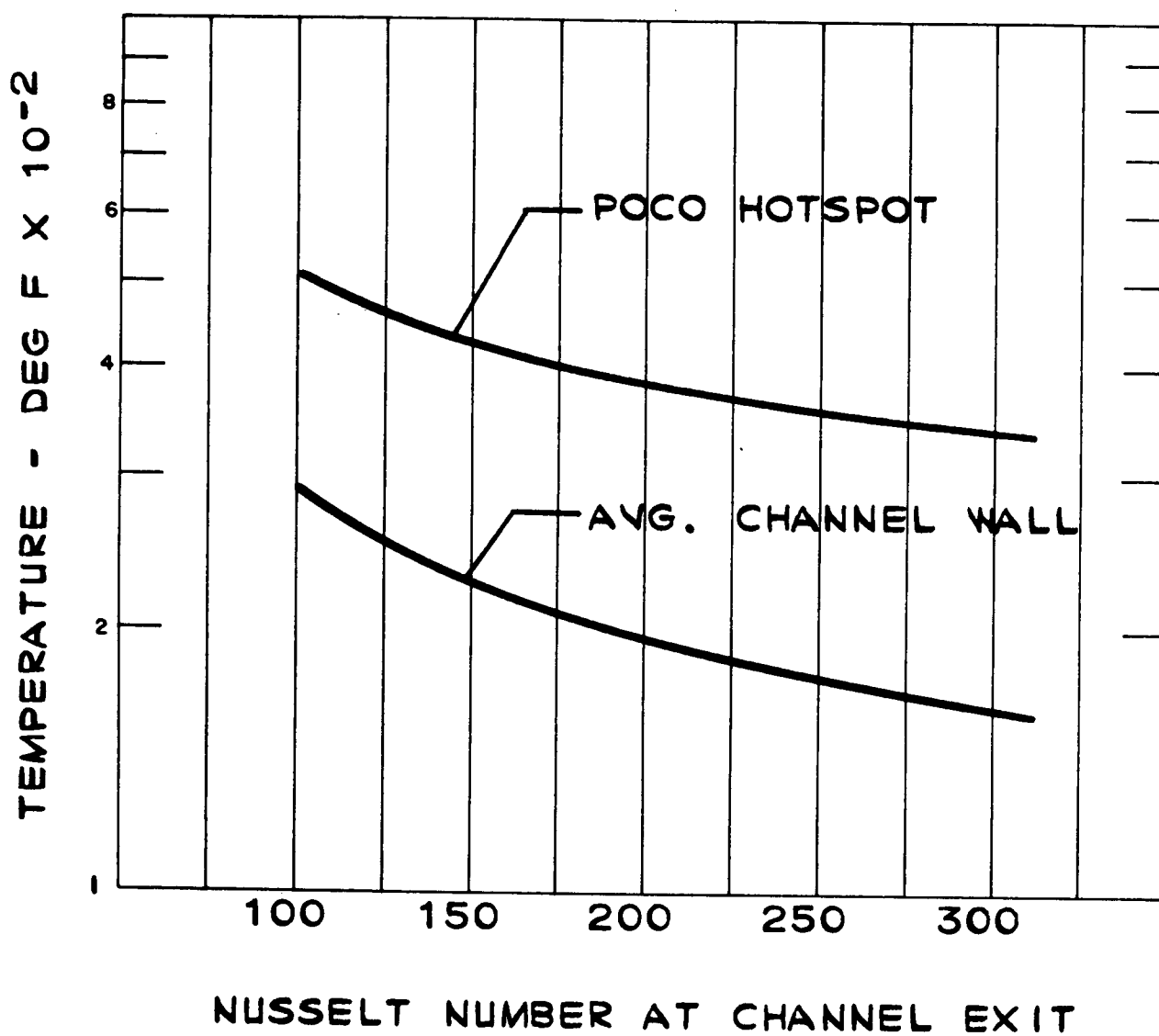


FIGURE 3.3-22



# ACHX MASS FLOW RATES FINNED CHANNEL

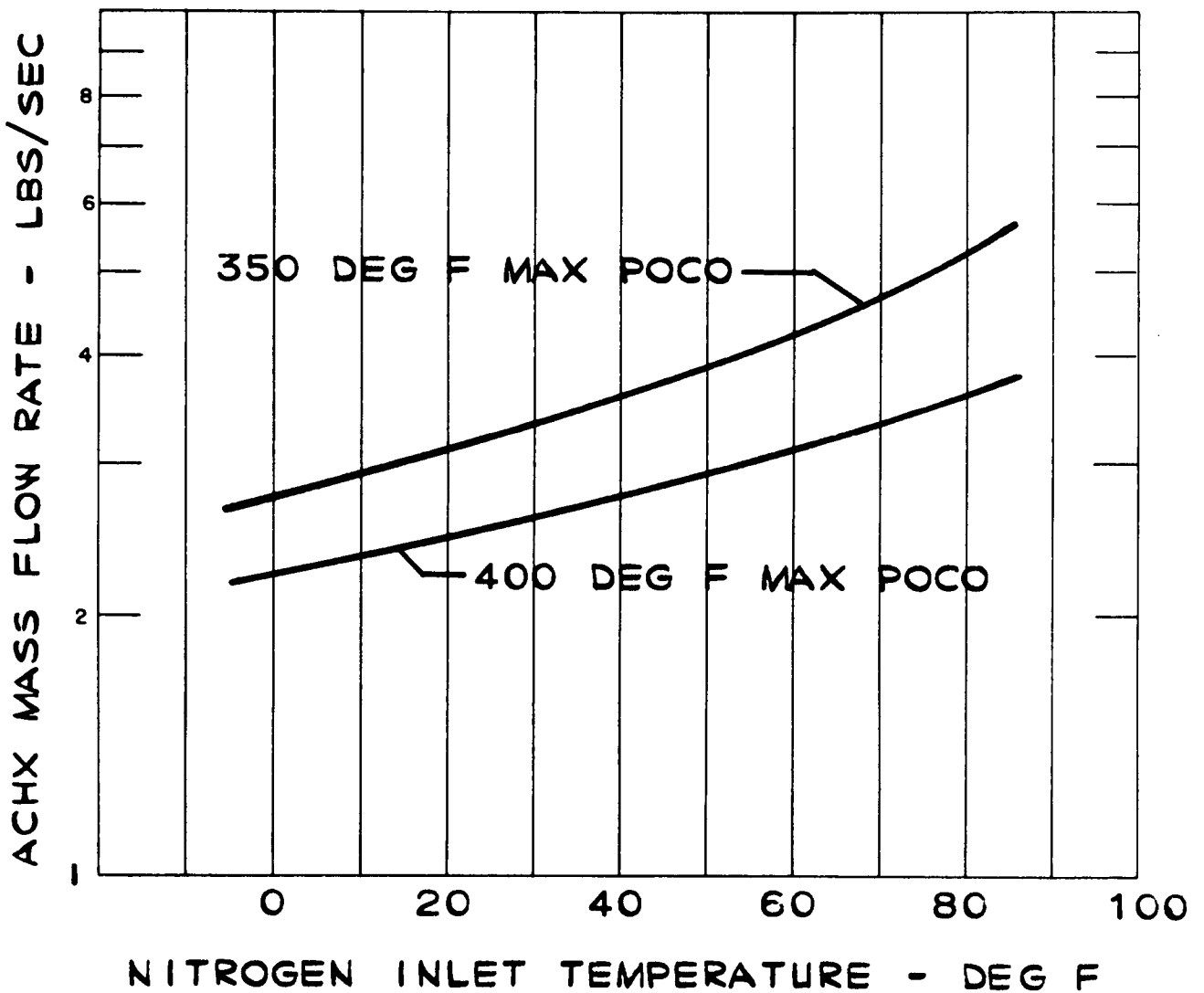


FIGURE 3.3-23

# INLET TUBE MACH NUMBER FINNED CHANNEL

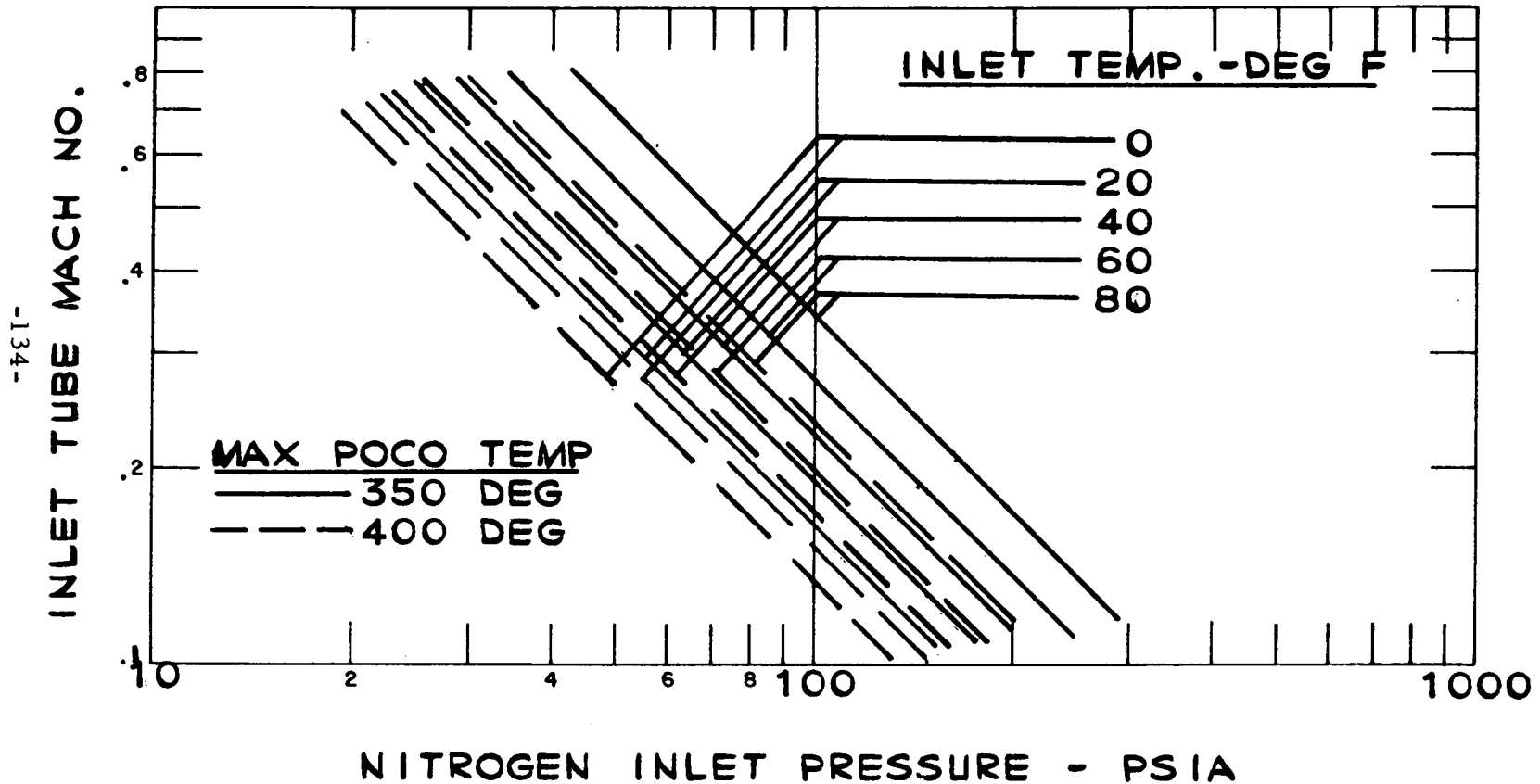


FIGURE 3.3-24

# HEADER MACH NUMBER F INNED CHANNEL

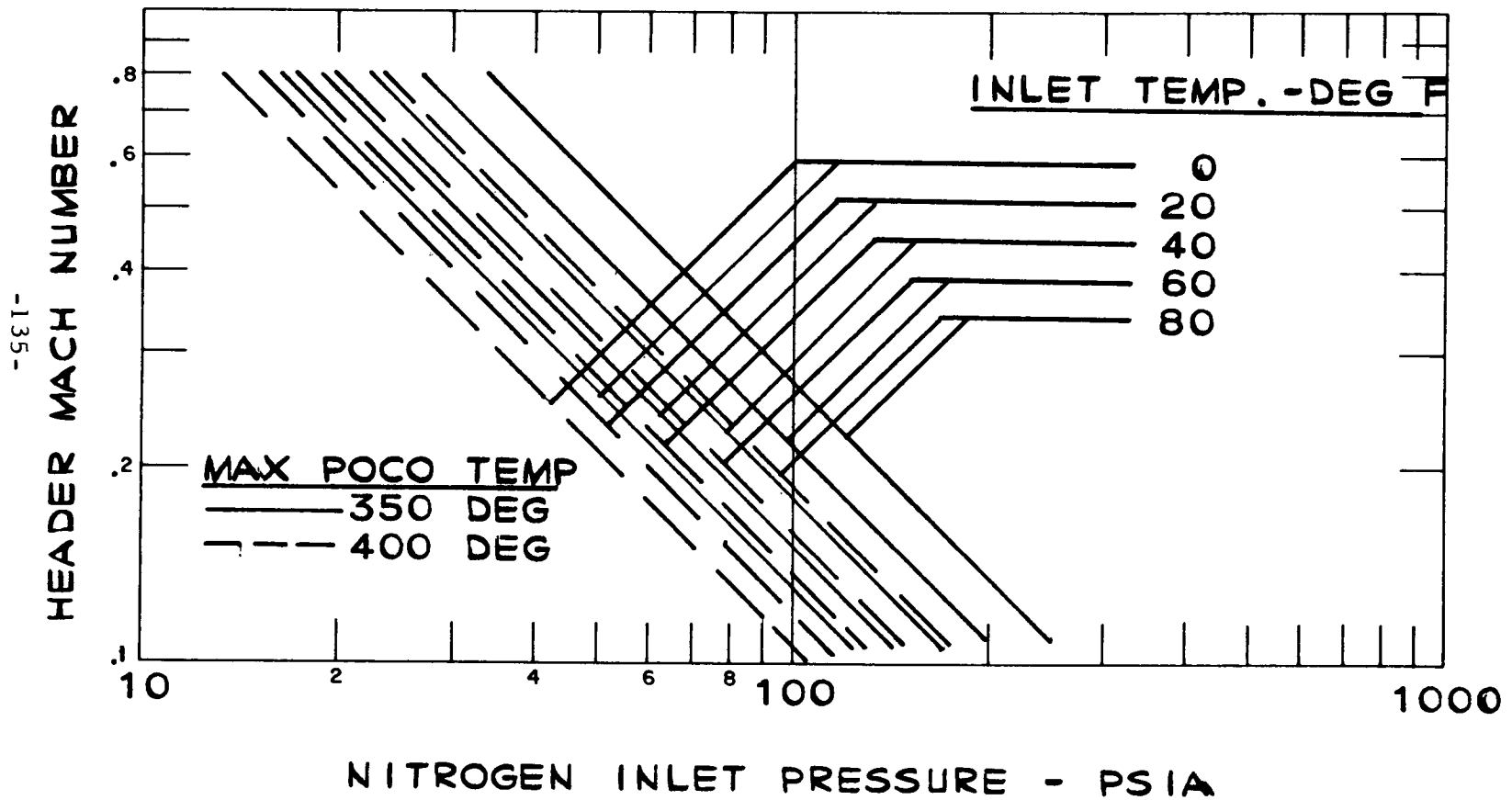


FIGURE 3.3-25

#### 3.3.4.1 Design Requirements and Criteria

The heat source unit structural components are designed to withstand the static and dynamic g-loads imposed during the mission lifetime. The maximum load requirements resulting from various mission environments are summarized in Table 3.3-V for both the Earth Orbital and Super Orbital designs. The loads in Table 3.3-V represent limit levels or maximum anticipated flight levels. For the purpose of design these loads are increased by the appropriate safety factors given in Table 3.3-VI. The reentry environment represents the most critical design environment.

For the Earth Orbital design, two reentry modes are considered, (1) an abort from the INT-21 launch trajectory which imposes the worst inertial loads on the HSU, and (2) the reentry from earth orbit which although considerably less severe than the INT-21 in terms of structural loads will occur while the HSU is at operating temperature. The HSU design temperature for the INT-21 abort case was taken as 500°F and for the reentry from orbit case, 1900°F. The allowable stress limits for both the Cb-1%Zr and T-111 materials used in the heat source plate and support structure are listed in Table 3.3-VI for both 500°F and 1900°F.

In the Super Orbital reentry analysis, a maximum reentry angle of minus fifteen degrees (-15°) was considered in the design of the HSU plate and support truss. The peak loads for the -15° lunar reentry case have been applied at the operating temperature of 1900°F. The effect of higher reentry angles with increased loads on HSU weight was evaluated but no design effort was expended for these higher reentry angles. (Weight increase estimates for super-orbital HSRV designs are summarized in section 3.4.3.3).

#### 3.3.4.2 Earth-Orbital - HSU Structure Design

The maximum temperature of the HSU and support system during the INT-21 reentry is 500°F. The total HSU mass that the struts support is 1571 lbs. A summary of the results of the stress analysis for the major structural components in the heat source plate and support system are presented in Table 3.3-VII. A more detailed discussion of these components is contained in the subsequent paragraphs.

a. Heat Source Support Plate -- The heat source support plate is a built-up welded structure of Cb-1%Zr refractory metal which is supported at four peripheral locations. The 56.50 inch diameter plate supports a total fuel source weight (66 individual heat sources) of 726 lbs. which is assumed to be uniformly distributed over the plate's circular surface. The plate is designed to support the total heat source mass under a peak axial inertial load of 53.4 g at 500°F. A thick-walled square cross-sectional ring around the full periphery of the plate serves both as inlet and outlet headers for the ACHX system and as a rigid structure to uniformly transmit the concentrated

TABLE 3.3-V

Summary of Structural Design Requirements

A. Reentry

Earth Orbital	<u>INT-21 Abort</u>		<u>Reentry from Orbit</u>	
<u>Load Condition</u>	<u>Axial-g</u>	<u>Lateral-g</u>	<u>Axial-g</u>	<u>Lateral-g</u>
Maximum Lateral Load	31.0	4.6	6.0	0.5
Maximum Axial Load	38.1	4.1	7.8	0.4
Maximum Axial Load (Zero angle of attack)	42.7	0.0	8.1	0.0

Super Orbital (Reentry Angle =  $-15^{\circ}$ )

Load Condition	Axial-g	Lateral-g
Maximum Lateral Load	65.5	11.2
Maximum Axial Load	81.2	9.7
Maximum Axial Load (Zero angle of attack)	93.3	0.0

B. Launch (HSRV Axis Normal to Launch Vehicle Axis)

Maximum g-Load (Saturn I-B)

Axial  $\pm$  4.0                      Lateral  $\pm$  9.0

C. Miscellaneous Loads

	Maximum g-Loads	
	<u>Axial</u>	<u>Lateral</u>
Pad Abort	10.0	2.0
Chute Deployment & Air Snatch	8.2	2.0

D. ACHX Maximum Operating Conditions

Pressure = 100 psi

Temperature = 500°F

TABLE 3.3-VI

Structural Design Criteria

A. Safety Factors

All Flight Conditions (Includes Launch, Abort and Reentry) 1.25

Pressurized Systems (ACHX)

Proof 1.5

Burst 2.0

Component Buckling (Such as Struts in Compression) 1.5

B. Temperature Stress Limits

HSU Temperature	<u>INT-21 Abort</u> 500°F	<u>Earth Orbit Reentry</u> 1900°F	<u>Super Orbit Reentry</u> 1900°F
-----------------	------------------------------	--------------------------------------	--------------------------------------

Material Yield  
Strength (1) (2)

T-111	53 KSI	37 KSI	37 KSI
Cb-1%Zr	33 KSI	22 KSI	22 KSI

(1) Shear Yield is 60% of these values

(2) Butt Weld Allowable 80% of these values

Fillet or Slot Weld Allowable 60% of the Values

TABLE 3.3-VII

Summary of HSU Stress Analysis

<u>Component</u>	<u>Design Conditions</u>	(ksi)	<u>Computed Stress</u> (kilogram/sq. meter) $\times 10^{-6}$	<u>Safety Factor</u>
ACHX Header	150 psi Proof Pressure and 500°F	7.5	5.27	2.64
ACHX Channel	150 psi Proof Pressure at 500°F	19.37	13.62	1.36
HS Plate Facesheet	$A_x = 53.4 \text{ g}$ $T = 500^\circ\text{F}$	23.32	16.39	1.42
HS Plate Fitting	$A_x = 47.62 \text{ g}$ $A_n = 5.12 \text{ g}$ $T = 500^\circ\text{F}$	29.65	20.84	1.11
T-111 Strut Pins	$A_x = 47.62 \text{ g}$ $A_n = 5.12 \text{ g}$ $T = 500^\circ\text{F}$	28.61	40.70	1.11
T-111 Struts	$A_x = 47.62 \text{ g}$ $A_n = 5.12 \text{ g}$ $T = 500^\circ\text{F}$	47.67	33.51	1.11
Strut Support Ring (Ti-6Al-4V)	$A_x = 47.62 \text{ g}$ $A_n = 5.12 \text{ g}$	90.35	63.52	1.275

attachment loads to the plate. The upper facesheet or panel of the builtup heat source plate consists of a flat sheet of .16 inch thickness to which are welded ACHX coolant channels or embossments. These coolant channels which run between the rows of heat sources are also contoured to provide cradle support for the heat sources. The plate is supported by the truss system at 90 degree points on the plate periphery by means of rigid fittings designed to transmit the plate inertial loads down through the insulation layer to the truss system which consists of eight struts which are pinned to these, fitting just below the insulation layer.

The worst loading for the earth orbital plate design occurs under the launch abort reentry condition (INT-21 trajectory) where the peak axial load is 53.4g including a factor of safety of 1.25 (Table 3.2-III). The HSU temperature for the INT-21 launch abort reentry trajectory is, however, only 500°F. Although the HSU is at a higher temperature of 1900°F for the orbit decay reentry and the yield strength of the material is reduced by approximately 33% in going from 500°F to 1900°F the loads are lower by almost 80%. Hence, the INT-21 early launch orbit case is the more critical condition. The plate depth for the earth orbit design is 2.75 inches not including the additional height of coolant channels. The upper face sheet of the plate which is also the back wall of the ACHX coolant channels is sized by ACHX requirements and hence, is heavier than required to resist plate flexural loads. The upper face sheet is sized at 0.16 inches and the coolant walls at .07 inches based on ACHX requirements. In evaluating the lower face sheet thickness the additional material in the coolant channels was assumed to contribute to the plate rigidity and hence, was added to the upper face sheet.

A lower face sheet thickness of .12 inches is required to resist local face sheet buckling. Using the full effective width of the unsupported face sheet between internal ribs gives a maximum plate bending stress of 23,316 psi, providing a safety factor of 1.42 for the INT-21 peak load case.

During orbit decay reentry the maximum bending stress in the plate face sheets is 4412 psi which when compared to the 22,000 psi yield strength of Cb-1%Zr at 1900°F results in a very conservative margin of safety of 3.98. The maximum plate deflection under the abort design load of 53.4 g is .288 inches. This, however, is based on a square plate model with corner supports with no contribution allotted to the plate for the heavy ACHX header around the plate periphery. The internal ribs which join the two face sheets and are spaced at 3.88 inch intervals, were sized at .08 inches in order to insure against local shear or compression instability. In order to fabricate this composite plate, the final fabrication procedure will be to join the bottom face sheet to the internal ribs by means of either plug or slot welding. If slot welding is used, a .625 inch slot weld would be required at each rib intersection, as well as at the mid-point between intersections to resist the maximum shear loads in the plate.



b. ACHX System -- The operating conditions for the ACHX headers and coolant channels for launch pad cooling are assumed to be a maximum operating pressure and temperature of 100 psi and 500°F respectively. At this temperature, the Cb-1%Zr material properties that are considered are the short-time yield and ultimate strength.

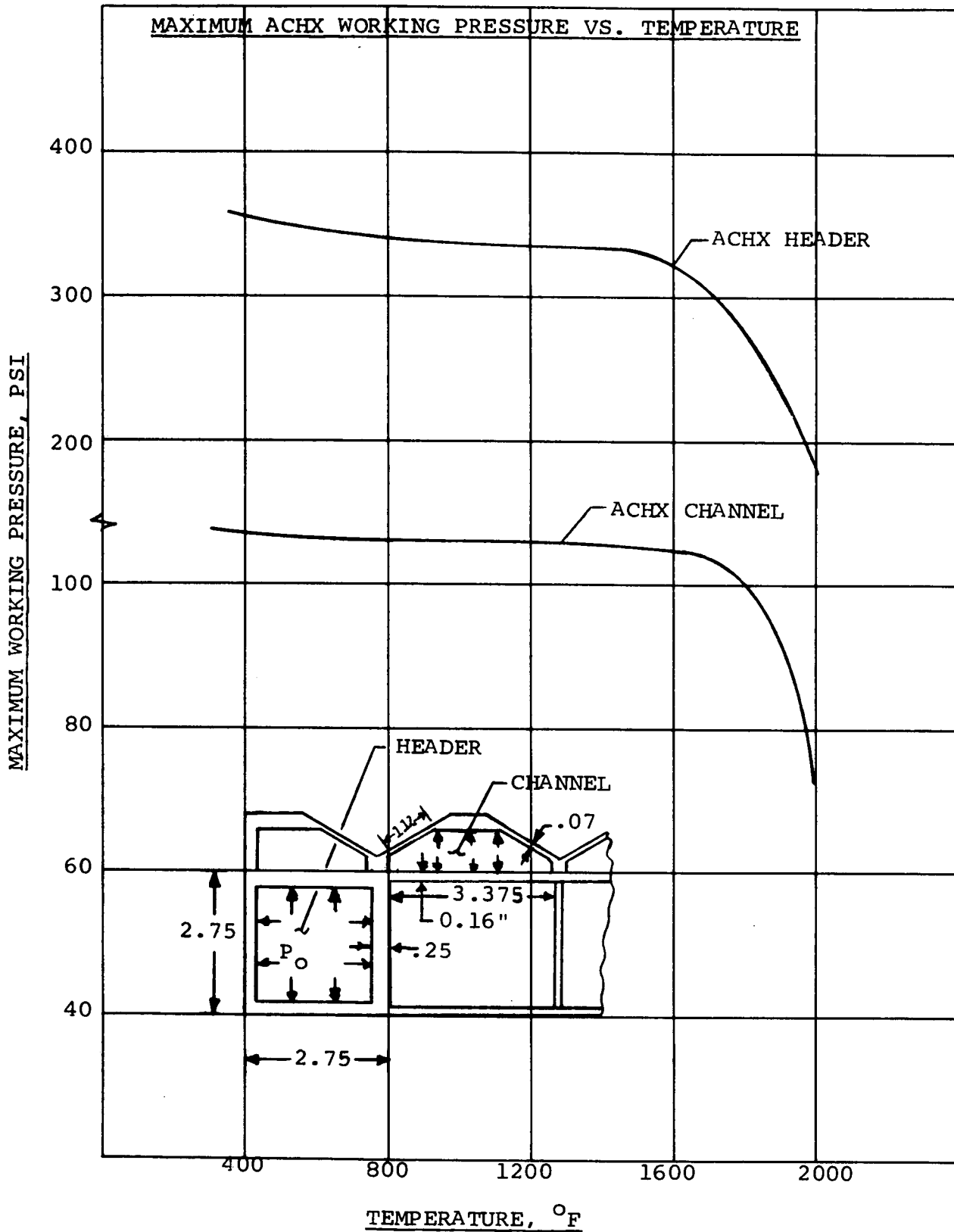
The design procedure used for the ACHX system was to design for a proof pressure of 1.5 times the maximum operating pressure and a burst pressure of 2.0 times the maximum operating pressure. Resulting stresses for the proof pressure must be below the material yield strength and stresses for burst pressure must be below the ultimate strength. For the Cb-1%Zr material and the design temperature of 500°F the ACHX design will be governed by the proof pressure and material yield strength criteria. The maximum bending stress in the .25 inch thick header walls based on a proof pressure of 150 psi is 7500 psi. For an allowable stress of 26,400 psi which is the material yield strength of 500°F, reduced by a 1.25 factor to account for reduced weld strength, the minimum margin of safety in the headers is 2.52.

The coolant channels consist of the upper plate face sheet of 0.16 inch thickness and coolant walls of .07 inch thickness. The resulting maximum bending stress occurs in the .07 inch walls and is 19,372 psi, which again based on the allowable stress of 26,400 psi results in a margin of safety of 0.36. For the thermal test facility model, cool down of the HSU from its nominal operating temperature of 1900°F might be accomplished by reutilizing the ACHX system; this, however, is not a design requirement for the flight design. The pressure capability of the ACHX system will decrease at the higher temperature since material strength falls off and creep effects are introduced. Figure 3.3-26 shows the maximum ACHX working pressure capability versus temperature.

Although short-time cool down periods are considered i. e., one hour, creep deformation and stress rupture properties of Cb-1%Zr were still considered for temperatures above 1300°F. The criteria used for creep failure was to compare proof-pressure stresses (1.5 times maximum working pressure levels) to the one-hour one-percent creep stress for Cb-1%Zr and burst pressure stresses to the one hour rupture stress. The results of Figure 3.3-26 indicate that the header could withstand a 100 psi working pressure at 2000°F but that the maximum temperature for the coolant channels under a maximum working pressure of 100 psi is approximately 1800°F.

c. Support Struts -- The struts which are the major components of the support system are designed to survive the maximum axial compressive stresses and buckling loads experienced during reentry. The two reentry cases considered are (1) INT-21 orbit injection (maximum loads) and (2) orbit decay (maximum temperature). Although for the INT-21 reentry the HSU is at a lower temperature than for orbit decay reentry (500°F compared to 1900°F) the peak inertial loads are approximately 4.8 times higher for INT-21 reentry and hence, it is considered, in the absence of thermal growth effects

FIGURE 3.3-26



vs. the critical reentry condition. The effect of thermal growth of the HSU on strut stresses was considered in the final strut design.

The INT-21 reentry load condition which governs the strut design occurs at the instant of peak axial inertial load when the HSU will experience a combination of a 47.62 g axial load and a 5.12 g lateral load including a design factor of safety of 1.25. In order to define the worst vehicle orientation for application of the lateral load, it is only necessary to find the load distribution for two vehicle orientations as shown in Figure 3.3-27 since because of symmetry these represent the two bounds. It is shown that the vehicle orientation which results in the worst strut load occurs where the lateral load is applied in the plane containing the vehicle axis and one of the lower truss/aeroshell ring attachment points. For this condition and the above combination of axial and lateral inertial loads, the maximum strut load for a HSU weight of 1571 lbs is 22,883 lbs. The T-111 tubular strut with a 1.0-inch O.D. and a .188 inch wall thickness has a cross-sectional area of .48 in<sup>2</sup> resulting in a maximum compressive stress of 47,673 psi. The yield strength of T-111 at 500°F, the maximum temperature in the strut during the INT-21 reentry, is 53,000 psi resulting in a structural margin of safety of .11.

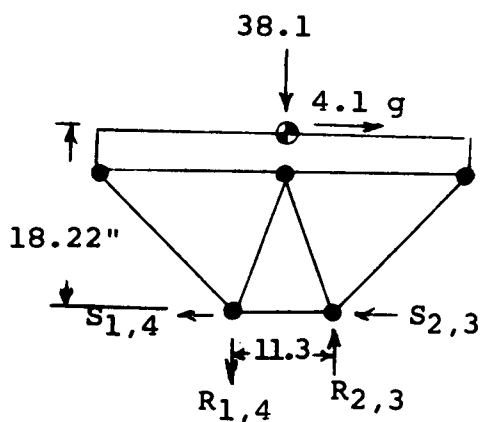
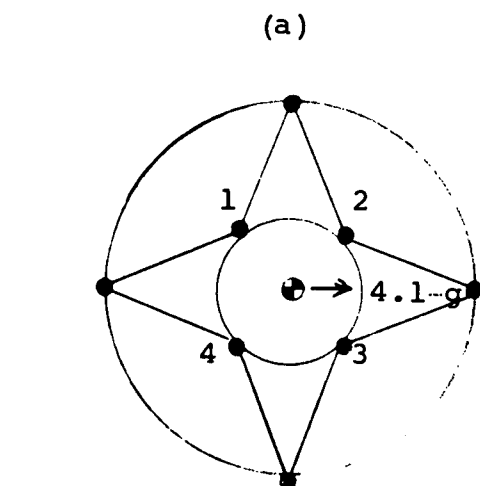
The critical buckling load in the 20.90 inch long strut is 48,025 lbs. Using a factor of safety of 1.5 on column buckling instead of the standard 1.25 on the compressive stress, the strut design load for buckling is 27,460 lbs. resulting in a margin of safety of .75. This is felt to be conservative enough to account for reduced capability in the strut due to deflection-dependent end moment or for slight rotational effects at the built-in end.

The strut design was also evaluated for bending stresses and deflections due to the relative thermal growth of the HSU during heat up to operating temperature. During launch pad operation, the HSU is held in equilibrium at about 350°F which results in minimal thermal mismatch for the struts to absorb in bending. For the launch abort condition, the HSU temperature is assumed to be 500°F while the lower truss and aeroshell is assumed to be at 100°F. This results in a relative radial thermal growth of the HSU with respect to the upper truss/HSU pinned attachment of .028 inches, which for the strut to absorb, would require a deflection at the pinned end of the strut perpendicular to its axis of .046 inches and an end load perpendicular to the strut axis of 16.0 lbs. These thermal effects do not result in additional stress at the hot end of strut but do increase the strut stresses at the lower or built-in end of the strut.

The increase of stress results from (1) the axial strut load applied with the thermally-induced end deflection of .046 inches will result in an additional bending stress at the lower end of the strut equal to 12,531 psi and (2) the bending moment from the 16.0 lb. end load adds another 3981 psi. The total

FIGURE 3.3-27

DISTRIBUTION OF HSU LOADS AT STRUT/RING ATTACHMENTS

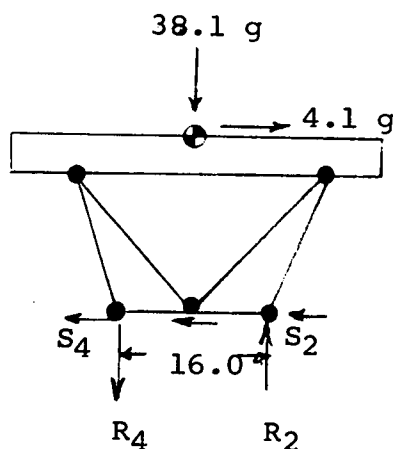
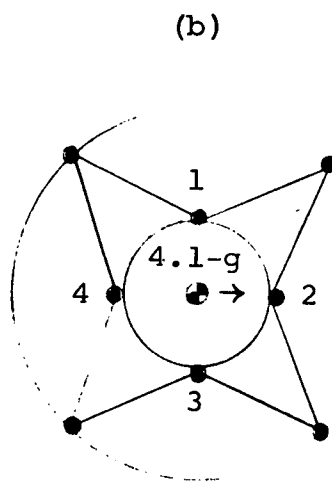


TOTAL REACTIONS

$$R_2 = R_3 = \frac{W \times 38.1}{4} + \frac{W \times 4.1 \times 18.22}{2 \times 11.3}$$

$$= 9.52 W + 3.3 W = 12.82 W$$

$$R_1 = R_4 = 9.52 W - 3.3 W = 6.22 W$$



TOTAL REACTIONS

$$R_1 = R_3 = \frac{W \times 38.1}{4} = 9.52 W$$

$$R_2 = 9.52 W + \frac{W \times 4.1 \times 18.22}{16.0}$$

$$= 9.52 W + 4.67 W = 14.19 W$$

$$R_4 = 9.52 W - 4.67 W = 4.85$$

NOTE: LOAD FACTORS SHOWN ARE LIMIT

maximum stress at the built-in end of the strut combining these effects with the inertial load stresses is 64,185 psi which is well below the yield strength of 80,000 psi for T-111 at 100°F.

The thermal forces are considerably higher for a heat up of the HSU to the 1900°F operational temperature. Using thermal analysis results where the average temperature of strut is approximately 1200°F and the titanium ring is 418°F the relative radial thermal growth of the HSU with respect to the truss is approximately 0.10 inches. In order to absorb this, the struts would have to experience an end deflection and end load perpendicular to their axes of .156 inches and 53.8 lbs, respectively. The maximum bending stress at the lower end of the strut produced by this end load is 13,386 psi which causes no concern during the operational phase. During orbit decay reentry an additional bending stress of 7204 psi resulting from the strut load of 3879 lbs. from peak inertia loads and the thermal end deflection of .156 inches occurs at the lower end of the strut and is added to the above thermal-moment stress of 13,386 and HSU inertial load stress of 8081 psi. The total maximum stress of 28,671 psi at the built-in end however, is still well below the T-111 yield strength of 53,000 psi for that end of strut which experiences a maximum temperature of 500°F. Hence, the thermal stress effects for normal operation will not change the strut design.

d. Heat Source Plate Attachment Fittings -- The heat source plate is attached to the support truss by means of four rigid Cb-1%Zr fittings. These are located at the plate periphery and are welded to both the rigid ACHX header and to the plate face sheets. These fittings penetrate through approximately 1.5 inches of insulation beneath the heat source plate and are joined to the truss system struts just below the insulation layer. At each of the four attachment locations the fitting and two intersecting struts are pinned together.

Because of the angle that the struts make with the vehicle axis, direct strut loads introduce both an axial load and a lateral load, (or kick load) to the fitting. For a maximum strut load of 22,883 lbs. and a strut angle of 37.5 degrees to the horizontal in the plane of strut, the maximum loads transmitted to the fitting through the T-111 pin from the two struts consist of an axial component of 27,862 lbs. and a lateral component of 35,228 lbs. The resulting maximum combined stress in the Cb-1%Zr fitting is 32,299 psi which is close to the allowable stress of 33,000 psi for Cb-1%Zr at 500°F. This is conservative, however, since the strut load for the two intersecting struts would not be each equal to 22,892 lbs. A more detailed examination of load distribution in the system of struts showed that when one strut carried the maximum load of 22,892 lbs. the other strut mate which intersects at the same plate fitting carried a load of only 15,354 lbs. This occurs when the lateral inertia load is applied in the same plane containing the vehicle axis and one of the attachment points on the aeroshell ring. When the lateral load is applied at 45 degrees to this orientation, i. e., in a plane containing the vehicle axis and one of the fitting on the plate, it is possible that each of the two struts pinned to same

fitting could have a maximum load of 20,676 lbs. Consequently, this represents the worst load case for any fitting with a resulting maximum stress of 29,655 psi and margin of safety of .11. The maximum shear load in the T-111 shoulder bolt which serves as the pin is 44,923 lbs. Based on two shear areas the maximum shear stress in the 1.0" diameter bolt is 28,613 psi compared to an allowable shear stress of 31,800 psi.

e. Retention Bolts -- The 66 heat sources are held in place on the heat source plate by 146 T-111 bolts, 0.164 inch in diameter. The bolts are located between rows of heat sources and are threaded into the solid upper flats of the ACHX coolant channels. In the plate interior, the bolt allotment is two per heat source. Each T-111 bolt has a load capability of 636 pounds for the abort reentry and 487 pounds for reentry from orbit. For two bolts this corresponds to an applied inertia load capability of 126-g and 88-g for the abort and orbit reentry conditions respectively, which is considerably more than any imposed structural load which applies tension to these bolts.

#### 3.3.4.3 Super Orbital HSU Structure

The design requirements for the HSU plate and support system are considerably more severe for the super orbital design than for the earth orbital design. For a lunar return at a  $-15^\circ$  reentry angle, inertia loads are slightly more than twice the INT-21 levels while the HSU is at an operating temperature of  $1900^\circ\text{F}$  as compared to  $500^\circ\text{F}$  for the design INT-21 load condition. As a result of the HSU support plate depth has been increased to 3.5 inches to reduce face sheet thickness and conserve weight; nevertheless, the new plate face sheet thickness and internal rib thickness increase to .25 inch and .16 inch respectively. Plate structural weight increases from 640 lbs. to 910 lbs. indicating the compounding effect of these higher loads on the strut support system. Preliminary calculations show that a strut area of  $1.75\text{ in}^2$  is required to support the increased weight and higher reentry loads and temperatures. This strut area is intolerable because of the resultant heat leak and local aeroshell hot spots.

A more efficient concept for reacting super orbital loads is a secondary support scheme which can remain unloaded during the launch, operational and initial reentry phases of the mission, but will take over the load supporting function from the strut system during the peak reentry loads period. (A sketch of this concept is shown in section 3.4.3).

Since the strut system lacks the flexibility to elastically deform and allow the HSU to set down on four peripheral pads on the aeroshell directly under each plate fitting, a crushup system is required to provide the required axial

translation. The proposed concept provides an annular column of crush up material to be located between the lower strut ring and aeroshell attachment ring, the former ring being an additional member to the earth orbital design. During assembly, these mating rings will be bolted together axially preloading the crushup material between them in order to insure a good structural load path from the strut system to the aeroshell. In addition, the webs of the mating rings will be pinned to resist torque loads about the vehicle axis with axially slotted holes provided to allow relative axial movement when crushup occurs. The four peripheral bearing pads below the plate fittings are separated from the fitting by the insulation layer so that thermal short circuiting does not occur. A rigid ring is provided under these pads to improve the load distribution from the four pads into the aeroshell when the peak reentry inertia loads are applied.

In brief, the total support system will function as follows. The launch, operational, and initial reentry loads (when the HSRV vehicle is undergoing a period of stabilization) of the HSU will be carried by the strut system as in the earth orbital design and these loads are transmitted through the strut attachment ring into the aeroshell. With the HSRV vehicle stabilized in a proper reentry attitude and beginning to decelerate rapidly, the strut system and consequently the crushup system, will experience increasing compressive loading until the maximum design crush strength is reached whereupon the entire HSU system will move forward under deceleration until the plate fittings bottom out on the peripheral bearing pads. The insulation layer between the fitting and bearing pads will also be crushed in the process without offering significant resistance. At full compression, four spring-loaded pins will engage into aligned holes in the strut ring locking the strut ring to the aeroshell attachment ring and thereby preventing rearward movement of the HSU. The crushup system will be designed to crush before any possibility of strut failure. For the strut cross-sectional area of .48 in<sup>2</sup> and a maximum temperature of 1900°F, the maximum allowable strut load is 17,760 lbs. For a HSU weight of 1840 lbs., this corresponds to an axial inertia load of 57.0 g; this, however, will be lower when simultaneous lateral loading occurs.

Since the maximum allowable strut loading is controlled by the crushup design and will be lower than the earth orbital design, no additional beefing up of the attachment ring or local aeroshell will be required.

### 3.4 HEAT SOURCE REENTRY VEHICLE (HSRV) DESIGN

The results of the analyses and design of the HSRV aeroshell, reentry thermal protection and thermal control subsystem are presented in this section. Both the reference earth orbital mission vehicle and necessary modifications to the reference HSRV to enable it to survive super-orbital reentry environments are described.

### 3.4.1 Earth Orbital Reentry Vehicle

The HSRV reference configuration utilized during this design study is basically the configuration which evolved as a result of NAS 3-10938. The aeroshell is a 60° half angle blunt cone fabricated from aluminum honeycomb and covered with a low density ablator (Avcoat 5026-39) heatshield for reentry protection. A 360° vented conical frustum shaped 2D graphite aerodynamic fence is attached to the rear of the aeroshell with a ball lock tiedown and release system. The purpose of this fence is to prevent the HSRV from becoming stable rearward during reentry. A ballute located in the annulus around the periphery of the vehicle is provided to limit the terminal velocity prior to impact and is deployed by releasing and jettisoning the fence and rear cover.

A circular planar array of heat source units is mounted in cradles on a Cb-1%Zr heat source plate with the heat source units mounted flush to the base plane of the aeroshell. A truss support system utilizing one piece tubular refractory metal (T-111) struts and pin end joints is the only structural tie between the aeroshell and the heat source plate. Total system heat leak is kept below 1 KW<sub>t</sub> with the use of multi-foil insulation in a simplified planar arrangement.

The new capsule configuration includes a covering of graphite for thermal protection. Therefore, the cover plate capsule retention system utilized in NAS 3-10938 which also provided a thermal barrier to protect the fuel capsules from severe aerodynamic heating during reentry was unnecessary and has been eliminated. Retention bars between capsules are utilized for capsule tiedown and the graphite surface of the fuel capsule is exposed.

The separate structural tie plate utilized in NAS 3-10938 between the multi-foil insulation and the heat source plate has been eliminated. The heat source plate has been designed to be capable of reacting internally the radial kick loads developed by the strut geometry.

The BeO heat sink utilized in NAS 3-10938 has been eliminated. The increased mass of the Cb-1%Zr heat source plate is adequate as a heat sink and the problems associated with ensuring adequate thermal contact between the BeO and the heat source plate are avoided.

#### 3.4.1.1 Heat Shield

The Apollo heat shield material (Avcoat 5026-39/HC-G) was selected as the thermal protection system for the HSRV. The thermal effort was oriented towards the definition of heat shield requirements utilizing this material. This definition is normally complicated by the multiplicity of possible reentry conditions. However, the Apollo design experience has shown that heat shield requirements are normally dictated by total integrated heating for the envelope of possible trajectories at the same entry velocity. The only qualification is



that none of the significant parameters (e.g., pressure gradient, shear) exceeds the acceptable limits for the material. For the range of entry conditions defined by NASA for HSRV entry at orbital velocities, none of these parameters is exceeded. Therefore, design trajectories were chosen on the basis of maximum integrated heat load. This section describes the procedures used to define an adequate heat shield design for the HSRV.

#### a. Design Considerations

To define the heat shield thicknesses for the HSRV, it is necessary to evaluate the influence of several factors. The items most significant in the heat shield design include the aerodynamic heating environment, and initial temperature together with the allowable maximum reentry structural temperature. This latter temperature has been defined as 232°C (450°F) from structural considerations.

The selection of the design trajectory is reasonably complex due to the multitude of reentry environments possible. Not only do the reentry velocities and angles vary because of different abort modes, but even for a given set of reentry conditions ( $V_e, \gamma_e$ ) a wide range of environments is possible due to vehicle dynamics. Therefore, it is possible that the heat shield requirement at each location on the aeroshell can be designed by a different trajectory. The Apollo design experience, however, allows a priori selection of the design trajectories on the basis of maximum integrated heat load. Thus, the stagnation and mid-cone points of the aeroshell are designed by an orbital decay entry initially at zero angle of attack, ( $\gamma_e = \alpha_e = 0^\circ$ ), and the shoulder, maximum diameter and base regions are designed by an orbital decay entry which is initially tumbling.

Another factor which influences the heat shield design is the initial reentry temperature. For this study, it was assumed that the initial condition was identical to the structural operational temperature in space. The initial reentry altitude was chosen at 137 KM (450 KFT). The structural operational temperature during space operation is based upon a one-dimensional analysis of the total HSRV heat leak wherein the total heat leak is assumed to be uniformly dissipated over the total radiating area of the aeroshell. Vacuum thermal conductivity properties of Avcoat 5026-39/HC-G were utilized for this heat leak analysis.

During the descent from 137 KM (450 KFT) to 122 KM (400 KFT) the heating is essentially free molecular and the stagnation pressure less than  $10^{-2}$  torr. In this environment vacuum properties are applicable. Thus, the analysis was performed in two parts; first, the ablator/structural thermal response was calculated during the descent to 122 KM (400 KFT) using vacuum properties. Using the temperature gradients at 122 KM (400 KFT) as the initial condition, the thermal response was calculated from 122 KM (400 KFT) to impact using atmospheric properties. It is significant to note that there is a

significant bondline temperature rise during the descent from 137 KM (450 KFT) to 122 KM (400 KFT) especially at the smaller heat shield thicknesses.

A significant tradeoff exists between the operational and reentry temperature since increasing the heat shield thickness increases the operational temperature but decreases the reentry temperature rise. Since the reverse is also true, it therefore becomes necessary to determine the thickness which not only limits the operational temperature to adequate levels but also maintains acceptable reentry temperatures.

#### b. Reference Design

The design of the reference heat shield was based on a priori selection of the design trajectories. Figure 3.4-1 shows the bondline temperature at 122 KM (400 KFT) and maximum temperature during reentry as a function of heat shield thickness for the stagnation and midcone points of the aeroshell on the orbital decay trajectory. It is interesting to note that the bondline temperature at 122 KM (400 KFT) shows a decreasing slope with thickness. The one-dimensional heat leak analysis exhibits the opposite trend. However, during free molecular heating in the descent from 137 KM (450 KFT) to 122 KM (400 KFT) the smaller thicknesses exhibit a significant bondline temperature rise whereas the larger thicknesses exhibit a much smaller rise. Thus, the trend at 122 KM (400 KFT) is reversed. The design thickness for these two locations is selected such that the maximum bondline (structural) temperature does not exceed 232°C (450°F).

Figure 3.4-2 shows the bondline temperature at 122 KM (400 KFT) and maximum temperature during reentry as a function of heat shield thickness for the shoulder, maximum diameter (cylinder) and base regions of the aeroshell. Note that the design trajectory is orbital decay, initially tumbling. The bondline temperature at 122 KM (400 KFT) is shown as decreasing, then increasing with heat shield thickness. Again, the free molecular heating during tumbling descent to 122 KM (450 KFT) results in a significant bondline temperature rise at the smaller thicknesses and a small rise at the larger thicknesses. The combination of this effect with the variation of bondline temperature with thickness during space operation results in the trend illustrated. The design thickness for these three locations is selected such that the maximum bondline (structural) temperature does not exceed 232°C (450°F).

Table 3.4-I summarizes the heat shield thickness, total integrated heating, and design trajectory for these body locations. The data presented does not include a safety factor since the design procedure, which assumes the worst trajectory at each location, is in itself conservative.

Figure 3.4-1

AVCOAT 5026-39/HC-G REQUIREMENTS  
ORBITAL DECAY ENTRY (STAGNATION & MIDCONE POINTS)

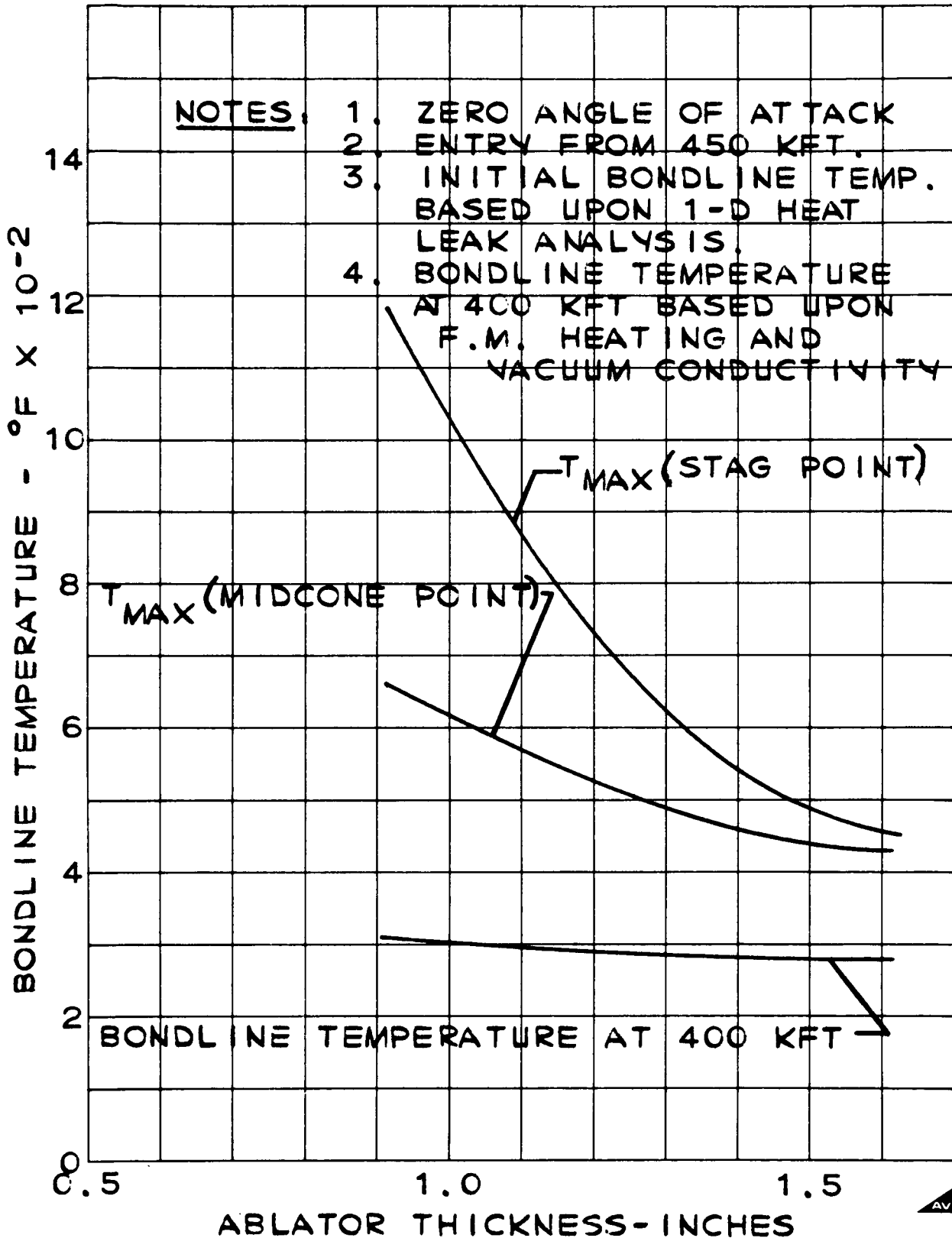


Figure 3.4-2

AVCOAT 5026-39/HC-G REQUIREMENTS

ORBITAL DECAY ENTRY (SHOULDER, BASE, CYLINDER POINTS)

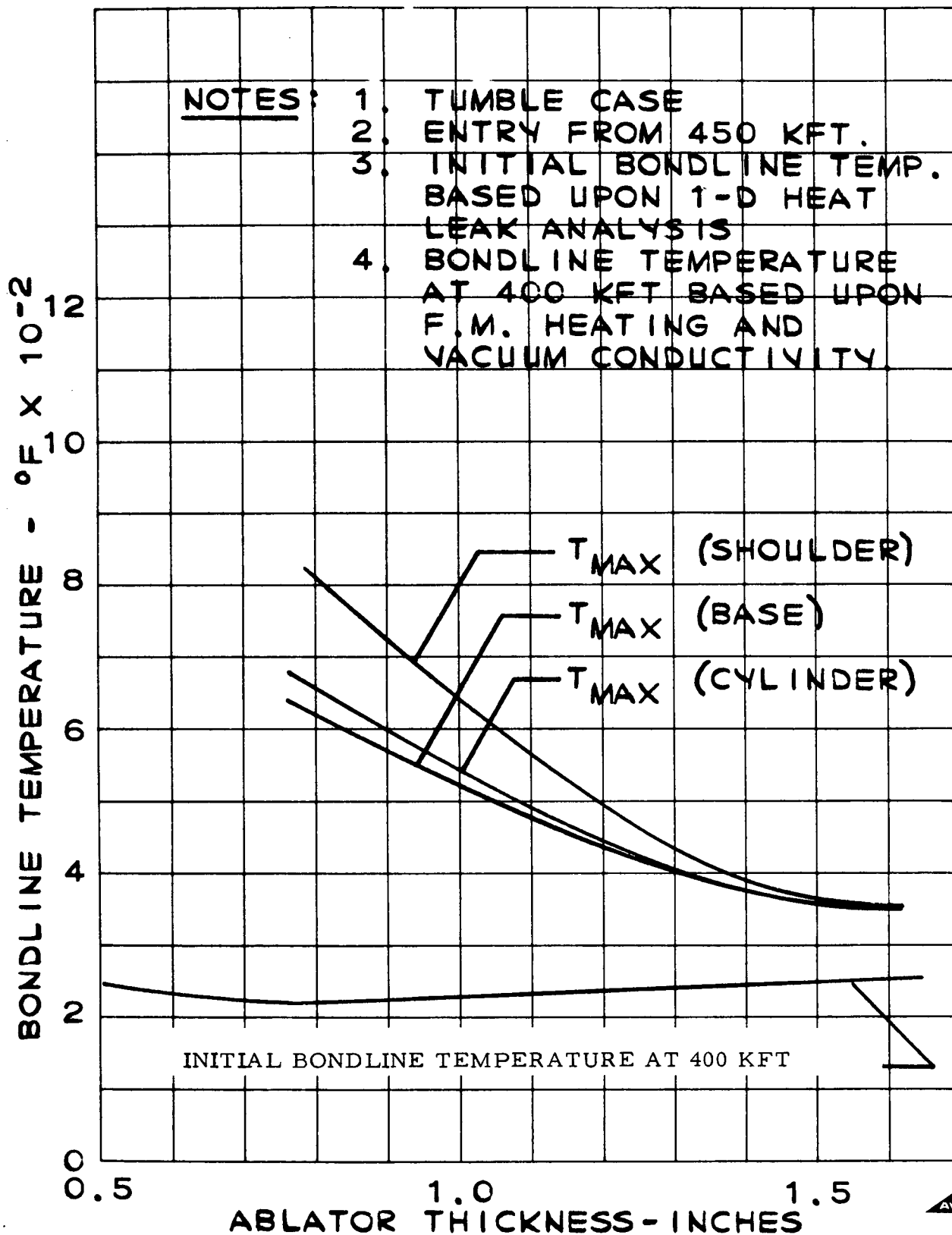
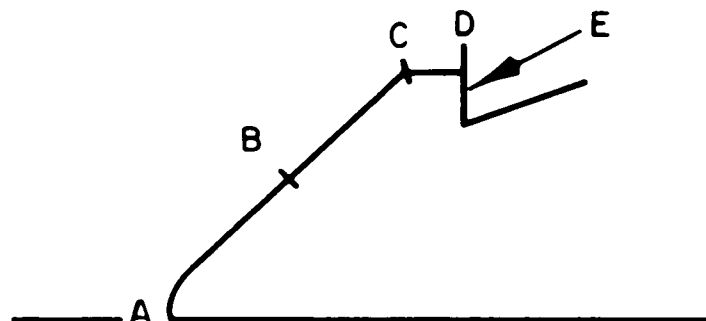


TABLE 3.4-I

## HEAT SHIELD REQUIREMENTS AVCOAT 5026-39/HC-G



LOCATION	HEAT SHIELD THICKNESS		DESIGN TRAJECTORY	INTEGRATED HEATING (JOULES/CM <sup>2</sup> )
	(CM.)	(IN.)		
A	4.03	1.59	ORBITAL DECAY - ZERO ANGLE OF ATTACK	43700
B	3.55	1.40	"	17300
C	3.20	1.26	ORBITAL DECAY - TUMBLING	24260
D	2.97	1.17	"	10030
E	2.89	1.14	"	6970

The aerodynamic fence thickness of 2.21 CM. (0.87 in.) is dictated by dynamic loads considerations. An analysis was performed to determine the thermal response of the 2-D graphite fence during a tumbling orbital decay entry, which represents the worst aerodynamic heat load. A similar analysis was performed for the T-111 HSU hold-down bolts. The results indicate that the temperature levels and gradients through both the fence and bolts are such that they maintain their structural integrity throughout reentry. The transient response of both the fence and HSU hold-down bolts is illustrated in Figure 3.4-3 for this trajectory.

#### 3.4.1.2 Aeroshell Structure

##### a. Structural Load and Temperature Requirements

The critical structural load environments and requirements considered for the aeroshell structure have been defined in Table 3.3-V of Section 3.3.4. In addition to the inertial loads shown in Table 3.3-V, the aeroshell must be capable of resisting the peak reentry aerodynamic pressure loads. For the INT-21 abort trajectory the peak stagnation pressure,  $P_s$ , is 20.86 psi (design pressure =  $1.25 \times 20.86 = 26.2$  psi). The maximum pressure on the aeroshell cone can be expressed as  $P_s (\sin \theta \cos \alpha + \cos \theta \sin \alpha)$ , where  $\theta$  is the cone angle of 60 degrees and  $\alpha$  is the angle of attack. The angle of attack at peak loading for the INT-21 trajectory is 24.7 degrees resulting in a maximum pressure of 20.68 psi (design pressure =  $1.25 \times 20.68 = 25.84$  psi). The aerodynamic pressure loads for the orbit decay reentry are considerably lower than for the INT-21 abort with a peak stagnation pressure of only 3.95 psi limit; hence, the orbit decay reentry is not considered a critical design environment.

In addition to reentry structural loads the aeroshell will experience thermal loading during both long-term operation in orbit and during earth reentry.

The aeroshell, however, is designed to ensure that the peak operational temperature in the aeroshell will not exceed 300°F to prevent degradation of the heat shield, bond, and shell structure. Thermal studies in fact, indicate that the peak operational temperature for earth orbit is only 222°F. The temperature in the strut support ring particularly at the strut attachment, will be higher and the use of a higher temperature material like titanium is required. During the peak load phase at reentry it is assumed that the aeroshell temperature would not exceed 350°F but would be allowed to increase beyond this level from peak loading to impact. The reentry loading profile does experience a sharp drop after peak loads with the reduction of loads being considerably greater than any reduction in strength of the aeroshell material.

# FENCE AND BOLT TEMPERATURE HISTORIES ORBITAL DECAY RETURN-TUMBLING

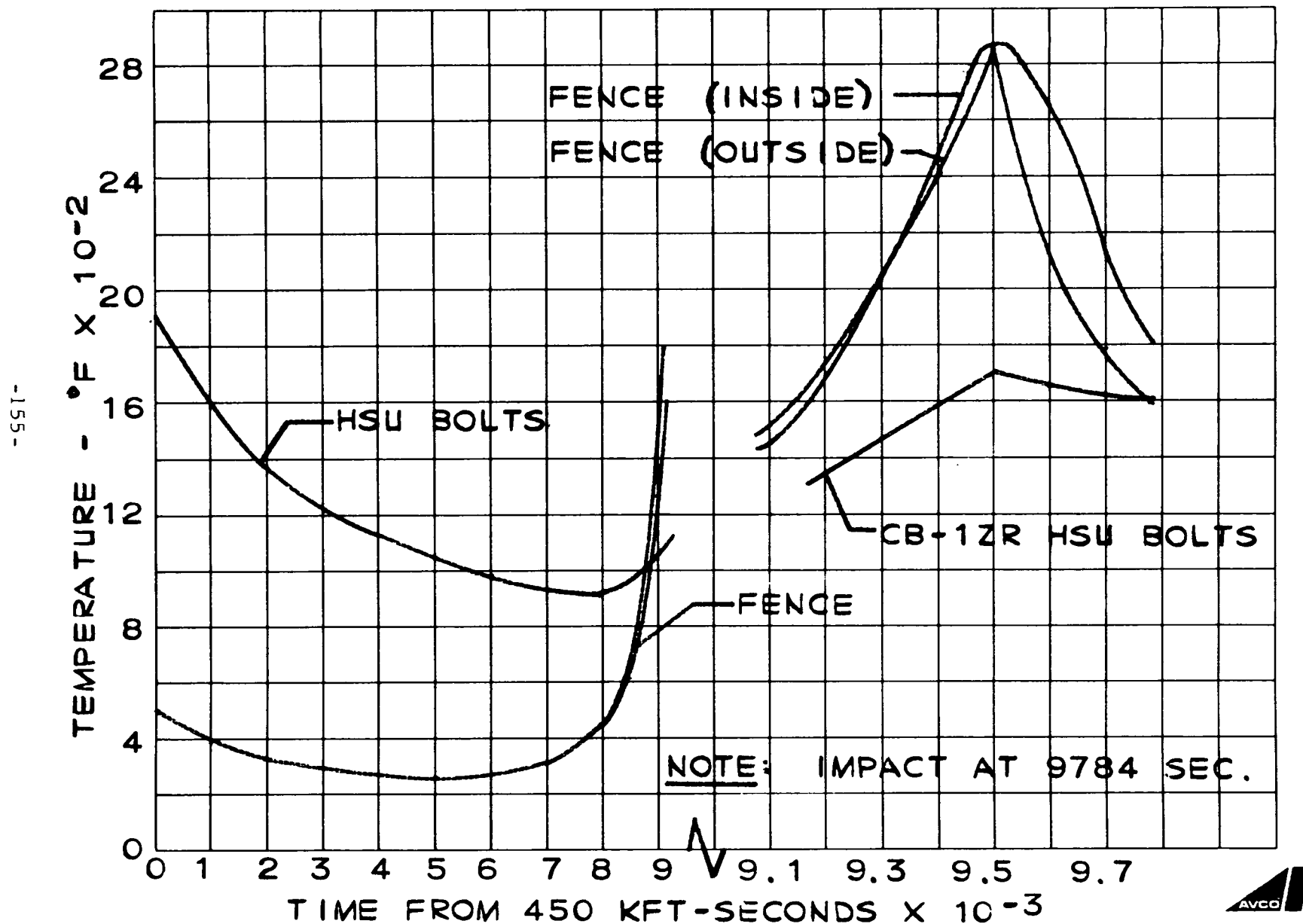


Figure 3.4-3

## b. Aeroshell Structural Design and Performance

The major design modifications in the reference aeroshell design from the previous study include a larger vehicle diameter, an increase in strut support ring diameter, higher loads resulting from increased mass, somewhat more severe reentry conditions, higher heat leaks and local attachment temperatures because of increased strut area to support the increased heat source loads.

Since maximum operational temperatures in the aeroshell will be held below 300°F, aluminum is still considered as the prime aeroshell material with 2024-T81 aluminum alloy specified since it is better than other aluminum alloys in retaining strength capabilities after long-term exposure to elevated temperatures (200°F to 300°F).

The nominal honeycomb facesheet and core thickness requirements were reevaluated for the increased vehicle diameter of 84 inches and the increased aerodynamic design loads. The results of both a symmetrical and asymmetrical membrane stress analysis are represented in Figure 3.4-4 which gives the variation in minimum honeycomb faceshell thickness versus vehicle radius.

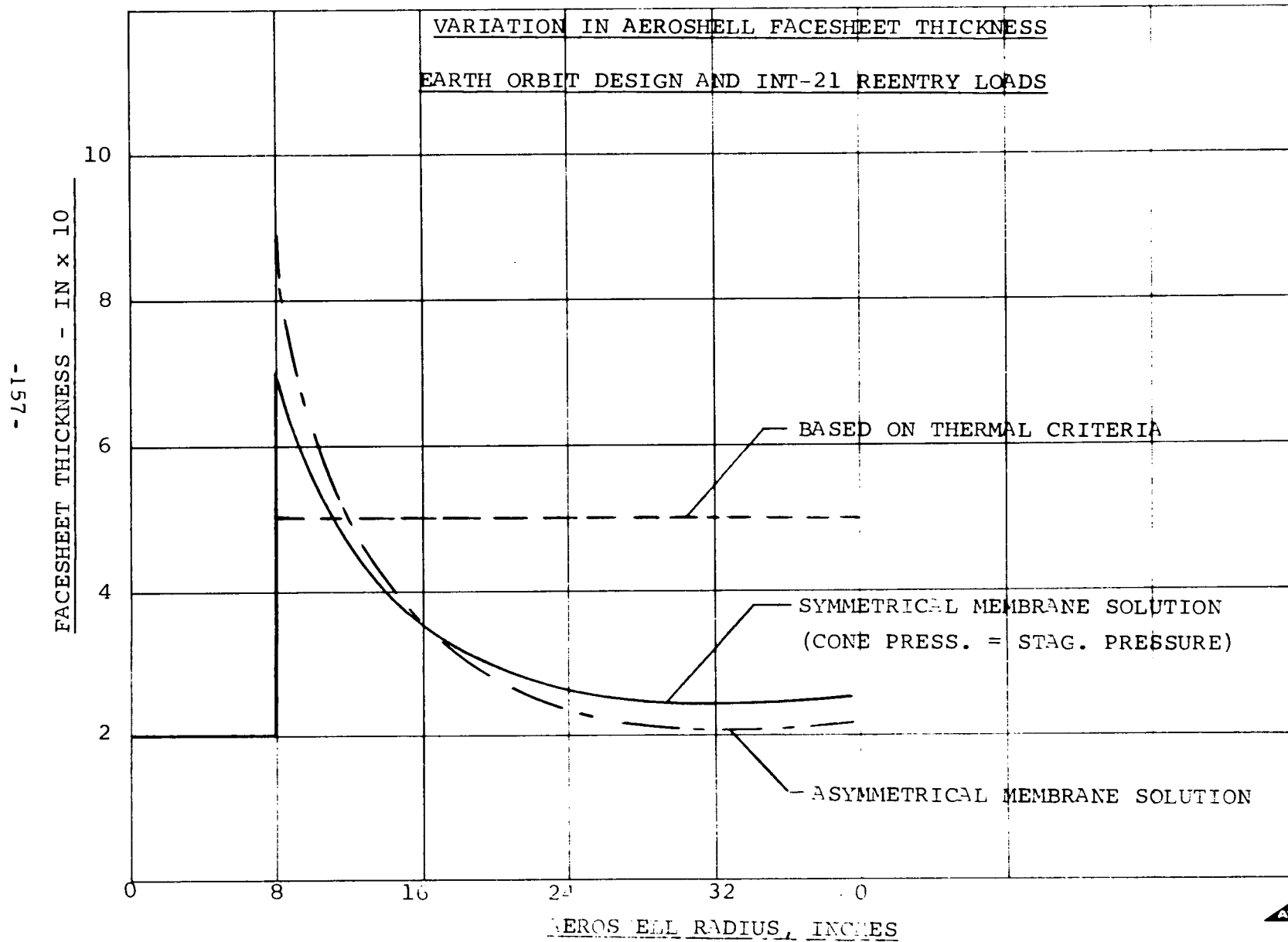
The facesheet thickness was sized on the basis of effective stress.

$\sigma_{\text{eff}} = \sqrt{\sigma_{\theta}^2 - \sigma_{\theta}\sigma_{\psi} + \sigma_{\psi}^2}$  where  $\sigma_{\theta}$  is circumferential stress and  $\sigma_{\psi}$  is meridional stress. As indicated by these curves, the major area of the honeycomb aeroshell, from the radial station of 24 inches out to the base of the aeroshell requires only a .026 inch face sheet thickness. From 24 inches down to the strut support ring at a radius of 8 inches, the face sheet thickness must be increased to .092 inches because total pressure load is increasing and the circumferential length of the shell over which the load is distributed is decreasing. The total aeroshell pressure load outboard of this ring is transmitted down the aeroshell by the face sheets in tension to the ring where it is reacted by the HSU inertia load. In order to carry the higher loads in this region, the facesheets could (1) be tapered to insure stress distribution or (2) reinforced in a step-like fashion by additional back-up sheets. Increasing the nominal face sheet of the entire aeroshell to take care of local stress concentrations is not desirable because of the additional weight involved. The face sheet thickness required for the spherical nose section is less than the established minimum gage of .02 inches.

A thermal analysis, however, indicated that .026 inch face sheets resulted in excessive operational aeroshell temperatures because of insufficient thermal conduction away from the strut support ring. The nominal face sheet thickness was consequently increased from .026 inches to .05 inches to improve thermal conduction in the aeroshell. The use of .05 inch face sheets resulted in a maximum aeroshell temperature of 222°F.



FIGURE 3.4.4



From a structural standpoint, the .05 inch face sheets are conservative except again in the region approaching the support ring, where increasing membrane stresses will govern. At the support ring, additional local bending effects will necessitate further shell "beef-up". This added requirement is treated in the following discussion of ring shell joint loads.

The thermal analysis results also showed that the average operational temperature in the strut support ring for earth orbit is approximately 418°F and that the maximum temperature where the struts are attached is 500°F. Since aluminum would lose most of its strength for prolonged exposure at these temperatures, a titanium (Ti-6Al-4V) ring is used which will withstand these temperatures for long-term exposure without a major loss of strength. The use of titanium for the ring is also beneficial for thermal reasons, the relatively poor conductivity of titanium helps to insure tolerable local temperature levels in the aluminum aeroshell.

The ring design is a channel section, 2.5 inch in height with 1.7 inch flanges and a nominal thickness of .2 inches. The system of eight struts attach rigidly to this ring at four symmetrical locations. This ring must be rigid enough to distribute the concentrated loads from the struts to the aeroshell. Because of the strut angle of 37.5 degrees, the ring must support both radial or inplane kick loads and vertical loads. For the INT-21 peak loads, the vertical component and radial component (kick load) are 27,872 lbs. and 18,162 lbs. respectively. The ring was analyzed for the combined in-plane and out-of-plane bending due to applied strut loading for the worst INT-21 reentry loads.

The maximum stress in the ring was found to be 90,346 psi which if compared to a tensile yield strength of 115,200 psi for Ti-6Al-4V at 100°F results in a safety factor of 1.275. The ring analysis is conservative since the shell which provides some restraint to the ring was neglected and consideration of the ring/shell interaction would have reduced the ring stresses somewhat.

A joint analysis of the titanium ring and the aluminum aeroshell was performed to evaluate the interaction forces and determine if local shell thicknesses are adequate to resist the local bending effects. The results of the joint analysis indicated an interaction moment of 484 in-lbs/in and a shear of 1,588 lbs/in. which produces a maximum ring stress of 45,561 psi. At the ring attachment, the aeroshell is solid aluminum, .56 inch thick, and the combined local stress at the joint based on the above interaction loads is 22,272 psi. The allowable for 2024-T81 aluminum at 350°F assuming no operational temperature effects for the INT-21 launch abort case is 56,000 psi. The bending moment at the junction, however, is not the maximum since the shear contribution to moment will attain its maximum value at a meridional distance  $x = \pi/4 \hat{r} = 1.83$  inches away from the joint, which is approximately where the transition between the solid section and honeycomb occurs. In order to resist combined membrane and bending stresses at this point, a face sheet thickness of .125 inches is

required. At the radial station of 12.0 inches, which represents a meridional distance of 4.62 inches from the joint, bending stresses are determined to be small relative to membrane stress and the nominal face sheet thickness of .05 inches is found to be adequate.

### c. Fence Design and Performance

The conical fence design shown in Figure 1.0-1 is fabricated from a 2D laminated graphite fabric composite. The total height of the fence is 14.70 inches or  $.373 R_B$  and the slant length is 16.2 inches. The minimum mean radius at the aeroshell is 34.5 inches and the maximum mean radius at the base is 41.5 inches. The hole arrangement at the base consists of 24 equally spaced rectangular holes approximately 6.3 inches high and 8.0 inches wide. The ligament width between holes is 1.5 inches.

The maximum pressure loads imposed on the fence occur at the instant of peak lateral loading for the INT-21 reentry. The loads as well as distribution is shown in Figure 3.4-5 for this case. It is seen that the pressure varies both axially and circumferentially. In the axial direction, there is a step increase in pressure where the flow reattaches on the fence. At the windward meridian, the surface pressure increases from 630 psf to 1020 psf limit. The pressure also decreases circumferentially going to zero at  $\pm 90^\circ$  from the windward meridian and beyond because of the shadowing effects of the HSRV aeroshell. The flow reattachment point also varies circumferentially going to zero at  $\pm 90^\circ$ .

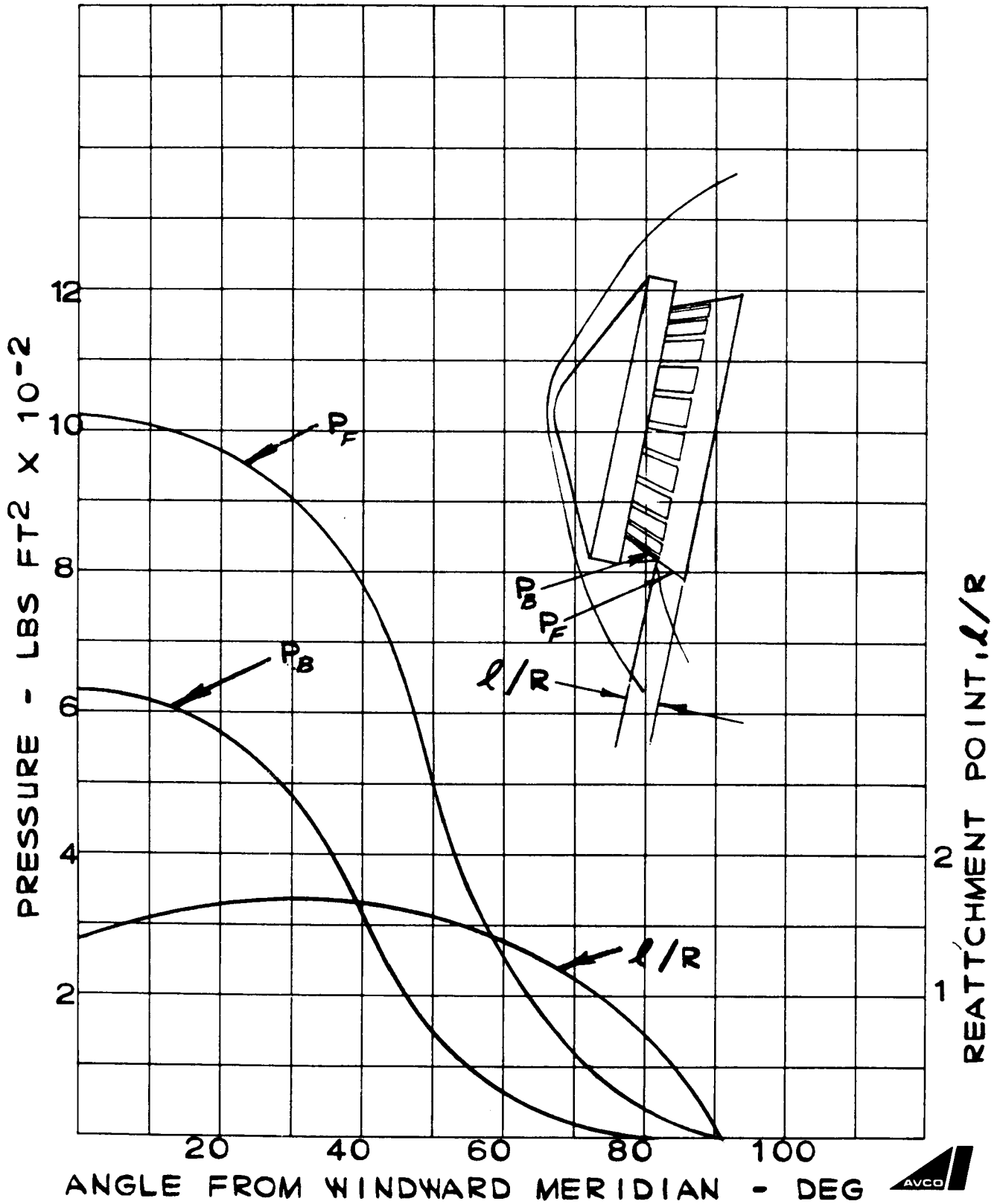
In the fence analysis, it was necessary to make simplifying assumptions about the loading; (1) the fence pressure varies circumferentially as  $P_W \cos \theta$  up to a  $\theta = \pm 90$  degrees and is zero beyond that and (2) the reattachment point is constant with circumference being taken as  $r/R_B = .17$ , its maximum value. To evaluate circumferential bending in the solid section of the fence that this type of loading will produce, the section which is 9.00 inches long, is treated as a circular ring where lateral motion is restrained by tangential shear developed by the ligaments.

The ligaments (or support legs) are assumed to offer no resistance to circumferential bending or resulting radial deflections. The total radial load for the full solid length of fence at the windward meridian is 73.36 lbs./in. Based on this loading and the cosine distribution described, the maximum stress computed in the fence is 1867 psi, which is well below the 2-D ultimate strength of 8000 psi. The maximum radial deflection for the fence is .26 inches.

The maximum axial ligament stress resulting from the total fence moment load of 22,000 in-lbs. and an axial load of 2775 lbs. is only 146 psi and hence causes no concern.

FIGURE 3.4-5

# FENCE PRESSURES INT 21 PEAK N/W



In addition to aerodynamic loads, the 2-D fence will experience thermal gradients which develop additional stress in the fence. Typical radial temperature profiles resulting in the 2-D fence during the orbit decay-tumble reentry mode are shown in Figure 3.4-6. Two temperature profiles are shown, one at maximum load and the second for the maximum surface temperature differential. The resulting thermal stresses in the fence produced by the radial temperature profile at maximum reentry loading is shown in Figure 3.4-7, the peak thermal stress of 390 psi occurring at the free or upper edge in the circumferential direction. The thermal stresses for the case of maximum temperature differential ( $\Delta T = 600^{\circ}\text{F}$ ) are shown in Figure 3.4-8. The maximum stress is 1100 psi and occurs again in the circumferential direction at the free edge where bending effects are present. It is apparent that thermal stresses in the 2-D material are not severe even for large temperature differences. The reasons for this are that the 2-D material possesses a very low coefficient of thermal expansion ( $.61 \times 10^{-6}$  in/in/ $^{\circ}\text{F}$ ) and a relatively low modulus ( $2.7 \times 10^6$ ). In view of the large margin of safety on pressure load stresses, it appears that the additional presence of thermal stresses will not jeopardize the reference design.

### 3.4.1.3 Thermal Control

The adequacy of the HSRV thermal design has been demonstrated by investigation of the thermal performance during normal operation in orbit. The maintenance of acceptable temperatures and heat losses within the boundaries of the aeroshell is quite complex and requires extensive thermal network analysis in order to derive an optimized design concept. The analytical method, assumptions and results are summarized in the following section.

#### a. Analytical Model

(1) Environmental Considerations -- Two environmental cases have been considered, i.e., normal operation in orbit and SPF test conditions. For normal operation, Figure 3.4-9 (100 N.M. circular polar orbit, 90 degree inclination, sun in the orbit plane and permanent heat shield orientation towards Earth), the following incident heat loads have been established (Reference 2.1-1):

Solar Radiation:  $Q_s = 0$

Earth Thermal:  $Q_t = 63 \text{ Btu/hr} - \text{ft}^2$

Earth Albedo:  $Q_a = 53 \text{ Btu/hr} - \text{ft}^2$  (Orbital Average)

For the Space Power Facility (SPF) test, the environment is defined as a cold wall radiatively coupled to the ablator surface with a form factor  $F = 1.0$  and emittances  $\epsilon = 0.9$  and  $1.0$  for the cold wall surface and ablator surface respectively, resulting in an effective emittance  $\epsilon = 1.0$  since the ablator surface is small in comparison to the test chamber surface.

FIGURE 3.4.6

TEMPERATURE PROFILES IN 2-D FENCE

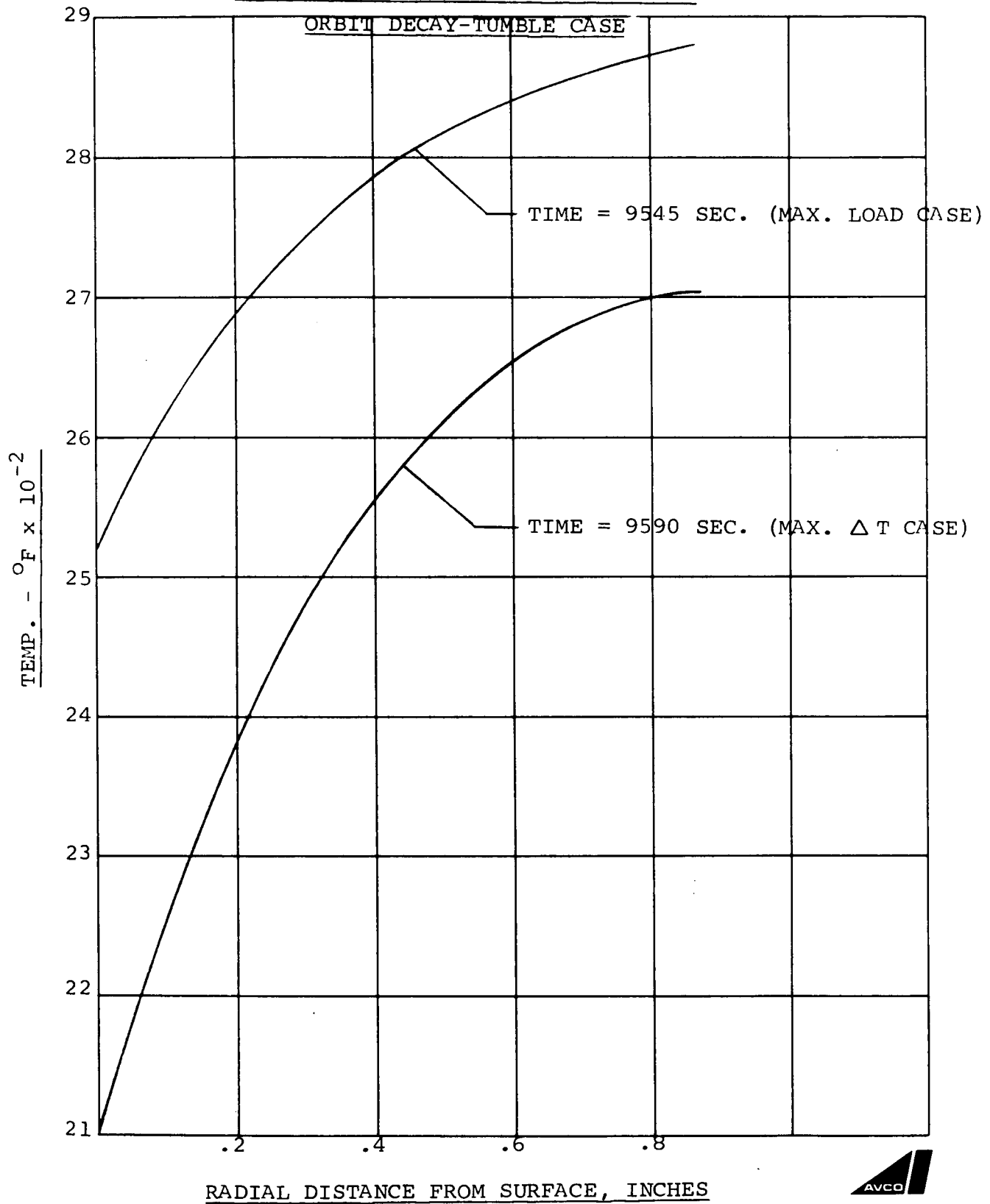


FIGURE 3.4.7

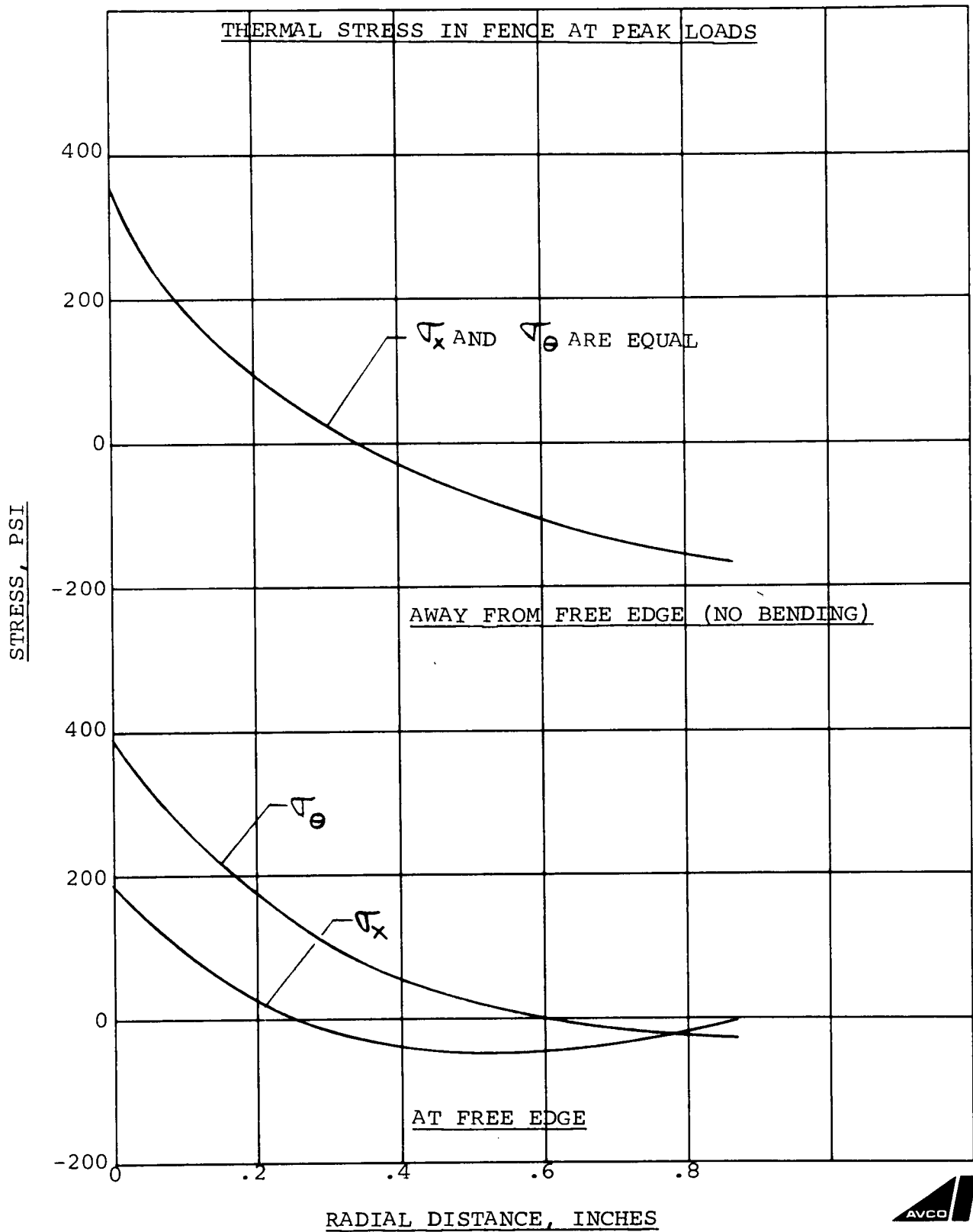
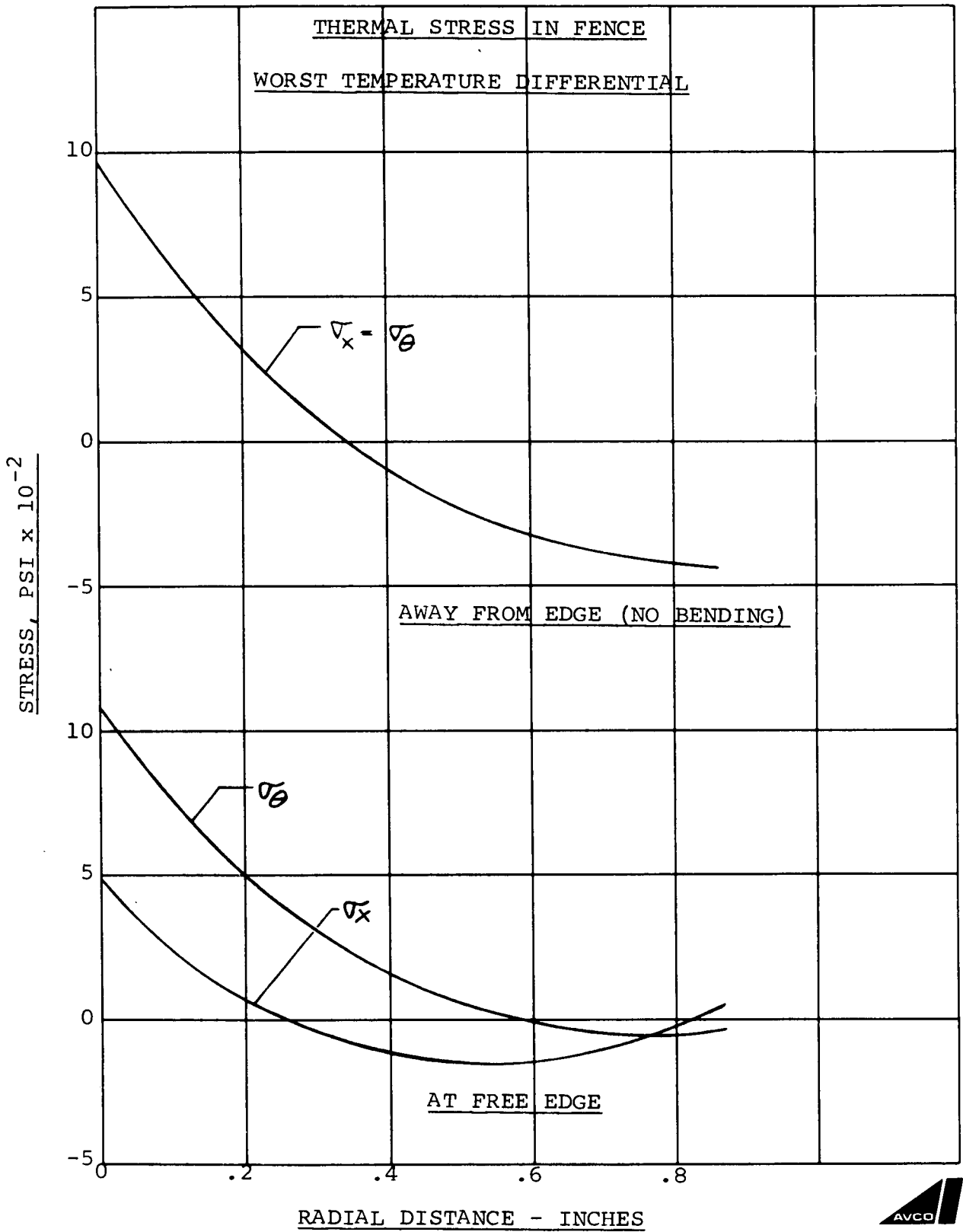
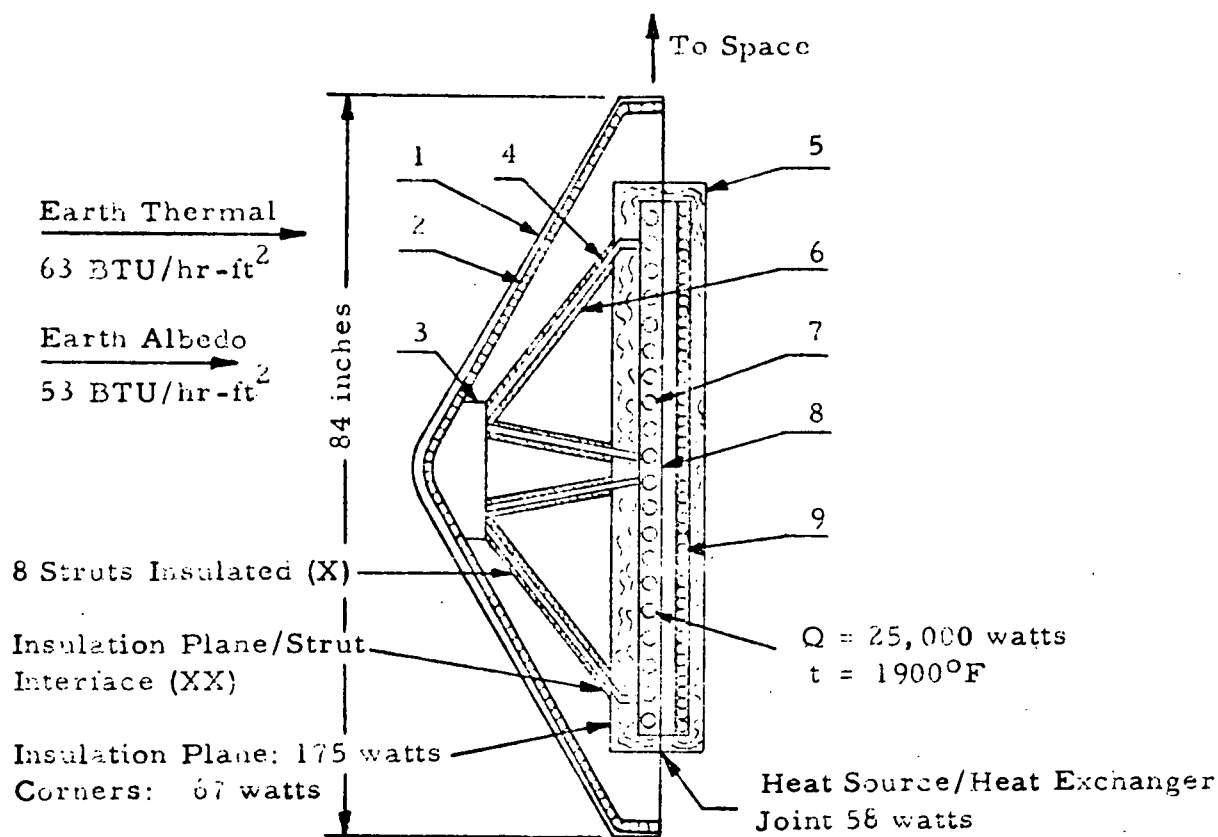


FIGURE 3.4.8







(x)  $Q = 256$  Watts, Result of this study  
 (xx)  $Q = 101$  Watts, Result of this study

Component	Material	Dimensions	Thermal Conductivity (Btu/hr-ft-°F)
1. Heat Shield	5026-39-HC-G	Thickness: 1.4 inches	0.048 (Vacuum
2. Aeroshell Structure	Al Honeycomb	Facesheet Thickness: 0.05-0.092 in. Core Height: 0.51 inch	110.
3. Attachment Ring	Ti	Thickness: 0.25"	10.
4. Strut (8 Total)	T-111	Length: 20.0 inches Cross Section: 0.48 inch <sup>2</sup>	38.
5. Insulation Assembly	Multifoil	Thickness: 1.5 inch	0.002
6. Strut Insulation	Multifoil	Thickness: 1.0 inch	0.002
7. Fuel Capsules	PuO <sub>2</sub> , T-111, Pt		
8. Support Structure	Cb1Zr		38.
9. Heat Exchanger	Cb1Zr		38.

Figure 3.4-9  
 INT 21 Reference Design, Normal Operation in Orbit

Internally, the temperature at the heat source/strut end is maintained at 1900°F (1038°C). Insulation plane thermal losses are assumed to be 30 Btu/hr-ft<sup>2</sup>, corresponding to a thermal conductivity  $k \approx 0.002$  Btu/hr - ft-°F of the insulating material. To account for insulation plane/strut interface edge losses, 40% of the strut thermal losses  $Q_{STRUT}$  are added to the insulation plane losses in addition to fixed losses of 67 watts through insulation corners and 58 watts through the HS-HSHX joint. This approach was used after conversations with Thermo Electron Corporation (TECO).

Total heat losses are then summarized as follows:

<u>Component</u>	<u>Watts</u>	<u>Remarks</u>
Insulation plane	175	Fixed loss, corresponding to 30 Btu/hr - ft <sup>2</sup> ,
Insulation corners	67	Fixed loss, Ref. 2.1-1, Fig. 3-90
HS-HSHX Joint	58	Fixed loss, Ref. 2.1-1, Page 191 corrected for diameter.
Insulation plane/strut	101*	Variable, 40% of strut loss.
Strut	256*	Variable, function of strut design, aeroshell end temperature and strut insulation performance.

For optimum Brayton system performance, it is desirable that the sum of the above heat losses do not exceed 1000 watts.

\*Actual values computed for Earth Orbital HSRV - Normal operation in orbit case.

(2) Aeroshell/Ablator Bondline Temperature Restrictions -- The hot-spot temperature that exists at the aeroshell end of the truss members is a major concern. Considerations for limiting temperatures include degradation in mechanical properties of both the ablator adhesive and substructure material and outgassing of the ablator itself under the long-time exposure to elevated temperatures and the hard vacuum of space. Although, in general, it is felt that 300°F is a feasible design temperature limitation for the candidate low-temperature ablator (Avcoat 5026-39/HC-G), ablator adhesives, and substructure construction, it would be prudent to design for substantially lower temperatures (200°F) if the truss design would permit it.

(3) Ablator and Coating Design Requirements -- Ablator and coating properties have been maintained constant and are as follows:

Material	k Btu/hr. ft -°F	$\alpha$	$\epsilon$	$\alpha/\epsilon$	Remarks
Ablator 5026-39 HC/G	0.048	---	---	---	in vacuum
Coating, zinc oxide/ potassium silicate	---	0.3	0.9	0.333	(Ref. 2.1-1)

The specified white coating has been selected after initial tradeoff between an uncoated ablator, Teflon/silver and zinc oxide/potassium silicate with properties as follows:

	$\alpha$	$\epsilon$	$\alpha/\epsilon$
Ablator	0.6	0.9	0.666
White	0.3	0.9	0.333
Teflon/silver	0.1	0.7	0.143

For the uncoated ablator, the absorptance  $\alpha$  is undesirably high. Tradeoff results indicated that no benefit is expected from a change to the much more sophisticated Teflon/silver coating system since both  $\alpha$  as well as  $\epsilon$  are reduced if compared with the white coating.

(4) Aeroshell Design Requirements -- The aeroshell is an aluminum honeycomb structure with minimum face sheet thickness dictated by structural requirements. Face sheet thicknesses were then increased as required to promote heat conduction in the radial direction, in particular, at the interface with the strut attachment ring, with the result of better heat distribution over the total aeroshell area. The attachment ring, made of titanium, will further tend to reduce truss heat losses since the thermal conductivity of titanium is smaller by an order of magnitude if compared with aluminum.

(5) Strut Design Requirements -- The dimensions of the eight hollow T-111 struts are dictated by thermo/structural considerations with the specific thermal control requirement that the ratio of cross section to length is a minimum such that conductive losses are largely reduced. The struts are insulated with a one-inch thick layer of high-performance multifoil insulation. In case of the Earth orbital reentry vehicle, the effective strut length is 20 inches and the cross section 0.48 in<sup>2</sup>.

(6) Thermal Analysis -- The temperature of the system in space is determined by the balance between entering and leaving thermal energy. In the case of the HSRV aeroshell orbiting around the Earth, the following energy sources and sinks have to be taken into consideration:

- External Energy: Earth thermal radiation and earth-reflected solar energy (albedo)
- Internal Energy: Heat leakage from the radioisotope heat source through the HSRV structure (strut, strut insulation, insulation plane and corners, heat-source/heat exchanger joint).
- Dissipated Energy: Heat radiated away from the total area of the aeroshell.

As noted earlier, the following study is based on a 100 nm, circular polar orbit with the sun vector in the orbit plane and a permanently Earth-oriented aeroshell which receives maximum albedo radiation when the IRV passes the subsolar point (worst case assumption). In this case, the external energy level is determined by the magnitude of impinging Earth thermal radiation and Earth albedo only.

The thermal network for the reference design (Figure 3.4-9) considers a quarter HSRV section divided into 60 nodes. Internally, heat is conducted through the struts and insulation subsystem and radiated in a complex mode between surfaces acting as either energy sources or sinks. The temperature at the heat source/strut end is maintained at 1900°F (1038°C). Internal radiation ( $\epsilon = 0.9$ ) is considered between the insulation plane and aeroshell, strut insulation and insulation plane as well as strut insulation and aeroshell. Individual form factors have been considered for each radiative coupling.

(7) Insulation Subsystem -- A major design objective was to limit the total heat loss through the HSRV aeroshell to 1000 watts or less, during normal operating conditions. Design features used to minimize the heat loss, besides strut thermal considerations (minimum ratio of cross section to length), were the inclusion of multifoil insulation around the heat source and struts. During the course of this study, a variety of insulation materials ( $k = 0.002$  to  $0.018$  Btu/hr-ft-°F) and thicknesses (0.5 to 1.5 inch) have been considered; the maximum thickness dictated by the availability of clearance between adjacent structures. For the HSRV design, the following insulation system has been selected.

- Insulation plane: 1.5 inch thick multifoil insulation,  $k = 0.002$  Btu/hr-ft-°F, heat loss 30. Btu/hr-ft<sup>2</sup>, insulation corner and HS-HSHX-joint losses as shown in Figure 3.4-9.
- Struts: One inch thick multifoil insulation,  $k = 0.002$  Btu/hr-ft-°F.

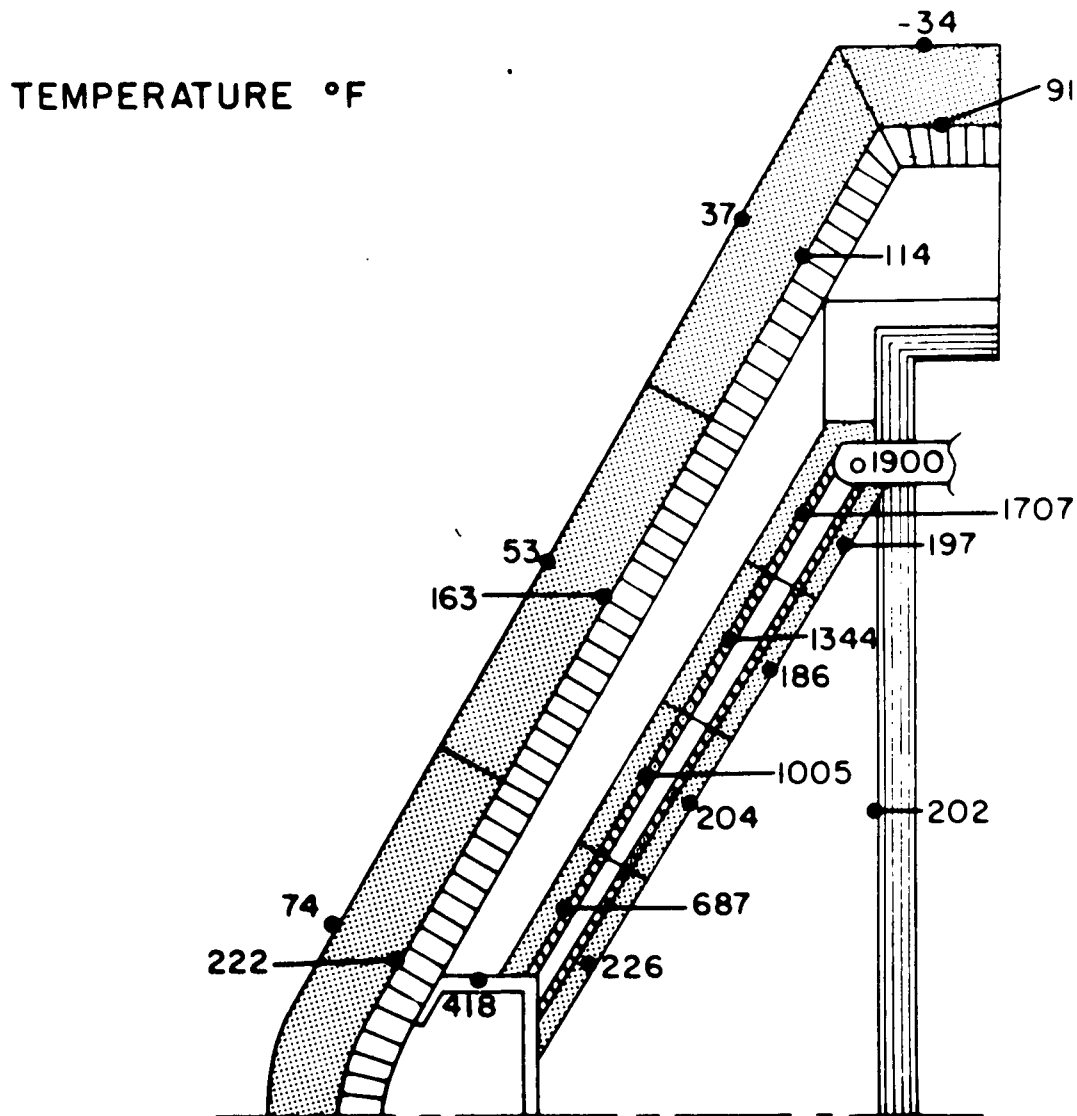
(8) Results -- Steady-state temperature distributions and heat-losses are shown in Figures 3.4-10 for the INT-21 and 3.4-11 for the SPF test case. Aeroshell hot spot temperatures below 300°F can be expected which would be the upper limit in accordance with section 3.4.1.3 (a).

Figure 3.4-10

# HSRV STEADY-STATE TEMPERATURE DISTRIBUTION

## NORMAL OPERATION IN EARTH ORBIT

(INT-21)



**TOTAL HEAT LEAK - 657 WATTS**

HEAT LOSS SUMMARY		Watts
Insulation Plane		175
Insulation Corners		67
HS-HSHX Joint		58
Insulation Plane/Strut		
Interface		101
Struts		256
Total:		657

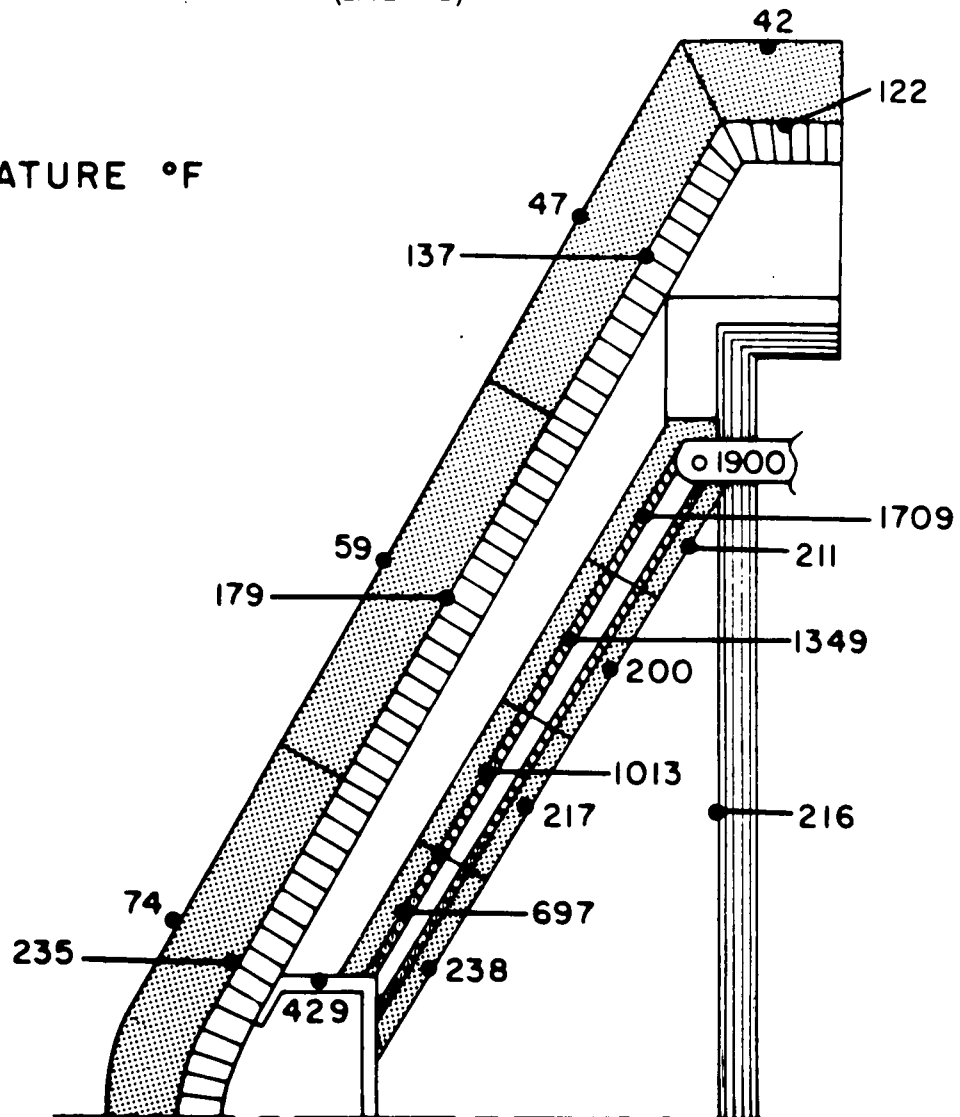
Note: All temperatures in °F

Figure 3.4-11

# HSRV STEADY-STATE TEMPERATURE DISTRIBUTION SPF TEST, COLDWALL @ 0°F

(INT-21)

TEMPERATURE °F



## TOTAL HEAT LEAK - 654 WATTS

### HEAT LOSSES

	Watts
Insulation Plane	175
Insulation Corners	67
HS-HSHX Joint	58
Insulation Plane/Strut	
Interface	101
Struts	<u>254</u>

Total: 655

Note: All temperatures in °F.

Temperatures at the aeroshell end of the struts are acceptable for the titanium attachment ring. In general, all temperatures are well within limits. The difference in temperatures at the ring section of the ablator and aeroshell is caused by different assumptions in the thermal model, i.e., radiation to space in the INT-21 case and exposure to the cold wall environment in case of the SPF test.

Study results are summarized as follows:

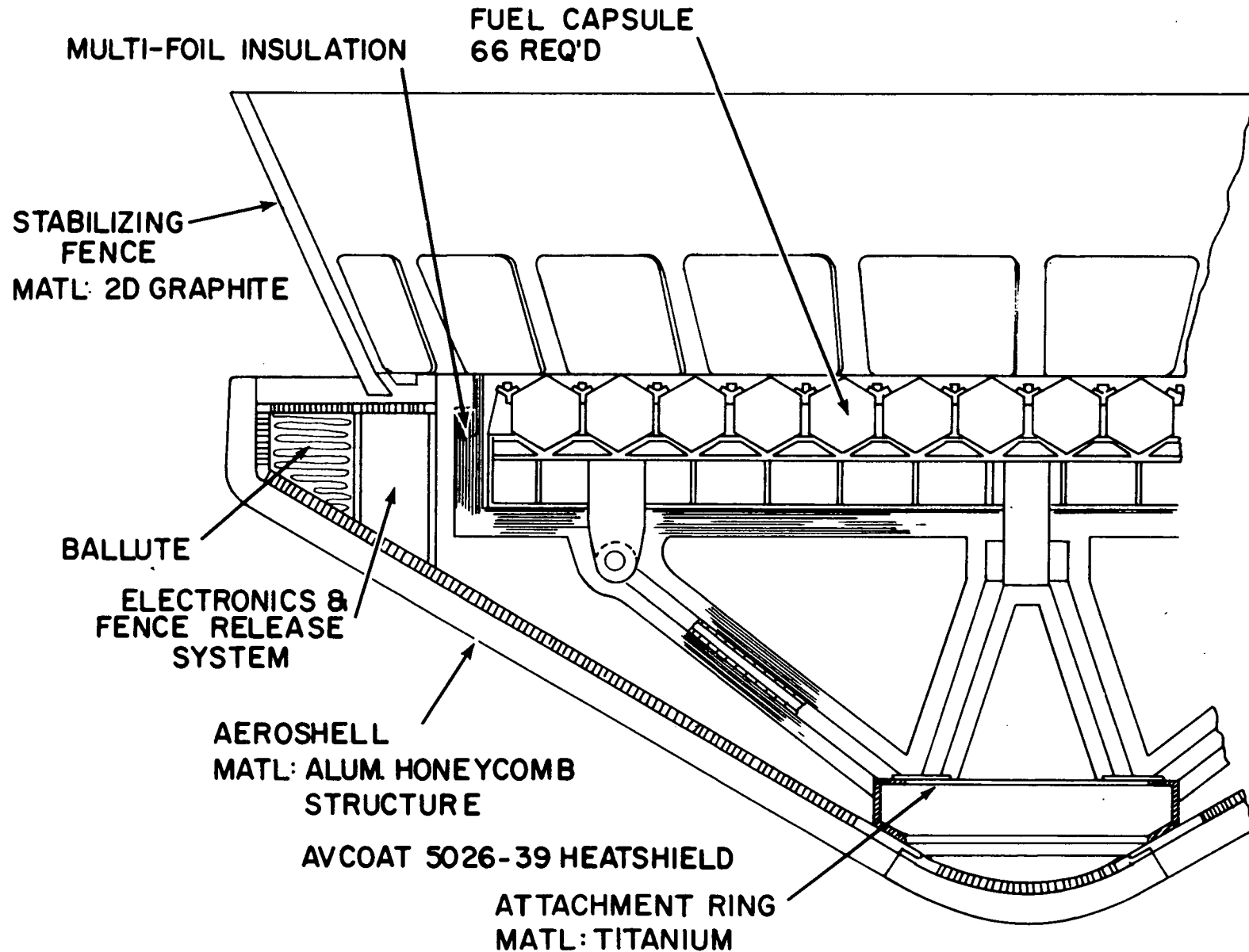
- All temperatures and heat losses are within acceptable limits.
- The aluminum aeroshell tends to distribute internal heat loads quite well and thus to reduce hot-spot temperatures to an acceptable level.
- The titanium attachment ring contributes significantly towards aeroshell hot-spot reduction.
- The selected strut design is thermally acceptable.
- The theoretical insulation system performance appears to be good. Since this is a critical area and affected by the interaction of many parameters, careful thermal design supported by testing is mandatory to insure adequate performance concurrent with predicted results.

The design objective is to modify the reference concept from NAS 3-10938 to accommodate a revised fuel capsule design and to survive the increased earth orbital injection loading of a new booster (INT-21). The existing design concept of a  $60^\circ$  half angle blunt cone aeroshell with a circular planar array of heat source units mounted on a heat source plate with a truss support system would be maintained with only detail changes allowed as required. Minimum weight and envelope would be design considerations with a maximum limit on the vehicle base diameter of 92.00 inches. Total system heat leak is limited to 1 KW<sub>t</sub> with a limitation of 300°F on the aeroshell bond line to prevent long term bond degradation.

#### 3.4.1.4 HSRV Design

The reference 25 KW<sub>t</sub> earth orbital H. S. R. V. configuration as shown in Figure 3.4-12 is a  $60^\circ$  half angle blunt cone with an outside base diameter of 84.00 inches. With a nose radius equal to 25% of the base radius and a cylinder length and fence height limited to 15% and 35% of the base radius respectively, due to subsonic stability considerations, this results in a total vehicle length of 43.62 inches.

## HSRV - EARTH ORBITAL (INT-21)



-172-

Figure 3.4-12



The basic structure of the aeroshell consists of aluminum honeycomb sandwich with 0.050 inch thick face sheets and a 0.460 inch thick core. Local thickening of the face sheets and/or filling of the core cells is provided at regions where support is required to adequately handle the loads. An example of this is in the region of the 15.50 diameter titanium truss attachment ring.

The reference heatshield material is the Apollo thermal protection system (Avcoat 5026-39) in either the gunned or molded configuration. The gunned version used on the nose and cone section of the aeroshell consists of an epoxy resin gunned into a fiberglass honeycomb matrix. The honeycomb is attached to the substructure with HT 424 tape to ensure an adequate bond, and once this has been determined, the resin is gunned into the cores. Fiberglass edge members are required at joints and interfaces to eliminate the existence of open cells. The molded version would be used in the cylinder and base region of the aeroshell to reduce interface difficulties introduced in the transition zones from cone to cylinder and cylinder to base. Test data indicates that the thermal performance of the gunned and molded Avcoat 5026-39 is practically identical and, therefore, similar thicknesses would be adequate.

To facilitate assembly of the aeroshell with the heat source, a removable nose cap is utilized. The nose cap is bolted around its periphery by a series of structural bolts protected by removable ablator plugs. A flexible RTV gasket is used to provide a seal that will allow thermal expansion.

The fence is fabricated from 0.87 inch thick 2-D graphite. It has 24 venting holes equally spaced around its periphery at the base. The fence is attached to the rear door of the aeroshell with an insulated clamping system to reduce the heat input from the fence to the aeroshell. Eight gas generator operated redundant ball locks hold the cover/fence combination over the ballute cavity. When triggered by a baroswitch at the desired altitude the ball locks are used to jettison the rear door and the fence thus allowing deployment of the ballute.

A 56.50" diameter heat source plate is required to support the 66 heat source units arranged in a planar array with the top of the capsules located flush to the base plane of the aeroshell. The heat source plate is a built-up welded Cb-1%Zr structure consisting of two face sheets spaced 2.75 inches apart with internal stiffening webs and with the auxiliary coolant heat exchanger (ACHX) supply and return headers forming the periphery and serving as the main structural members. Individual ACHX cooling channels are located in the triangular passages formed by adjacent capsule cradles and are connected to the supply header by holes in the top plate and to the return header by holes properly sized to balance the flow between channels based on heat load. Four attachment fittings located 90° apart hang below the heat source plate and penetrate through the 1.50 inch thickness of multifoil insulation. These fittings form the pin end interface with the truss support system.

The truss support system utilizes eight refractory metal (T-111) struts each with a cross sectional area of 0.48 inch<sup>2</sup> and a length of 19.900 inch at an angle of 37° 30' measured with respect to the plane of the base of the aeroshell. The truss support system is the only structural tie between the aeroshell and the heat source plate and has been sized to react all inertia loading conditions. Strut geometry was selected based on a trade off between maximum length and corresponding required cross sectional area in order to reduce the heat leak. Heat leak was further reduced by applying a 1.00 inch thickness of multifoil insulation to all strut surfaces.

Final layout drawings of the earth orbital (INT-21) HSRV are presented in figures 3.4-13, -14, and -15.

A summary of the weights of the reference 25 KW<sub>t</sub> earth orbital H. S. R. V. configuration is presented in Table 3.4-II. Included are the major axis inertias and the c. g. location.

The suggested assembly procedure for the HSRV is as follows.

Pack the ballute into the designated annular area around the periphery of the aeroshell and set the preassembled fence/rear cover combination onto the rear of the vehicle with the aeroshell mounted ball locks protruding into the ball-lock receptacles mounted on the rear cover. Utilizing the ball-lock access doors, manually cock the ball locks and preload the system by going through a torquing sequence of the ball-lock adjustment nuts. Install the ball-lock access door covers.

Place the heat source plate on an assembly table with the heat source unit cradles against the table and the four strut fittings pointed upward. Install the .050 inch thick Cb-1%Zr inner insulation face to the heat source plate with the .060 inch thick spacers and the #6 screws. Layup the required number (estimated at 60) of .0005 inch thick molybdenum insulation foils on this inner insulation face alternating between the planar and cylindrical sections so that the circumferential interface between sections is alternate overlapping layers. Install the .050 inch thick titanium outer insulation face over the fittings and temporarily hold it in position with radial clamps to maintain its position relative to the inner insulation face and keep it from crushing the insulation foils. Install the strut system to the heat source plate fittings with four T-111 pins. Layup the required number (estimated at 60) of .0005 inch thick molybdenum insulation foils to the eight 1.00 inch diameter tubular struts including the fittings and pins at the heat source plate end.

Assemble the heat source plate/strut combination to the aeroshell by lowering it into the aeroshell until the feet at the base of the struts interface with the 15.50 inch diameter titanium mounting ring in the aeroshell. Taking advantage

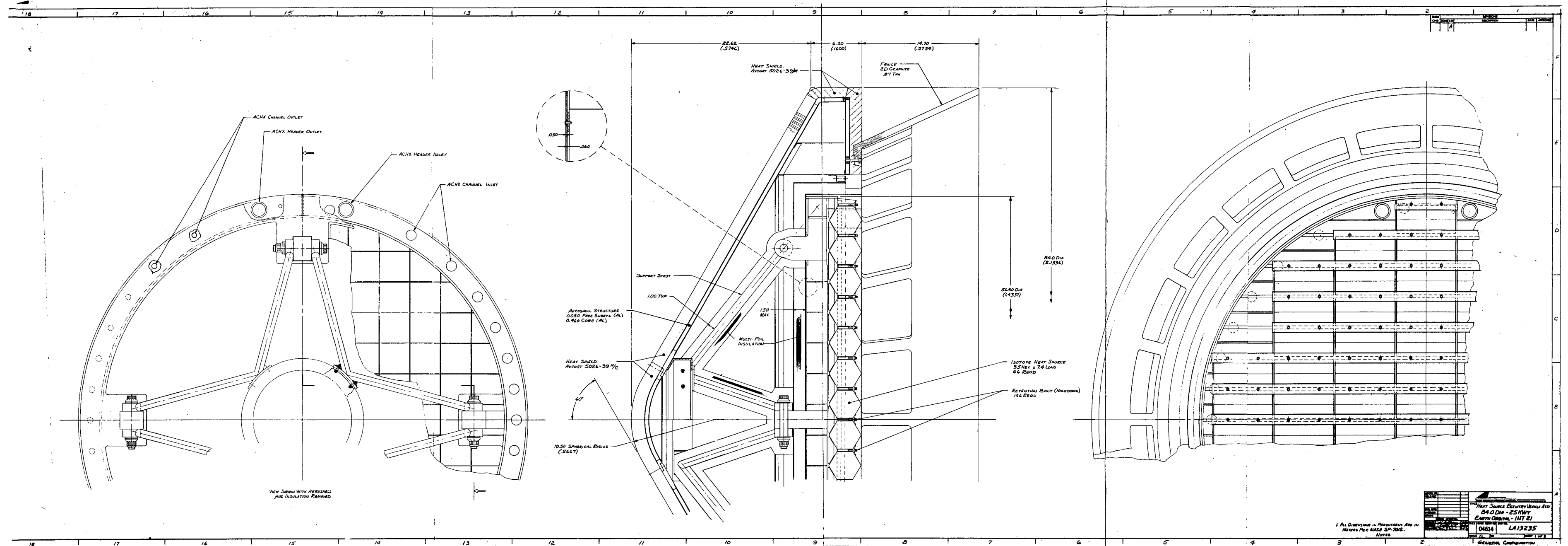


FIGURE 3.4-13 HSRV(INT-21) REFERENCE DESIGN DETAIL LAYOUT-SHEET 1

FOLDOUT FRAME /

FOLDOUT FRAME 3

FOLDOUT FRAME 3

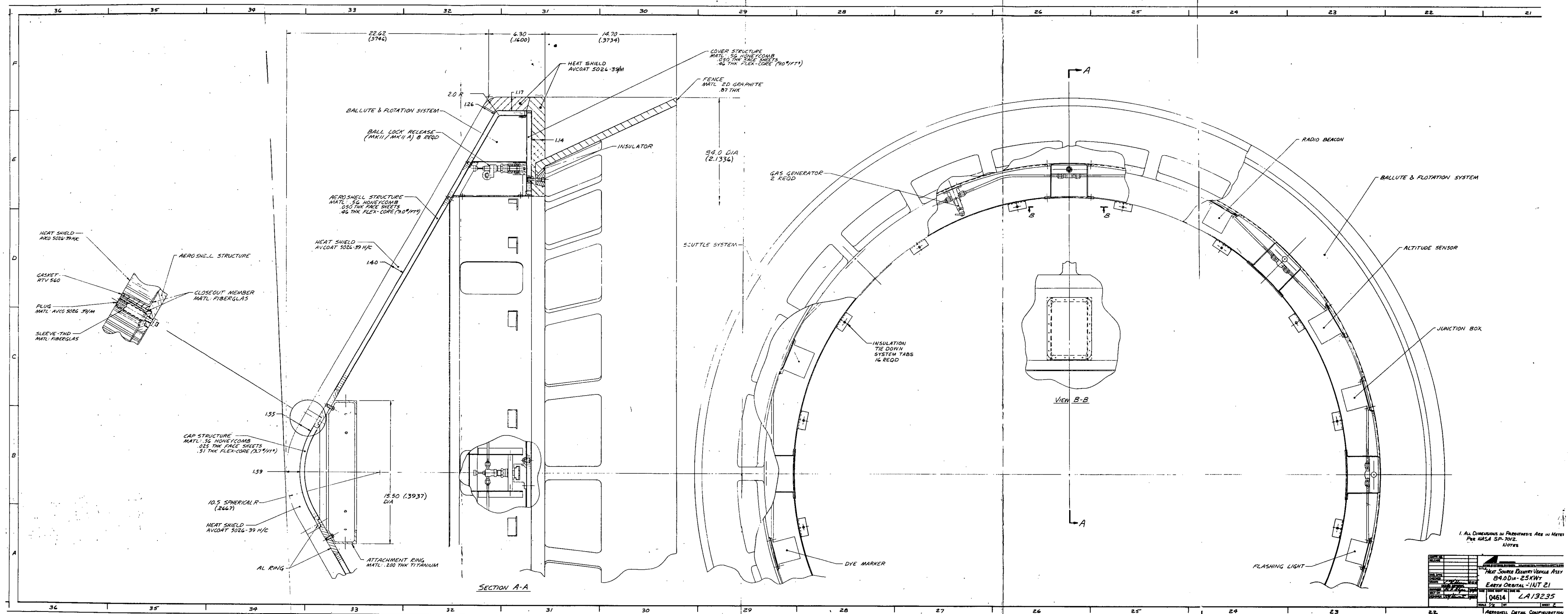
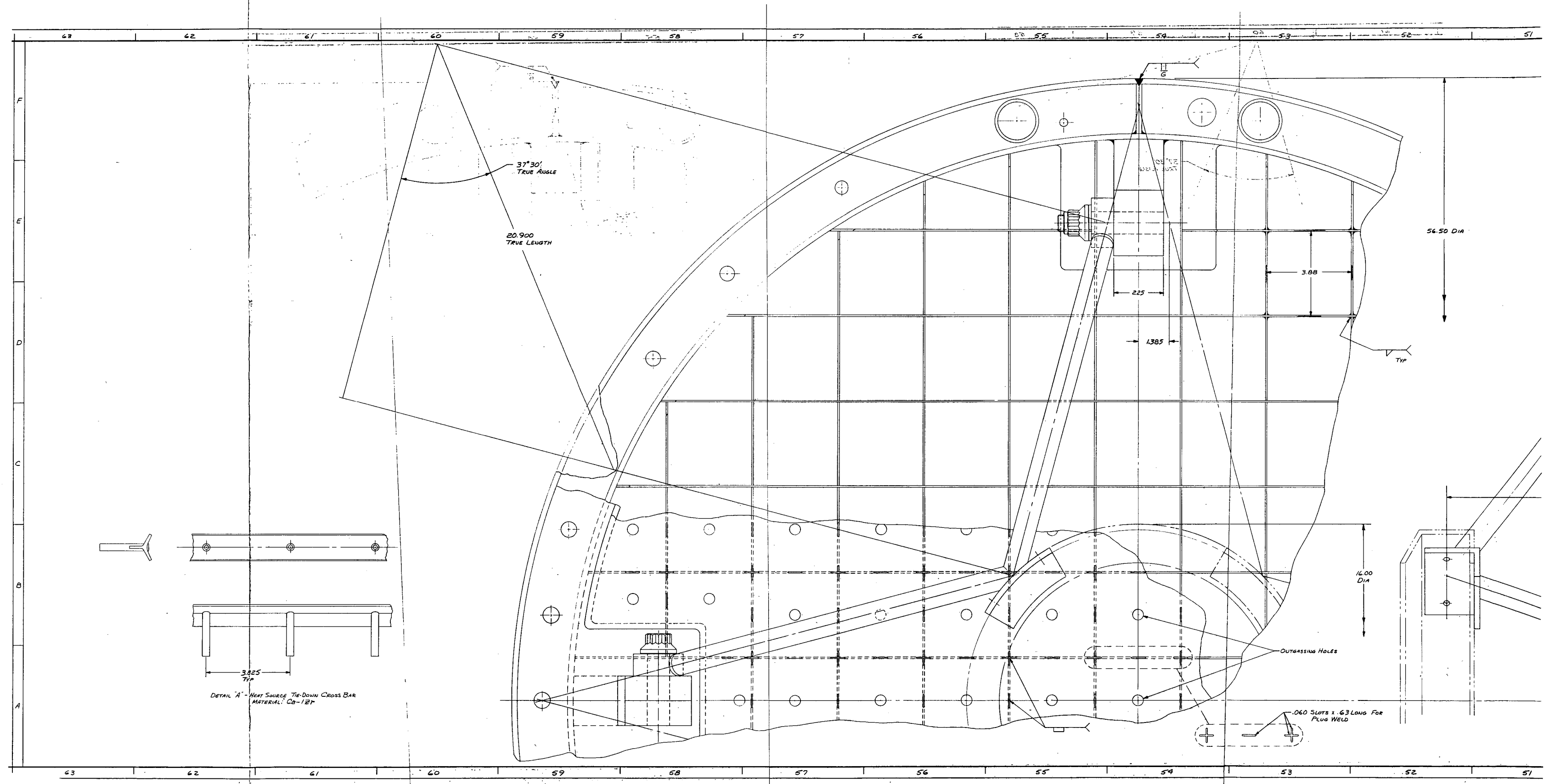


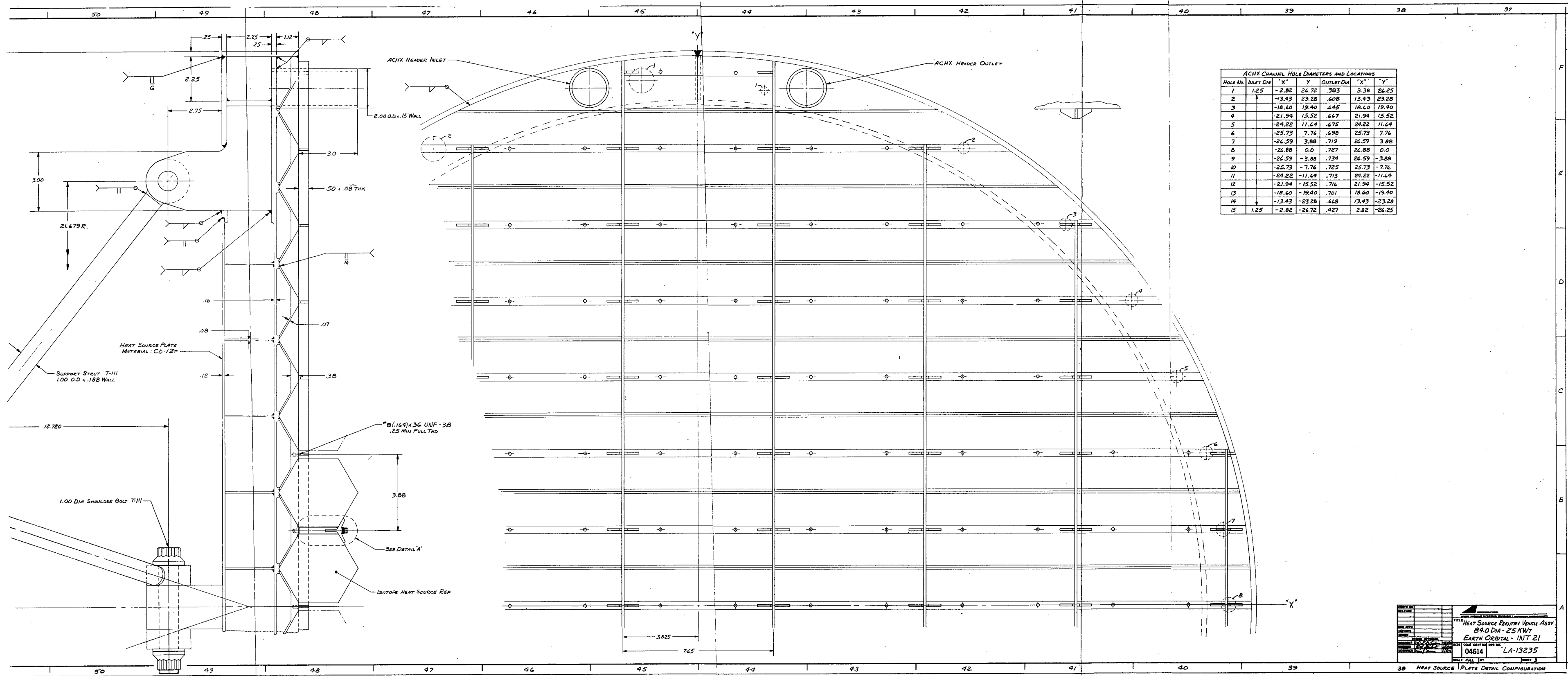
FIGURE 3.4-14 HSRV(INT-21) REFERENCE DESIGN DETAIL LAYOUT-SHEET 2

FOLDOUT FRAME 1

FOLDOUT FRAME 2

FOLDOUT FRAME 3





FOLDOUT FRAME 1

FOLDOUT FRAME 2

FOLDOUT FRAME 3

TABLE 3.4-II

MASS PROPERTIES SUMMARY

H. S. R. V. - Earth Orbital, 84.0 Dia., 25 KW<sub>t</sub> (Ref.: LA 13235)

	Weight (lbs)
Heat Source	1570
Fuel Capsules (66 at 11.0 lb. each)	726
Heat Source Plate	640
Support Structure	79
Insulation	125
Aeroshell	597
Heatshield and Bond	267
Structure	185
Fence	145
Safety Items	130
Ballute (V <sub>T</sub> = 50 ft./sec.)	90
Flotation Aids	20
Location Aids	20
TOTAL	<u>2297 lbs.</u> (1042 KG)

X<sub>cg</sub> = 24.436 inches (measured from nose of aeroshell heatshield)  
 (0.621 Meters)

$$\frac{X_{cg}}{D_b} = .291$$

$$I_{Roll} = 319 \text{ slug-ft.}^2 \quad (432 \text{ KG-Meter}^2)$$

$$I_{Pitch} = I_{Yaw} = 177 \text{ slug-ft.}^2 \quad (240 \text{ KG-Meter}^2)$$

of the access provided by the removable aeroshell nose cap, install the eight strut tie down bolts radially through the titanium ring. Install the aeroshell nose cap with peripheral bolts and heatshield plugs.

Install the sixteen bolts and insulator pads tying the outer insulation face to the aeroshell and remove the radial clamps.

Utilizing remote handling equipment and the necessary safety precautions, install the 66 fuel capsules with the 15 required tie down bars and the 146 required #8 screws.

### 3.4.2 Super-Orbital Reentry Vehicle

Modifications to the reference earth orbital HSRV necessary to survive lunar return super-orbital reentries are defined in this section. Emphasis has been placed on the reentry heat shield material selection; heat leak/thermal control requirements for this class of HSRV; and on definition of methods of reentry vehicles/HSU support concepts that would alleviate potential heat leak and weight penalties. The Apollo heat shield material (Avcoat 5026-39) appears to be the preferential thermal protection system for the lunar return reentries. An HSU support system with crushup pads used to take out high "g" loadings has also been defined as a potential solution to both heat leak and strut weight problems.

#### 3.4.2.1 Heat Shield

The Apollo heat shield material (Avcoat 5026-39/HC-G) was selected as the thermal protection system for an HSRV with superorbital capability. Since the material is tailored for this environment it seems a logical choice. However, the dependency of the allowable bond temperature, during space operation, on both the heat shield material and the HSRV design is a very important consideration.

As an example, if the HSRV Design was modified by increasing the strut cross-section to handle the increase in axial loads experienced during super-orbital entry, the total heat leak would increase substantially leading to bondline temperatures that are unacceptable from a long term heat shield and bond standpoint as well as reentry structural considerations. The main contributor to this problem is Apollo heat shield material itself. Its low vacuum thermal conductivity, 0.083 joule/meter-sec-°K (0.048 Btu/ft-hr-°F) coupled with the associated increase in heat leak results in excessive bondline temperatures.

One possible solution would be to use another heat shield material with a higher vacuum thermal conductivity. One such candidate, TWSP, (Tape Wrapped Silica Phenolic), is a flight proven material with a thermal conductivity of 0.50 joule/meter-sec-°K (0.29 Btu/ft-hr-°F). Its use would certainly relieve



the bondline temperature problem during space operation. However, the stagnation point thickness requirements to limit bondline (structural) temperature to  $232^{\circ}\text{C}$  ( $450^{\circ}\text{F}$ ) during entry is 3.81 cm. (1.5 in.) for all credible trajectories under consideration. Since the density of TWSP is approximately 2.8 times that of the Apollo material, use of TWSP would result in an increased heat shield weight of approximately 2.6 times that of a design utilizing Apollo material. This weight increase, coupled with the increased vehicle weight due to a heavier strut system, makes such a design unattractive.

The proposed HSRV superorbital design utilizes a crush-up reaction system to handle the increased loads with no increase in the strut cross-section over the orbital design. Such a design leads to essentially the same total heat leak during space operation and thus, similar bondline temperatures. For such a design, use of the Apollo heat shield material is feasible and attractive.

The design analysis for the superorbital entry trajectories utilized 122 KM (400 KFT) as the initial entry altitude. Since descent from 137 KM (450 KFT) to 122 KM (400 KFT) is only a matter of seconds at superorbital entry velocities, the effect of deleting the heating in this range has a negligible effect on the thermal response characteristics. For the superorbital entry trajectories under consideration, the most severe are those resulting in the maximum integrated heating. Among the superorbital trajectories, the zero angle of attack skip limit entry condition requires maximum heat shield thickness at the stagnation and midcone points of the aeroshell. The maximum bondline (structural) temperature during entry is shown as a function of thickness in Figure 3.4-16 for these two body points. Note that the thickness requirements to limit the maximum bondline (structural temperature to  $232^{\circ}\text{C}$  ( $450^{\circ}\text{F}$ )) are less than those for orbital decay. The skip limit tumbling entry condition requires maximum heat shield thickness at the shoulder, maximum diameter (cylinder) and base regions among the super-orbital trajectories and these results are shown in Figure 3.4-17. Again, note that the thickness requirements are less than those for an orbital decay entry.

Since the thickness requirements for the superorbital trajectories under consideration are less than the orbital design requirements, and since orbital decay is a credible trajectory for launch of a superorbital HSRV design, the heat shield design as shown previously is applicable for both orbital and super-orbital HSRV designs within the acceptable envelope of entry conditions. Accelerated erosion of the Apollo heat shield material at levels of aerodynamic shear exceeding  $766 \text{ newton/meter}^2$  ( $16 \text{ lbs/ft}^2$ ) precludes use of the material at conditions where this level of aerodynamic shear is exceeded. This restriction bounds the envelope of acceptable entry conditions to entry angles less than  $-20^{\circ}$  at lunar return velocities.

Figure 3.4-16  
AVCOAT 5026-39/HC-G REQUIREMENTS

SKIP LIMIT LUNAR RETURN

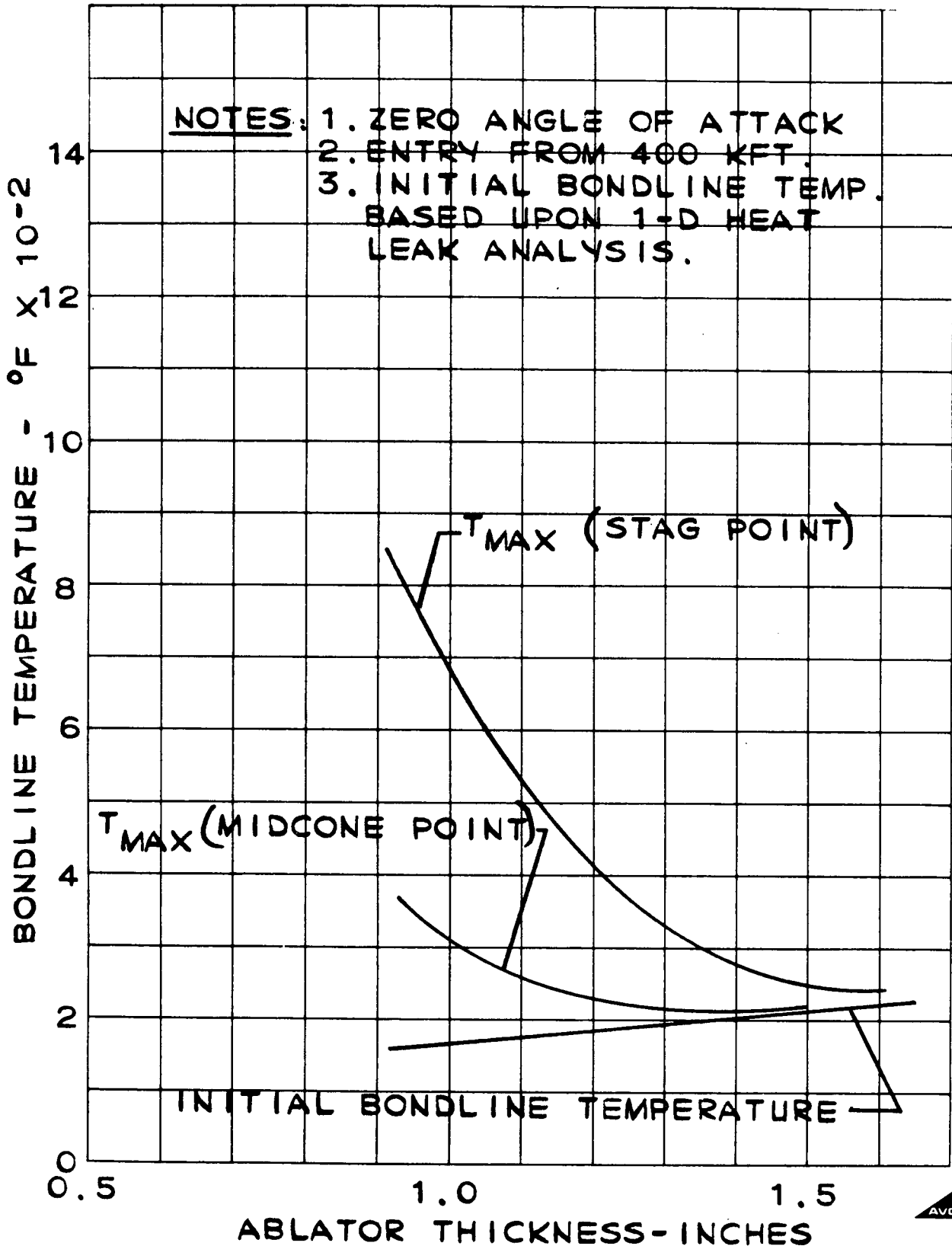
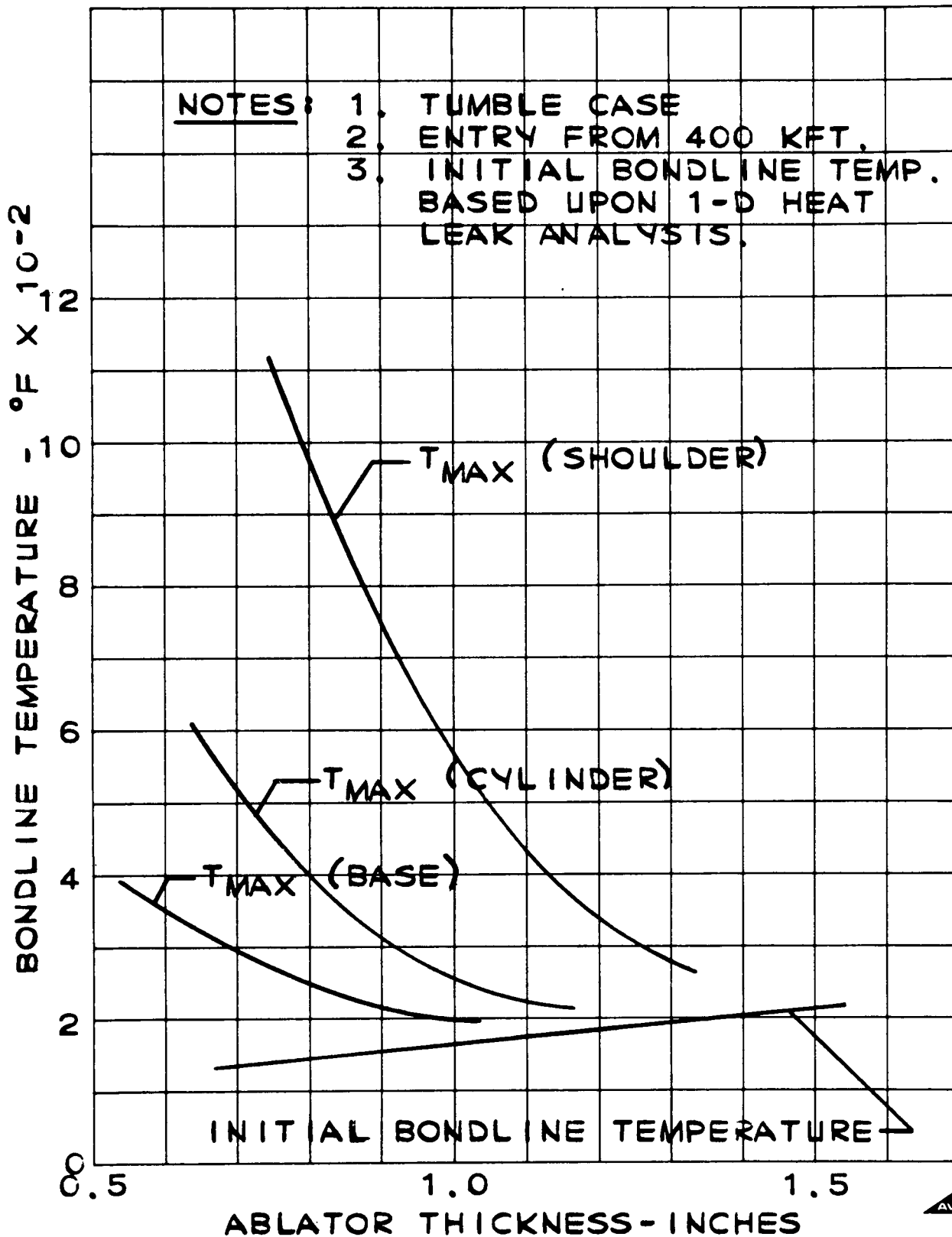


Figure 3.4-17

AVCOAT 5026-39/HC-G REQUIREMENTS  
SKIP LIMIT LUNAR RETURN



The aerodynamic fence thickness of 3.175 CM. (1.25 in.) is dictated by dynamic loads considerations for superorbital entry conditions. An analysis was performed to determine the thermal response of the 2-D graphite fence during a tumbling skip limit entry, which represents the worst aerodynamic heat load. A similar analysis was performed for the Cb-1%Zr HSU hold-down bolts. The results of the fence analysis indicates that the thermal gradients through the fence thickness are so severe that thermal stress considerations might preclude use of this material. Use of a 3-D graphite might enable the conductance through the thickness to be increased, thus reducing the thermal gradients and relieving the thermal stress problem. The transient response of the inside and outside surfaces of the 2-D graphite fence is shown in Figure 3.4-18. Note that the coolest part of the fence is at an interior point and the maximum temperature gradient is about  $1000^{\circ}\text{C}$  ( $1874^{\circ}\text{F}$ ) in 2.0 CM (0.81 in.). The maximum HSU bolt temperature is about  $1630^{\circ}\text{C}$  ( $2960^{\circ}\text{F}$ ). The Cb-1%Zr bolts lose their strength characteristics at much lower temperatures. Another material must be used for the HSU hold-down bolts; possibly tungsten.

#### 3.4.2.2 Thermal Control (Super-Orbital)

The adequacy of the super-orbital reentry vehicle thermal design has been demonstrated, like in the HSRV case, by investigation of the thermal performance during normal operation in orbit. Two design versions have been analyzed, a crushup and a no-crushup design. The maintenance of acceptable temperatures and heat losses within the boundaries of the aeroshell is quite complex and requires extensive thermal network analysis in order to derive an optimized design concept. The analytical method, assumptions and results are summarized in the following section.

##### a. Analytical Model

Environmental Considerations -- One environmental case has been considered, i. e., normal operation in orbit, Figure 3.4-19. For orbital considerations, incident heat loads, internal environment and a summary of total heat losses see section 3.4.1.3 a. The previous HSRV Thermal Control sections are fully applicable to the super-orbital reentry vehicle with the exception that in the case of the super-orbital reentry vehicle, the effective strut length has been reduced to 17.5 inches. The cross-section remains at  $0.48\text{ in}^2$  in case of the crushup design but is increased to  $1.75\text{ in}^2$  for the no-crushup design case.

##### b. Results

Steady-state temperature distributions and heat losses are shown in Figure 3.4-20 for the no-crushup design and 3.4-21 for the crushup design case. An inspection of the no-crushup case thermal distribution indicates that

# FENCE AND BOLT TEMPERATURE HISTORIES LUNAR RETURN-SKIP LIMIT TUMBLING

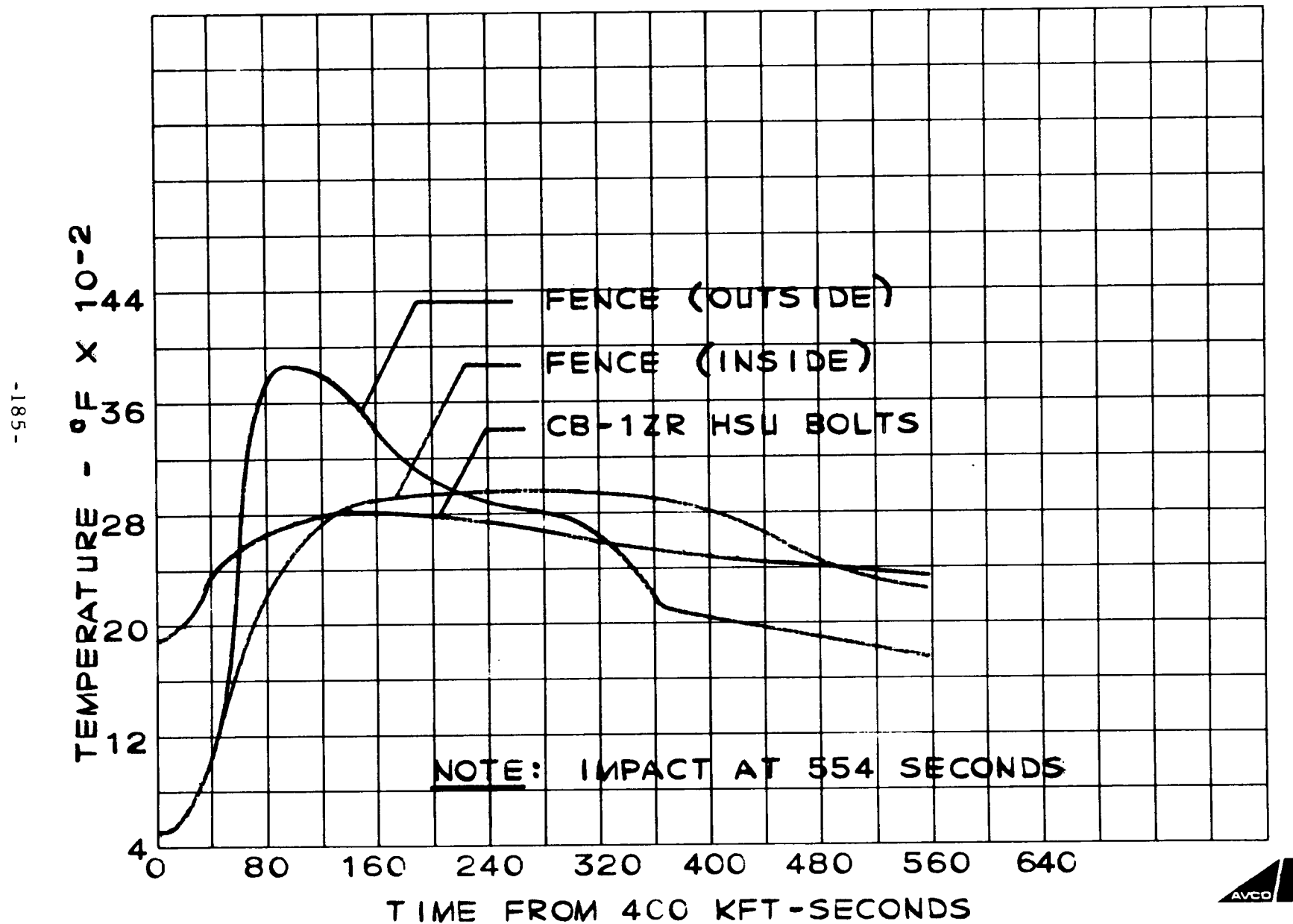
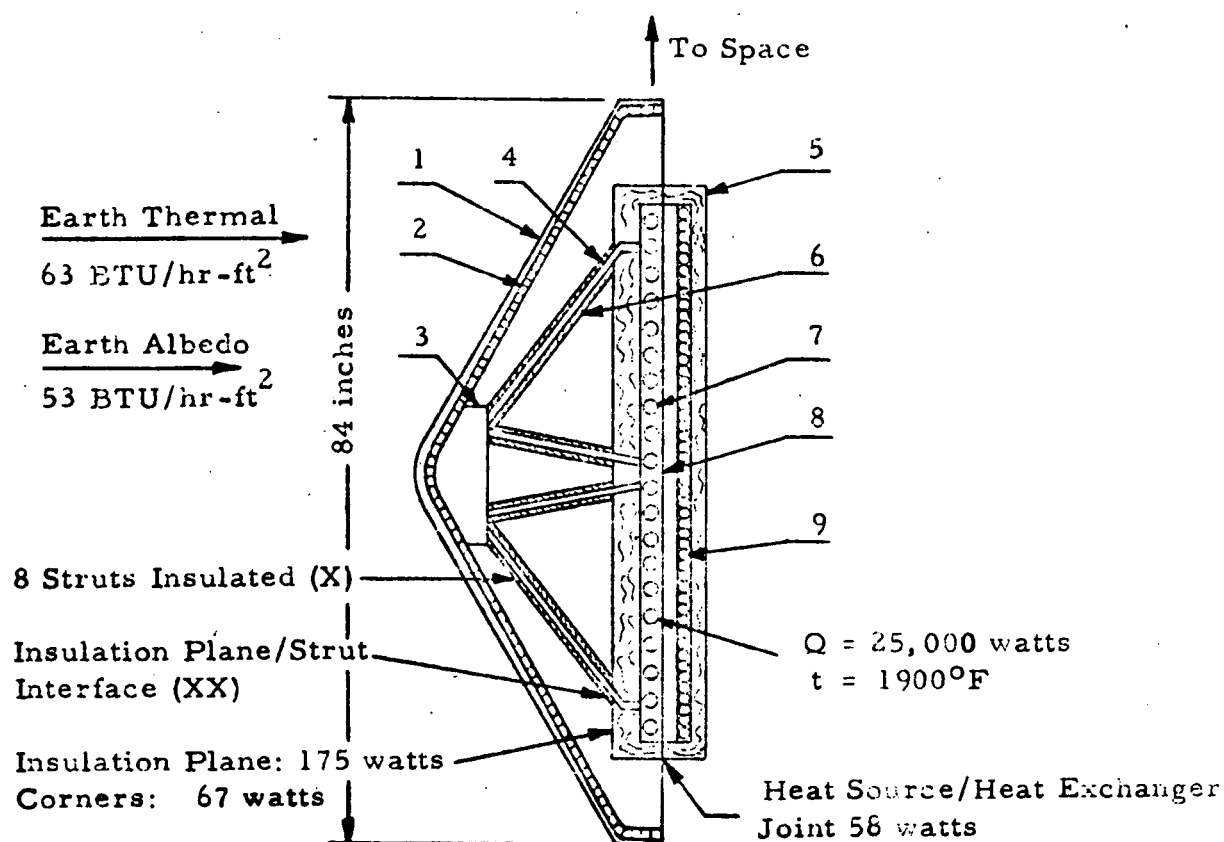


Figure 3.4-18



(x)  $Q = 282/590 \text{ Watts}$  (Crushup/no crushup design), Results of this study  
 (xx)  $Q = 102/234 \text{ Watts}$  (Crushup/no crushup design), Results of this study

Component	Material	Dimensions	Thermal Conductivity (Btu/hr-ft-°F)
1. Heat Shield	5026-39-HC-G	Thickness: 1.4 inches	0.048 (Vacuum)
2. Aeroshell Structure	Al Honeycomb	Facesheet Thickness: 0.05-0.065 in. (1) Core Thickness: 0.51 inch	110.
3. Attachment Ring	Ti	Thickness: 0.25"	10.
4. Strut (8 Total)	T-111	Length: 17.5 inches Cross Section: 0.48 inch <sup>2</sup> (2)	38.
5. Insulation Assembly	Multifoil	Thickness: 1.5 inch	0.002
6. Strut Insulation	Multifoil	Thickness: 1.0 inch	0.002
7. Fuel Capsules	$\text{PuO}_2$ , T-111, Pt		
8. Support Structure	CblZr		38.
9. Heat Exchanger	CblZr		38.

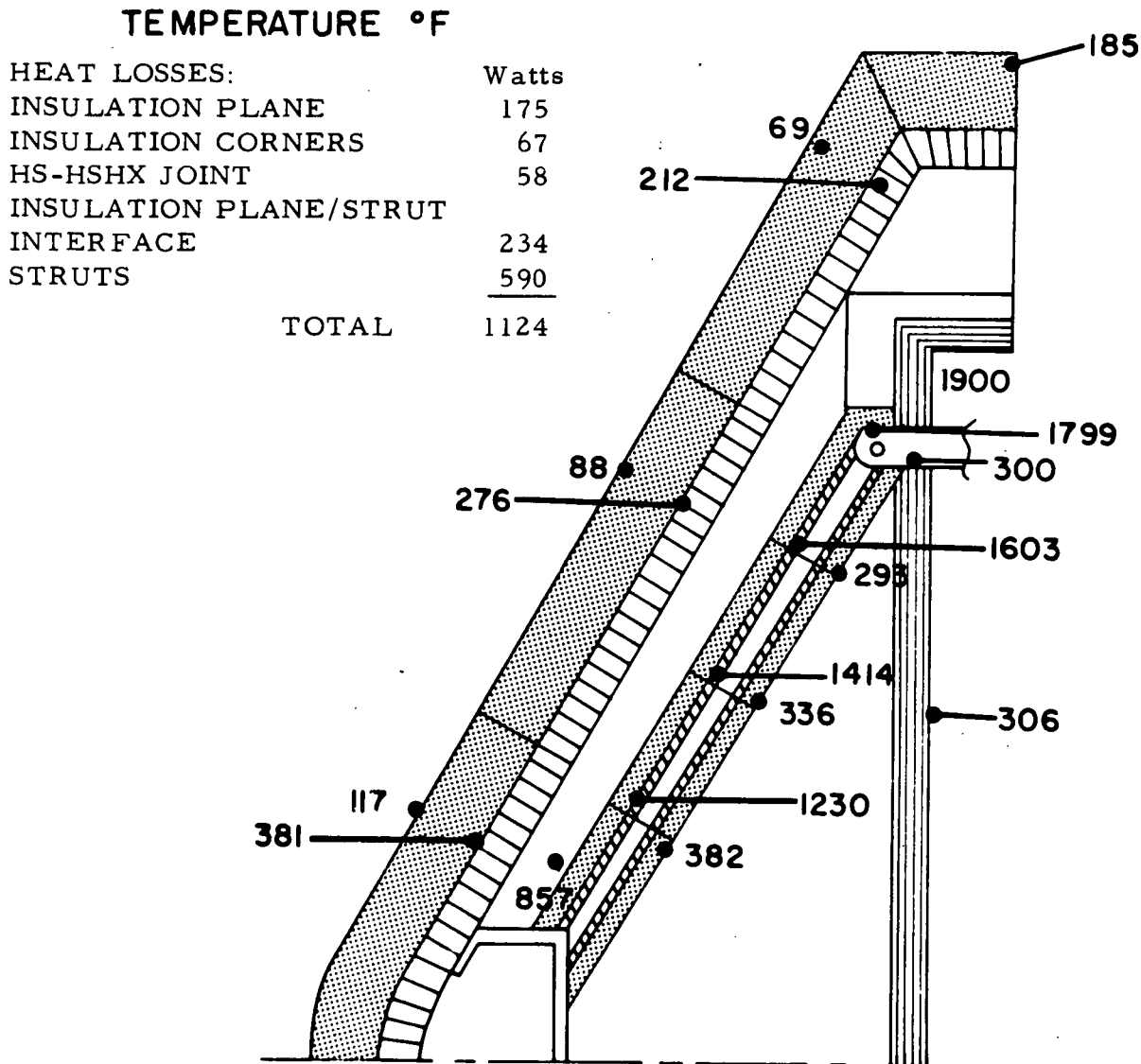
(1) 0.05 to 0.165 in. for the no-crushup design  
 (2) 1.75 in<sup>2</sup> for the no-crushup design

Figure 3.4-19  
 Super-Orbital Reentry Vehicle  
 Reference Design, Normal Operation in Orbit

Figure 3.4-20

# SUPERORBITAL (INCREASED STRUT AREA) HSRV STEADY-STATE TEMPERATURE DISTRIBUTION

NORMAL OPERATION IN EARTH ORBIT



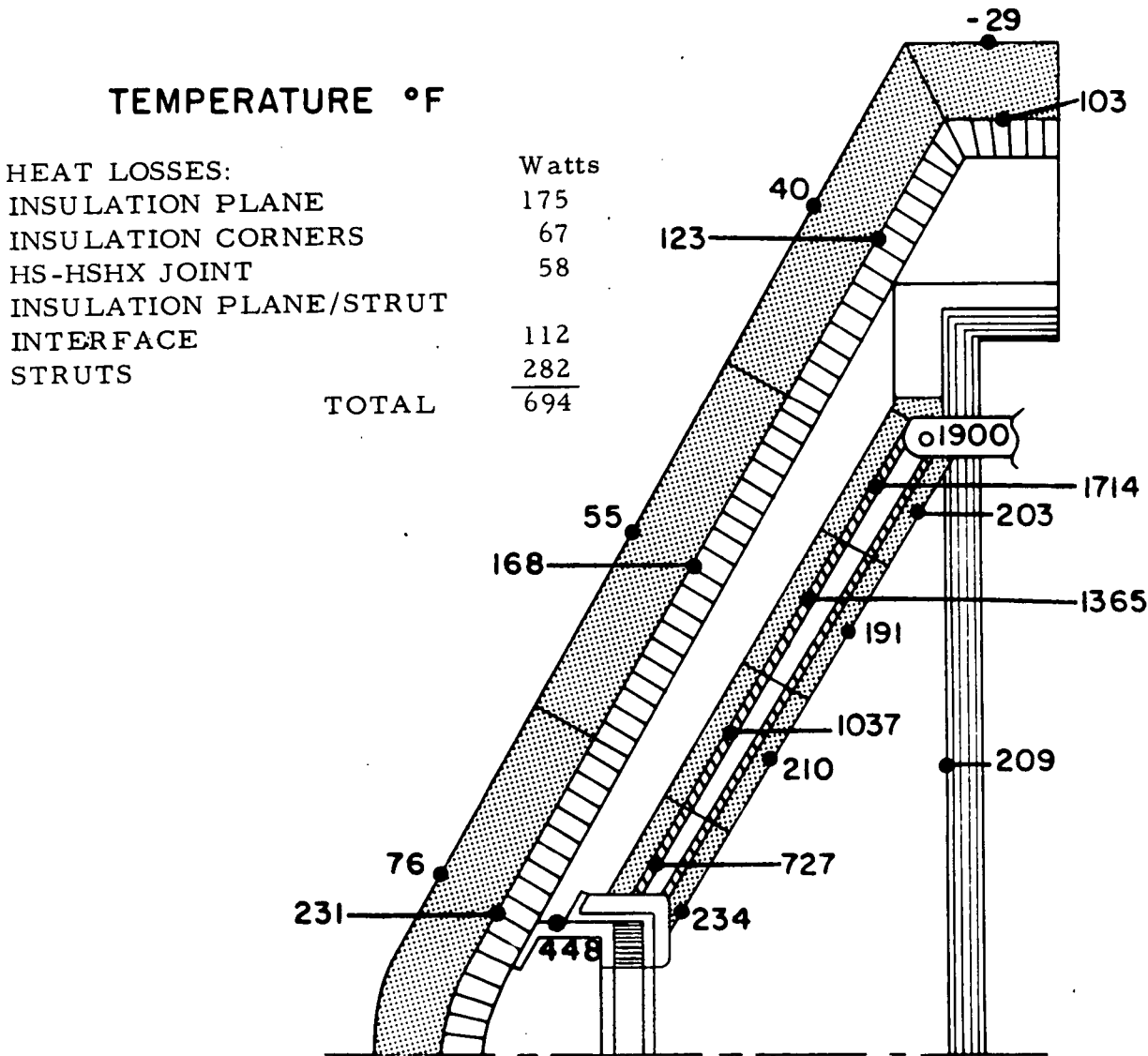
TOTAL HEAT LEAK - 1124 WATTS

FIGURE 3.4-21

# SUPERORBITAL (CRUSH-UP) HSRV

## STEADY-STATE TEMPERATURE DISTRIBUTION

### NORMAL OPERATION IN EARTH ORBIT



TOTAL HEAT LEAK - 694 WATTS



the maximum aeroshell/ablator bond line temperature (300°F, section 3.4.1.3) is exceeded by 80°F and therefore not acceptable. Also, the total heat loss exceeds the required 1 KW by 124 watts. It is concluded that the no-crushup design is thermally unacceptable.

In contrast, the crushup design case, Figure 3.4-22, is thermally well balanced. The attachment ring and aeroshell/ablator bondline temperatures as well as the heat losses are acceptable.

Study results are summarized as follows:

- The no-crushup design is thermally not acceptable.
- The crushup design, however, is thermally well balanced.
- All temperatures and heat losses are within acceptable limits.
- The aluminum aeroshell tends to distribute internal heat loads quite well and thus to reduce hot-spot temperatures to an acceptable level.
- The titanium attachment ring contributes significantly towards aeroshell hot-spot reduction.
- The selected strut design is thermally acceptable.
- The theoretical insulation system performance appears to be good. Since this is a critical area and affected by the interaction of many parameters, careful thermal design supported by testing is mandatory to insure adequate performance concurrent with predicted results.

#### 3.4.2.3 Super Orbital Reference Design - Structural Performance

The design requirements for the HSU plate and support system are considerably more severe for the super orbital design than the earth orbital design. Not only are the reentry inertia loads for a lunar return (-15° reentry angle) more than twice the INT-21 levels but the HSU is at an operating temperature of 1900°F compared to 500°F for the INT-21 abort reentry resulting in an appreciable strength reduction in the HSU structure. To compensate somewhat for these two factors, the HSU support plate depth was increased to 3.5 inches to reduce the required increase in facesheet thickness and conserve weight; nevertheless, the plate facesheet thickness and internal rib thickness increased to .25 inch and .16 inch respectively. This results in an increase of plate structural weight from 640 lbs. to 910 lbs. indicating the compounding effect of higher loads on the strut support system. Preliminary calculations of the strut system revealed that a strut area of 1.75 in.<sup>2</sup> is required to support the increased weight and higher reentry loads and temperatures. This strut area was determined to be intolerable in terms of heat leak and local aeroshell hot spots.

Since the strut size cannot be scaled up to meet the lunar return reentry load and temperature requirements because of thermal constraints it is proposed to include a secondary support scheme which will remain unloaded during the launch, operational and initial reentry phases of the mission but will take over the load supporting function from the strut system during the peak reentry loads. Since the strut system lacks the flexibility to elastically deform and allow the HSU to set down on four peripheral pads on the aeroshell directly under each plate fitting, a crushup system is required to provide the required axial translation. The proposed concept provides an annular column of crushup material to be located between the lower strut ring and aeroshell attachment ring, the former ring being an additional member to the earth orbital design. During assembly, these mating rings will be bolted together axially preloading the crushup material between them in order to insure a good structural load path from the strut system to the aeroshell. In addition, the webs of the mating rings will be pinned to resist torque loads about the vehicle axis with axially slotted holes provided to allow relative axial movement when crushup occurs. The four peripheral bearing pads below the plate fittings are separated from the fitting by the insulation layer so that thermal short circuiting does not occur. A rigid ring is provided under these pads to improve the load distribution from the four pads into the aeroshell when the peak reentry inertia loads are applied. In brief, the total support system will function as follows. The launch, operational, and initial reentry loads (when the HSRV vehicle is undergoing a period of stabilization) of the HSU will be carried by the strut system as in the earth's orbital design and these loads are transmitted through the strut attachment ring into the aeroshell. With the HSRV vehicle stabilized in a proper reentry attitude and beginning to decelerate rapidly, the strut system and consequently the crushup system will experience increasing compressive loading until the maximum design crush strength is reached whereupon the entire HSU system will move forward under deceleration until the plate fittings bottom out on the peripheral bearing pads. The insulation layer between the fitting and bearing pads will also be crushed in the process without offering significant resistance. At full compression, four spring-loaded pins will engage into aligned holes in the strut ring locking the strut ring to the aeroshell attachment ring and thereby preventing rearward movement of the HSU. The crushup system will be designed to crush before any possibility of strut failure. For the strut cross-sectional area of  $.48 \text{ in}^2$  and a maximum temperature of  $1900^\circ\text{F}$ , the maximum allowable strut load is 17,760 lbs. For a HSU weight of 1840 lbs., this corresponds to an axial inertia load of 57.0 g; this, however, will be lower when simultaneous lateral loading occurs. Since the maximum allowable strut loading is controlled by the crushup design and will be lower than the earth orbital design, no additional beefing up of the attachment ring or local aeroshell will be required.

#### 3.4.2.4 Design Description

The 25 KW<sub>t</sub> super-orbital HSRV configuration as shown in Figure 3.4-22 is identical to the 25 KW<sub>t</sub> earth orbital configuration described in Section 3.4.1.4 except in the areas where design changes were necessary to increase the structural capability in order to survive the higher inertia loading of super-orbital reentry.

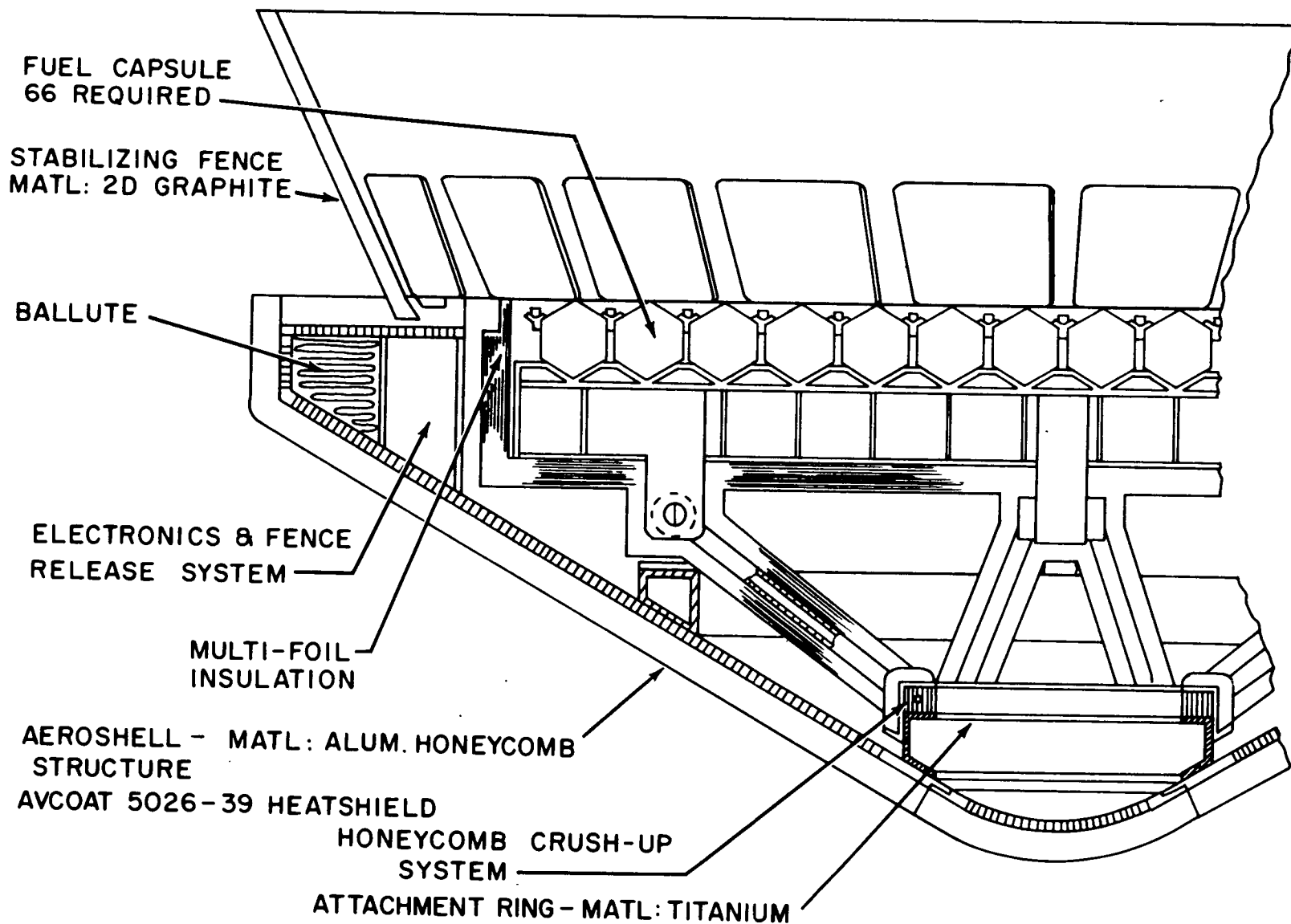
The aeroshell face sheet thickness has been increased as has the 2-D graphite fence thickness. The structural capability of the heat source plate was increased by the combined effects of increasing the face sheet thicknesses and by spacing them further apart thus making the total plate depth greater.

An investigation of the heat leak down the struts of the truss support system revealed that an increase in the structural capability of the struts would result in an increase in the heat leak beyond the acceptable 1 KW<sub>t</sub> limit. Therefore, the alternate approach of limiting the loads seen by the struts by installing crushable honeycomb between the rings at the base of the truss support system was selected. The honeycomb is designed to crush during reentry (at 35 g's) thus allowing the heat source plate to move forward 1.0 inch and bear directly on the aeroshell mounted load reaction pads located under each heat source plate fitting. In this way, the struts do not have to be changed in cross section to increase their structural capability so the heat leak during the major portion of the mission remains within acceptable limits. During the final phase of reentry with a direct heat path to the aeroshell, the heat leak will certainly violate the 1 KW<sub>t</sub> maximum but at this point the mission is nearly over and this is comparatively unimportant.

Due to the steep increase in axial inertia load with increasing reentry angle and the corresponding weight penalty that must be paid, several different reentry angles were selected to study to more closely identify the penalties that must be paid. Figure 3.4-23 depicts the weight growth of the HSRV as a function of increasing entry angle. Tables 3.4-III, -IV, and -V, show the weight and diameter growth of the HSRV for -15°, -25°, and -38° reentry angles (at Lunar Return Velocity).

A detailed layout of the reference super-orbital design is shown in Figure 3.4-24.

# HSRV - SUPER ORBITAL



-192-

Figure 3-4-22

Figure 3.4-23

## SUPER ORBITAL SYSTEM WEIGHTS

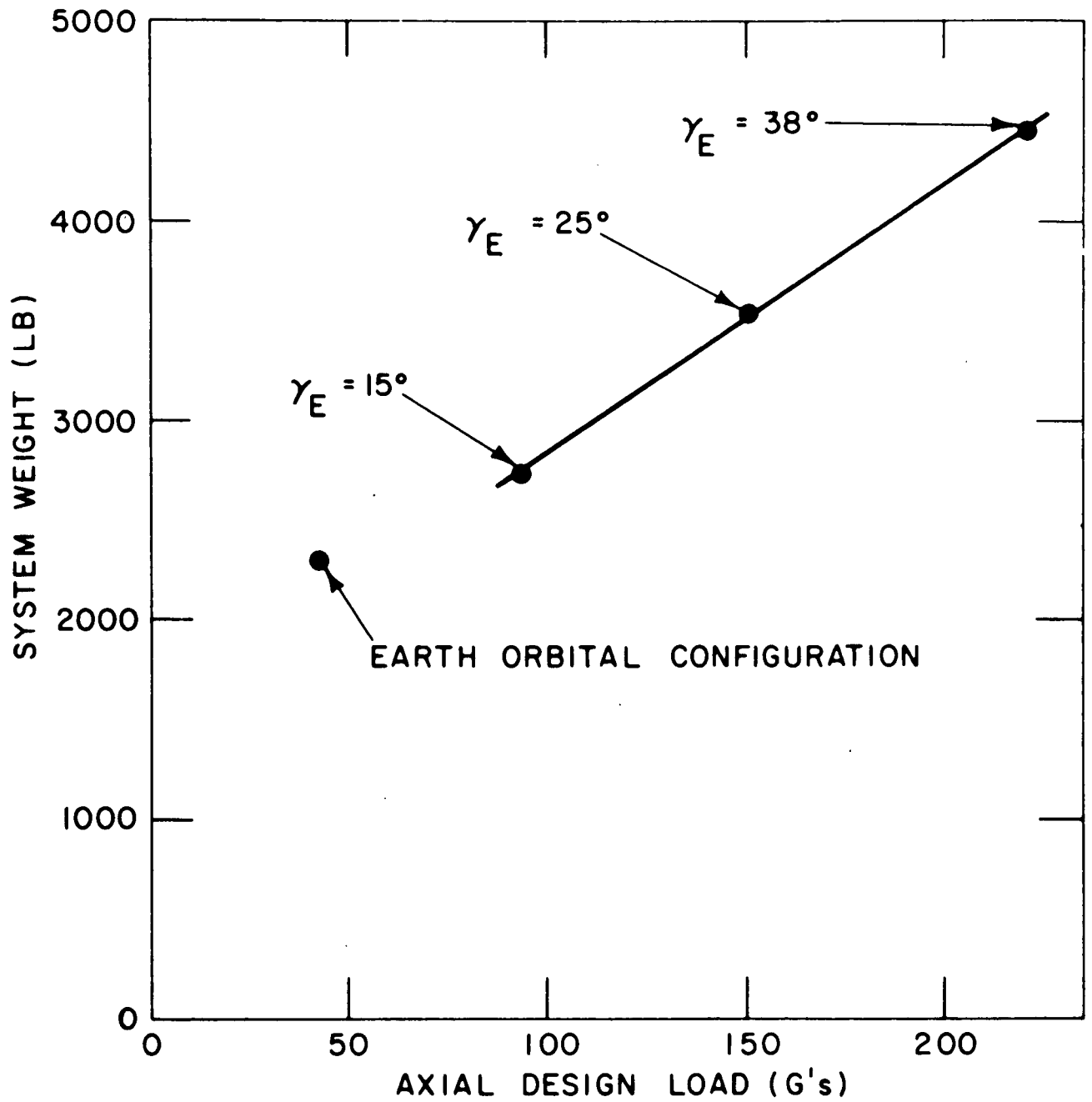


TABLE 3.4-III

MASS PROPERTIES SUMMARYH.S.R.V. - Super Orbital at  $-15^\circ$ , 84.0 Dia., 25KW<sub>t</sub> (Ref. LA13244)

	Weight (lbs.)
Heat Source	1869
Fuel Capsules (66 at 11.0 lb., each)	726
Heat Source Plate	910
Support Structure	104
Insulation	129
Aeroshell	744
Heatshield and Bond	267
Structure	269
Fence	208
Safety Items	130
Ballute ( $V_T = 60$ ft./sec.)	90
Flotation Aids	20
Location Aids	20
TOTAL	<u>2743 lbs.</u> (1244 KG)

$X_{cg} = 23.966$  inches (measured from nose of aeroshell heatshield)  
 (0.609 Meters)

$$\frac{X_{cg}}{D_b} = .285$$

$$I_{Roll} = 376 \text{ slug-ft.}^2 \quad (510 \text{ KG-Meter}^2)$$

$$I_{Pitch} = I_{Yaw} = 211 \text{ slug-ft.}^2 \quad (286 \text{ KG-Meter}^2)$$

TABLE 3.4-IV  
MASS PROPERTIES SUMMARY

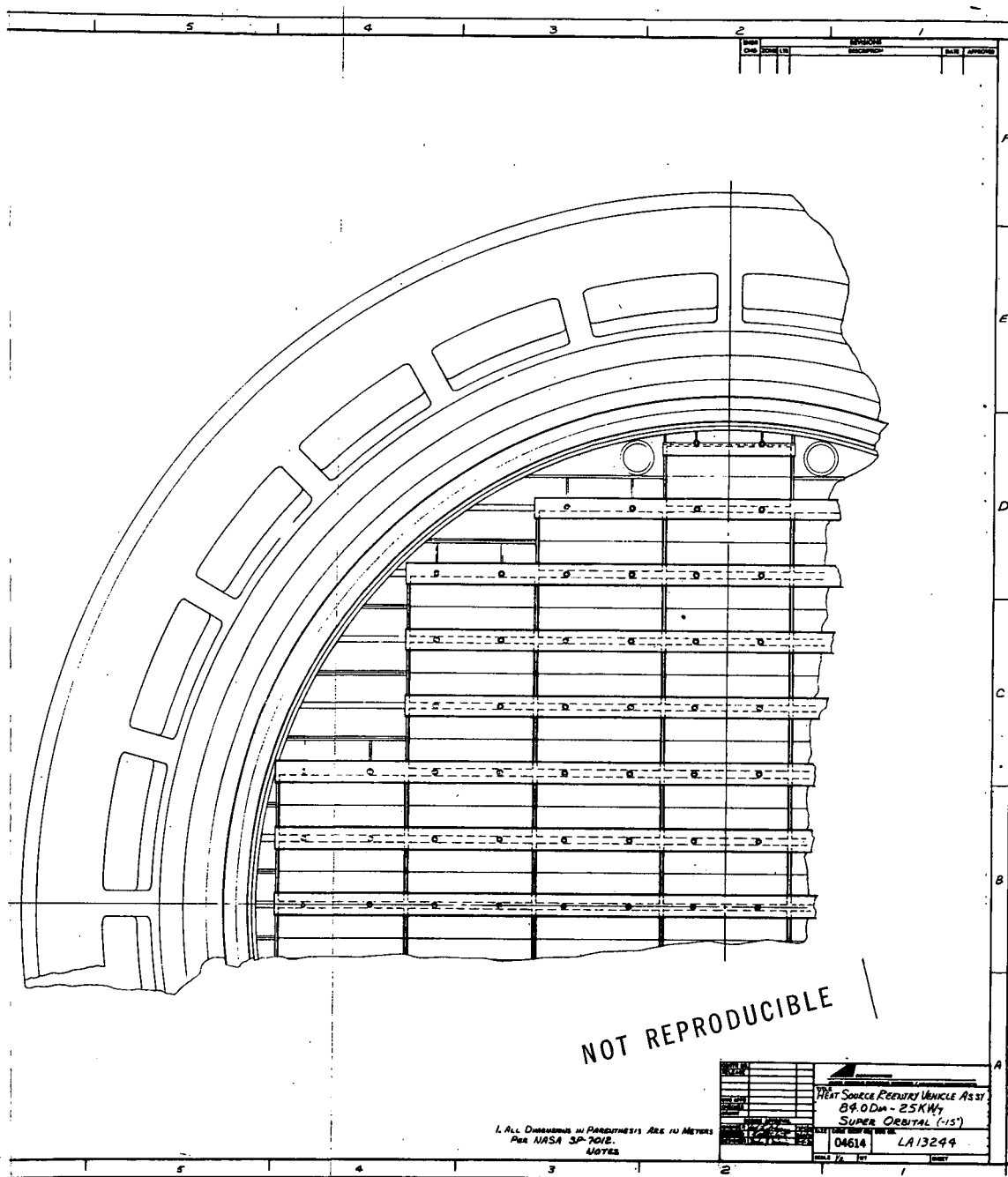
H. S. R. V. - Super-Orbital at  $-25^{\circ}$ , 88.0 Diz., 25 KW<sub>t</sub>

	Weight	(lbs.)
Heat Source		2395
Fuel Capsules (66 at 11.0 lb., each)	726	
Heat Source Plate	1427	
Support Structure	108	
Insulation	134	
Aeroshell		960
Heat Shield and Bond	300	
Structure	370	
Fence	290	
Safety Items		205
Ballute ( $V_T = 60$ ft./sec.)	150	
Flotation Aids	35	
Location Aids	20	
TOTAL		<u>3560 lbs.</u> (1615 KG)

TABLE 3.4-V  
MASS PROPERTIES SUMMARY

H. S. R. V - Super-Orbital at  $-38^{\circ}$ , 92.0 Dia., 25 KW<sub>t</sub>

	Weight	(lbs.)
Heat Source		2926
Fuel Capsules (66 at 11.0 lb., each)	726	
Heat Source Plate	1950	
Support Structure	111	
Insulation	139	
Aeroshell		1224
Heat Shield and Bond	335	
Structure	506	
Fence	383	
Safety Items		300
Ballute ( $V_T = 60$ ft./sec.)	235	
Flotation Aids	45	
Location Aids	20	
TOTAL		<u>4450 lbs.</u> (2018 KG)





### 3.4.3 Aeroshell Thermal Simulation

The prime objective of this effort was to design an aeroshell test article which possesses the same thermal characteristics as the reference IRV (earth orbital concept) when subjected to testing in the NASA/LeRC SPF facility. In order to properly simulate the thermal characteristics of the test article and reference design requires both the temperature level and distribution be matched as closely as possible. While the solution to this problem could be obtained simply by duplicating the reference aeroshell design, alternate low cost approaches can be used if relaxation in the degree of simulation are allowed.

#### 3.4.3.1 Design Considerations

One of the major problems in simulating temperature distributions in a test facility with those in flight is that the boundary conditions differ. In orbit solar, albedo and earth radiation energy are directed towards the aeroshell while the surface radiates to "black" space ( $-460^{\circ}\text{F}$ ). In the facility however the system radiates to a  $0^{\circ}\text{F}$  cold wall. For the reference orbit in the study (low earth) a fortunate situation exists in that the energy exchange in orbit between albedo, earth radiation and aeroshell surface radiation (to  $-460^{\circ}\text{F}$  space) produces temperatures very close to a system radiating to a  $0^{\circ}\text{F}$  coldwall. This comparison can be seen by reviewing Figures 3.4-10 and -11, where steady-state thermal analysis results are shown. However, it should be noted that while this favorable situation exists for the earth orbital mode other phases of flight will not be so easily simulated (e. g. HSU deployment mode where in test radiation will be to the coldwall rather than to space). Adjustments to the heat loading or form factors between the surfaces involved may be required to produce acceptable temperature matching conditions between flight and test for both the steady state and transient cases.

In an effort to reduce the costs associated with the fabrication of an aeroshell test article, modifications to the reference HSRV design have been suggested and are described in Table 3.4-VI. The costs associated with the fabrication of these concepts is shown in Table 3.4-VII.

Three main points should be stressed when considering these alternative designs; 1) care must be taken if aluminum sheet is substituted for honeycomb to insure that the proper radial heat conduction is obtained, 2) it will be difficult to interpret the results if mahogany is substituted for ablator since the temperature and pressure variations throughout the tests will product different effects on the conductance of the two materials, 3) thermal capacitance of the reference design must be closely simulated in order to obtain a realistic transient response in the test article.

TABLE 3.4-VI

AEROSHELL CONCEPTS FOR THERMAL SIMILITUDE TESTS

CONCEPT	REMARKS
1. AVCOAT 5026-39 (Honeycomb)/Aluminum Honeycomb	Reference design
2. AVCOAT 5026-39 (Molded)/Aluminum Honeycomb)	Lower Ablator Fabrication Costs With Thermal Characteristics Very Close to Honeycomb Ablators.
3. AVCOAT 5926-39 (Molded)/Aluminum Sheet	1. Low Cost Ablator 2. Aluminum Sheet Structure Must Have Proper Thermal Competence and Ability to Transfer Heat Radially.
4. Phillipine Mahogany/Aluminum Sheet	1. Mahogany Must Have Conductance Under All Possible Pressure and Temperature Conditions Similar to Ablator. 2. Aluminum Sheet Structure Remarks Same as Above.

TABLE 3.4-VII

## AEROSHELL COSTS FOR THERMAL SIMILITUDE TESTS

ITEM	CONTRACT DOLLARS			
	CONCEPT 1	CONCEPT 2	CONCEPT 3	CONCEPT 4
AVCOAT 5026-39 (HONEYCOMB)	42400			
AVCOAT 5026-39 (MOLDED)		30300	30300	
PHILLIPINE MAHOGANY				13000
ALUMINUM HONEYCOMB	46800	46800		
ALUMINUM SHEET			26230	26230
TOTAL COST	89200	77100	56530	39230

NOTE: COSTS INCLUDE MATERIAL, TOOLING, BONDING, FABRICATION AND ASSEMBLY,  
BUT DOES NOT INCLUDE INSPECTION

Figure 3.4-25 shows the recommended aeroshell concept for the thermal simulation tests. Note that the molded ablator has been substituted for the reference honeycomb material and that aluminum sheet has been used. This design is the best compromise of all those discussed earlier in satisfying both the thermal performance characteristics and low cost objectives. In the design of the structure, adequate provisions have been made to allow lifting of the system during all test procedures.

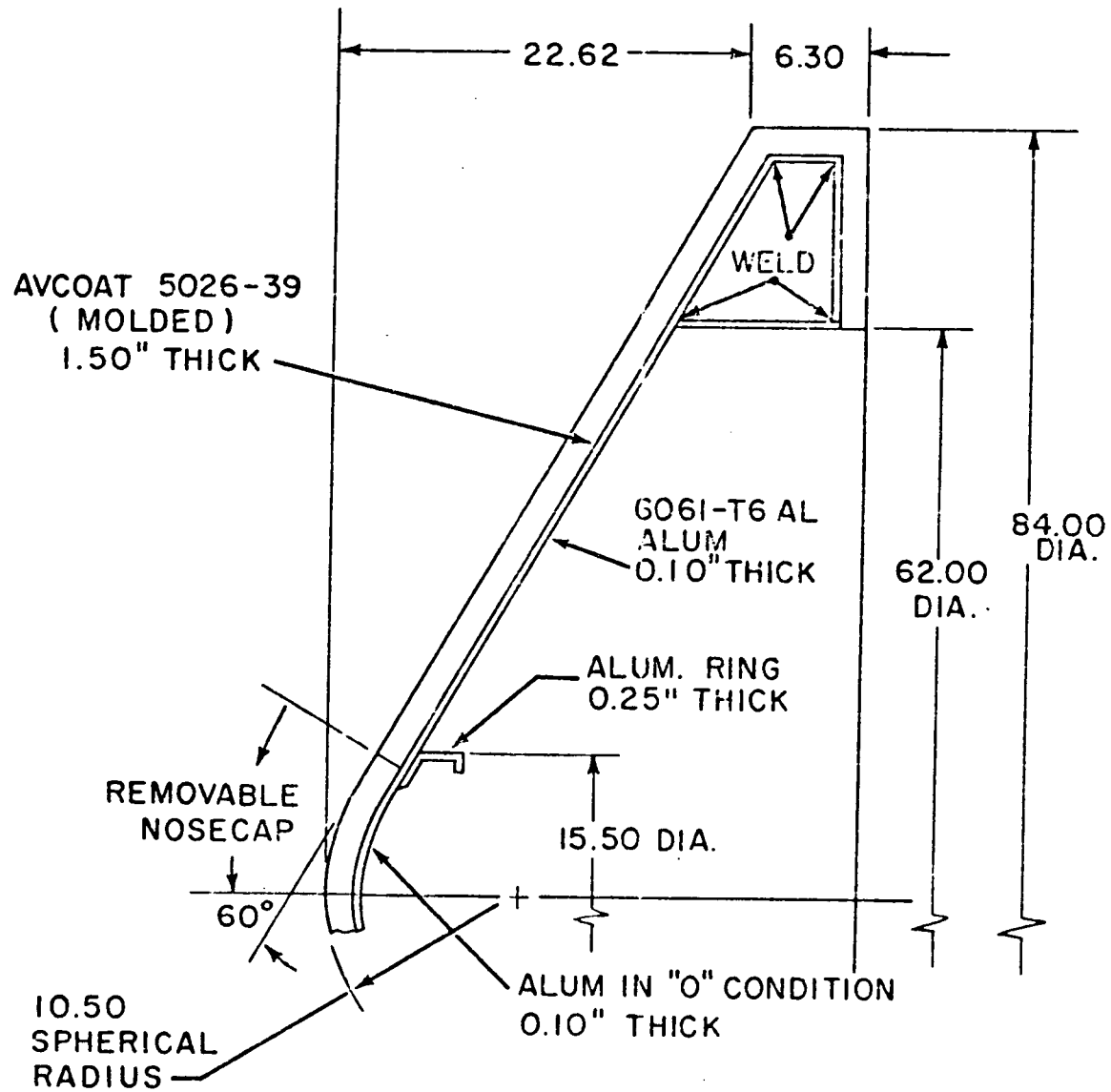
### 3.5 REFERENCES

- 3.2-1 McAlister, K. W., et al.: Aerodynamic Characteristics of a Large-Angle Blunt Cone With and Without Fence-Type Afterbodies.
- 3.2-2 Campbell, J. F., Longitudinal Aerodynamic Characteristics of Several High-Drag Bodies at Mach Numbers from 1.50 to 4.63, NASA TN D-3915 (April 1967).
- 3.2-3 Davenport, E. E., Some Supersonic Aerodynamic Characteristics of  $120^\circ$  Cones and a Tension Shell Model, NASA/Langley Working Paper 391 (April 1967).
- 3.2-4 Krumins, M. V., A Ballistic Range Study of Aerodynamic Characteristics of Mars Probe/Lander Shapes, AIAA Paper 67-176.
- 3.2-5 Keys, J. W., Longitudinal Aerodynamic Characteristics of Blunted Cones at Mach Number of 3.5, 4.2 and 6.0, NASA TN D-2201 (February 1964).
- 3.2-6 Coakley, T. J., Dynamic Stability of Symmetric Spinning Missiles, J. Spacecraft, Vol. 5, No. 10, pp. 1231-1232 (October 1968).
- 3.2-7 Allen, R. A., Air Radiation Graphs: Spectrally Integrated Fluxes Including Line Contributions and Self Absorptions, AERL Rept. 230 (September 1965).
- 3.2-8 Allen, R. A., Air Radiation Tables: Spectral Distribution Functions for Molecular Band Systems, AERL Rept. 236 (April 1966).
- 3.2-9 Yoshikawa, K. K. and D. R. Chapman, Radiative Heat Transfer and Absorption Behind a Hypersonic Normal Shock Wave, NASA TN D-1424.
- 3.3.1 Burns, R. K., "Two-Dimensional Steady-State Thermal Analysis of the Pioneer Heat Source for Use in the Isotope Brayton Application," Internal Memorandum 5221-004, NASA/LeRC, May 1970.

- 3.3-2 Lewis, D. R., Gaski, J. D., and Thompson, L. R., "Chrysler Improved Numerical Differencing Analyzer for 3rd Generation Computers - Rep. TN-AP-67-287, Chrysler Corp. (NASA CR-99595), Oct. 20, 1967
- 3.3-3 Thermophysical Properties of Heat Transfer Solid Materials, TPRC Purdue University, McMilland Co., 1967.
- 3.3-4 Kreith, F., "Principles of Heat Transfer," International Text-book Company, Scranton, Pa., 1958.
- 3.3-5 Perlmutter, M., "Inlet and Exit-Header Shapes for Uniform Flow Through a Resistance Parallel to the Main Stream," J. of Basic Engineering, September, 1961.
- 3.3-6 Rohsenow, W. M. and H. W. Choi, "Heat, Mass and Momentum Transfer," Prentice-Hall, Englewood Cliffs, N. J., 1961.

Figure 3.4-25

## THERMAL SIMULATION AEROSHELL



#### 4.0 HEAT SOURCE HEAT EXCHANGER

The basic heat source heat exchanger (HSHX) previously developed in NASA 3-10938 is illustrated in Figure 4.0-1. The circular heat exchanger consists of 18 tubes which spiral out from a center manifold and terminate at two tubular ring headers which form the circumference of the heat exchanger. The Brayton cycle gas is distributed to nine of the spiral tubes through the upper ring header. The gas is collected in the central reversing manifold and enters the nine return tubes which makes the return pass across the heat exchanger core to the bottom outlet ring header. The use of this type of heat exchanger results in an almost flat temperature distribution across the isotope heat source as well as across the HSHX during normal operation.

The modifications to the HSHX design to accommodate the larger isotope heat source array were minor and consisted of increasing the diameter of the heat exchanger from 53 inches (134.6 cm) in diameter to 55.5 inches (141 cm), and changing the inlet and exit manifolds to clear the revised IRV aerodynamic fence.

A HSHX design for a ground test unit employing a superalloy material was investigated. It was concluded that, while the superalloy design would work, it would be limited to a low number of operating cycles (i. e., startup and shutdown of system) and have a low margin of over-temperature capability. However, the cost saving is potentially significant. NASA chose Haynes-188 as the superalloy fabrication material after review of the study results. The analyses performed in the study are summarized in the following subsections.

##### 4.1 HSHX - SUPERALLOY EVALUATION

The design material of the HSHX developed under NAS 3-10938 was Cb-1%Zr alloy. This refractory was required due to the long term vacuum and high operating temperatures associated with the HSHX design requirements. As part of this study, the use of a superalloy HSHX design which would be adequate for a ground test system was evaluated. This test unit would have a considerably shorter life time requirement than the flight system. The approach taken for this evaluation was to review the candidate superalloys, select the most promising one, and revise the design of the HSHX to use the superalloy as dictated by a preliminary heat exchanger structural analysis.

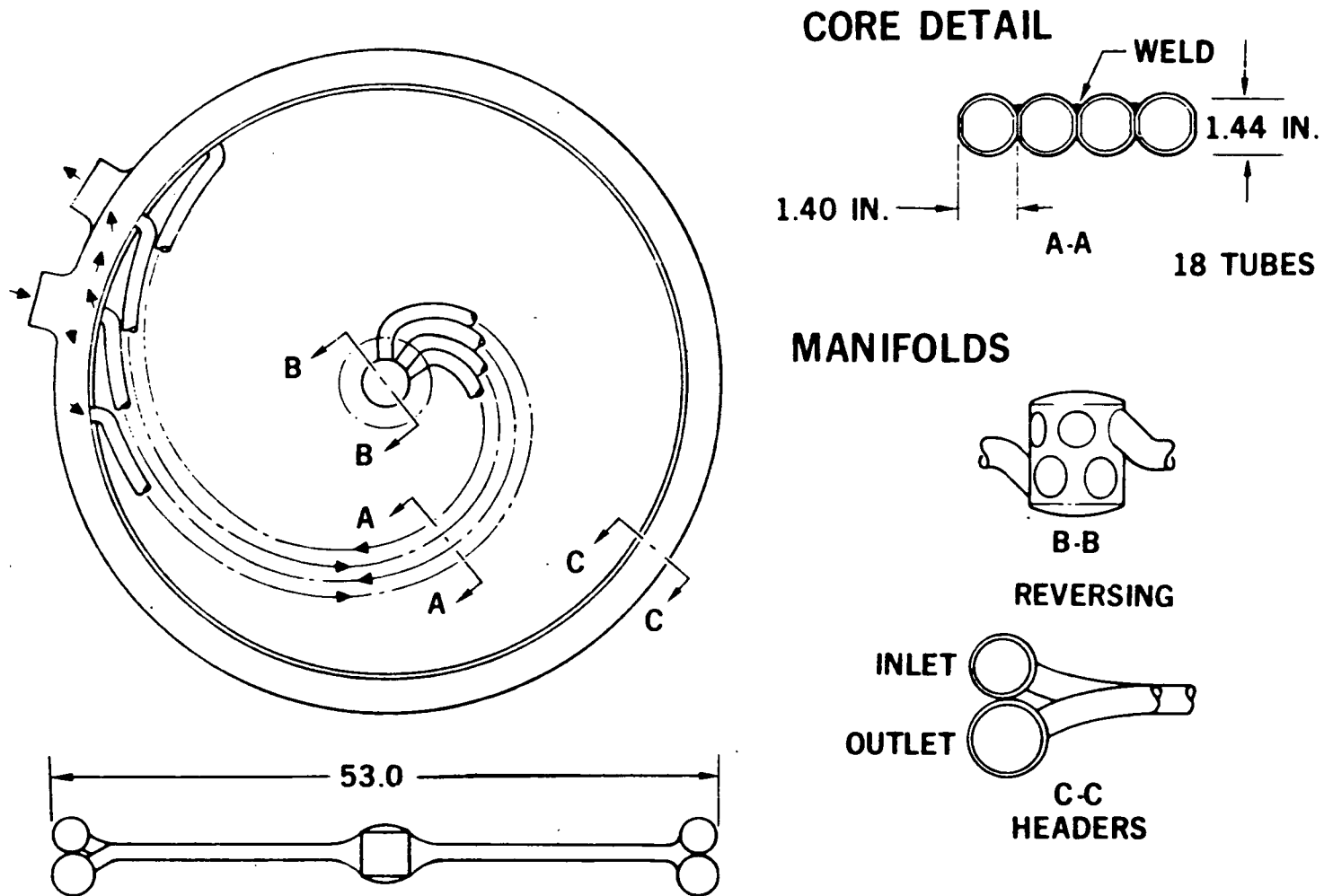


Figure 4.0-1 - Spiral Heat Source Heat Exchanger



## Selection of Superalloy Material

Important criteria which were considered in the selection of the superalloy for the HSHX test unit were:

- (a) Ductility and fabricability
- (b) Welding and brazing characteristics
- (c) Mechanical properties at service temperatures
- (d) Aging characteristics
- (e) Effects of prolonged exposure in vacuum

Other factors investigated included low cycle fatigue properties, heat transfer properties, and coating compatibility.

## Ductility and Fabricability

The HSHX is constructed from tubes approximately 1.4 in. OD by 0.030 in. wall thickness and welded into the circular header tubes. These tubes are manufactured from sheet materials by rolling and welding. The finished tubes also need to be bent to the spiral shape (shown in Figure 4.0-1) before assembly of the unit. The following superalloys were considered: Haynes 188, L605, Inconel 625, and Hastelloy X. The room temperature and operating temperature properties of the candidate alloys are shown in Table 4.1-I. These properties are important considerations for determining the fabricability of the sheet materials. Highly ductile materials are capable of being formed into the complicated shapes required by this design. Table 4.1-I illustrates that HA 188 has the highest room temperature ductility, which indicates that the tube forming and tube bending processes can be accomplished more readily than if Hastelloy X were used. However, all of these materials are susceptible to work hardening during tube forming and bending, and solution annealing will be required to restore ductility to the finished formed tubes.

## Welding and Brazing Characteristics

The basic spiral configuration of the HSHX unit involves a considerable amount of welding and brazing. All of the candidate alloys can be joined without undue difficulty. They can be welded by any of the generally used welding methods, such as TIG, MIG, electron beam, or resistance welding. AiResearch has experience in welding all of the candidate superalloys.

Brazing does not impose any difficulties in joining these materials. Vacuum or controlled atmosphere furnaces capable of rapid heating and

TABLE 4.1-I

MECHANICAL PROPERTIES OF CANDIDATE SUPERALLOYS  
(SHEET MATERIAL)

ALLOY	1,000 HR STRESS RUPTURE  1600°F (KSI)	TENSILE PROPERTIES					
		ROOM TEMP.			1600°F		
		FTY (KSI)	FTU (KSI)	EL (%)	FTY (KSI)	FTU (KSI)	EL (%)
HA188	9.9	67.0	130	62	35	55	65
L605	10.0	67.0	146	58	35	47	30
INCONEL 625	7.0	53.0	124	59	36	41	101
HASTELLOY X	6.0	52.0	114	43	26	37	50

cooling cycles produce the most consistent results. The selection of the brazing alloy depends upon the usable temperature range of the filler metal and its stability to prolonged exposures at elevated temperature under vacuum conditions.

Since the unit operates at a maximum temperature approaching 1700°F, the brazing alloy selected needs to have sufficient strength at this temperature. Figure 4.1-1 shows that at 1700°F the rate of evaporation of nickel, palladium, and cobalt are practically equal, and that this group is one order of magnitude better than gold and two orders of magnitude better than chromium. This indicates that filler materials rich in chromium will be susceptible to evaporation loss under the testing conditions. Nickel-palladium and cobalt-palladium alloys appear most satisfactory from a vacuum stability point of view, but their high brazing temperatures (~2300°F) would have an adverse effect on the mechanical properties of the superalloys. Nickel-silicon boron alloys, such as AMS 4779, have brazing temperatures in the range 1900°-2100°F. The melting range of these alloys is only a little above the operating temperature of the joints. Although the remelt temperature will be higher than the original melting temperature, nevertheless, the joint strengths at 1700°F may be inadequate for these alloys.

The nickel-gold-palladium alloys have melting ranges of 1850°-2100°F and the 50 percent Au, 25 percent Pd, and 25 percent Ni alloy (Palniro 1) is particularly recommended for brazing nickel and cobalt base superalloys for vacuum applications. This alloy has a melting range of 2015°-2050°F and is usually brazed at 2070°F, a temperature which will not affect the mechanical properties of the tubing materials.

#### Properties at Service Temperature

In the temperature range of 1500°-1700°F, there is not a great deal of difference between the stress rupture properties of the alloys evaluated. Figure 4.1-2 illustrates the approximate 1000-hour rupture properties of two cobalt-base alloys (L605 and HA 188) compared with two nickel-base alloys (Inconel 625 and Hastelloy X). It can be seen that the cobalt-base alloys have superior rupture strengths throughout this temperature range. Elevated temperature tensile properties are depicted in Figure 4.1-3. These data also show that the cobalt-base alloys have higher strength at anticipated service temperatures.

FIGURE 4.1-1  
EVAPORATION RATES OF SOME ELEMENTS UNDER VACUUM

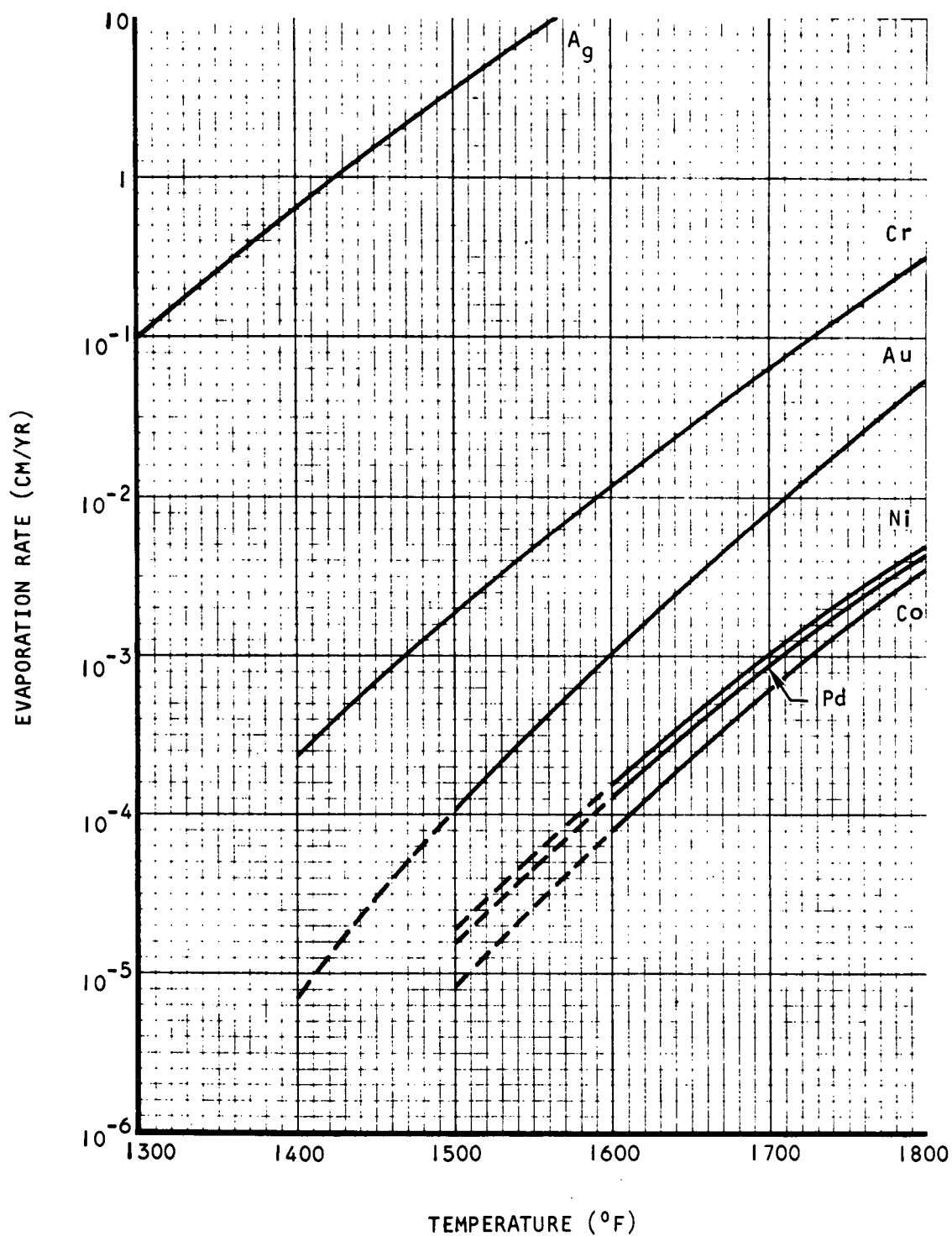
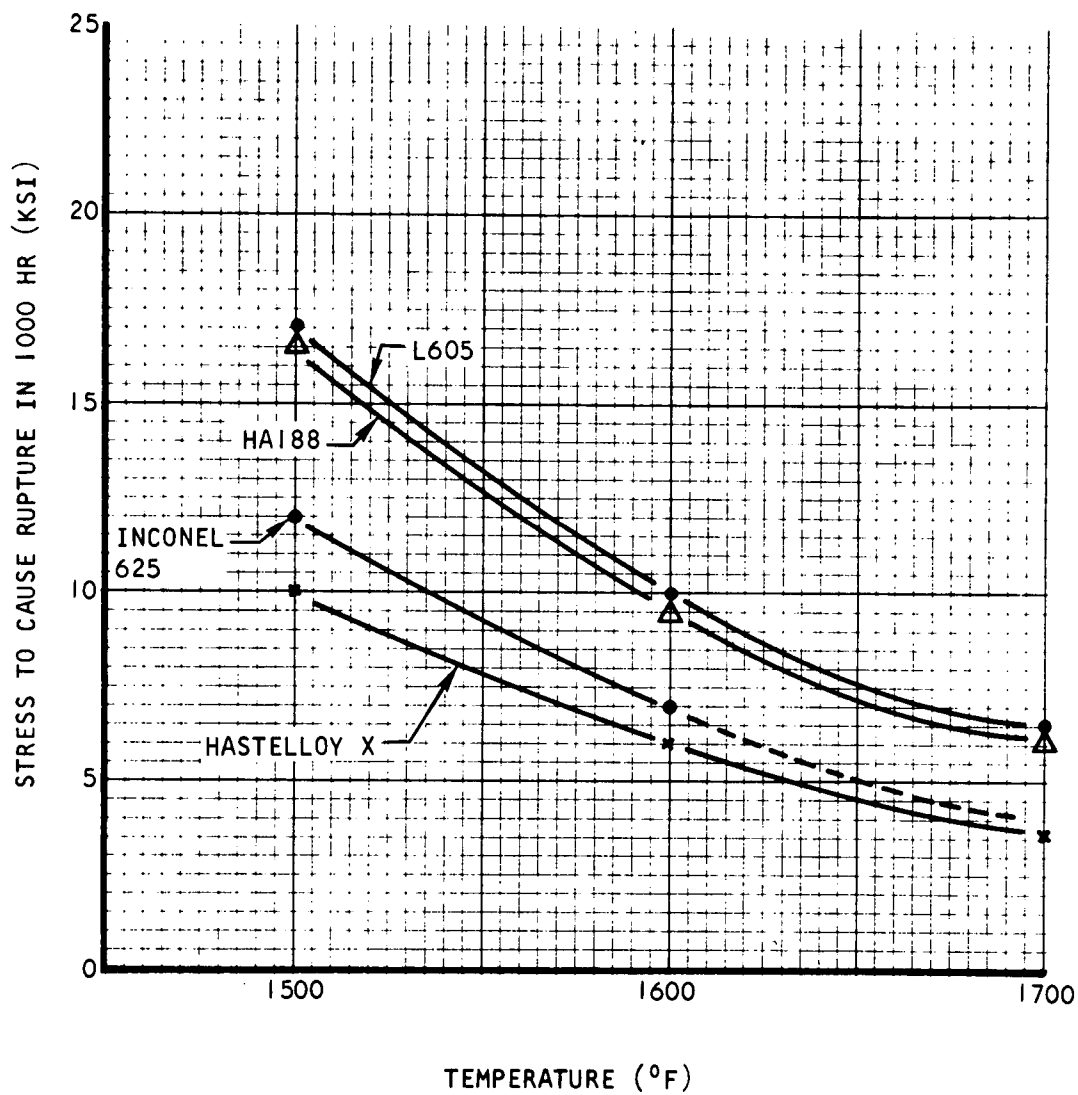
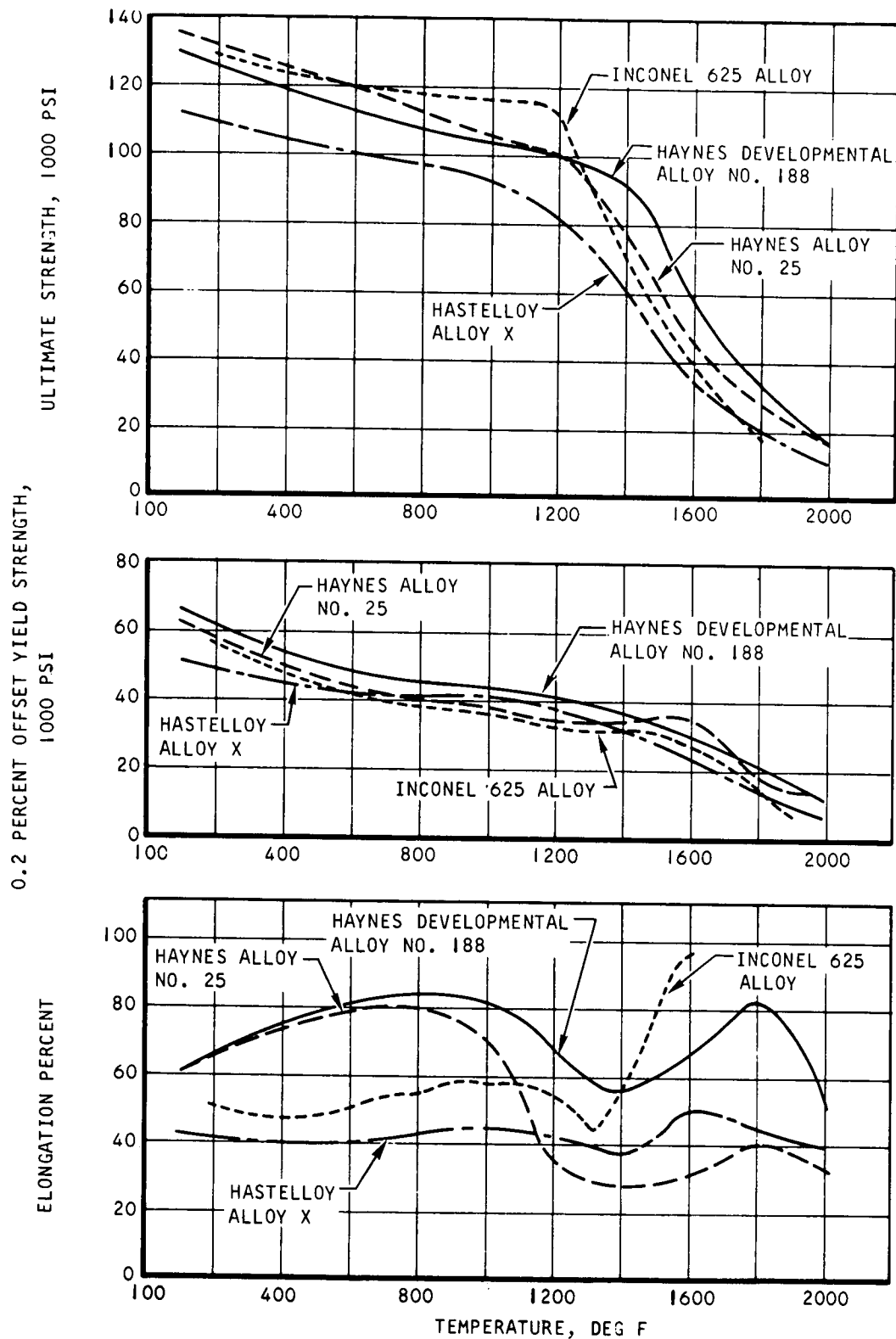


FIGURE 4.1.2  
COMPARATIVE STRESS RUPTURE PROPERTIES  
OF SHEET MATERIAL



**FIGURE 4.1-3**  
**COMPARATIVE TENSILE DATA,**  
**SHEET MATERIAL SOLUTION HEAT TREATED CONDITION**



### Aging Characteristics

None of the alloys considered are appreciably strengthened by age hardening, but all of them suffer some slight degradation of ductility when exposed at temperatures in the 1100°-1700°F range for long periods of time. The reasons for this embrittling effect is attributed to the formation of Laves phase (based on the formula, A<sub>2</sub>B). The nickel-base alloys (Hastelloy X and Inconel 625) are practically immune to Laves phase formation, and work recently conducted at the Stellite Division, Cabot Corporation, shows that HA 188 exhibits some loss in room temperature ductility after more than 3000 hours exposure in the 1300°-1700°F temperature range. A much more pronounced embrittling effect was reported for L605 (see Figure 4.1-4).

### Effects of Prolonged Exposure to Vacuum

When exposed to vacuum at elevated temperatures, pure unalloyed metals will evaporate at a rate determined by the following modification of the Langmuir equation:

$$S = 1.85 \times 10^6 \frac{Kp}{s} \sqrt{\frac{M}{T}}$$

where S = rate of sublimation, cm/yr

p = vapor pressure, torr

s = density of the solid material, gm/cm<sup>3</sup>

M = molecular weight of metal in the gas phase

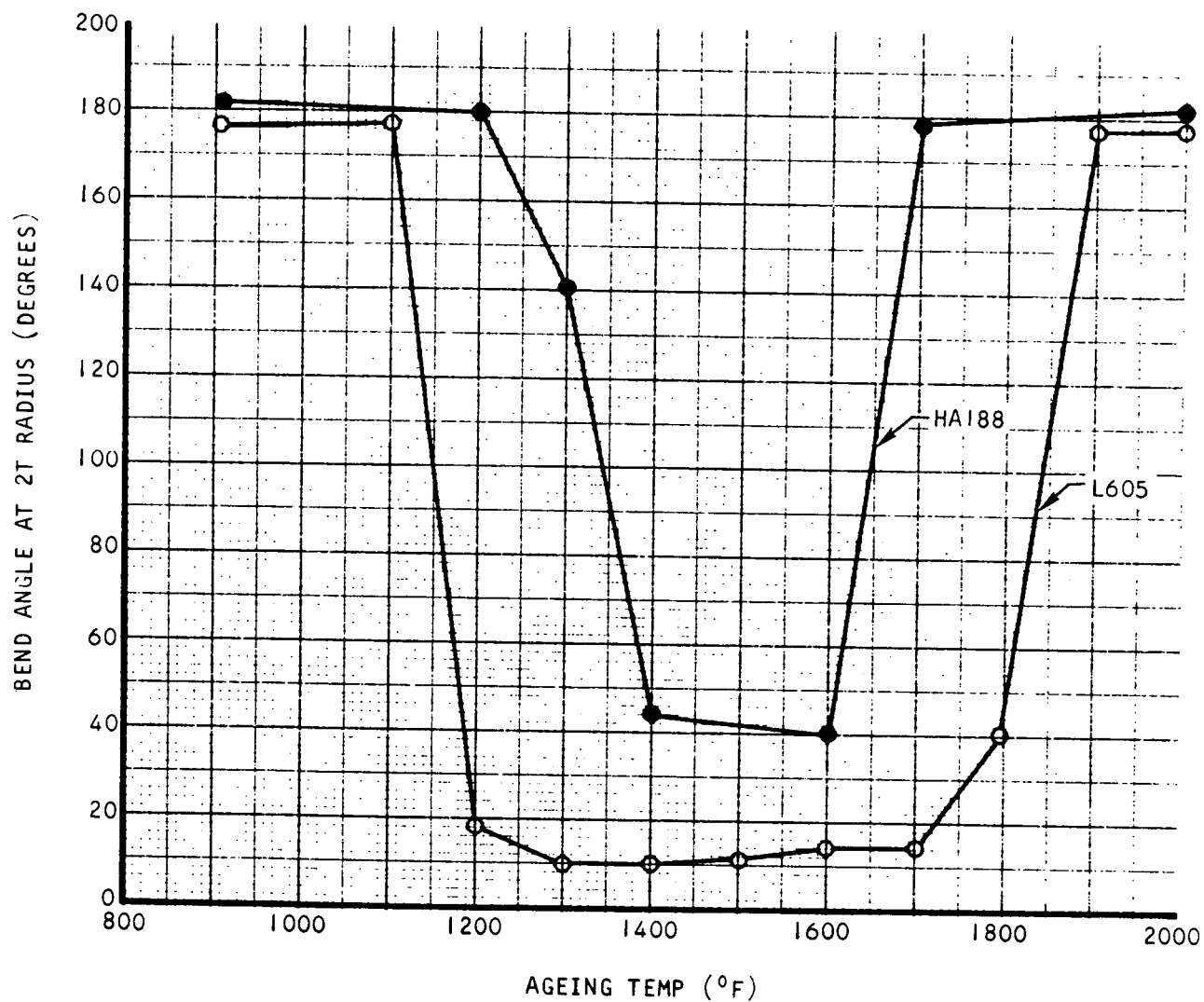
T = temperature, °K

K = evaporation coefficient

Multicomponent alloys will not be affected in the same way as pure metals. Evaporation of alloy constituents is nonlinear with time and results in concentration gradients of the more volatile constituents throughout the thickness of the member. Further, the changes in composition and microstructure may result in important changes in physical and mechanical properties.

Charlot and Westerman studies the evaporation of Hastelloy X-280 and L605 in vacuum at 2048°F and 2192°F. In 2000 minutes (33 hours) the weight loss at 2048°F was equivalent to a penetration of 0.2 mils. Assuming a linear rate of penetration, the penetration at 5000 hours would be only 30 mils. The approximation they have made to convert weight loss to

FIGURE 4.1-4  
EFFECT OF AGEING FOR 300 HR.  
ON ROOM TEMPERATURE BEND DUCTILITY





penetration depth, however, is very rough and ignores void formation and nonuniform attack. Their data, therefore, are of little value for predicting total penetration in 5000 hours at 1670°F.

Work conducted at Oak Ridge National Laboratory showed that the rate of evaporation of HA 188, L695 and AISI 316 were all of the same order of magnitude when tested at 1500°-1700°F under a vacuum of  $10^{-9}$ - $10^{-10}$  torr. Hastelloy N, however, had an evaporation rate almost one order of magnitude less than HA 188. Evaporation of iron, manganese, and chromium from the surface of the cobalt-base alloy causes a relative increase in concentrations of cobalt, tungsten, and silicon at the surface, resulting in the formation of brittle Laves phase ( $\text{Co}_2\text{W}$ ). At 1500°-1700°F, however, the evaporation rate is small (approximately  $10^{-4}$  mg/cm<sup>2</sup>/hr) and "swiss cheese" effect was scarcely noticeable at 870°C (1600°F). Consequently, the loss of mechanical properties caused by prolonged exposure (3000-5000 hours) to a vacuum of  $1 \times 10^{-5}$  torr in the service temperature range will probably be significant but acceptable from a purely evaporation standpoint. It is significant to point out that Cb has an evaporation rate of about 7 orders of magnitude less than any of the superalloys.

D. T. Bourgette at ORNL has reported the results of long-time exposure of Type 316 stainless steel in vacuum at high temperatures (800° to 1000°C).

- (a) Subsurface void formation
- (b) Grain growth at surfaces
- (c) Excessive void formation in grain boundaries
- (d) Disappearance of precipitation phases
- (e) Material loss from edges of surface grains

These effects are depicted graphically in Figure 4.1-5.

### Heat Transfer Properties

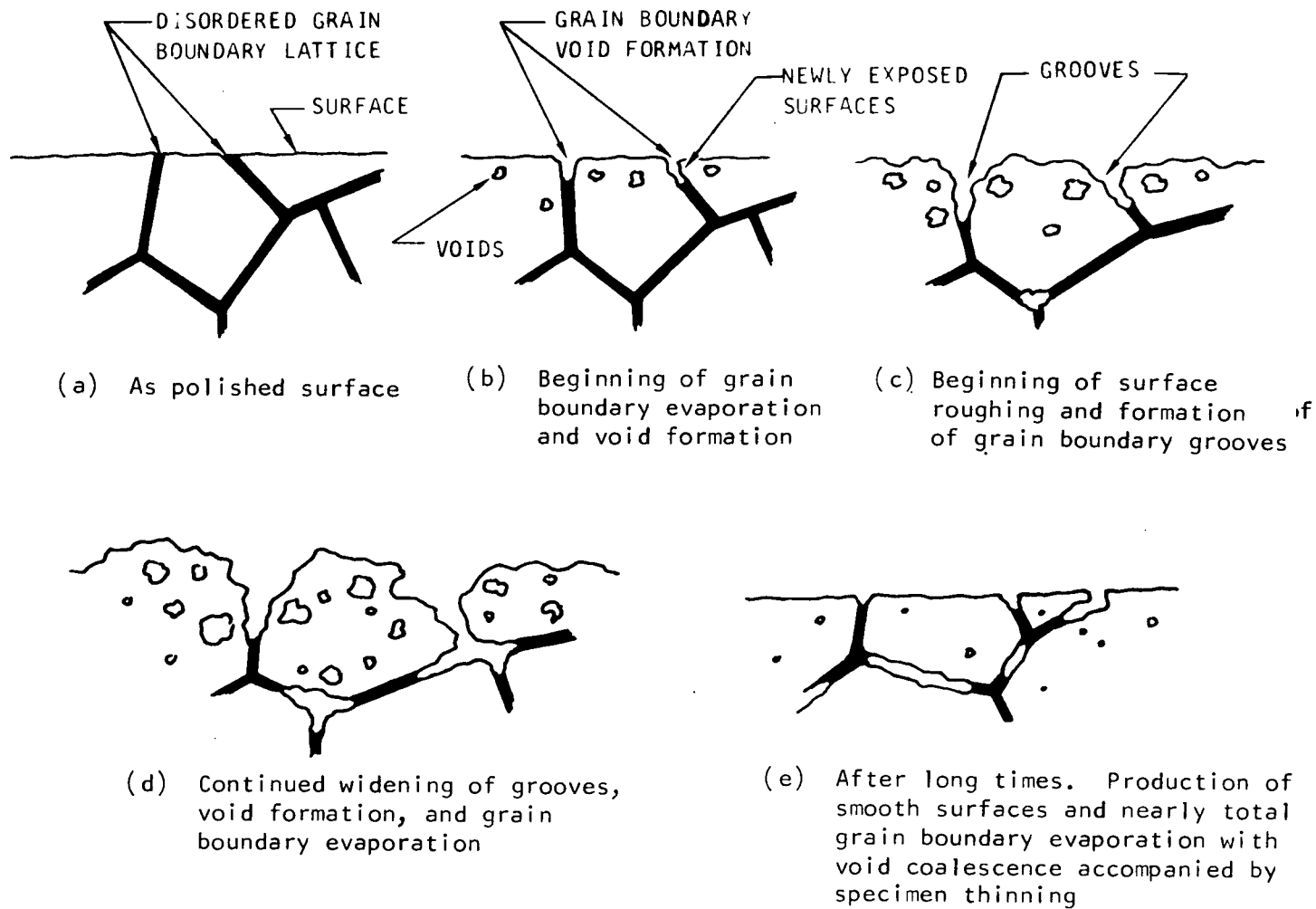
Some of the physical properties of the candidate alloys are shown below in Table 4.1-II.

TABLE 4.1-II

Alloy	Thermal Conductivity (Btu/ft <sup>2</sup> /hr/°F/in)			Coeff. Thermal Expan. (in/in/°F × 10 <sup>-6</sup> )		
	1400°F	1600°F	1800°F	1400°F	1600°F	1800°F
HA 188	-	-	-	9.2	9.7	10.3
L605	165	181	197	8.61	9.06	9.41
Inconel 625	144	158	175	8.5	8.8	-
Hastelloy X	166	180	195	8.81	9.02	9.20

FIGURE 4.1-5

Evaporation Problem of Materials in Vacuum Using an Evaporation Sequence for Thin Specimens of Type 316 Stainless Steel Exposed to High Vacuum Between 1475° and 1835° F as an Example



## Coating Compatibility

In order to duplicate the emissive characteristics of coated columbium alloy, it will be necessary to coat the surfaces of the superalloy with iron titanate. Apparently, this coating has never been applied to HA 188 before, but communication with Oak Ridge National Laboratory suggests that such a combination is quite feasible and that the adhesion of the diffused coating should be satisfactory.

Walek and his co-workers at Pratt and Whitney Aircraft have studied the application of iron titanate to AISI 310 stainless steel tubes. The tubes, coated with a 4 mil thick coating of iron titanate, were tested at 1350°F for 20,000 hours in a vacuum of  $10^{-8}$  mm Hg. The appearance of the specimen at room temperature had not appreciably changed by the test exposure, and apart from the edges of the specimen, the coating remained well bonded to the substrate. A stable thermal emittance of about 0.88 was demonstrated throughout the entire 20,000 hours of testing.

## Summary

Based on the above survey Haynes 188 was selected as the best candidate superalloy for the test unit. This selection was based mainly on its high ductility and strength at the HSHX operating temperatures.

## 4.2 DESIGN DESCRIPTION

The revised HSHX design is shown schematically in Figure 4.2-1. The major modification introduced in this study was the means in which the gas flow reversal takes place at the center of the spiral. Previously (Figure 4.0-1) this flow reversal was accomplished by a cylindrical manifold located at the hub of the spiral. In the current design this is accomplished by connecting every third tube together with a short "U" tube type piece. In order to fill the core of the spiral as much as possible with tubes, two of the three tube pieces are fabricated with a compound bend which allows them to go over or under the adjacent tubes to connect with the appropriate return tube. Thus the maximum height of the hub of the spiral is approximately three times the diameter of the tube (i. e., 4.32 in.). The eighteen tubes which make up the heat exchanger core are approximately 70 in. long and are constructed from 0.045-in. sheet stock. The inlet ring manifold is 2.40 in. in diameter while the exit ring manifold is 3.30 in. in diameter. The overall weight of the HSHX is 195 lb. All external surfaces of the heat exchanger are coated to provide a high emittance surface ( $\epsilon = 0.88$ ).

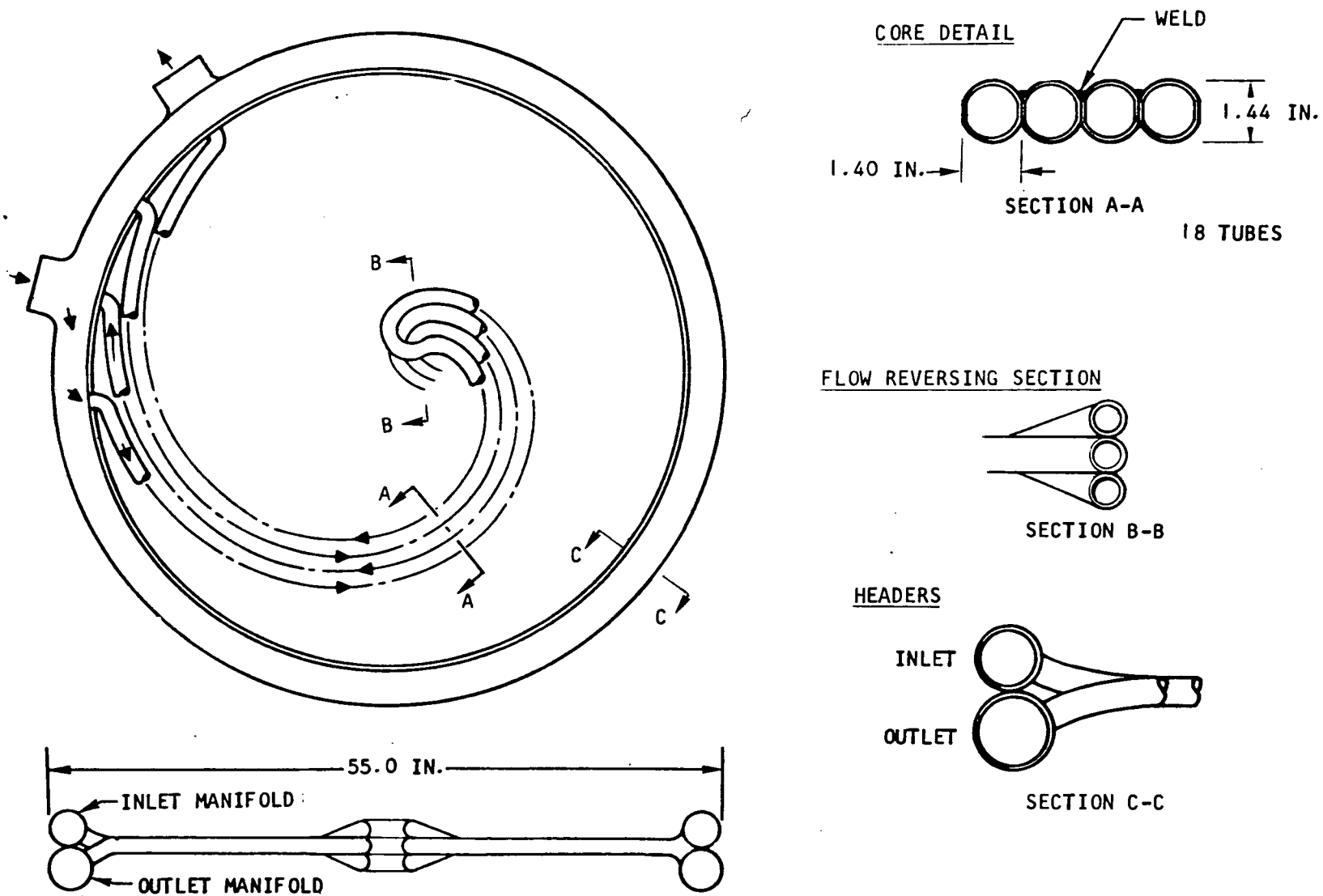


Figure 4.2-1 - Spiral Heat Source Heat Exchanger

#### 4.2.1 Thermal Analysis

##### Pressure Drop and Flow Distribution

Pressure drop and flow distribution should be considered simultaneously when discussing design requirements for the heat source heat exchanger. Based on structural and fabrication considerations, the tubes and the inlet and outlet manifolds are made with a circular cross section. The tubes and the manifolds must be judiciously sized to keep low overall pressure drop and to keep the maldistribution of the flow to the heat exchanger tubes within acceptable limits. As fluid is drained from the inlet manifold into the tubes conservation of momentum will result in a tendency for the static pressure to increase in the direction of the manifold flow. Proper selection of the inlet and outlet manifold sizes along with a U-flow configuration will result in the momentum recovery along the inlet manifold offsetting pressure drops due to cumulative inlet manifold friction and outlet manifold friction and momentum changes.

The design procedure is to assume theoretically uniform flow to various tubes of the heat exchanger and then size the inlet and outlet manifolds so that the pressure drop from the inlet to the outlet flange of the heat exchanger is the same for the flow paths that go through the first and last tubes. The pressure drop through the path that includes the middle tube can then be evaluated, and the fractional maldistribution approximated as:

$$\text{Flow maldistribution} = \frac{2 \left( \sqrt{\Delta P_{\max}} - \sqrt{\Delta P_{\min}} \right)}{\sqrt{\Delta P_{\max}} + \sqrt{\Delta P_{\min}}}$$

The heat source heat exchanger component pressure drops and subsequent calculated flow distribution are summarized in Table 4.2-I.

##### Steady State

A thermal analysis was carried out for the heat source heat exchanger with the heat source diameter taken as 55.0 in. using an AiResearch Thermal Analyzer Computer program. The analysis considered the radiant heat interchange between the heat source and the HSHX, the conduction across the heat exchanger, and the convection between the Brayton fluid and the walls of the HSHX.

TABLE 4.2-I  
PRESSURE DROP SUMMARY

	Pressure Change, psi		
	First Loop*	Middle Loop	Last Loop**
Inlet manifold momentum	0	+0.172	+0.230
Inlet manifold friction	0	-0.045	-0.067
Inlet manifold to tube	-0.091	-0.105	-0.113
Tube friction momentum and turning losses	-0.40	-0.40	-0.40
Tube to outlet manifold	-0.063	-0.035	-0.023
Outlet manifold friction	0	-0.008	-0.012
Outlet manifold momentum	0	-0.120	-0.157
Net change in pressure	-0.554	-0.541	-0.54

Flow maldistribution  $\approx$  1 percent

\*Nearest from entrance  
\*\*Furthest from entrance

A sketch of the heat transfer model assumed for the analysis is shown in Figure 4.2-2. The heat flow in the system is simulated by a thermal-resistance thermal-capacitance network. Each element in the system is represented by a node in this electrical analog.

The surface of the heat source facing the HSHX is divided into several elements of equal areas. It is assumed that all the heat generated in the heat source ( $23.5 \text{ kw}_t$ ) is radiating from this surface and is distributed uniformly over the surface. The heat source temperatures in this analysis should be considered as effective source temperatures. Therefore, any temperature drop in the heat source elements must be added to these temperatures to get the maximum source temperature.

The surface of the HSHX facing the heat source is divided into many elements. Each of these elements is divided into two halves, one half faces the heat source and the other half faces the insulation on the back of the HSHX. Heat is transferred between these two halves by conduction and radiation and they are thermally connected, through convection, to the flowing Brayton fluid.

The assumptions used in the thermal analysis are summarized below.

- a. Each element is isothermal and assumes one discrete temperature
- b. Each surface is gray.
- c. The radiation reflected and emitted from each surface is distributed diffusely.
- d. The side walls and the surface on the back of the HSHX are perfectly insulated.
- e. An emissivity of 0.88 was assumed for the coated surfaces. The fact that these surfaces are gray and that heat is emitted as well as reflected by them, is accounted for by assuming an effective emissivity of 0.80.
- f. A prescribed and uniform heat flux exists at the elements of the heat source.
- g. The Brayton fluid in the HSHX is also divided into elements. Heat is transferred between each element and the surfaces of the HSHX by convection.

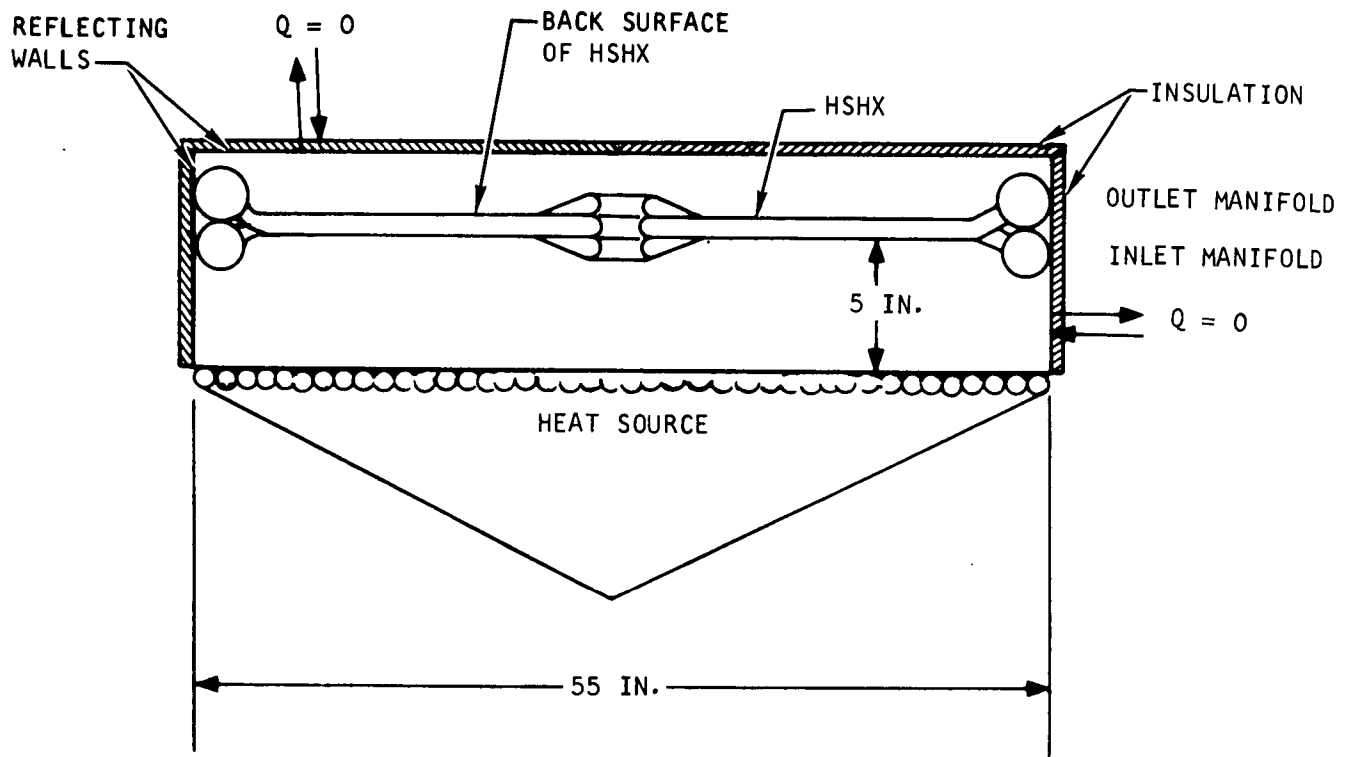


Figure 4.2-2 - Model Used for Heat Transfer Analysis



- h. The heat transfer coefficient inside the tubes and the manifolds of the HSHX is constant and is predicted by the Dittus-Boelter correlation for fully developed turbulent flow.

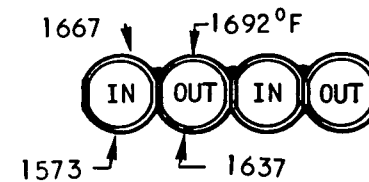
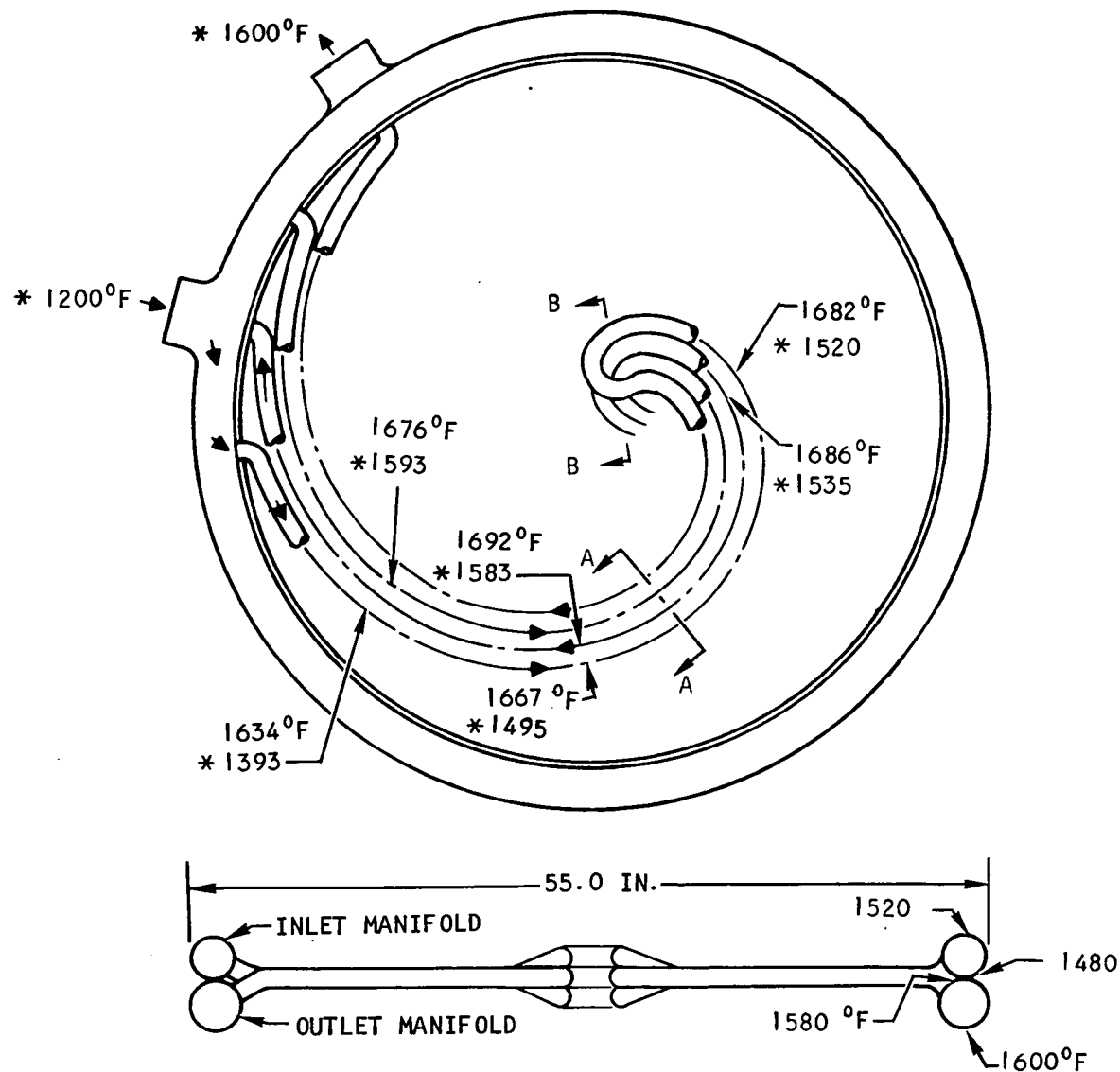
The steady-state temperature distribution in the HSHX is shown in Figure 4.2-3. A typical temperature distribution along one of the tubes and around the inlet and outlet manifolds is depicted in this figure. The Brayton fluid temperature rise is also shown. The fluid enters the HSHX at 1200°F; the temperature gradient along the tube is large in the inlet pass due to the high heat flux in this pass. The temperature gradient decreases gradually in the outlet pass. The fluid outlet temperature is 1600°F which corresponds to full output power of 23.5 kw<sub>t</sub>.

### Startup

During startup of the system, the heat source temperature is assumed to be brought up first to about 1600°F. This is accomplished with the insulation in place and no Brayton fluid flowing inside the HSHX. At this temperature the full power of the heat source is turned on and the gas starts flowing inside the HSHX. The inlet gas temperature obviously depends on the transient performance of the heat source heat exchanger as well as on the transient performance of the other components in the system. An inlet temperature profile was obtained in Ref. 2.1-1 from a computer program simulating a Brayton cycle space power plant. The program assumed that the change in the Brayton fluid flow rate during startup is as shown in Figure 4.2-4. The resulting inlet temperature profile, which is depicted in Figure 4.2-5 was used in the present analysis to obtain the transient temperature at various points in the HSHX cavity during startup conditions.

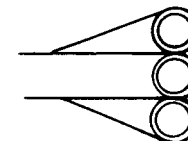
The thermal capacity of the heat source was assumed to be equal to the IRV heat source (150 Btu/°F). This thermal capacity is quite large compared to the thermal capacity of the HSHX. Hence, the transient behavior of the system is controlled by the heat source.

The gas temperature response at the outlet of the HSHX during startup is shown in Figure 4.2-6. This figure reveals that the gas outlet temperature reaches about 1400°F in about 5 min. It continues to rise in a more gradual manner to the desired value of 1600°F. The fast initial rise may be attributed, in part, to the small flow rates of the Brayton fluid immediately after startup. The steady-state condition is reached after about 200 min.



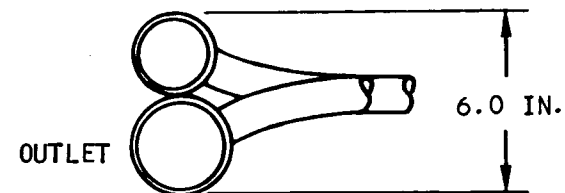
SECTION A-A

CORE DETAIL



SECTION B-B

FLOW REVERSING SECTION



HEADERS

\* FLUID TEMPERATURE

Figure 4.2-3 - Heat Source Heat Exchanger Steady-State Performance

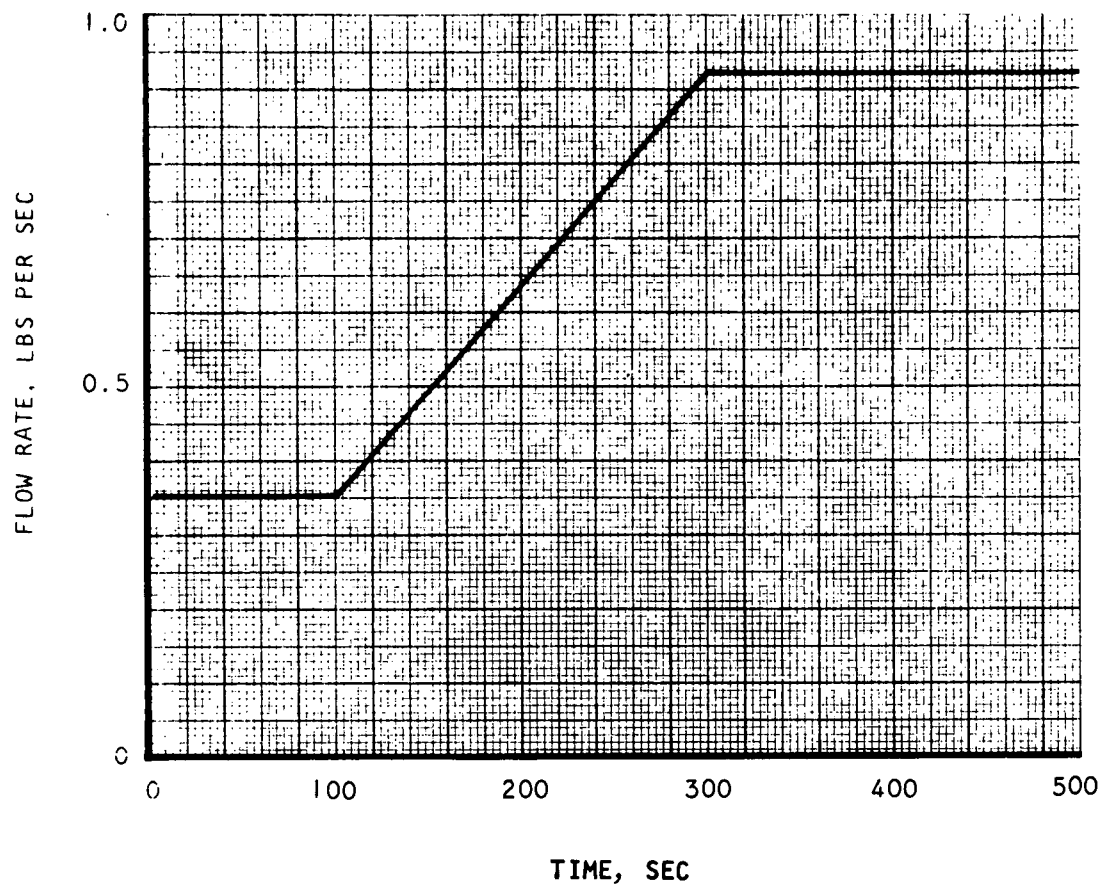


Figure 4.2-4 - Change of Flow Rate During Startup

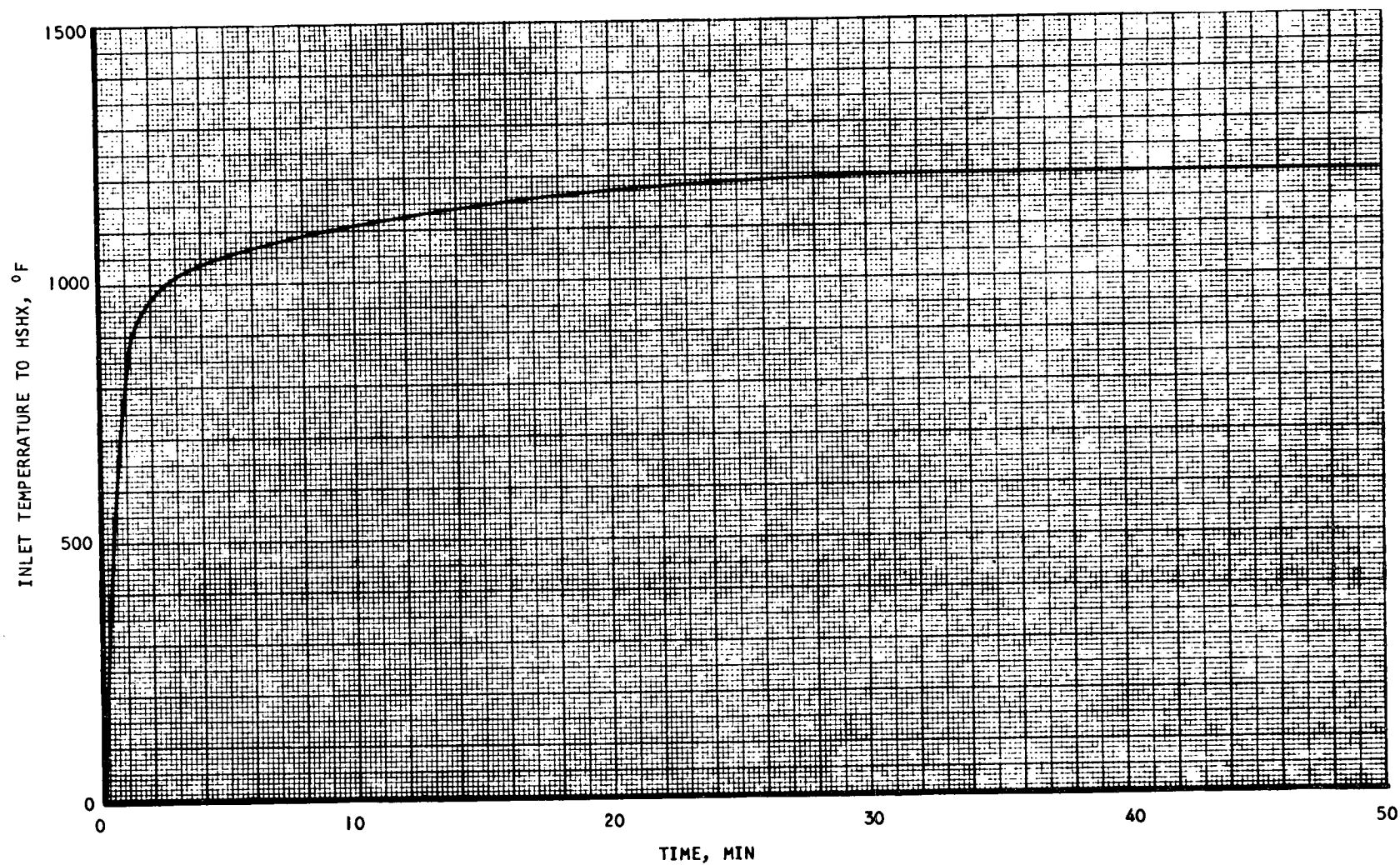


Figure 4.2-5 - Gas Inlet Temperature to HSHX During Startup

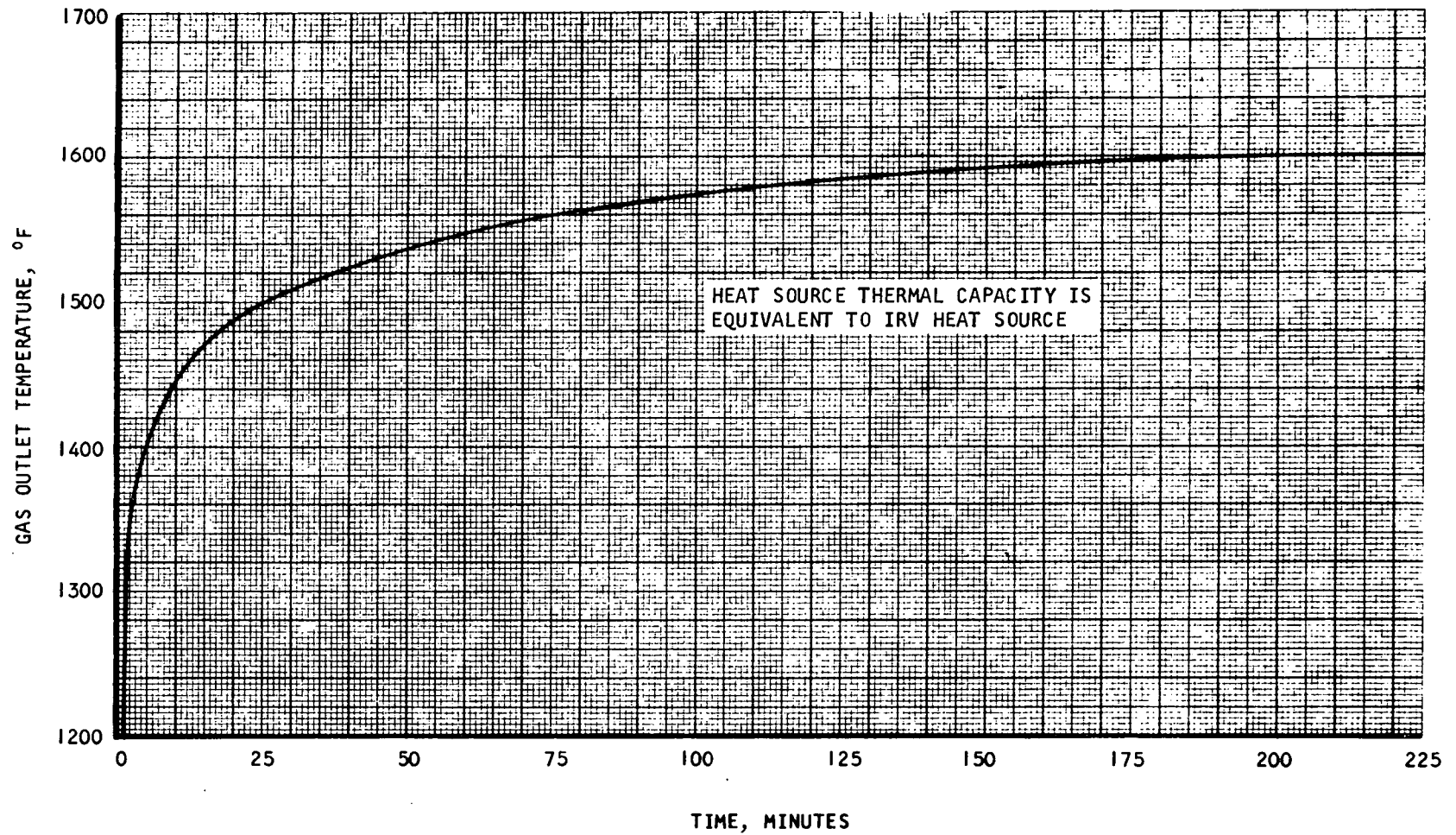


Figure 4.2-6 - Gas Outlet Temperature During Startup

The response of the maximum effective source temperature (at the center of the heat source) is shown in Figure 4.2-7. The initial temperature is assumed uniform and equal to 1600°F. The dip in the source temperature immediately after startup is due to the sudden flow of cold gas in the HSHX tubes.

Figure 4.2-8 shows the temperature response of the heat exchanger tubes at midpoint along the tube length. A temperature gradient across the HSHX was assumed initially. After startup this temperature gradient, as indicated by the temperature difference between the upper and lower surfaces of the tubes, reaches a steady state value of about 85°F in the inlet tubes and about 45°F in the outlet tubes. The dip in temperature in the inlet tubes immediately after startup is due to the cold gas entering the tubes during this period. This dip is absent in the outlet portion of the tube since the gas has already heated up by the time it reaches the outlet tube.

The temperatures of the inlet and outlet manifolds during startup are depicted in Figure 4.2-9 and 4.2-10 respectively. The temperature gradient around the circumference is more pronounced for the inlet manifold than for the outlet manifold. A temperature drop of 100°F was assumed across each manifold initially.

It may be noted that the present analysis was carried out for a heat source with a thermal capacity of 150 Btu/°F. A heat source with a smaller thermal capacity would cause the steady state conditions to be reached faster, but would not have an appreciable effect on the temperature gradients in the HSHX.

### Shutdown

The shutdown of the system may be accomplished by either deploying the insulation on the back of the HSHX or deploying the Isotope Reentry Vehicle heat source. In either case the Brayton fluid may be allowed to flow in the HSHX during the cooling of the system. A more severe transient cooling case would result if the gas flow is shut off simultaneously with the deployment of the insulation. Therefore, the following analysis is restricted to the case where there is no gas flow during the cooling of the system. In all the cases discussed below, it is assumed that the heat source has a thermal capacity equivalent to the IRV heat source (150 Btu/°F) and that the heat source is operating at full power.

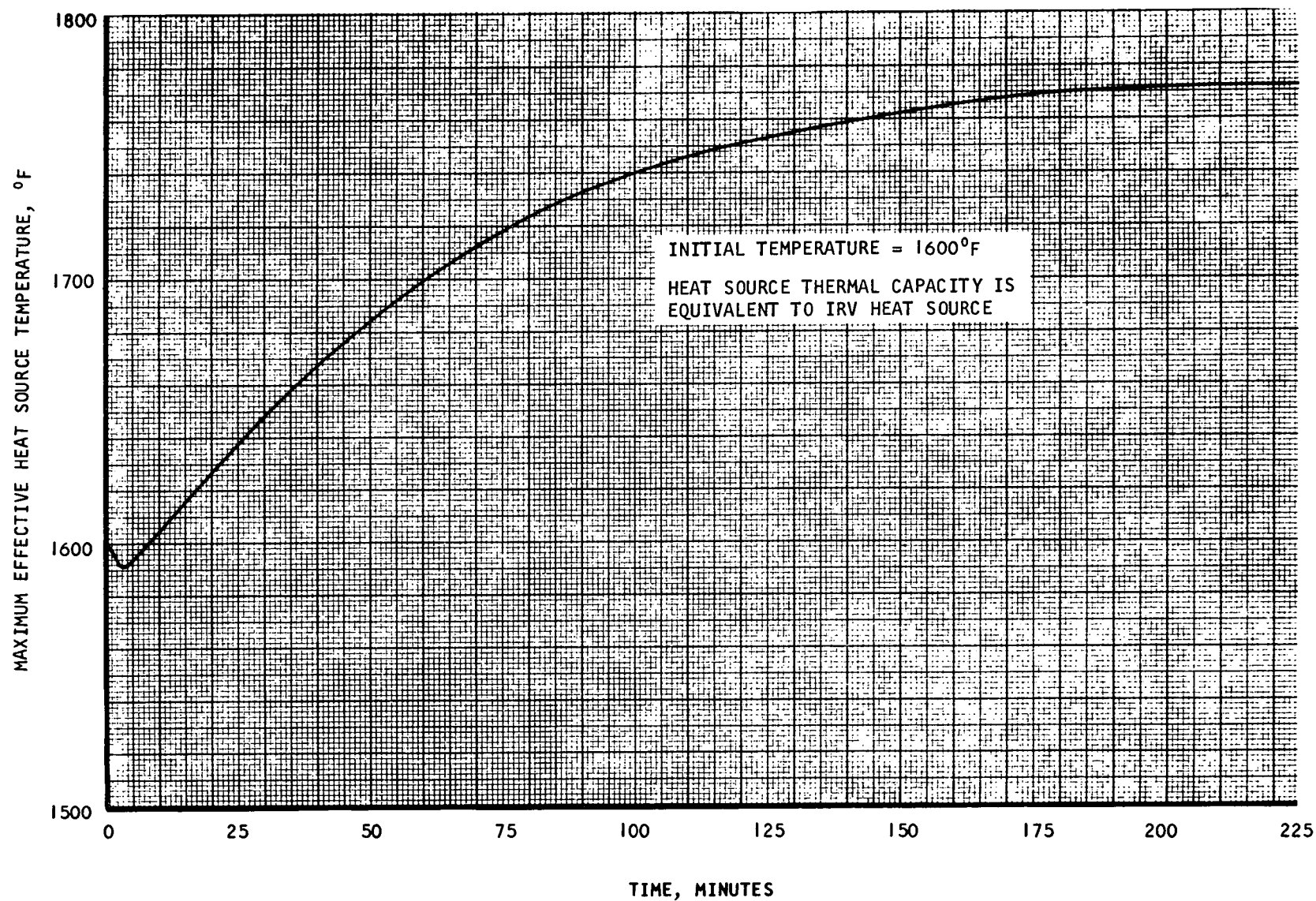


Figure 4.2-7 - Response of the Maximum Effective Source Temperature During Startup

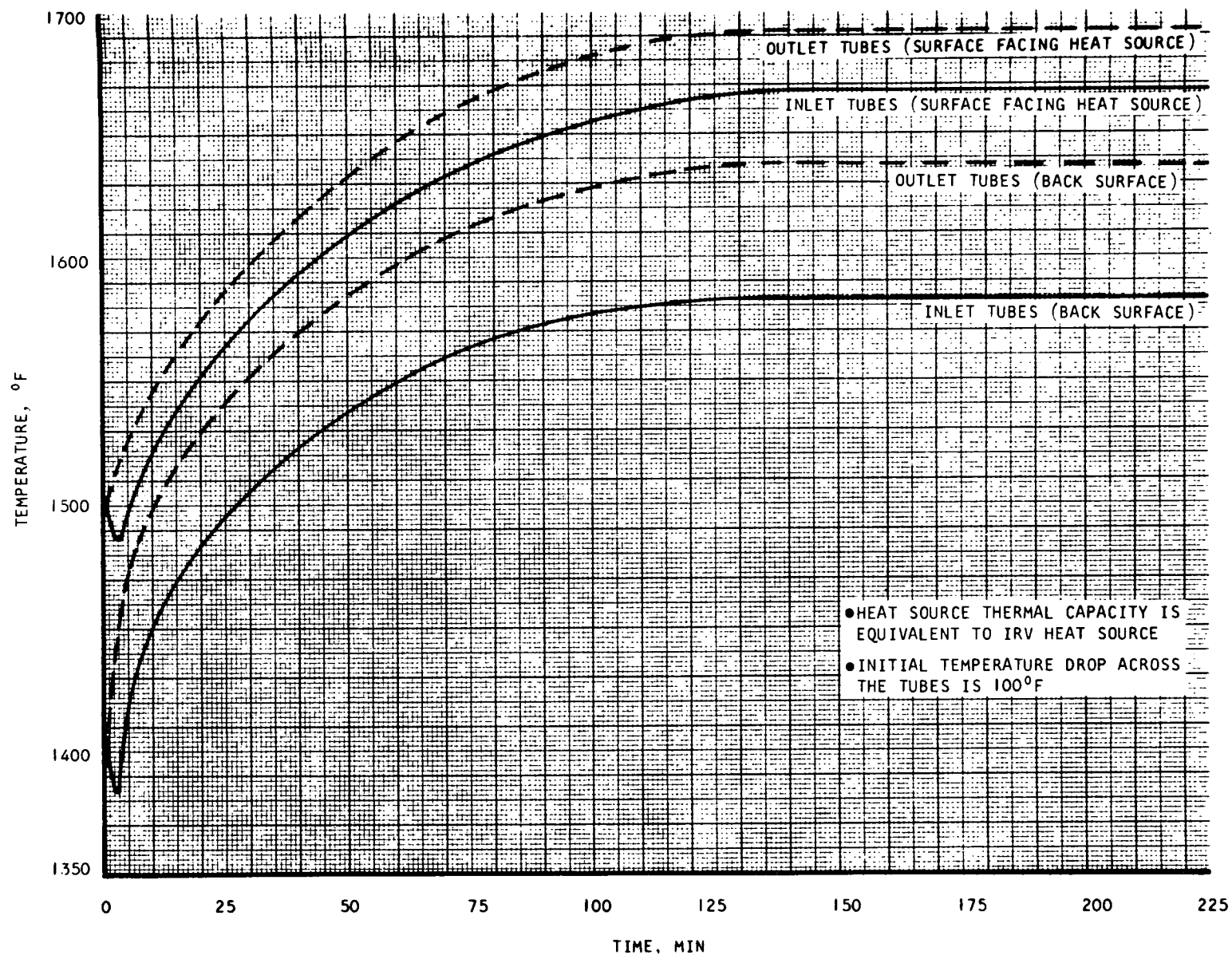


Figure 4.2-8 - Tube Temperature During Startup  
(Mid Point Along Tube Length)



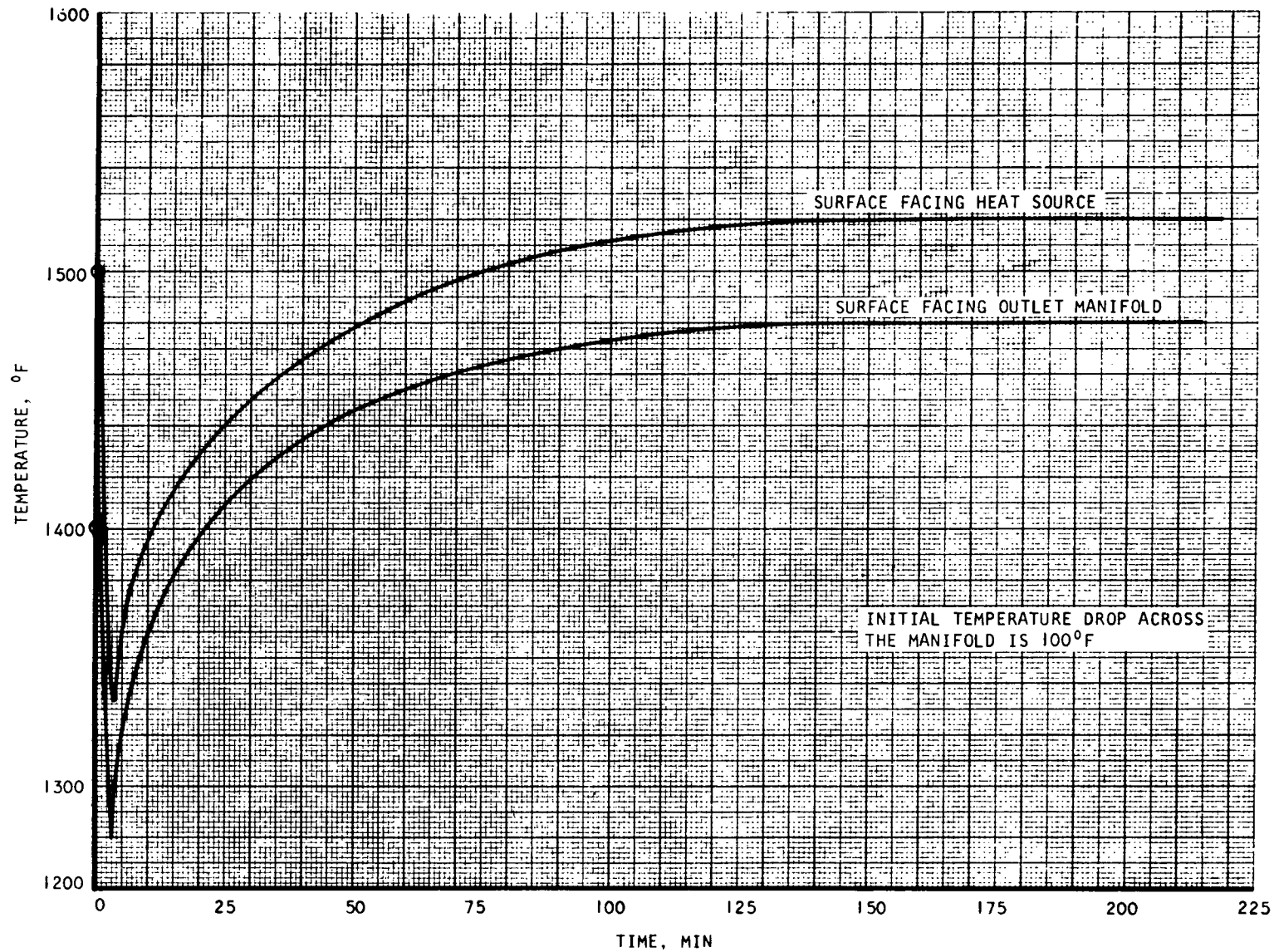


Figure 4.2-9 - Inlet Manifold Temperature During Startup

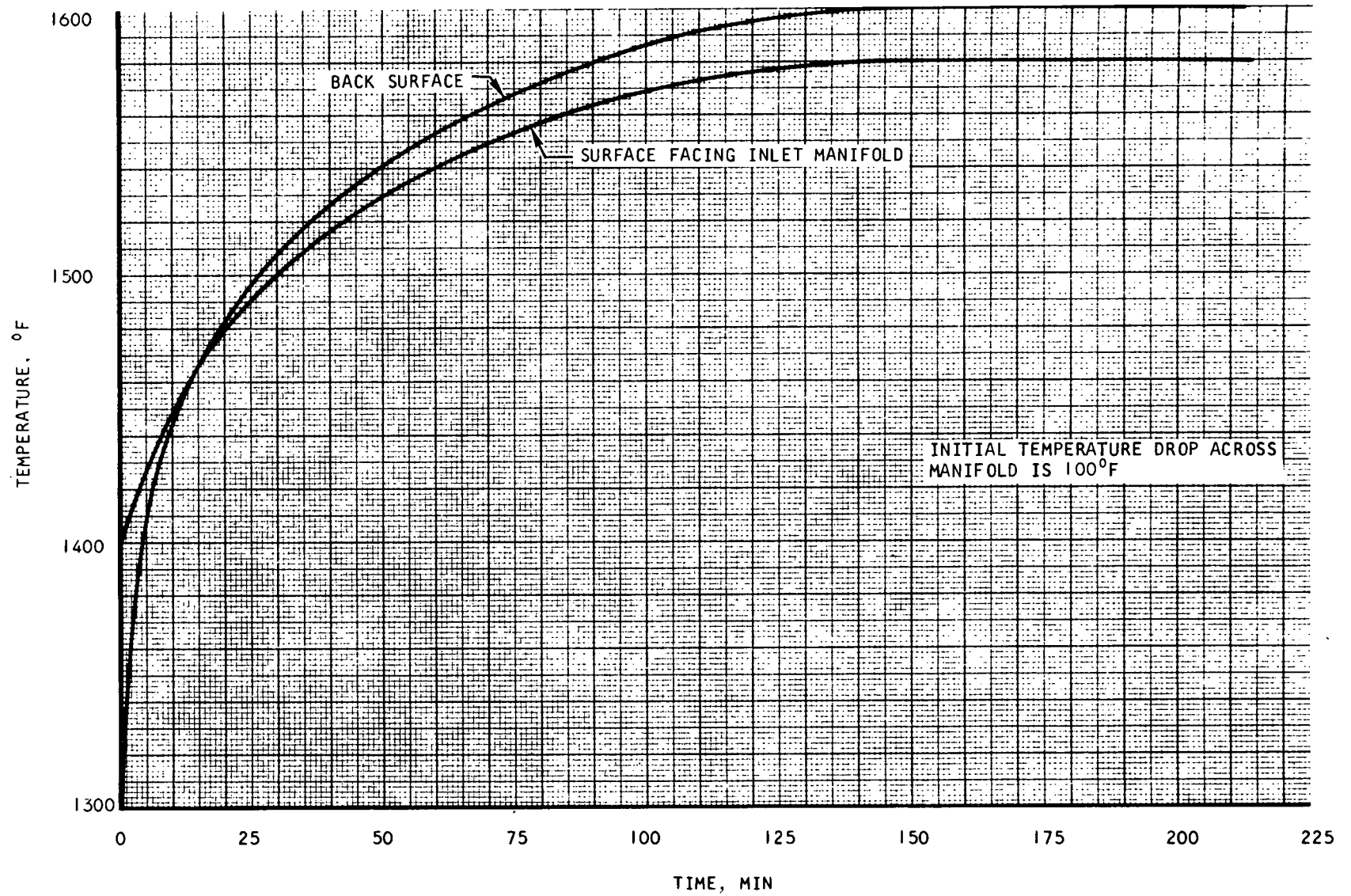


Figure 4.2-10 - Outlet Manifold Temperature During Startup

## 1. Heat Source Deployed

The heat source is deployed as shown in Figure 4.2-11. It is assumed that the HSHX does not "see" the heat source in this position. The HSHX cools down through radiation to a heat sink which is kept at 0°F. The analysis assumes that the gas flow into the HSHX is shut off simultaneously with the deployment of the heat source.

Figures 4.2-12 to 4.2-14 show the temperature response at various points in the HSHX during shut down. The initial temperatures were assumed to be the steady state temperatures with the heat source in position (see Figures 4.2.2 and 4.2.3)

Figure 4.2-12 depicts the temperature response of the HSHX tubes during shutdown. Since there is no gas flowing in the HSHX in this case the temperature along the tubes is quite uniform and there is no appreciable difference between the temperatures of the inlet and outlet tubes. Figures 4.2-13 and 4.2-14 depict the response of the inlet and outlet manifold temperatures, respectively, during shutdown. In Figure 4.2-13 the temperature of the portion of the manifold facing the outlet manifold shows a rise of 45°F, immediately after shutdown, before starting to cool down. This is due to the following reasons: (1) this portion of the inlet manifold does not "see" the heat sink, and (2) no gas is flowing inside the inlet manifold. The temperature drop across the inlet manifold reaches a maximum value of 380°F after about 10 minutes from the starting of the shutdown procedure. The maximum temperature drop across the outlet manifold is shown in Figure 4.2-14 to be about 130°F and is reached after 30 minutes.

## 2. Insulation Deployed

The cooling is accomplished in this case by deploying the insulation on the back of the HSHX, as shown in Figure 4.2-15, thus allowing the back surfaces of the HSHX to radiate to a heat sink which is kept at 0°F. The gas flow is assumed to be shutoff at the same instant the insulation is deployed. The thermal capacity of the heat source is assumed to be equal to the IRV heat source (150 Btu/°F). The initial temperature of the HSHX is the steady state temperature prevailing before the shutdown of the system.

Figure 4.2-16 shows the temperature response of the HSHX tubes. Due to the absence of gas flow inside the tubes, the temperature variations along the tubes and between the inlet and outlet tubes are very small. A severe

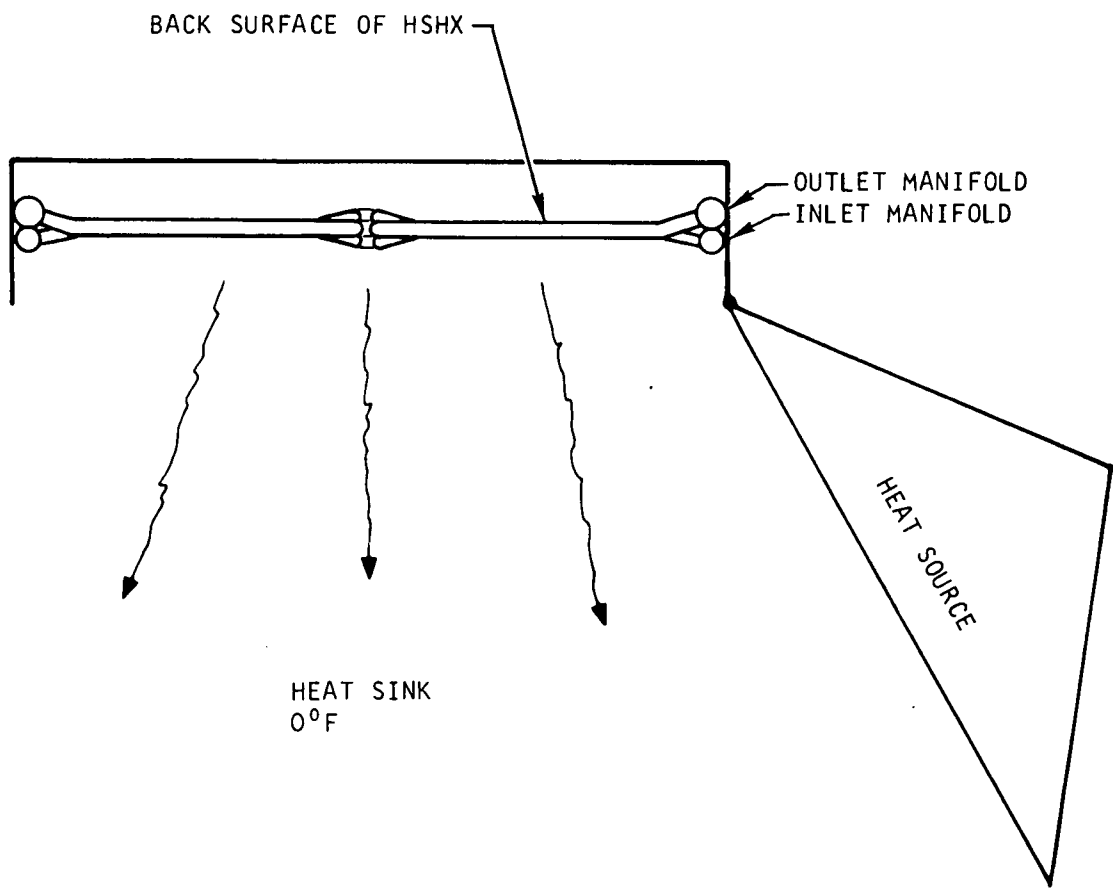


Figure 4.2-11 - Heat Source Deployed

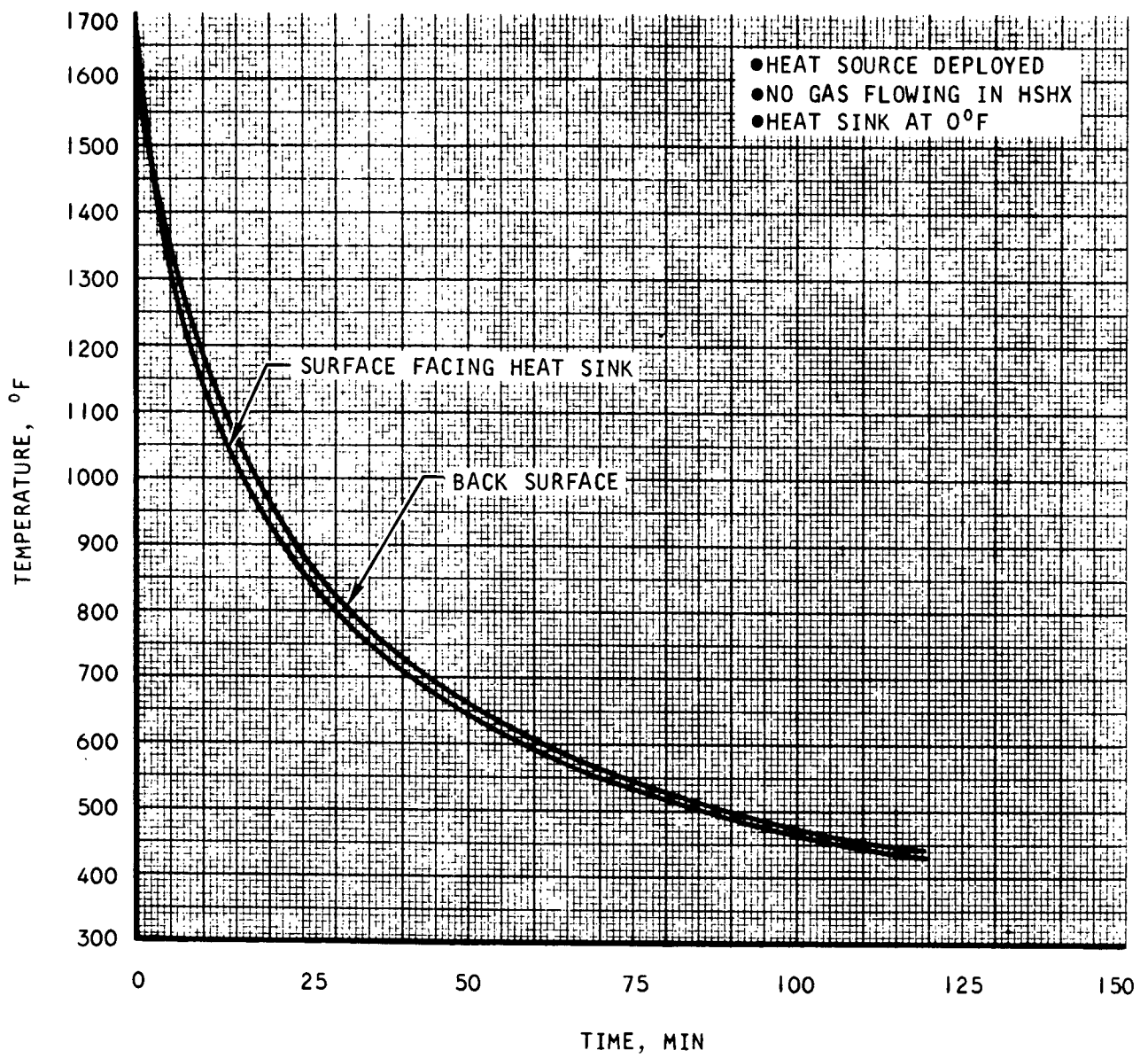


Figure 4.2-12 - Response of Average Tube Temperature During Shut Down

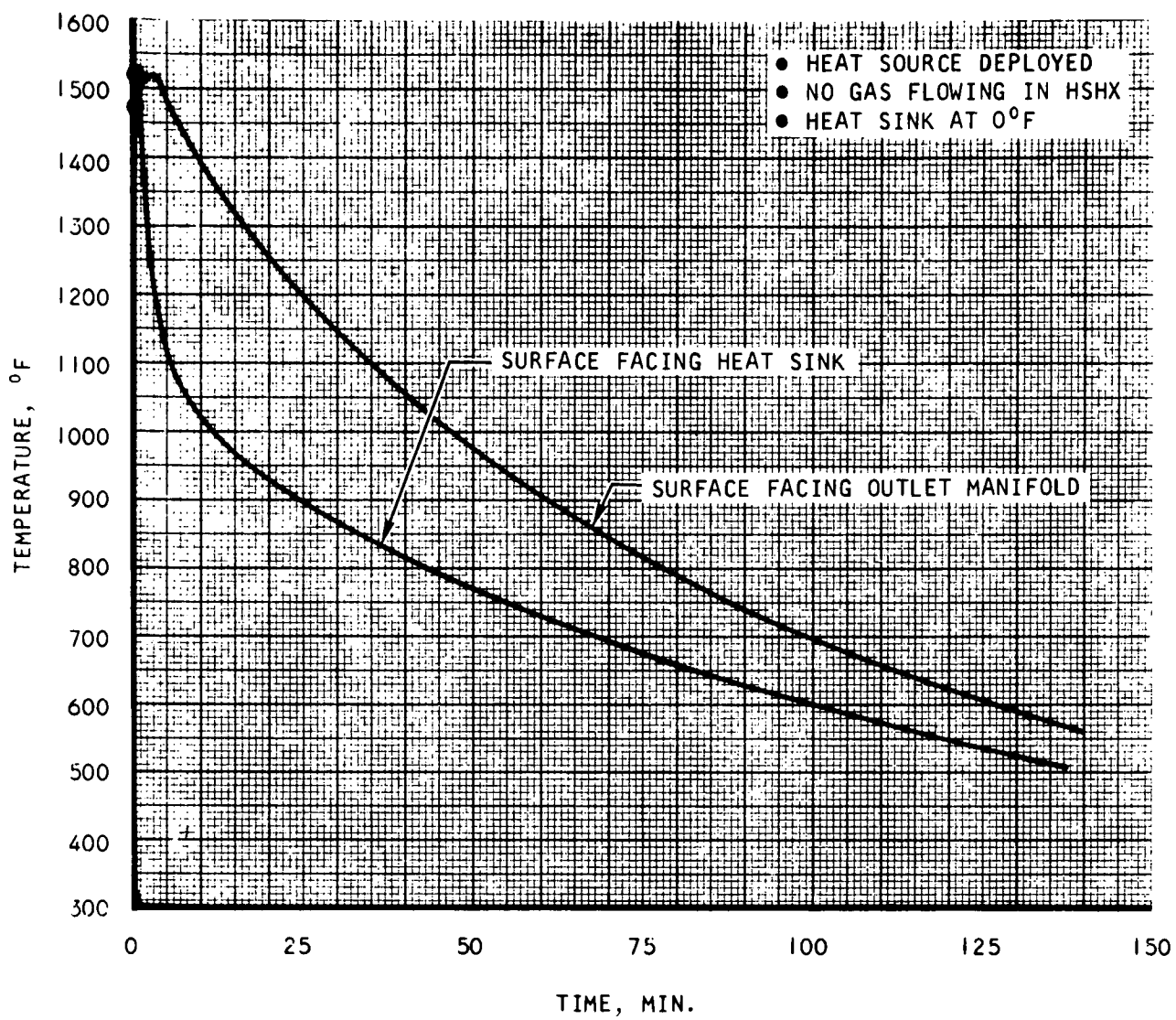


Figure 4.2-13 - Inlet Manifold Temperature During Shut Down

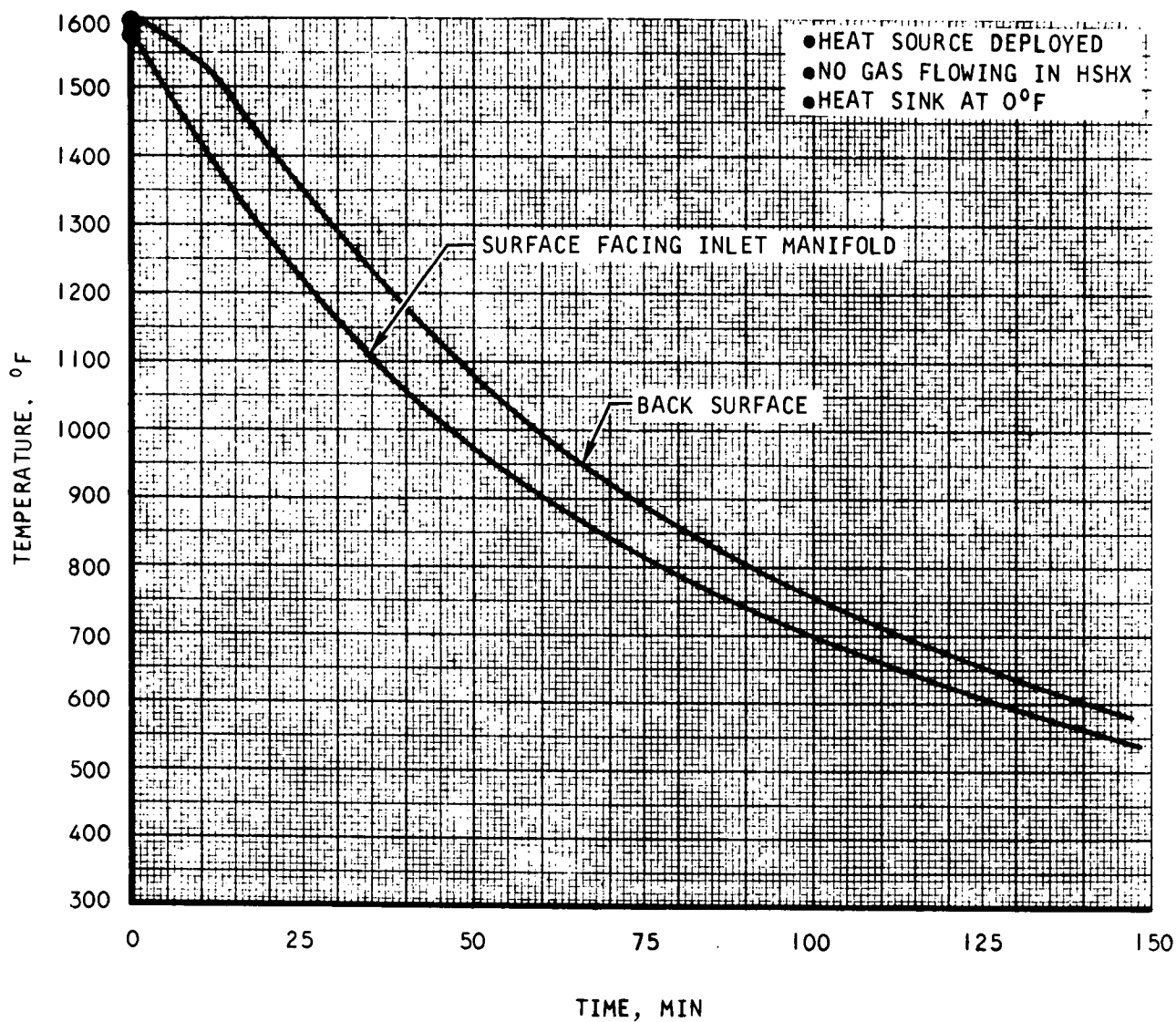


Figure 4.2-14 - Outlet Manifold Temperature During Shut Down

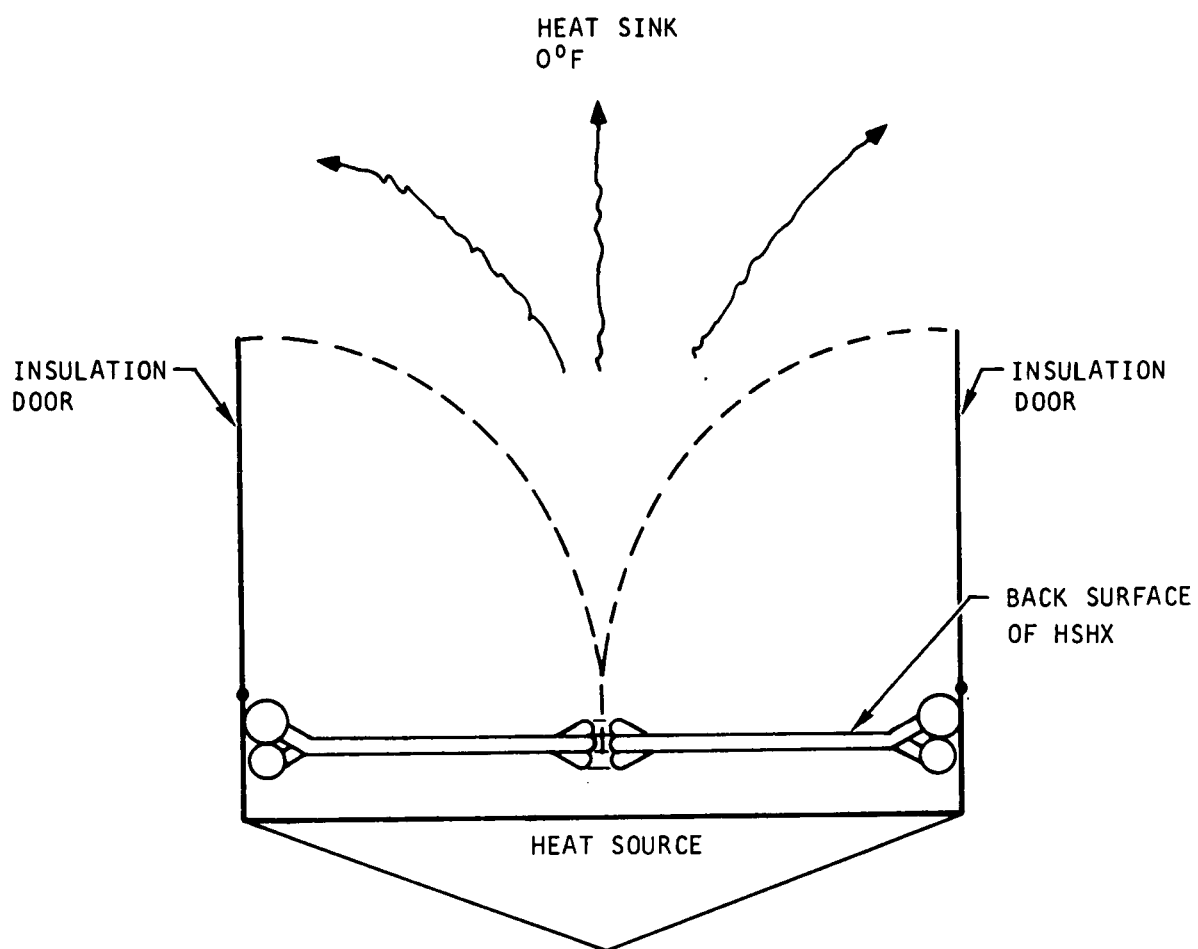


Figure 4.2-15 - Insulation Deployed



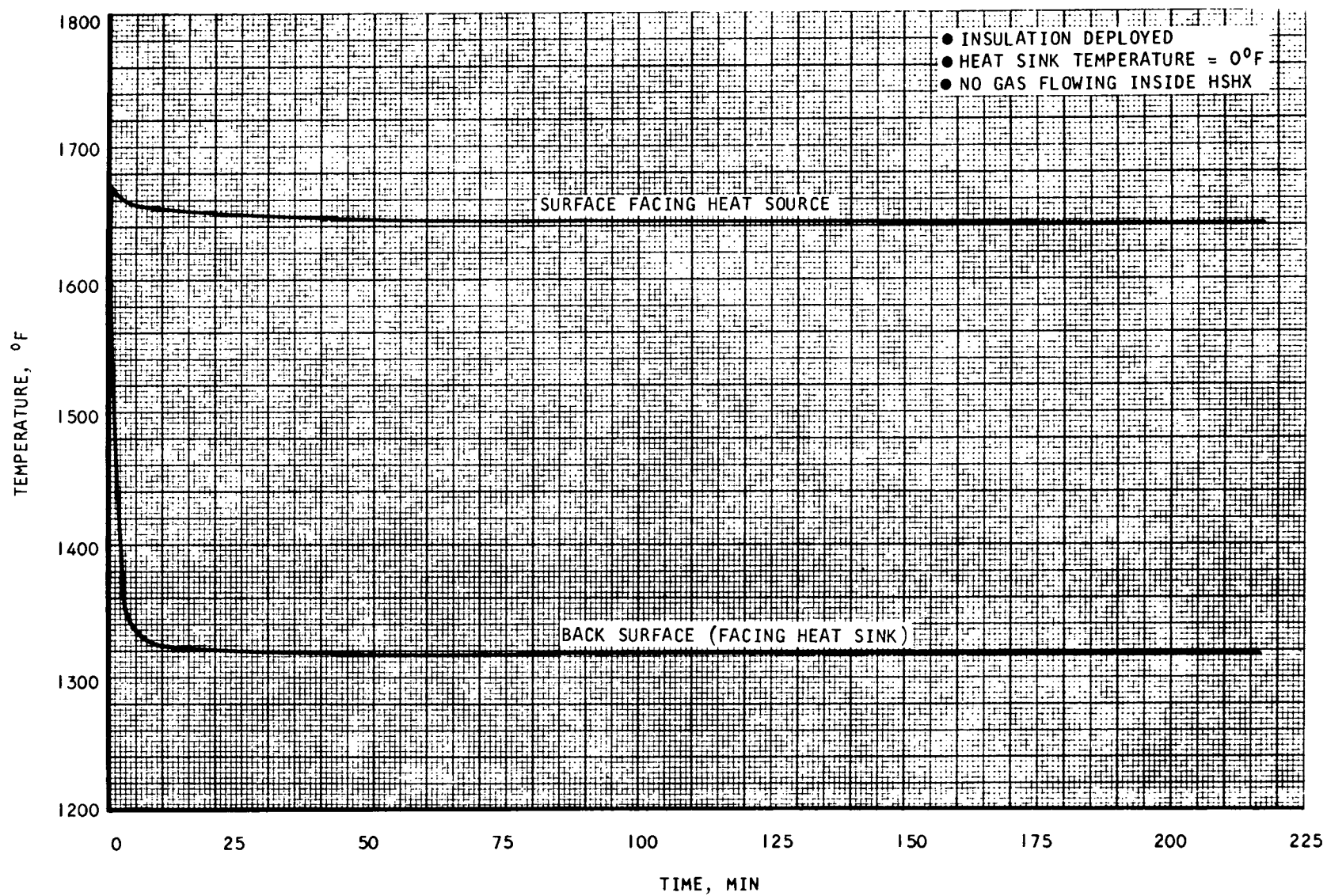


Figure 4.2-16 - Average Temperature of HSHX Tubes During Shut Down

temperature gradient is established, however, across the tubes, since one surface of the tubes faces the heat source (at about 1750°F) and the other surface faces the heat sink (at 0°F). Figure 4.2-16 shows a maximum temperature drop of 410°F across the tubes after steady state conditions have been reached during shutdown.

Figures 4.2-17 and 4.2-18 depict the temperatures of the inlet and outlet manifolds during shutdown. The worst temperature gradient occurs in the outlet manifold where a temperature drop of about 750°F is reached after 25 minutes. This is caused by the large diameter of the outlet manifold, the fact that one surface "sees" the heat sink while the other surface sees the inlet manifold and the heat source which are relatively hot, and the shut off of the gas flow in the outlet manifold. It may be noted that the temperature drops indicated in Figures 4.2-16 and 4.2-18 across the various parts of the HSHX would be significantly decreased if the gas continues to flow after the deployment of the insulation.

Finally, Figure 4.2-19 shows the distribution of the effective source temperature after 2 hr of cooling during shut down.

#### 4.2.2 Structural Design

A preliminary stress analysis was performed for the heat source heat exchanger using the superalloy, Haynes 188. The major structural effort was pressure containment design which included selection of material gauges, tube-manifold joint design and redesign of the center region to eliminate the reversing manifold. A thermal cycle life of 200 cycles was predicted for metal temperature estimates discussed above so the unit is expected to be satisfactory for the desired 50 cycle life. The weight of the heat exchanger excluding mounting provisions was estimated to be 192 lb.

The requirement for the ground test system was a design life of 5000 hr and 50 cycles. Operating conditions include a maximum gas pressure of 31.8 psi, 1692°F maximum tube temperature, and approximately 145°F steady-state temperature difference between the tube array and manifolds. Transient temperature differences were approximately the same as steady-state differences; however, they occur at lower metal temperatures and hence will not be critical. The design criteria for the HSHX were the same as in Reference 4.2-1.

#### Pressure Containment Analysis

The wall thickness of the tubes and manifolds were based on a constant internal pressure of 31.8 psi at the maximum steady-state metal temperature for the design life of the unit. The analytical methods described in

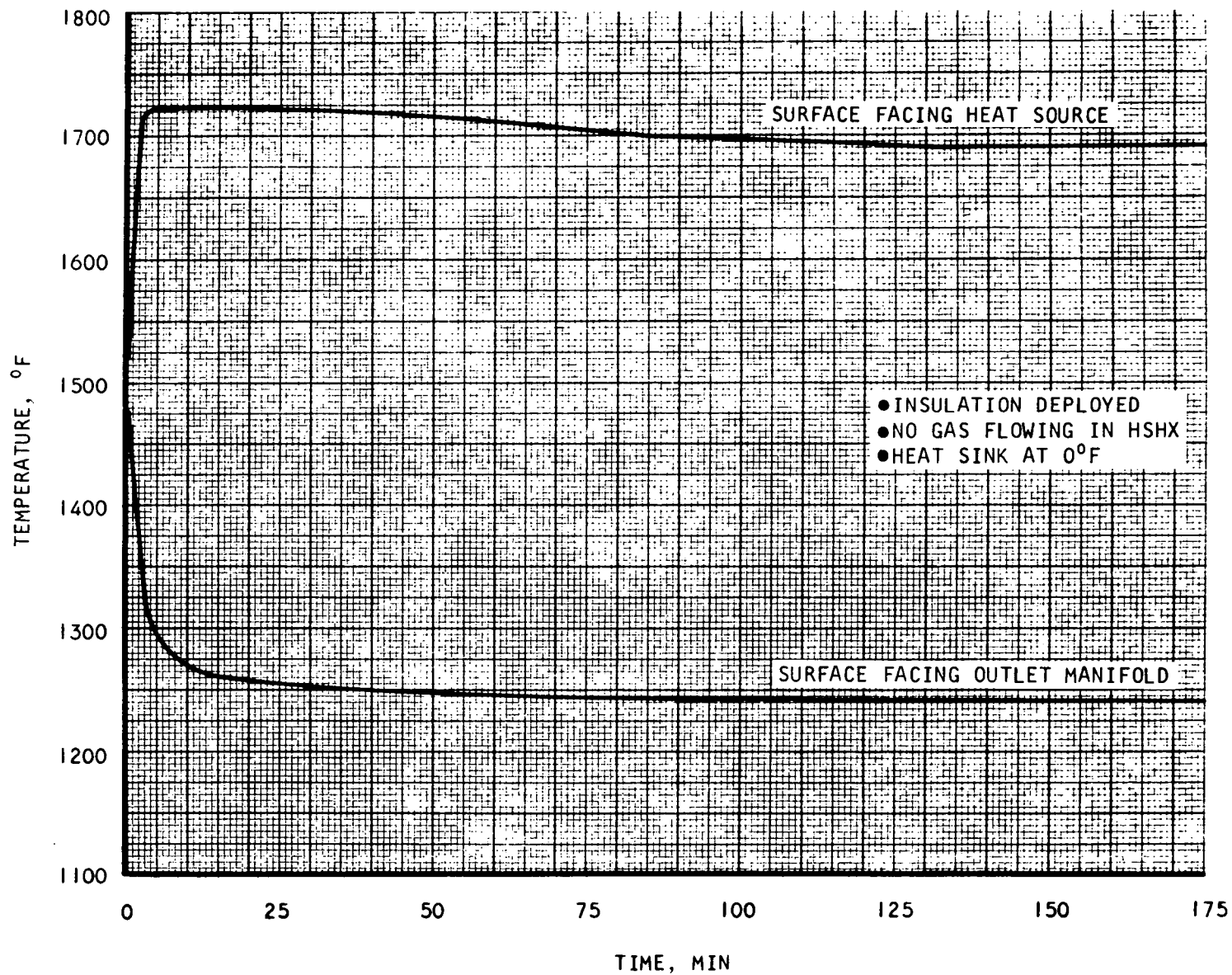


Figure 4.2-17 - Inlet Manifold Temperature During Shut Down

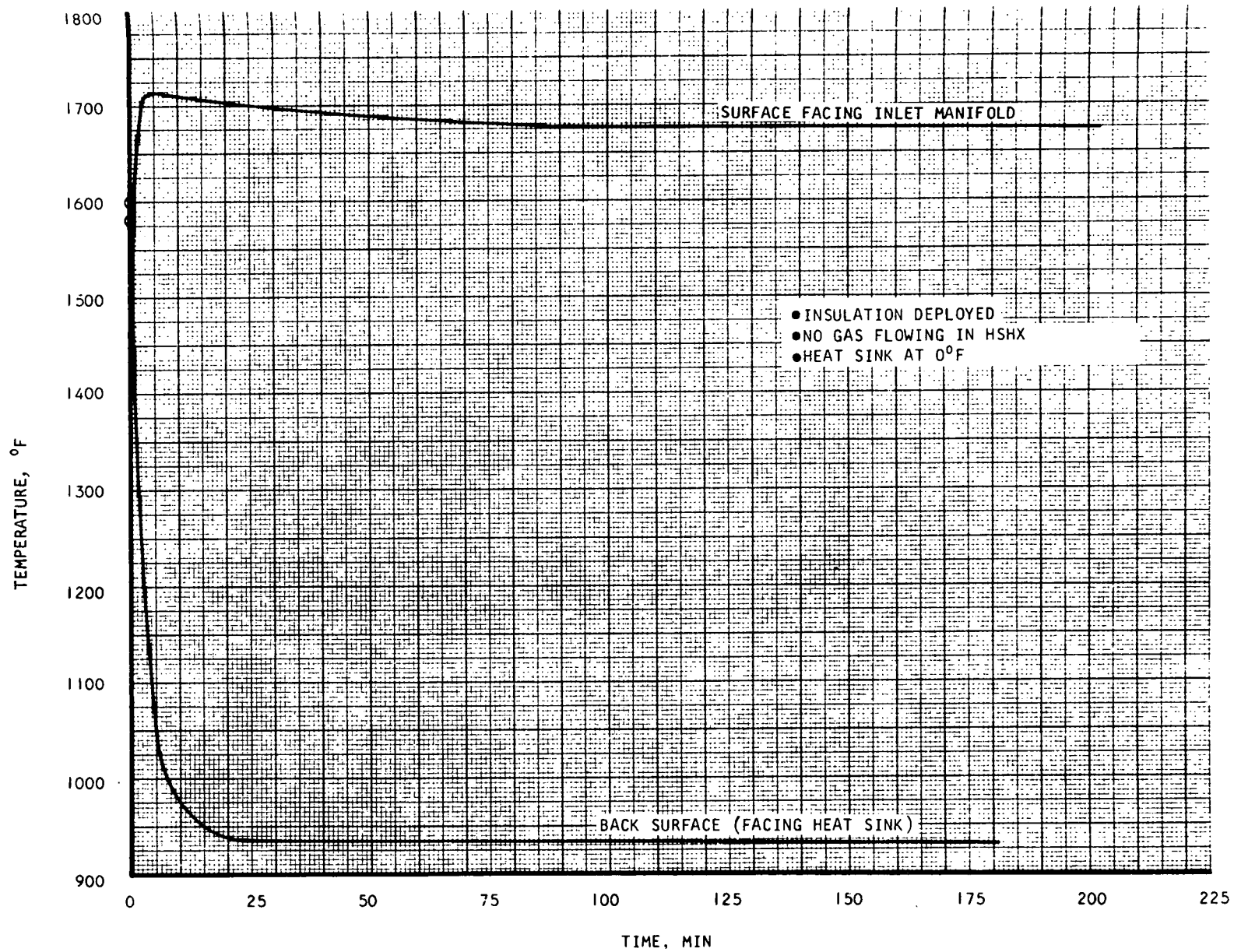


Figure 4.2-18 - Outlet Manifold Temperature During Shut Down

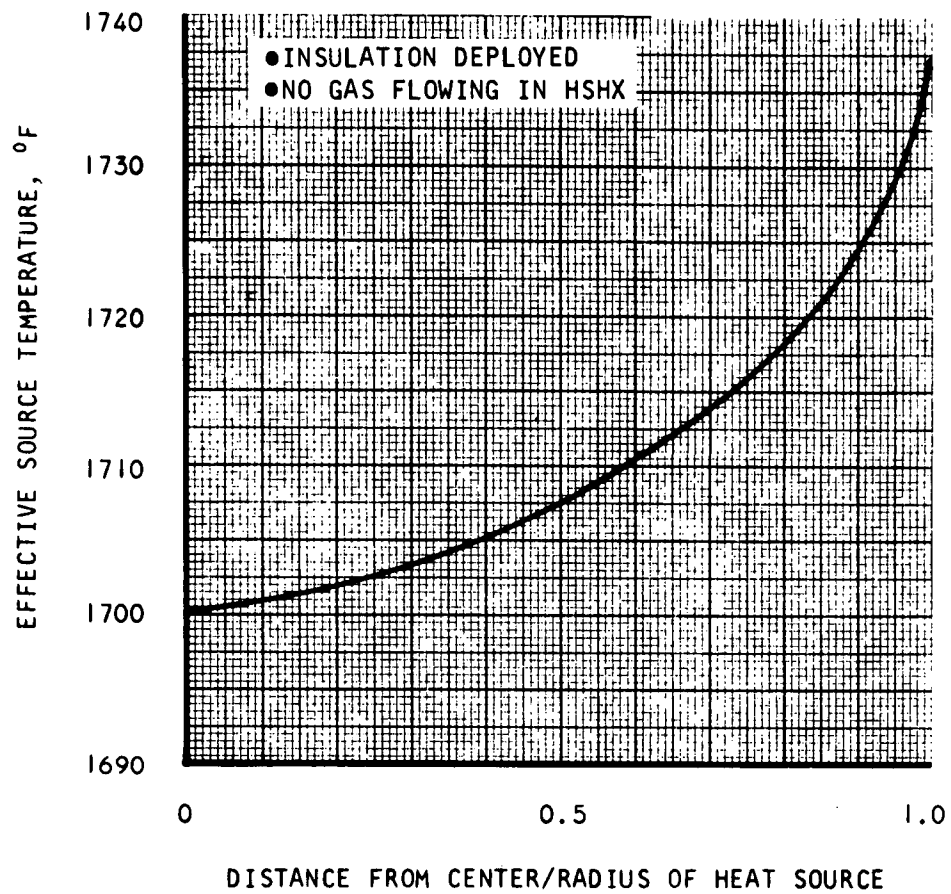


Figure 4.2-19 - Effective Heat Source Temperature Distribution  
After 2 hr of Cooling During Shut Down

Ref. 2.1-1 were used to compute required thicknesses, although minimum gauge limitations established the selected thicknesses in these components. The resulting temperatures, allowables, and wall thicknesses are listed in Table 4.2-II.

Fillet designs were established for the joints between the tubes and manifolds, and between the manifolds and their respective external inlet and outlet pipes. The required reinforcement was based on the unsupported pressure area following the approach described in Ref 4.2-1. Machined pieces, which can be butt welded to the manifolds, tubes, and pipes will be used to minimize thickness discontinuities which result in local bending stresses.

The return manifold was eliminated from the design to reduce the height of the heat exchanger and to avoid the inherently complicated construction and assembly procedures. The selected, simplified arrangement utilizes continuous tubes. Tube pressure stresses are satisfactory since the bend radius is less than that used at the joint between the tubes and the outer ring manifolds.

#### Thermal Stresses

The cycle life of the unit will depend primarily on creep damage due to thermal stresses developed during steady-state operating conditions and the predicted cycle life of the unit of about 200 cycles gives a safety factor of about 4 on the desired 50-cycle operating life. The time-temperature histories shown in Figures 4.2-8. through 4.2-10 predict that steady-state temperature differences are somewhat lower than the transient conditions at initiation of gas flow; however, steady-state conditions are more severe since component creep strengths are lower at the higher temperatures. Additional damage will be incurred during shutdown of the unit; however for typical shutdown tube and manifold temperatures decrease rapidly and creep damage will not be significant. Shutdowns where gas flow is interrupted will cause the most severe temperature gradients in the unit, however, this is not a typical operating condition and will occur a maximum of 2 or 3 cycles. When gas flow stops during heat source deployment, temperature differences between the tube array and manifolds of about 400°F (Figures 4.2-12 through 4.2-14. will occur, however, tube temperatures are greatly reduced and the damage to the tubes should not be significant. Large gradients can be developed across the manifolds both during heat source and insulation deployment when gas flow is interrupted, with the latter case being particularly severe as shown in Figures 4.2-17 and 4.2-18. For example, about an 800°F temperature difference would be developed across the outlet manifold and the maximum surface temperature remains at 1700°F. This temperature gradient leads to high thermal

TABLE 4.2-II

HAYNES 188 PRESSURE CONTAINMENT SUMMARY

Component	Maximum Operating Temperature °F	$\sigma_{allow}$ psi	Calculated Thickness, in.	Final Thickness, in.
Inlet Header	1520	2700	0.014	0.045*
Outlet Header	1600	1800	0.029	0.045*
Inlet Tubes	1668	1100	0.032	0.045*
Outlet Tubes	1692	900	0.039	0.045*

\*Minimum thickness for fabrication

strains since the colder ring material prevents thermal growth of the hotter sections. The cycle life of the ring under these conditions would be less than 100 cycles; however, since very few cycles are expected, the cumulative damage would probably not affect the 200 cycle estimate for steady-state damage.

The 200 cycle prediction is based on the analytical life estimating approach used in Ref. 4.2-1 for tube and inlet manifold steady-state temperatures (Figures 4.2-8 and 4.2-9) and as assumed typical loading cycle time of 30 sec.

The creep damage during each cycle arises from a total thermal strain in the tubes of about 0.003 in. /in. using the relation

$$\epsilon_{TOT} = 2.2 (\alpha \Delta T)$$

developed in Ref. The thermal expansion coefficient is  $10^{-5}$  in. / in. - $^{\circ}$ F and the  $\Delta T$  is  $145^{\circ}$ F. The resulting maximum plastic strain per cycle is about 0.001 in. /in. The creep damage per cycle is determined from the equation developed in the previous report

$$\phi_c = B^{\ell} \epsilon_{p \max}^{m\ell} t_{\max} / (m\ell + 1)A$$

where  $B = 71.2$  ksi

$t_{\max} = 30$  sec

$m = 0.15$

$\ell = 6.04$

$A = 0.78 \times 10^{12} (\text{ksi})^{6.04} - \text{sec}$

Creep damage is the dominating factor affecting cycle life at the average tube temperature of  $1670^{\circ}$ F. Therefore, the fatigue damage fraction will not affect the life estimate.

Thermal stresses were considered in a qualitative manner since mismatches in component thicknesses, which would lead to widely different response times, were avoided. For example, it is undesirable to substantially increase the ring manifold thicknesses since increased tube array restraint would result. For this reason, reinforcements over large arcs to support gravity loads must be avoided. Elimination of the central collector manifold was also consistent with the goal of avoiding potential thermal stresses which might govern the life of the heat exchanger.



### Weight Estimate

Weight calculations performed on the HSHX, fabricated from Haynes 188, indicated the total weight is 192 lb. This is based on a specific weight for Haynes 188 of 0.333 lb/in.<sup>3</sup> Contributing components in the weight estimate are the inlet and the outlet manifolds, the tubes, welds, and an emissive coating.

#### TOTAL WEIGHT OF HSHX

COMPONENT	WEIGHT LB
Manifolds	45
Tubes	97
Welds	28
Braze	12
Emissive Coating	10
TOTAL	192

### 4.3 FABRICATION

#### Design Description

The revised HSHX design is shown schematically in Figure 4.3-1. The major modification introduced in this study was the means in which the gas flow reversal takes place at the center of the spiral. Previously (Figure 4.0-1) this flow reversal was accomplished by a cylindrical manifold located at the hub of the spiral. In the current design this is accomplished by connecting every third tube together with a short "U" tube type piece. In order to fill the core of the spiral as much as possible with tubes, two of the three tube pieces are fabricated with a compound bend which allows them to go over or under the adjacent tubes to connect with the appropriate return tube. Thus the maximum height of the hub of the spiral is approximately three times the diameter of the tube (i. e., 4.32 in.). The eighteen tubes which make up the heat exchanger core are approximately 70 in. long and are constructed from 0.045-in. sheet stock. The inlet ring manifold is 2.40 in. in diameter while the exit ring manifold is 3.30 in. in diameter. The overall weight of the HSHX is 192 lb. All external surfaces of the heat exchanger are coated to provide a high emittance surface ( $\epsilon \approx 0.88$ ).

### Fabrication Sequence

The fabrication sequence envisioned for the HSHX is illustrated in Figures 4.3-2 through 4.3-8. The heat exchanger is constructed entirely from the Haynes-188 alloy. This material is available in sheet form of variable thicknesses upon special order. The tubes would be fabricated from sheet stock, welded and plainished to form smooth, uniform tubing 1.44 inches in O.D. and with a wall thickness of 0.045 inches. The tubing would be obtained from vendors which specialize in tube fabrication.

The forming of the tubes in their spiral shape is illustrated in Figure 4.3-2. Initially the tubes are drawn through a die to provide two flat surfaces where the tubes will be in contact with one another. Next the tubes are bent in their spiral shape in a tube bending die. Each tube is identical and 19 tubes are required for the heat exchanger. Finally one end of the tube is bent to provide the tube-manifold transition section. Next the small "U" tube section is fabricated from tube stock as illustrated in Figure 4.3-3. There are two types of "U" tubes, one is bent only in one plane and the other is bent in the plane of the spiral as well as at right angle to this plane to allow it to go over (or under) the two adjacent tubes. The part is also fabricated by bending operations. Finally a tube set (consisting of an inlet and exit tube) is formed by welding the "U" tube section to the appropriate tubes as illustrated in Figure 4.3-4. The heat exchanger core is made up of 9 such sets of spiral tubes.

The heat exchanger manifolds are made from 0.045 inch sheet stock as shown in Figure 4.3-5. With two rolling operations the quarter sections of one half of the ring manifolds are formed. Holes for the core and tubes and inlet and exit ducts are eloxed in the ring manifold sections as shown in Figure 4.3-6. The four half cylindrical sections are then welded together to form a wheel-like structure (Figure 4.3-6). The outer half of the ring manifolds are formed in a similar manner.

The next set of operations is the final heat exchanger assembly. The ring manifolds are mounted in an assembly fixture (Figure 4.3-7). Next the 9 spiral tube sets are alied in the assembly fixture and located appropriately and clamped into position. The tubes are then tack welded to the ring manifolds and to each other to hold the assembly in position. The tubes are then fully welded to the inlet and exit manifolds and each tube is welded to the adjacent tube as illustrated in Figure 4.3-8. Next the outer half of the ring manifolds are welded on as well as the inlet and exit ducts. The heat exchanger is then turned over and braze material is placed between the flattened surfaces of the tubes (see Figure 4.3-8), and the whole assembly brazed for 5 minutes at 1930°F in a vacuum brazing chamber. The complete assembly is then flame sprayed with a suitable high emittance coating.

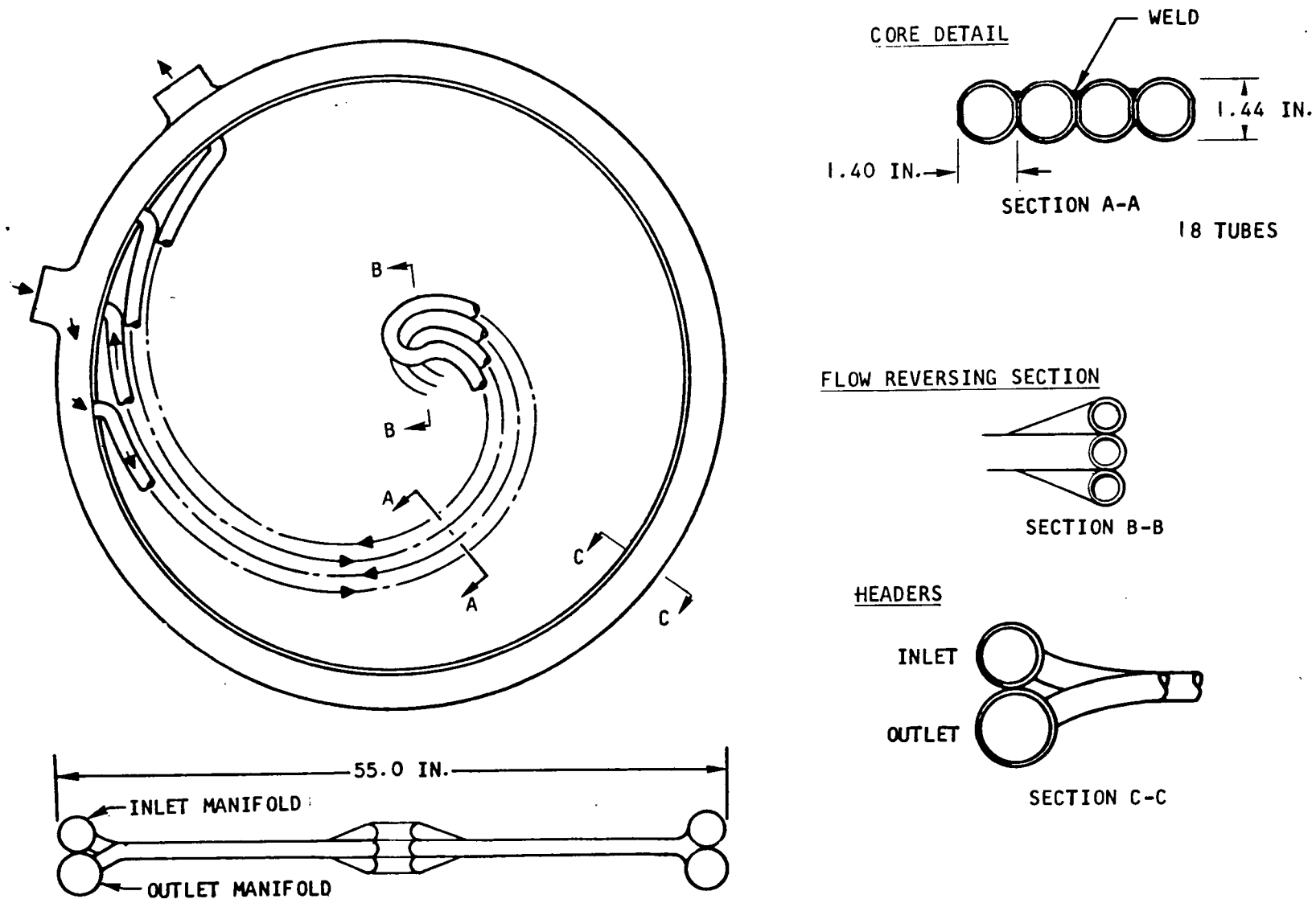


Figure 4.3-1 - Spiral Heat Source Heat Exchanger

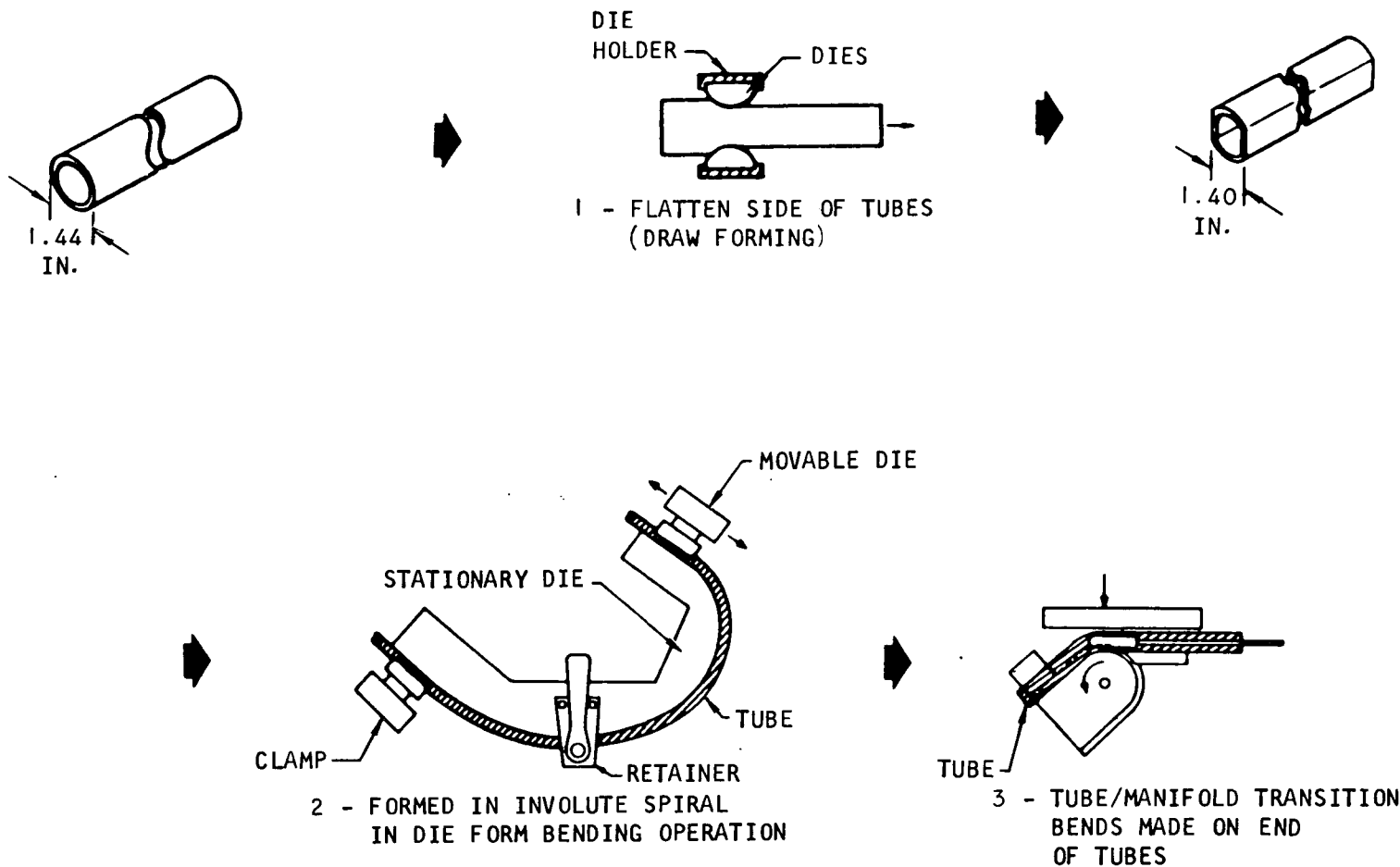
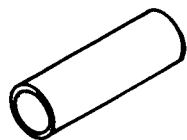
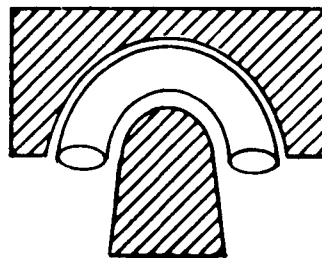


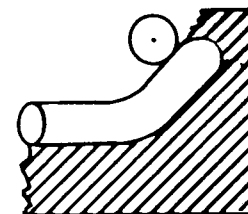
Figure 4.3-2 - Fabrication of Heat Exchanger Tubes



TUBE



BEND TUBE



COMPOUND-BEND

Figure 4.3-3 - Fabrication of "U" Tube Section

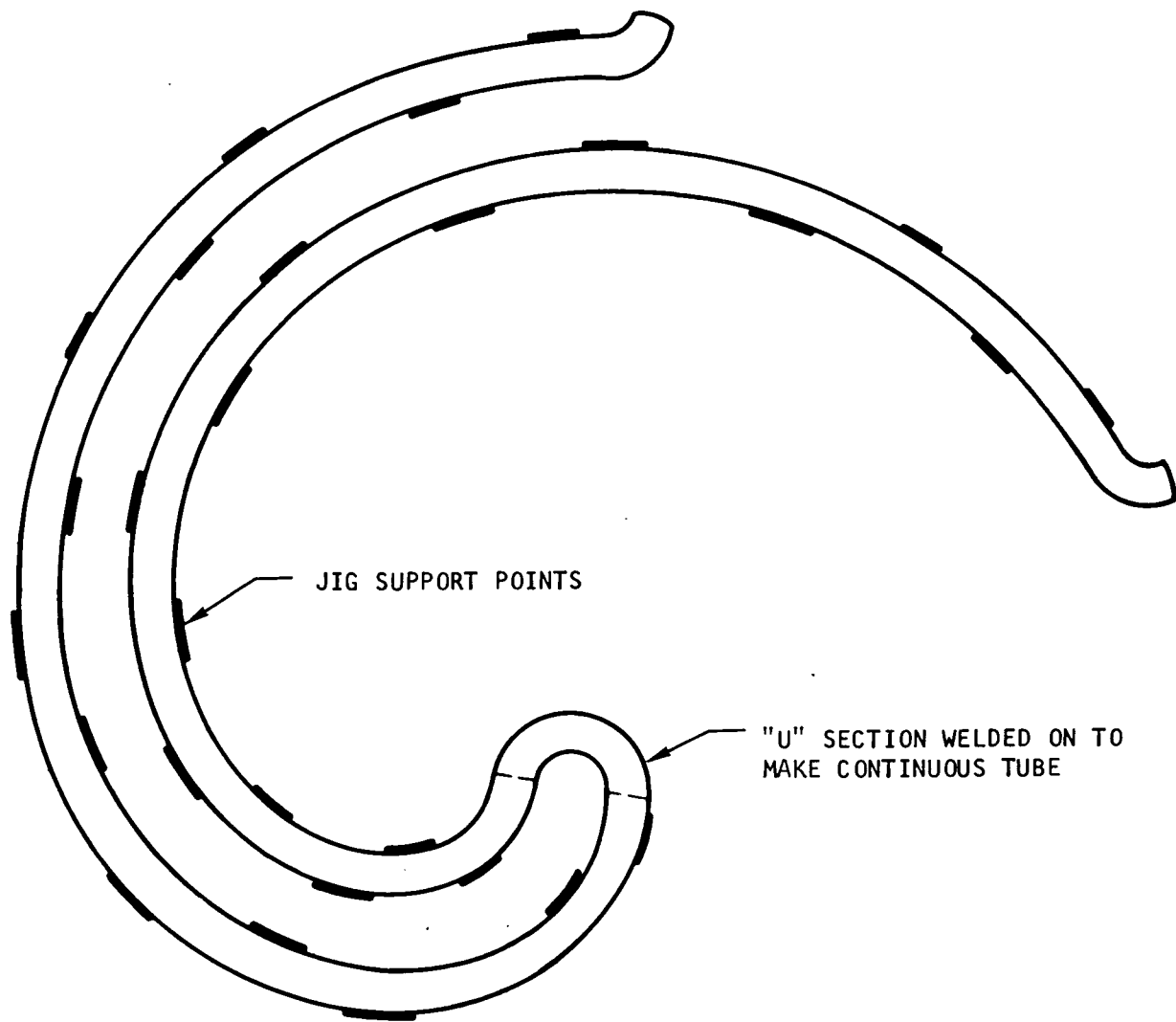


Figure 4-3-4 - Fabrication of Tube Set (9 Required)

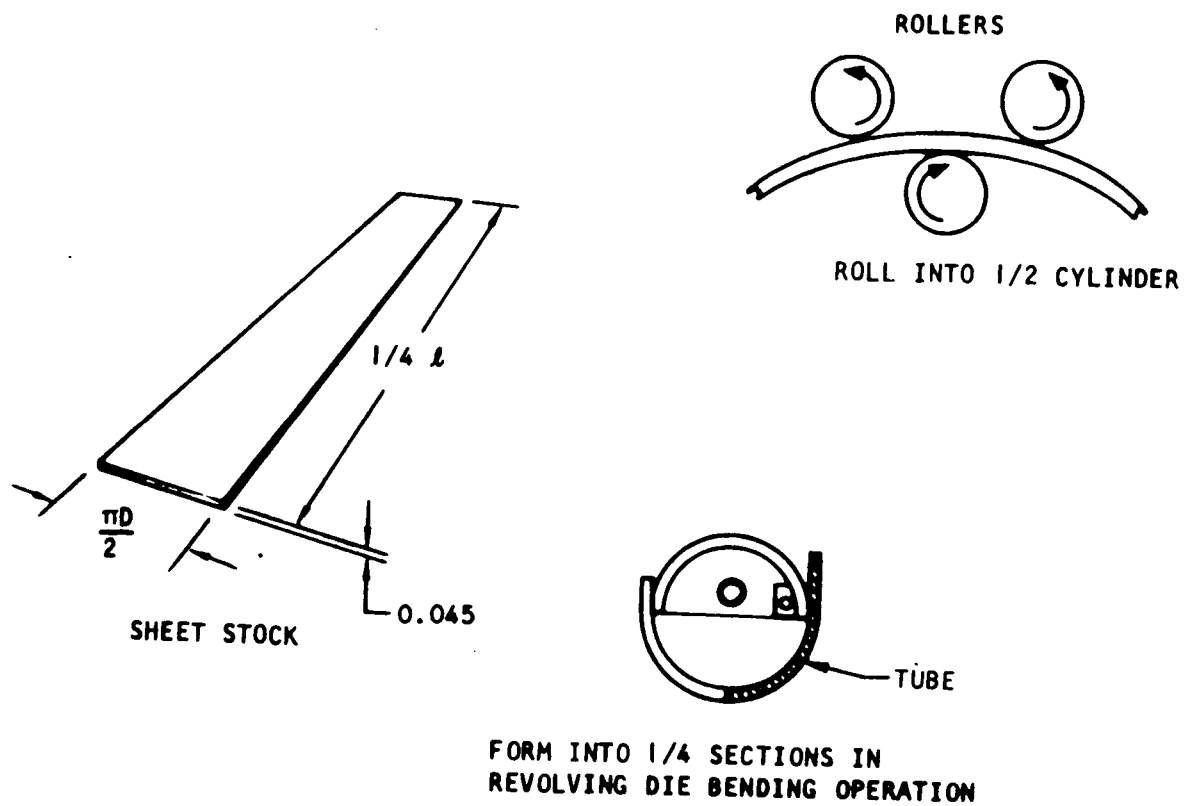


Figure 4.3-5 - Fabrication, Ring Manifolds

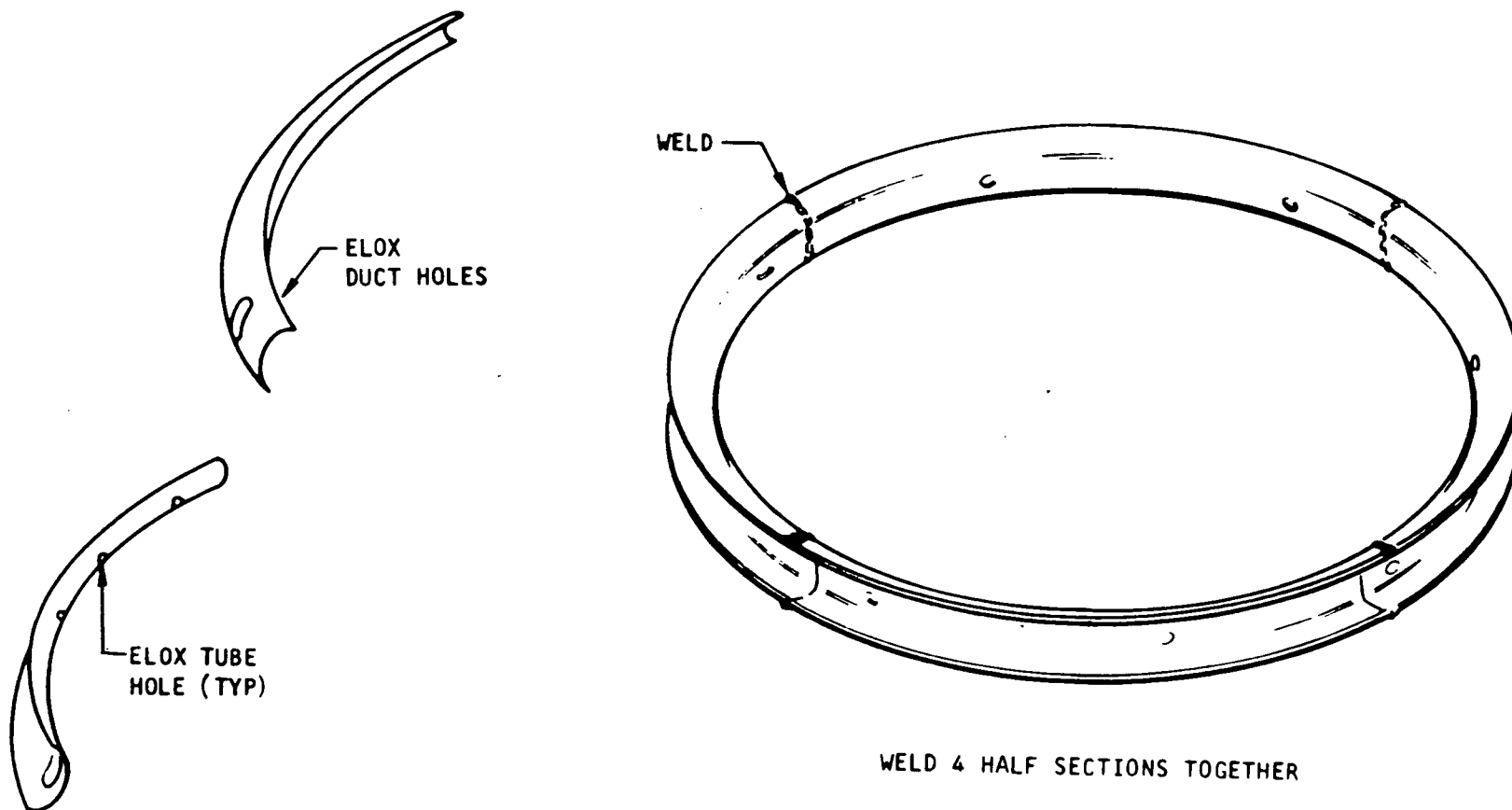
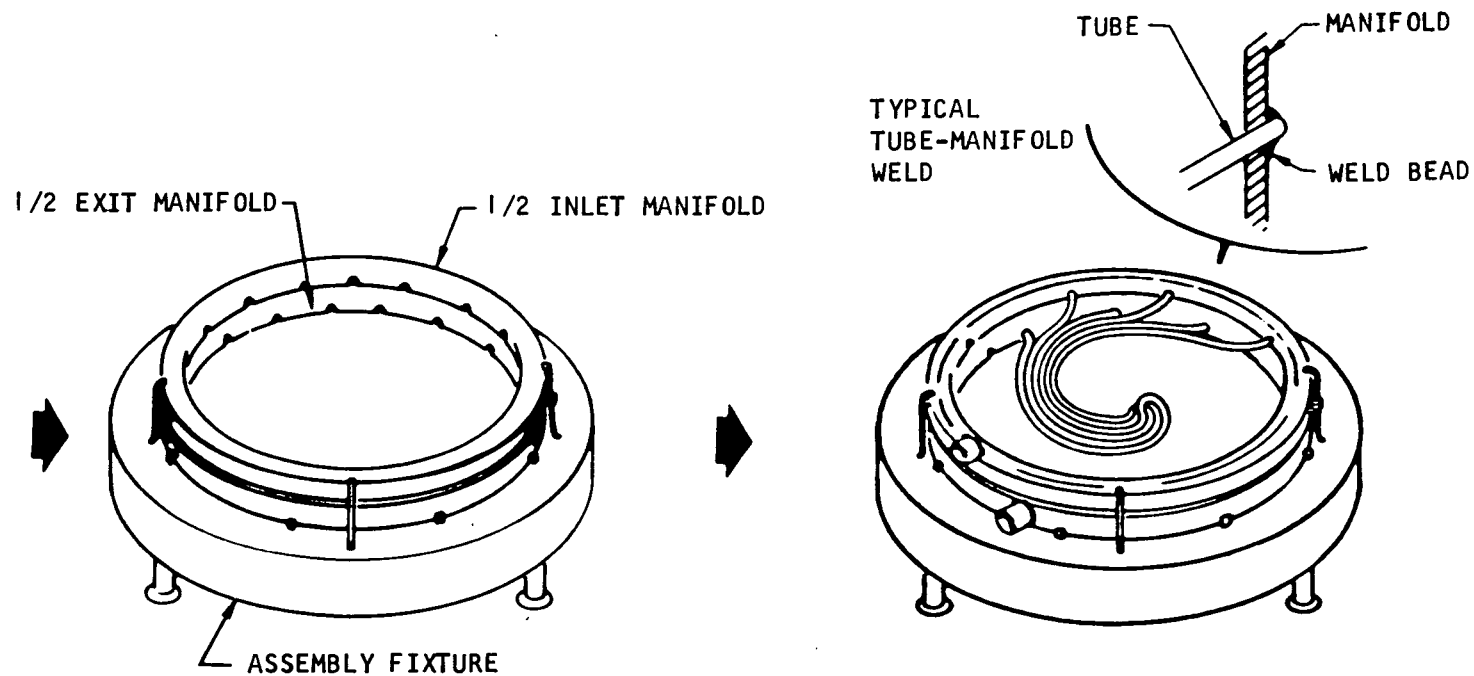


Figure 4.3-6 - Fabrication, Ring Manifolds (Continued)





1. PLACE INLET AND EXIT MANIFOLDS ON ASSEMBLY FIXTURE

1. PLACE ALL TUBES IN POSITION
2. TACK WELD TUBES TO MANIFOLDS
3. TACK WELD TUBES TOGETHER
4. WELD TUBES TOGETHER

Figure 4.3-7 - HSHX - Assembly

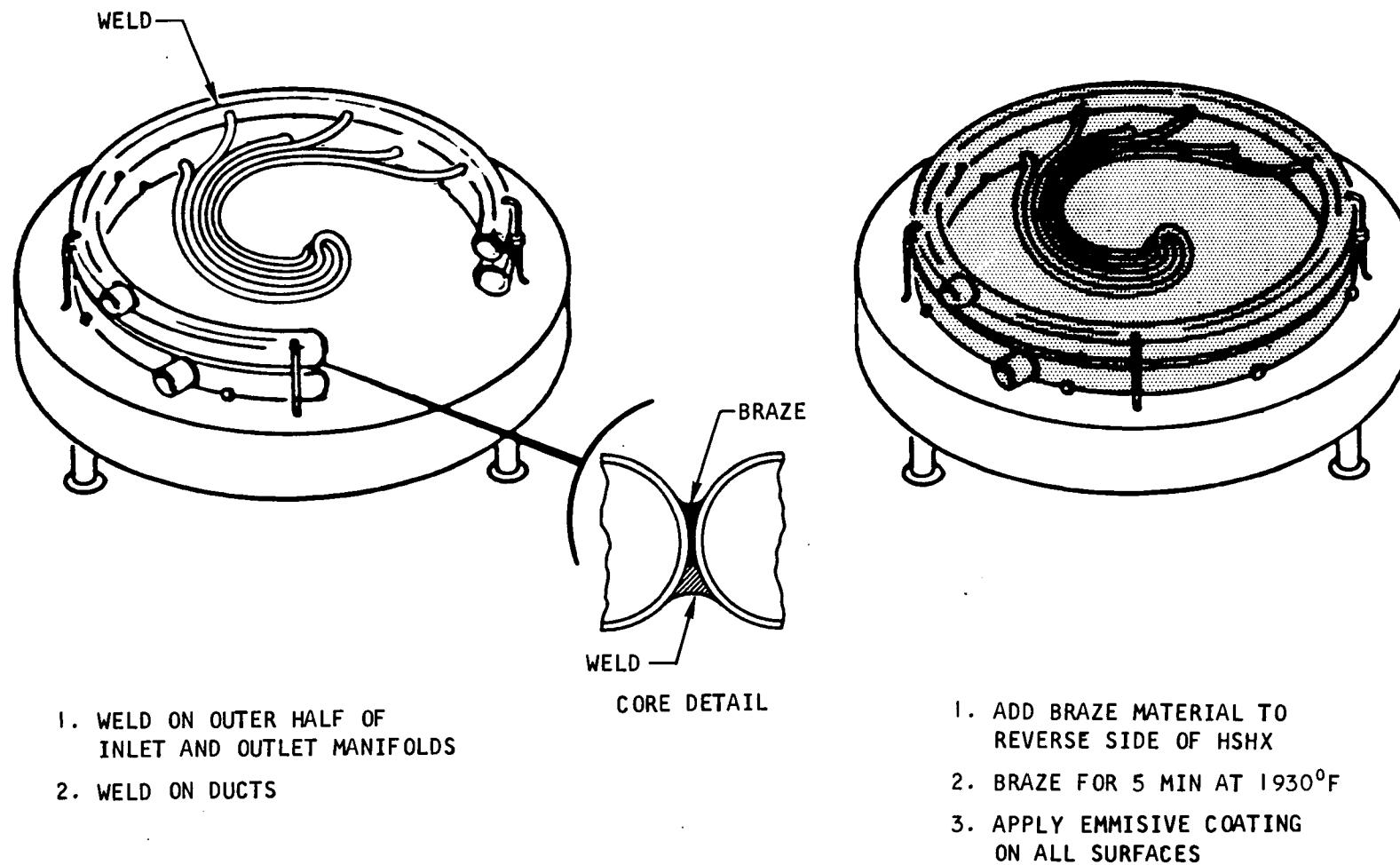


Figure 4.3-8 - HSHX Assembly -2

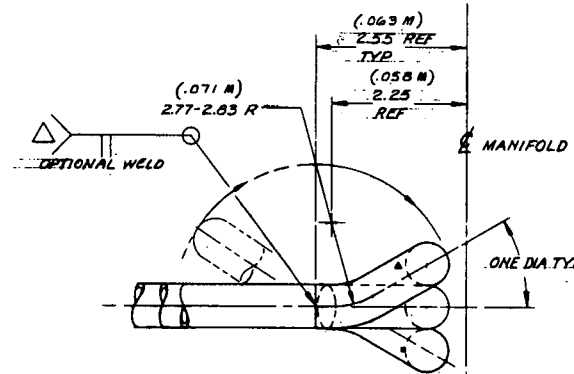
#### 4.4 DRAWINGS

<u>Title</u>	<u>Drawing No.</u>
Layout Heat Source Heat Exchanger	L198599
Manifold Outlet Assy. Heat Source Heat Exchanger	184542
Tube Heat Source Heat Exchanger	184544
Manifold Inlet Assy. Heat Source Heat Exchanger	184543

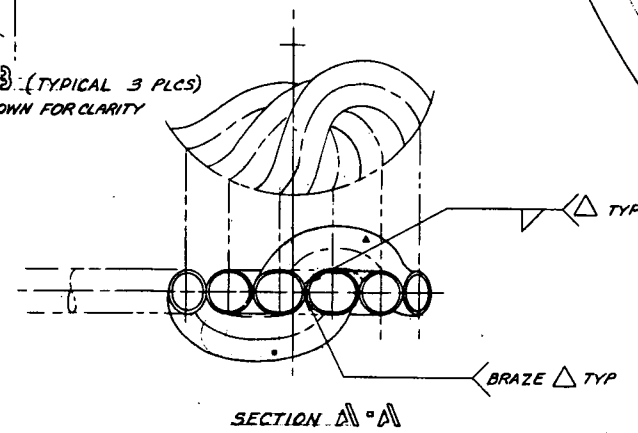
#### 4.5 REFERENCES

- 4.2-1 Coombs, M. G., C. E. Richard, and T. L. Trevarthen, Topical Report, Task I, Heat Source Heat Exchanger Design Study, Garret AiResearch, 70-6763, September 18, 1970.

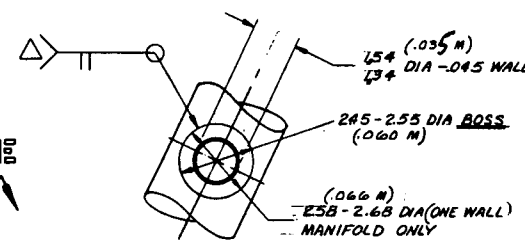
SECTION 11.10  
TYP 9 PCS



VIEW 13-13 (TYPICAL 3 PLCS)  
ROTATED AS SHOWN FOR CLARITY



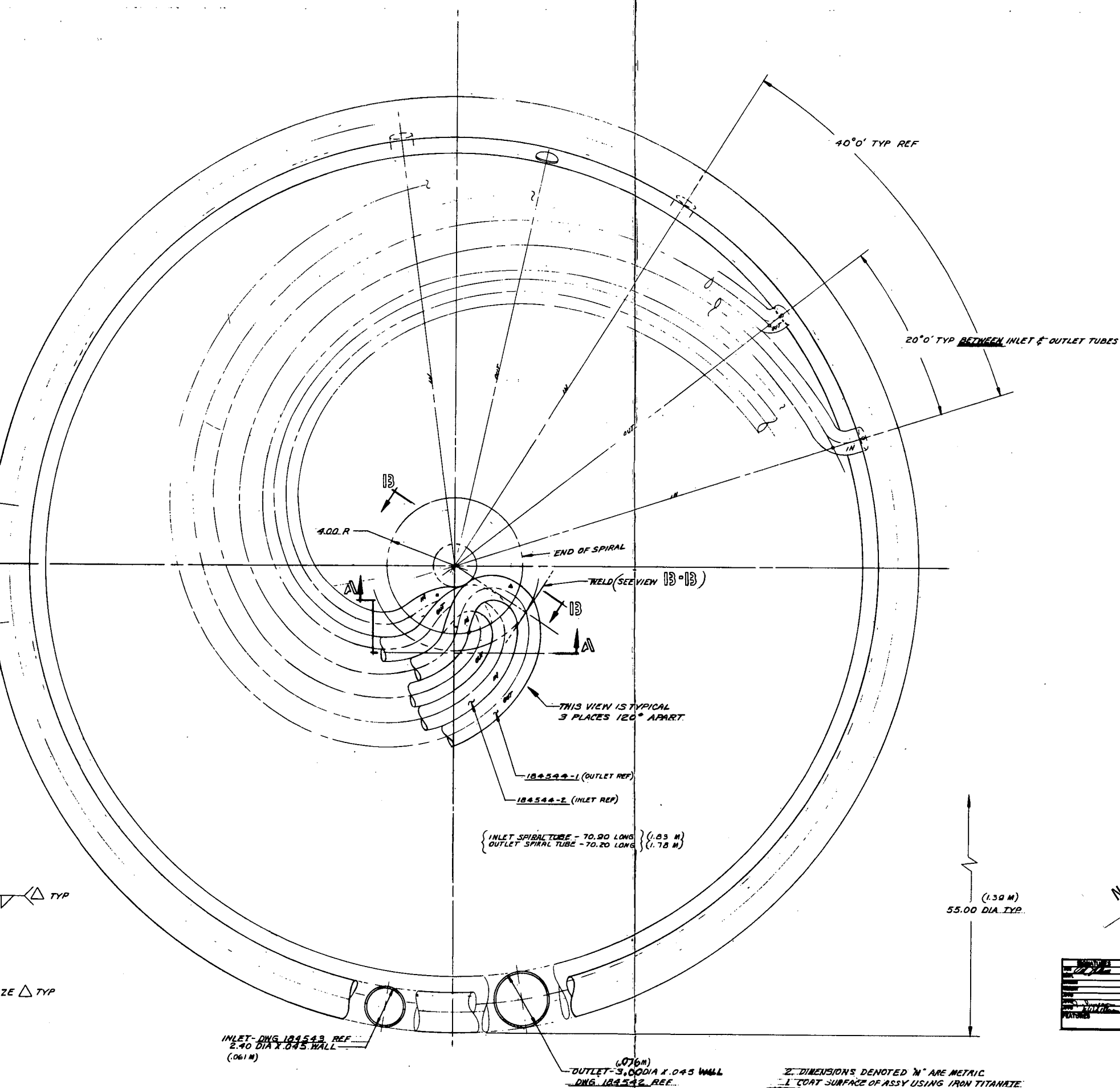
SECTION A - A




SECTION 12-12  
TYP-9 PLS

112-118 R (BOSS ONLY)  
(.027 M)

(.041 M)  
1.58-1.64 R  
(BOSS ONLY)



NOT REPRODUCIBLE

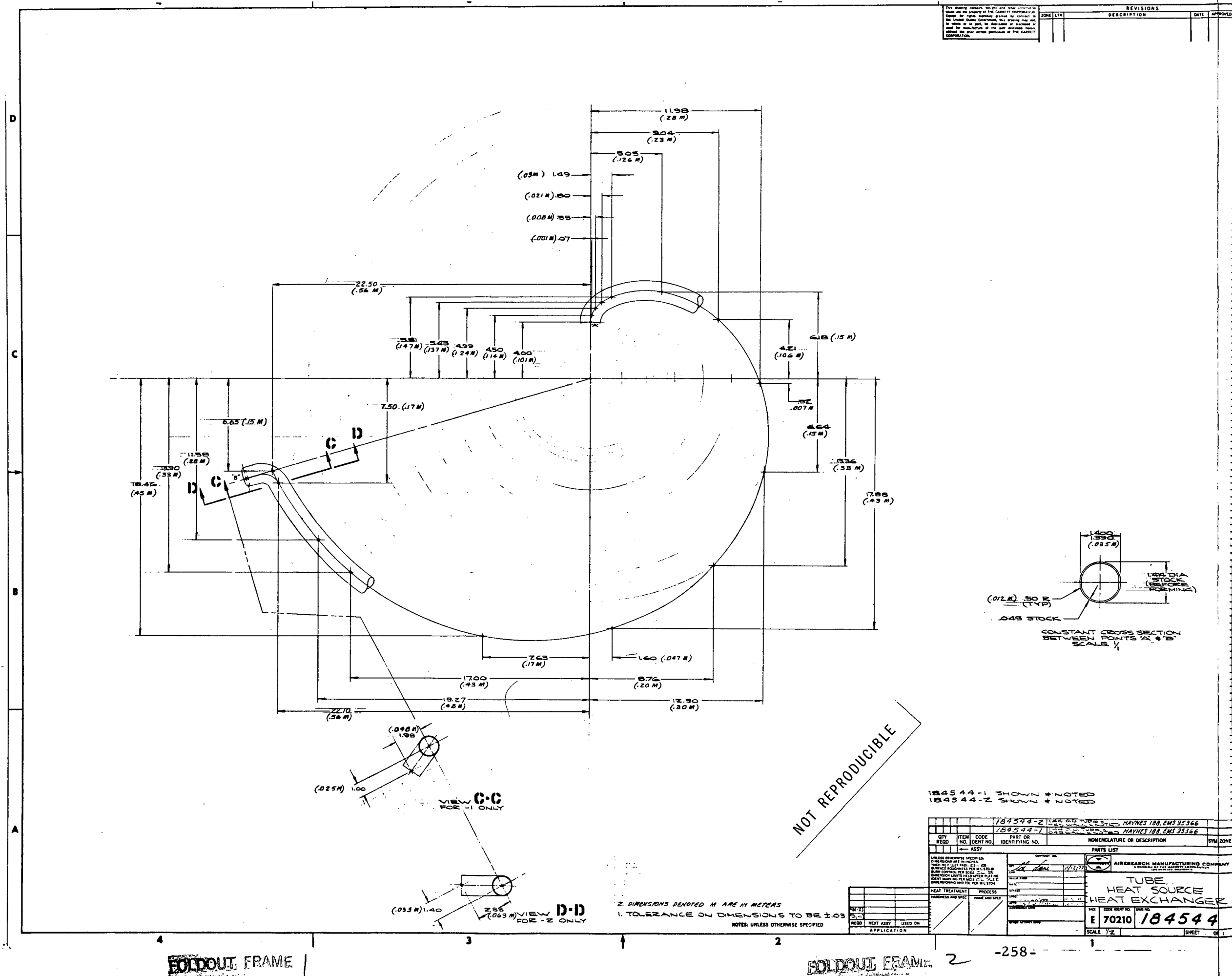
 FEDERAL BUREAU OF INVESTIGATION U. S. DEPARTMENT OF JUSTICE		AIRCRAFT/RAILROAD HIGHWAY/VEHICLE RECORDS - INVESTIGATIVE DIVISION OF FBI - FIELD OFFICE	
LAYOUT			
LAYOUT. HEAT SOURCE HEAT EXCHANGER			
REPORTING OFFICE <b>MEMPHIS</b>	DATE <b>4/17/68</b>	CASE NUMBER <b>44-1987-100</b>	INVESTIGATION OF <b>RENTAL</b>
NAME <b>WILLIAM J. RAY</b>	DATE <b>4/17/68</b>	CASE NUMBER <b>44-1987-100</b>	INVESTIGATION OF <b>RENTAL</b>
ADDRESS <b>201 N. GUYTON</b>	CITY/STATE <b>MEMPHIS, TENN.</b>	COUNTY <b>MEMPHIS</b>	INVESTIGATION OF <b>RENTAL</b>
TELEPHONE <b>228-1216</b>	TELETYPE <b>228-1216</b>	TELETYPE <b>228-1216</b>	TELETYPE <b>228-1216</b>
COMMENTS <b>RENTAL</b>	COMMENTS <b>RENTAL</b>	COMMENTS <b>RENTAL</b>	COMMENTS <b>RENTAL</b>
SCALE 1/2"		LT 198599	
SCALE 1/2"		LT 198599	
SCALE 1/2"		LT 198599	

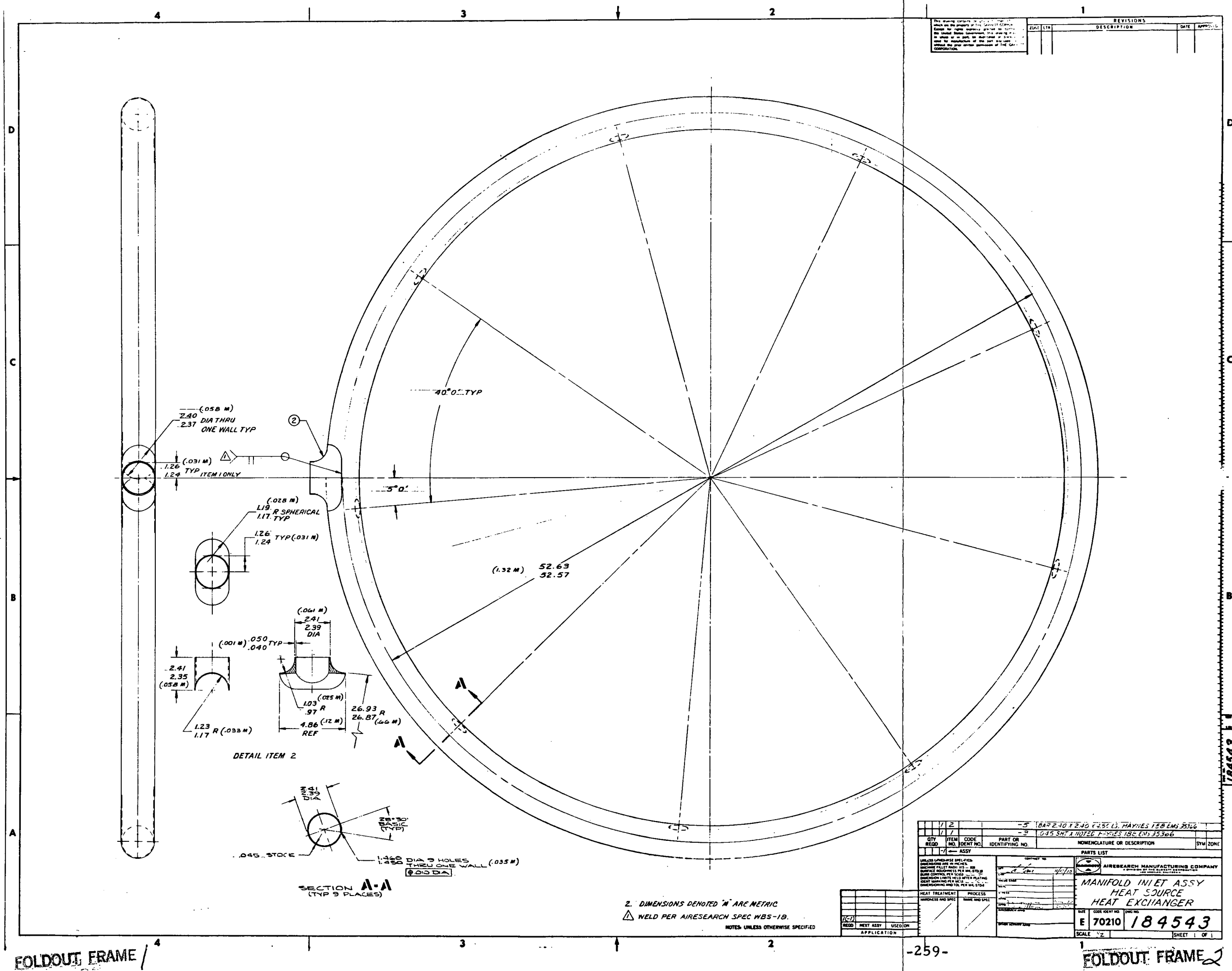
2. DIMENSIONS DENOTED "IN" ARE METRIC  
1. COAT SURFACE OF ASSY USING IRON TITANATE.  
NOTES: UNLESS OTHERWISE SPECIFIED

**FOLDOUT FRAME**

**FOLDOUT FRAME 2**

-257- EOLDOUT FRAME 3







543481

## APPENDIX A

### ANALYSIS OF ACHX TRANSIENT FOR THE EMERGENCY CASE OF COOLDOWN FROM STEADY STATE

A computer analysis of heat source response to initiation of ACHX operation has been made. The use of the ACHX as an emergency cooling mode for ground test application is a new concept and the computer results indicate that it is an effective one.

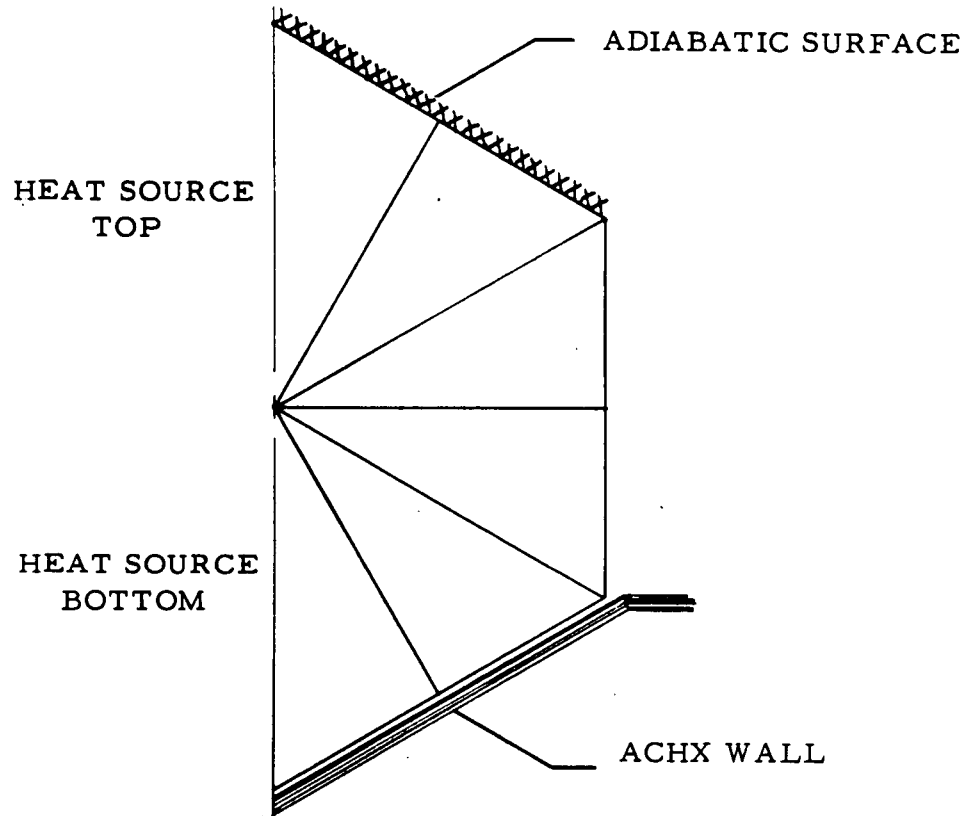
The case of interest is that one where the Brayton Engine is assumed to shutdown accidentally from normal operating temperatures followed by a failure of both primary and secondary heat dump modes, i. e. , both insulation doors and the HSRV deployment mechanism. The results of the analysis can also be applied to the case of accidental engine shutdown followed by use of the ACHX as the primary cooldown mode.

Calculations were made with the CINDA program using the thermal model shown in Figure 1. The heat source geometry was the current hexagonal design at 400 watts each. The top of the heat source was assumed to be adiabatic to account for engine shutdown. For simplicity a constant ACHX wall temperature was assumed. Two temperatures were used to bracket the range of heat source cooldown rate. A very optimistic ACHX wall temperature of 80°F was used to get a feel for the fastest cooldown rate, while 500°F was used to get a more realistic response. This higher wall temperature was found to be a reasonable one based on a simple calculation included herein as Appendix 1. An important variable in the calculation was the contact coefficient



Figure 1

THERMAL MODEL FOR ACHX COOLDOWN  
FROM STEADY STATE



between the graphite heat source and the ACHX wall. Since the design of the heat source hold-down or retention mechanism utilizes refractory metal bolts there is a differential thermal expansion between the metal and the graphite. This provides good contact at heat source loading temperatures and poor contact at steady state operation. These are the desired conditions for normal loading and operation. However, poor contact at operating temperature is not desirable for emergency ACHX cooldown. Two values of contact coefficient were used to bracket the range of contact. In addition to the nominal contact assumption of  $300 \text{ B/hr-ft}^2\text{-}^\circ\text{F}$ , a conservative value of  $100 \text{ Btu/hr-ft}^2\text{-}^\circ\text{F}$  was used to account for the improved contact as the temperature difference decreased during cooldown.

The results of the calculations are shown in Figures 2 and 3. Figure 2 is a plot of heat source temperature as a function of time for an  $80^\circ\text{F}$  ACHX wall and figure 3 is a similar plot for a  $500^\circ\text{F}$  wall. Both figures include the contact coefficient variation and two heat source temperatures -- one at the top of the heat source and one at the bottom. All computer runs ended at 5 minutes (real time) and were extrapolated to additional times. An arbitrary time cut-off corresponding to  $950^\circ\text{F}$  at the top of the heat source and/or  $350^\circ\text{F}$  at the bottom was chosen. The higher temperature corresponds to the oxidation initiation temperature of POCO graphite in air, and the lower value is a common oxidation limit of Cb-1%Zr in air.

Figure 2  
HEAT SOURCE RESPONSE TO ACHX COOLDOWN  
FROM STEADY STATE - 80°F ACHX WALL TEMP.

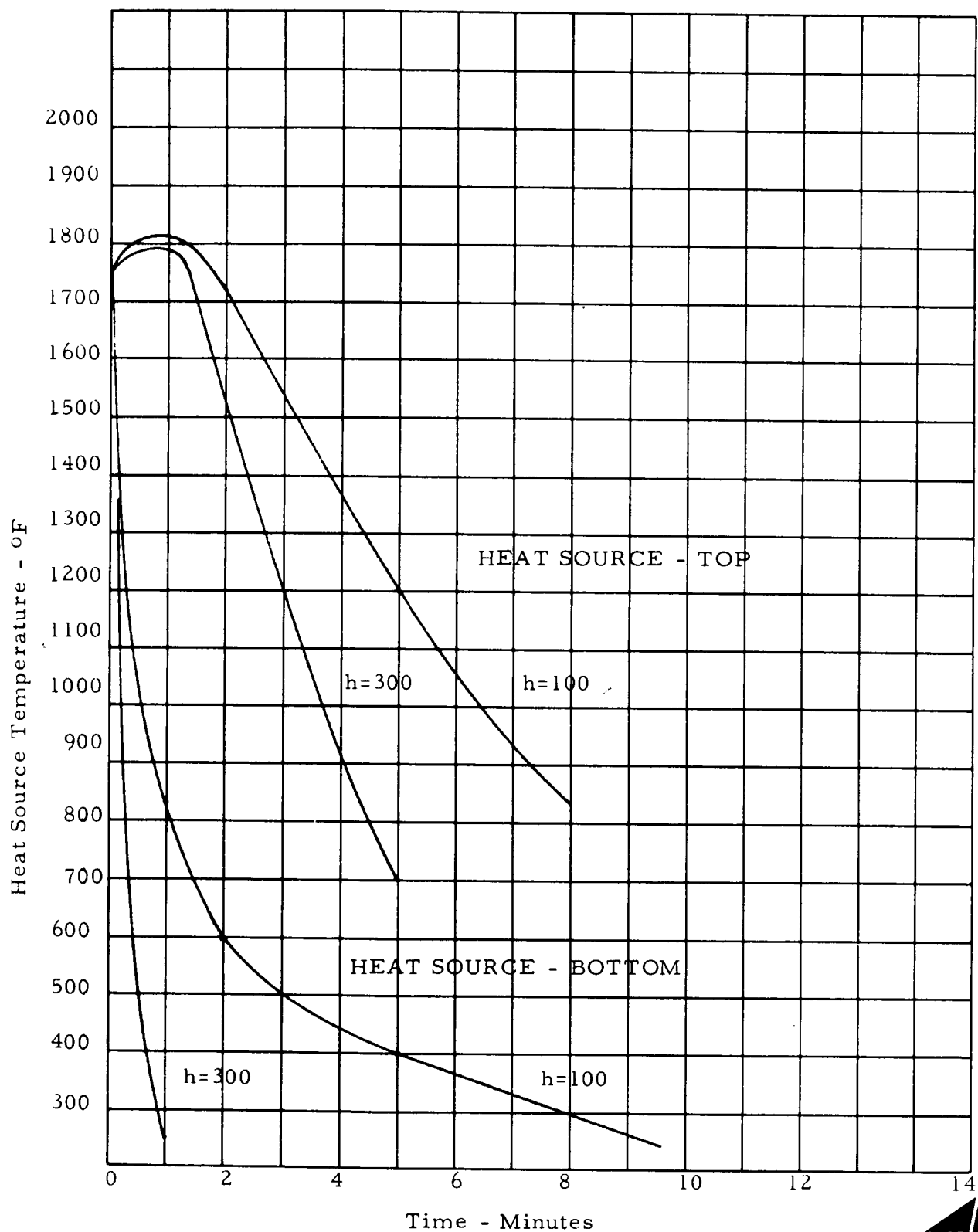
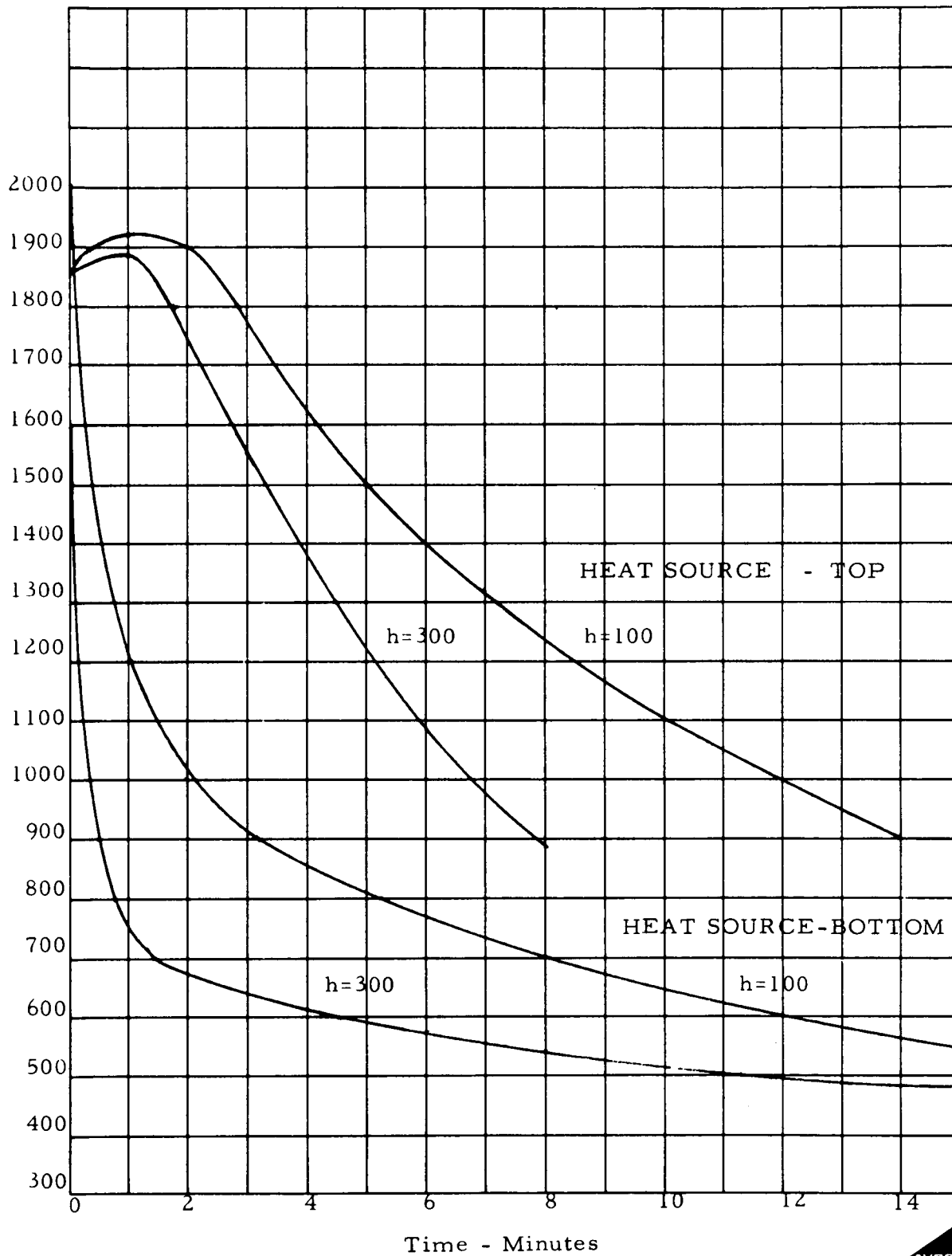


Figure 3

HEAT SOURCE RESPONSE TO ACHX COOLDOWN  
FROM STEADY STATE - 500°F ACHX WALL TEMP.



## APPENDIX B

### ORIFICE COMPUTATIONS - AUXILIARY COOLANT HEAT EXCHANGER (ACHX)

#### INTRODUCTION.

As discussed in paragraph 3.3.3, the heat source is provided with an integral auxiliary coolant heat exchanger (ACHX) sized to maintain the HSU temperature below 177°C (350°F) while in an oxygen atmosphere to minimize the probability of structure oxidation and to facilitate handling.

The auxiliary cooling system requirements were established based on nitrogen flowing in parallel through the ACHX channels. Variation in flow rates from channel to channel is required due to the variation of the number of heat sources in each row across the diameter of the circular heat source unit. The coolant flow rates and flow distribution requirements were calculated parametrically for ranges of inlet temperature and pressure. Based on the results, NASA selected inlet conditions of 16°C (60°F) and 69 newton/cm<sup>2</sup> (100 psi). Each flow channel is orificed at the return header to maintain a constant channel exit wall temperature across the heat source plate. The following analysis was utilized to determine the necessary orifice sizes for the selected design point under the restriction that total ACHX head loss not exceed 13.8 newton/cm<sup>2</sup> (20 psi).

#### NOMENCLATURE.

- p - static pressure (lb<sub>f</sub>/in<sup>2</sup>)
- p<sub>D</sub> - dynamic pressure (lb<sub>f</sub>/in<sup>2</sup>)
- ρ - coolant density (lb<sub>m</sub>/ft<sup>3</sup>)
- $\dot{m}$  - mass flow rate (lb<sub>m</sub>/sec)
- T - static temperature (°F)
- V - flow velocity (ft/sec)
- A - flow area (in<sup>2</sup>)
- L - flow length (in)

- C - discharge coefficient (dimensionless)
- Y - expansion factor (dimensionless)
- $f$  - friction factor (dimensionless)
- Re - Reynolds' number (dimensionless)
- D - diameter (in)
- $D_h$  - hydraulic diameter (in)
- $\mu$  - coolant viscosity (lb<sub>m</sub>/ft-sec)
- G - mass flux (lb<sub>m</sub>/ft<sup>2</sup>-sec)
- g - gravitational constant = 32.1739 ft-lb<sub>m</sub>/lb<sub>f</sub>-sec<sup>2</sup>
- R - gas constant = 0.383047 psia-ft<sup>3</sup>/lb<sub>m</sub>-°R (nitrogen)

#### Subscripts

- i - inlet header
- o - outlet header
- j - flow channel j
- m - mean value
- c - channel
- h - header
- T - total
- + - downstream station
- - upstream station
- x - local position

#### ANALYSIS.

Coolant flow rates and flow distribution requirements were established for the heat load distribution corresponding to the 25KW design. To establish the required mass flow distribution each channel is orificed at the return header. Knowledge of the static pressure distribution throughout the ACHX is necessary to determine the required orifice dimensions for the selected design point.

Due to the unusual flow distribution, dynamic head losses due to  $90^\circ$  turns, constrictions, etc., are not applicable in the classical sense. The most significant change in static pressure is in the inlet and outlet headers and is associated with the local change in momentum at each channel inlet and exit.

The following assumptions were made in the analysis to determine the static pressure distribution and orifice dimensions:

- o The connector to the inlet header is above the inlet to channel one; i.e., no friction head loss in header from connector to channel one.
- o Similarly, the connector to the return header is above the orifice at the exit of channel one; i.e., no friction head loss from channel one to connector.
- o The coolant flow in the inlet header is isothermal at the inlet temperature ( $60^\circ\text{F}$ )
- o The coolant flow in the return header is isothermal at the bulk exit temperature,  $T_o$ , where

$$T_o = \frac{\sum_{j=1}^{15} m_j T_{j0}}{\sum_{j=1}^{15} m_j} = 79.14^\circ\text{F}$$

- o Parameters in the inlet header are evaluated at  $p_{1j}$ ,  $T_1$ .
- o Parameters in the return header are evaluated at  $p_{oj}$ ,  $T_o$ .
- o Parameters in each channel are evaluated at  $p_{1j}$ ,  $T_{cm}$ ; where

$$T_{cm} = \frac{1}{2}(T_{1j} + T_{oj}) \text{ and } T_{1j} = T_1$$

- o Friction factor,  $f$ , is evaluated for smooth pipe and is approximated by (Ref. A3-1):

$$f = 0.046/\text{Re}^{0.2} \quad \text{in the channels}$$

and

$$f = 0.046/\text{Re}^{0.2} \left[ \text{Re}(D/D_h)^2 \right]^{0.05} \quad \text{in the headers}$$

where the term in brackets is a correction for curvature.

The static pressure distribution in the headers is approximated by (ref. A3-2):

$$p_{1x} = p_1 + p_{D1} \left( 1 - \frac{m_x^2}{m_1^2} \right) - 4f_{1x} \cdot L_x/D_h \cdot (\rho_x V_x^2/2g)_1 \quad (1)$$

$$p_{ox} = p_o + 2p_{D_o} \left( 1 - \frac{m_x^2}{m_1^2} \right) + 4f_{ox} \cdot L_x/D_h \cdot (\rho_x V_x^2/2g)_o \quad (2)$$

where:

TABLE A3-1

## INLET HEADER FLOW PARAMETERS

CHANNEL	$\dot{m}_j$ (LBS/SEC)	$T_{1j}$ (°F)	$L_{j \rightarrow j+1}$ (IN.)	$Re_{1j}$	$f_{1j}$	$4f(L_x/D_h) \cdot (\rho V^2/2g)$ (PSI)
1	0.14363	60.		$2.414 \times 10^6$	0.00369	0.00000
2	0.33886	60.	7.30	2.348	0.00370	0.21879
3	0.36833	60.	6.50	2.192	0.00374	0.17063
4	0.38309	60.	5.20	2.023	0.00379	0.11702
5	0.38309	60.	4.50	1.848	0.00384	0.08511
6	0.39767	60.	4.16	1.672	0.00390	0.06507
7	0.41090	60.	4.00	1.489	0.00397	0.05029
8	0.41090	60.	3.86	1.301	0.00405	0.03763
9	0.41090	60.	3.86	1.112	0.00414	0.02807
10	0.39767	60.	4.00	$9.243 \times 10^5$	0.00426	0.02057
11	0.38309	60.	4.16	7.418	0.00440	0.01421
12	0.38309	60.	4.50	5.661	0.00459	0.00930
13	0.36833	60.	5.20	3.903	0.00485	0.00539
14	0.33886	60.	6.50	2.213	0.00528	0.00236
15	0.14363	60.	7.30	$6.589 \times 10^4$	0.00634	0.00028
TOTALS	5.2621	60.				0.82475



TABLE A3-II

## RETURN HEADER FLOW PARAMETERS

CHANNEL	$\dot{m}_j$ (LBS/SEC)	$T_{oj}$ (°F)	$L_{j \rightarrow j+1}$ (IN.)	$Re_{oj}$	$f_{oj}$	$4f(L_x/D_h) \cdot (\rho v^2/2g)$ (PSI)
B-5	1	0.14363	65.31	2.343x10 <sup>6</sup>	0.00371	0.00000
	2	0.33886	69.00	2.279	0.00372	0.28315
	3	0.36833	76.57	2.128	0.00376	0.21798
	4	0.38309	79.91	1.964	0.00381	0.14757
	5	0.38309	79.91	1.794	0.00386	0.10608
	6	0.39767	83.02	1.623	0.00392	0.08025
	7	0.41090	86.00	1.446	0.00398	0.06143
	8	0.41090	86.00	1.263	0.00407	0.04556
	9	0.41090	86.00	1.080	0.00416	0.03373
	10	0.39767	83.02	8.973x10 <sup>5</sup>	0.00428	0.02457
	11	0.38309	79.91	7.202	0.00442	0.01689
	12	0.38309	79.91	5.495	0.00461	0.01102
	13	0.36833	76.57	3.789	0.00487	0.00637
	14	0.33886	69.00	2.149	0.00531	0.00278
	15	0.14363	65.31	6.397x10 <sup>4</sup>	0.00636	0.00033
TOTALS	5.2621	79.14				1.03779

$$PD_1 = (\rho V^2 / 2g)_1 = m_T^2 / 2A^2 \rho_1 g \quad (3)$$

$$PD_0 = (\rho V^2 / 2g)_0 = m_T^2 / 2A^2 \rho_0 g \quad (4)$$

and

$$\rho_1 = p_1 / RT_1 ; \quad \rho_0 = p_0 / RT_0 \quad (5)$$

The local friction factor,  $f_x$ , is a function of the local Reynolds number which is defined as:

$$Re_x = \rho_x V_x D_h / \mu_h = m_{j+D_h} / \mu_h \quad (6)$$

where the absolute viscosity is a function of the coolant temperature in the headers.

The pertinent flow parameters are summarized in Table A3-I for the inlet header and Table A3-II for the return header. The static pressure distribution in the inlet and return headers is given in Table A3-III.

A 3.175 cm. (1.25 in.) diameter inlet to each channel was selected to minimize head losses. The pressure drop at each inlet is calculated from:

$$\Delta p_{1j} = m_j^2 / C^2 \cdot 2 \rho_{1j} A_{1j}^2 g \quad (7)$$

where

$$C = 0.6 \text{ (sharp-edge)}$$

$$\rho_{1j} = p_{1j} / RT_1$$

The expansion factor,  $Y$ , normally appearing in equation (7) is taken as 1.0.

Normally, turning losses and friction losses in the channels would be accounted for. However, the dynamic head in each channel is so small that such losses are negligible and can be omitted from the analysis.

The remaining pressure drop is taken at the outlet orifice of each channel and is simply:

$$\Delta p_{0j} = p_{1j} - p_{0j} - \Delta p_{1j} = m_j^2 / (C^2 \cdot 2 \rho_{0j} A_{0j}^2 g) \quad (8)$$

where

$$C = 0.6$$

$$\rho_{0j} = p_{j-} / RT_{j-} = (p_{1j} - \Delta p_{1j}) / RT_{0j}$$

Again, the expansion factor,  $Y$ , normally appearing in equation (8) is estimated to be greater than 0.95 and is taken as 1.0 for simplicity. The unknown in eq. (8) is  $A_{0j}$ , the area of the orifice. Orifice diameters are calculated from:

TABLE A3-III  
HEADER STATIC PRESSURE DISTRIBUTION

CHANNEL	$P_{ij}$ (PSI)	$P_{oj}$ (PSI)
Inlet/Outlet	100.000	80.000
1	100.259	80.679
2	100.623	82.490
3	101.260	83.967
4	101.876	85.369
5	102.420	86.666
6	102.915	87.889
7	103.366	89.009
8	103.755	89.978
9	104.082	90.797
10	104.340	91.446
11	104.537	91.936
12	104.681	92.294
13	104.770	92.513
14	104.810	92.606
15	104.816	92.613

$$D_{oj} = (4A_{oj}^2/\pi)^{\frac{1}{2}} \quad (9)$$

Inlet losses, orifice pressure drop and orifice diameters are summarized in Table A3-IV. Note that due to the location of the inlet and outlet connectors, there is no pressure symmetry in the system which is reflected in the unusual orifice diameter distribution attained.

#### UPSTREAM ORIFICING.

If a larger total head loss was allowable it would be advisable to orifice at the inlet side of each channel with slightly rounded critical throat areas which would establish choked flow at each inlet. For this situation a discharge coefficient of 1.0 is a better approximation. The only information necessary to accurately distribute the required channel mass flows is the local static pressure and temperature distribution in the inlet header.

The mass flow through each orifice is given by:

$$m_j = 3.88A_{ij}p_{ij}/(RT_{ij})^{\frac{1}{2}} \quad (10)$$

The choked flow orifice diameters are given in Table A3-V. Note that a head loss of 52.5% of the upstream static pressure is taken at the orifice to each channel.

#### REFERENCES.

- A3-1. Rohsenow, W.M. and Choi, H.Y., "Heat, Mass and Momentum Transfer," Prentice-Hall, Inc., Englewood Cliffs, N.J., 1961. pp. 57-61.
- A3-2. Perlmutter, M., "Inlet and Exit-Header Shapes for Uniform Flow Through a Resistance Parallel to the Main Stream," Journal of Basic Engineering, September 1961.

TABLE A3-IV  
INLET AND ORIFICE PARAMETERS

CHANNEL	$\Delta P_{1j}$ (PSI)	$\Delta P_{oj}$ (PSI)	$D_{oj}$ (IN.)
1	0.169	19.411	0.383
2	0.938	17.195	0.608
3	1.101	16.192	0.645
4	1.184	15.323	0.667
5	1.178	14.575	0.675
6	1.263	13.762	0.698
7	1.342	13.014	0.719
8	1.337	12.438	0.727
9	1.333	11.950	0.734
10	1.246	11.648	0.725
11	1.154	11.446	0.713
12	1.152	11.234	0.716
13	1.064	11.192	0.701
14	0.900	11.303	0.668
15	0.161	12.040	0.427

TABLE A3-V

UPSTREAM CRITICAL ORIFICE PARAMETERS

CHANNEL	$P_{ij}$ (PSI)	$T_{ij}$ (°F)	$m_j$ (LBS/SEC)	$D_{cj}$ (IN.)
1	100.259	60.	0.14363	0.282
2	100.623	60.	0.33886	0.432
3	101.260	60.	0.36833	0.449
4	101.876	60.	0.38309	0.457
5	102.420	60.	0.38309	0.456
6	102.915	60.	0.39767	0.463
7	103.366	60.	0.41090	0.470
8	103.755	60.	0.41090	0.469
9	104.082	60.	0.41090	0.468
10	104.340	60.	0.39767	0.460
11	104.537	60.	0.38309	0.451
12	104.681	60.	0.38309	0.450
13	104.770	60.	0.36833	0.442
14	104.810	60.	0.33886	0.423
15	104.816	60.	0.14363	0.275

## APPENDIX C

### HS SUPPORT PLATE ANALYSIS - EARTH ORBIT

#### Heat Source Plate Analysis

#### Weight & Loads

Total weight heat source unit = 1366 Lbs.

Ultimate axial load  $(1.25 \times 42.7\text{-g}) = 53.38 \text{ g}$

#### Analytical Model

(a) For circular plate simply supported along edge: Timoshenko "Plates & Shells" Pg. 57

Maximum moment - center of plate

$$M_r = M_t = \frac{3 + \nu}{16} q a^2$$

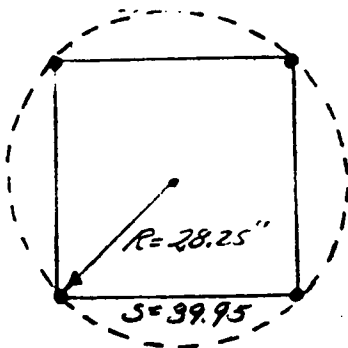
where:  $\nu$  (Poisson's ratio) = .3

$$q \text{ (distributed load)} = \frac{W \times g's}{\pi a^2}$$

$a$  = plate radius = 28.25"

$$\therefore M_r = M_t = \frac{3.3}{16} \times \frac{W \times g}{\pi a^2} \times a^2 = .066 W \times g's$$

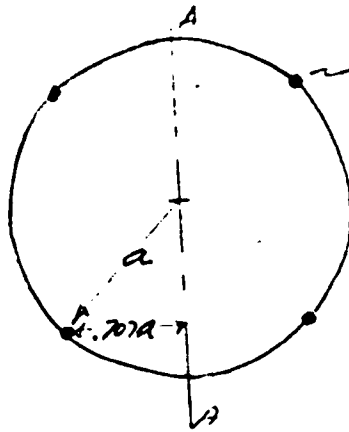
However, plate is supported at 4 equally spaced points on periphery. Since no available design formula exists for this case, a square plate model with



corner supports was used to size plate (Timoshenko, Pg. 219)

$$\text{At center } M = .11 q s^2 = .11 W \times g$$

From static equilibrium



Support Points (4)

Moment (unit width) at AA

$$\begin{aligned}
 M_{AA} &= \frac{\frac{q a^2 \pi}{2} \times .707a - \frac{q a^2 \pi}{2} \times \frac{4 a}{3 \pi}}{2a} \\
 &= \frac{q a^2 \pi}{4} (707 - .424) = .707 q a^2 \pi \\
 \text{or } M_{AA} &= .0707 W \times g \text{ (Lbs/In.)}
 \end{aligned}$$

This is an average unit width moment along diameter AA. The maximum moment would probably be 20-25% greater. It is felt that the square plate expression ( $M = .11 W \times g$ 's) would be best for design although slightly conservative.

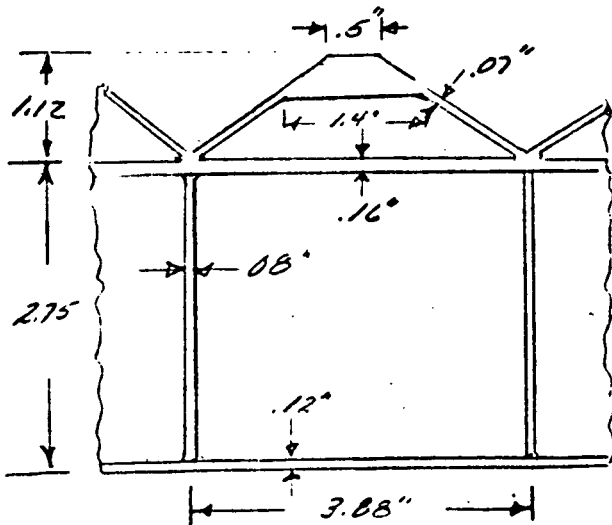
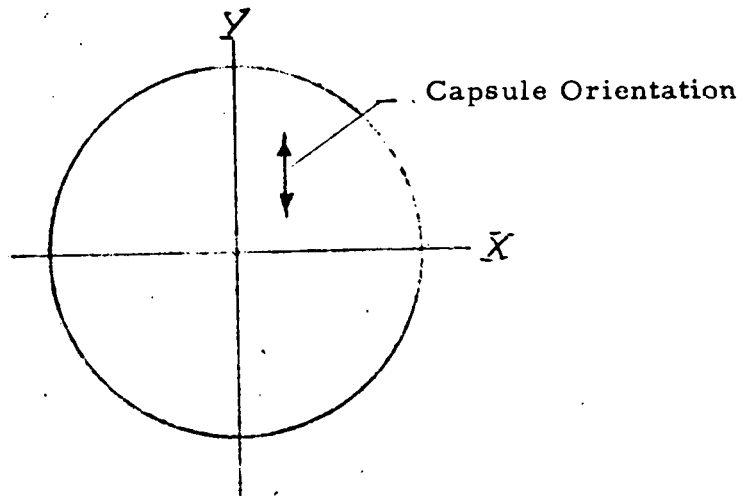
### Analysis

Assumptions:

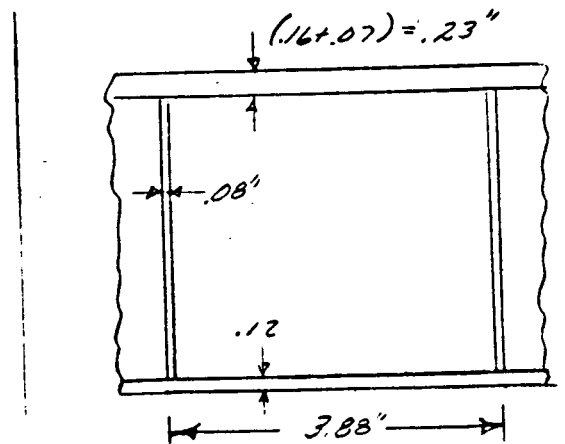
1. HS capsules and retention structure offer no contribution to flexural stiffness.
2. Although plate is anisotropic, a uniform flexural stiffness equal to the minimum value is assumed.



3. The peripheral ACHX header which is stiffer than the plate is neglected.
4. ACHX dimensions as shown (see ACHX analysis)



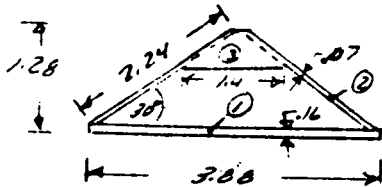
Cross-section showing  
flexure stiffness about  
XX axis



Cross-section for flexural  
stiffness Y Y Axis (minimum)

Compute  $I_{xx}$  of plate

First, find  $\bar{I}_{xx}$  of ACHX channel



No	A	Z	Az	$Az^2$	I
1	.6208	.08	.0497	.0040	.0013
2 @2	.3136	.72	.2258	.1626	.0328
3	.2829	.98	.2772	.2717	.0025
$\Sigma$	1.217		.5527	.4383	.0366

$$\bar{z} = \frac{.5527}{1.217} = .454''$$

$$I_{ACHX} = .4383 + .0366 - 1.217 (.454)^2 = .2241 \text{ in.}^4$$

Combine with lower plate facesheet

	A	Z	Az	$Az^2$	I
ACHX	1.217	3.044	3.7045	11.2766	.2241
L. Facesheet	.466	.06	.0280	.0017	.0005
Totals	1.683		3.7325	11.2783	.2246

$$\bar{z} = \frac{3.7325}{1.683} = 2.218''$$

$$I_{xx} = 11.2783 + .2246 - 1.683 (2.218)^2 = 3.223 \text{ in.}^4$$

$$I_{xx} \text{ (unit width)} = \frac{3.223}{3.88} = .8308 \text{ in.}^{-4}$$

$$Z = \frac{I_{xx}}{c} = \frac{.8308}{2.218} = .374 \text{ in.}^3$$

Find  $I_{yy}$

Member	A in <sup>2</sup>	z	Az	A <sub>z</sub> <sup>2</sup>	I
ACHX(minimum)	.892	2.705	2.4129	6.5268	.0039
L. Facesheet	.466	0.06	.0280	.0017	.0005
Totals	1.358		2.3849	6.5285	.0044

$$\bar{Z} = \frac{2.3849}{1.358} = 1.756''$$

$$I_{yy} = 6.5285 + .0044 - (1.358)(1.756)^2 = 2.345 \text{ in.}^4$$

$$Z_{yy} = \frac{2.345}{1.756} = 1.336 \text{ in}^3$$

$$\text{Unit width section modulus} = \frac{1.336}{3.88} = .344 \text{ in}^3$$

For HS plate design,  $Z_{yy} = .344 \text{ in}^3$  is used since it will result in max. stresses.

#### Abort Reentry

The maximum moment for the 1366 lb. heat source plate at an ultimate axial deceleration of 53.38-g (INT-21 condition)

$$M = .11 (1366) 53.38 = 8021 \text{ in. lbs.}$$

$$\sigma_{\max} = \frac{8021}{.344} = 23316 \text{ psi}$$

$$\text{M.S.} = \frac{\sigma_{\text{allow}} (500^\circ\text{F})}{\sigma_{\max.}} - 1 = \frac{33,000}{23,316} - 1 = .42$$

### Orbit Decay

$$A_x (\text{Ultimate}) = 1.25 \times 8.1 = 10.1 \text{ G's}$$

$$\text{HS temp.} = 1900^\circ\text{F}$$

$$\sigma_{\text{allow}} (\text{cb-1Zr @ } 1900^\circ\text{F}) = 22,000 \text{ psi}$$

$$M = .11 (1366) 10.1 = 1517.6$$

$$\sigma_{\text{max}} = \frac{1517.6}{.344} = 4412 \text{ psi}$$

$$\text{M.S.} = \frac{22,000}{4412} - 1 = 3.98$$

### Deflection

$$\text{INT-21} \quad A_x = 53.38\text{-g}$$

For square plate with corner supports

deflection at center is

$$w = \frac{0.257 W \times g \times S^2}{D}$$

$$\text{where } S = 28.25 \times 1.414 = 39.95$$

$$D = E I$$

$$E = 14.5 \times 10^6$$

$$I_{\text{AVE}} = \frac{.831 + .604}{2} = .718$$

$$\therefore D = 14.5 \times 10^6 \times .718 = 10.4 \times 10^6$$

$$w = \frac{.0257 \times 1366 \times 53.38 \times 39.95^2}{10.4 \times 10^6} = .288''$$

## Internal Ribs

### Earth Orbital Design

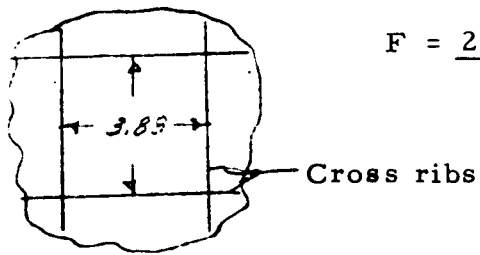
$$t_w = .08''$$

### Check Stability Under Compression

$$\text{Uniform load intensity, } q = \frac{W \times g}{\pi a^2}$$

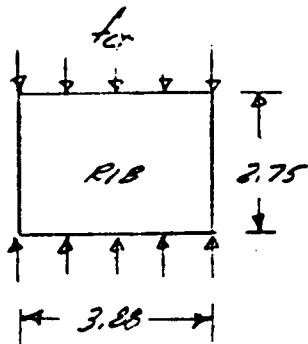
$$q = \frac{1366 \times 53.38}{\pi (28.25)^2} = 29.1 \text{ lbs/in}^2$$

This produces a line load on ribs



$$F = \frac{29.1 \times 3.88^2}{2 \times 3.88} = 56.45 \text{ lb/in.}$$

$$f_c = \frac{56.45}{.08} = 706 \text{ psi}$$



Assume simply supported edges

$$\text{Aspect ratio} = a/b = \frac{2.75}{3.88} = .71$$

$$f_{cr} = KE \left( \frac{t}{b} \right)^2 \quad \text{where } K = 4.1 \text{ for } a/b = .71$$

$$\text{critical } f_{cr} = 4.1 \times 14.5 \times 10^6 \left( \frac{.08}{3.88} \right)^2 = 25,274 \text{ psi}$$

M.S. = Large

### Check Shear Stress

Assume shear carried solely by ribs. Max shear stress in web given by

$$\tau = \frac{V(\text{for } 3.88 \text{ width})}{t d}$$

For circular plate (simply supported at edge)

$$V'_{\text{max}}(\text{unit width}) = \frac{q a}{2} = 29.1 \times \frac{28.25}{2} = 411 \text{ \#/in.}$$

$$\text{For } 3.88'' \text{ spacing } V_{\text{total}} = 3.88 \times 411 = 1600 \text{ lbs.}$$

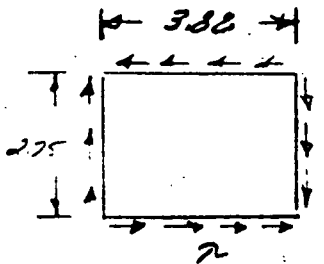
$$\tau = \frac{1600}{.08 \times 2.75} = 7249 \text{ psi}$$

$$\tau_{\text{allow}} = 60\% \times \sigma_{\text{ty}} (500) = 19,800 \text{ psi}$$

say 20,000 psi

$$\text{M.S.} = \frac{20,000}{7249} - 1 = 1.76$$

Check shear stability (simply supported edges)



From Roark "Formulas for Stress & Strain"

$$f_s (\text{critical}) = K \frac{E}{1-\nu^2} \left( \frac{t}{b} \right)^2$$

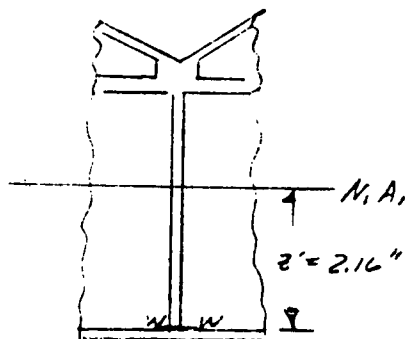
where b is short dimension

$$a/b = 3.88/2.75 = 1.41 \quad K = 60$$

$$f_s = 60 \times \frac{14.5}{.91} \times 10^6 \times \left( \frac{.08}{2.75} \right)^2 > \tau_{\text{yield}} \quad \therefore \text{not a criterion}$$

Since lower facesheet must be plug or slot welded to internal ribs, establish a maximum spacing.

Assume 0.5" long slot welds



Check unit shear stress at section 3-3  
assuming continuous weld.

$$S_s = \frac{V A Z'}{I b}$$

$$\text{where } V = 411 \times 3.88 = 1595$$

$$A = 3.88 \times .12 = .465 \text{ in.}^2$$

$$Z' = 2.16 \text{ in.}$$

$$\therefore S_s = \frac{1595 \times .465 \times 2.16}{3.223 \times .08} = 6213$$

$$I = 3.223 \text{ in.}^4 \text{ based on section width} = 3.88"$$

$$b = .08 \text{ in.}$$

Max. spacing "D" for .5" intermittent slot welds is then

$$D = \frac{20,000 \text{ psi} \times .5}{6213} = 1.6"$$

For slots welds at each cross rib intersection plus one at the mid-point between intersections, find weld length

$$L = \frac{6213 \times 1.95}{20,000} = .608" \text{ say } .625"$$





## Plate/Truss Fitting Analysis (cont'd)

$$H = 2 \times 22,883 \times .7951 \times .9681 = 35,228 \text{ Lbs.}$$

Combined bending and direct stress in vertical leg of fitting which is

3.0 inches deep and 2.25 inches wide is:

$$\sigma = \frac{6 M}{b h^2} + \frac{V}{b h} = \frac{6 \times 35,228 \times 2.75}{2.25 \times 3^2} + \frac{27,862}{2.25 \times 3.0} = 32,299 \text{ psi}$$

$$\tau_{\text{allow}} = 33,000 \text{ psi} \quad \text{Cb-1Zr @ } 500^\circ\text{F}$$

$$\text{M.S.} = \frac{33,000}{32,229} - 1 = .02$$

The horizontal leg of the fitting is made of a 2.0 inch thick web welded to heavy flanges, .25 inch thick and 7.0-inch wide

$$I (\text{horizontal leg}) = 7.47 \text{ in.}^4$$

$$A (\text{horizontal leg}) = 8.0 \text{ in.}^2$$

$$\text{Max. moment} = 35,228 \times 4.13 - 27,862 \times 1.5 = 103,699 \text{ in. lbs.}$$

Combined stress:

$$\sigma = \frac{103,699 \times 1.38}{7.47} + \frac{27,862}{8.0} = 22,628 \text{ psi}$$

$$\text{M.S.} = \frac{33,000}{22,628} - 1 = .46$$

In reality, when one strut is supporting a 22,883 Lb. load, its mating strut at their common fitting is carrying only a 15,354 Lb. load. This occurs for the case when the lateral load is in the plane of the vehicle center line and one of the attachment points on the strut support ring. For the lateral load, applied at an angle  $45^\circ$  to this, in the plane of the vehicle center line and one of the plate fitting, mating struts would support an identical load of 20,676 Lbs. For this case the maximum stress and margin of safety in the fitting would be 29,655 psi and .11, respectively.

## ACHX System Analysis

Design conditions:

Max. working pressure  $P_w$  - 100 psi.

Max. working temperature = 500°F (conservative)

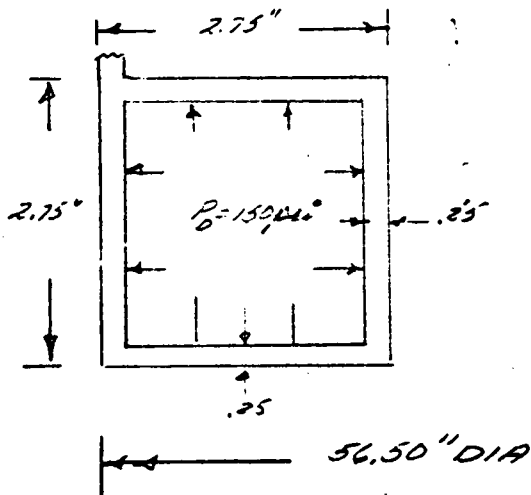
Design pressure =  $1.5 P_w = 150$  psi based on yield criteria

C -1Z yield @ 500°F = 33,000 psi

for welds, assume 80% base material strength

$$(80 \times 33,000 = 26,400 \text{ psi})$$

Header (welded at corners)



Flat section (treat as unit width beam fixed at ends)

$$\begin{aligned} \text{Max moment} &= \frac{1}{12} P \ell^2 \\ &= \frac{150 \times 2.50^2}{12} = 78.12 \text{ in. lbs.} \end{aligned}$$

$$\tau = \frac{6 M}{h^2} = \frac{6 \times 78.12}{.25^2} = 7500 \text{ psi}$$

$$\tau_{\text{allow(weld)}} = 26,400 \text{ psi}$$

$$\text{M.S.} = \frac{26,400}{7500} - 1 = 2.52$$

Check for Temp. = 2000°F (using ACHX system to cool down HSU (in thermal ground test) for a one hour period

For weld at 2000°F  $\sigma_{\text{yield}} = 80\% \times 20,000 = 16,000 \text{ psi}$

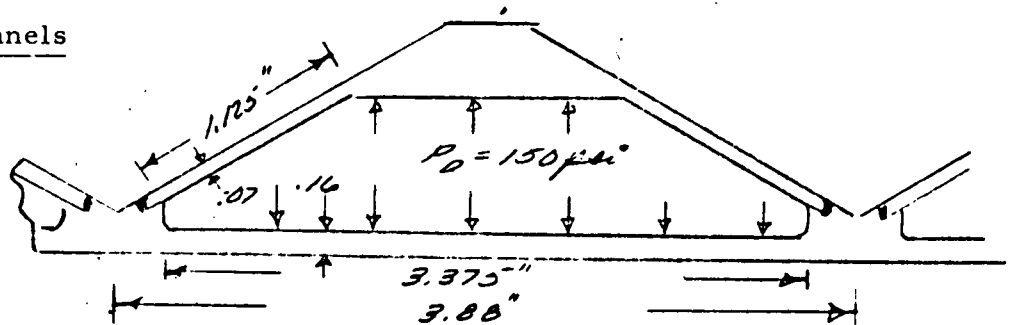
$$\sigma_{\text{1-hr. stress rupture}} = 80\% \times 22,400 = 18,000 \text{ psi}^*$$

\* However for stress rupture the design pressure is taken as  
 $P_D = 2 \times P_w = 200 \text{ psi}$ .

$$\therefore \sigma = \frac{200}{150} \times 7500 = 10,000 \text{ psi}$$

$$\text{M.S.} = \frac{18,000}{10,000} - 1 = .8$$

#### Coolant Channels



Check .07" channel wall

$$M = \frac{P_D l^2}{12} = \frac{150 \times 1.125^2}{12} = 15.82 \text{ in. lbs.}$$

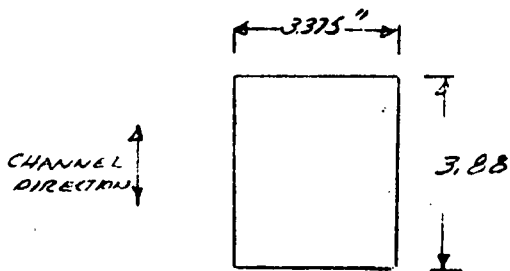
$$\sigma = \frac{6 \times 15.82}{.07^2} = 19,372 \text{ psi}$$

$$\tau_{\text{allow}} = 26,400 \text{ psi}$$

$$\text{M.S.} = \frac{26,400}{19,372} - 1 = .36$$

0.16" facesheet ~ treat as plate simply supported along

edges subjected to  $p = 150 \text{ psi}$



$$b/a = 3.88/3.375 = 1.15$$

$$M = \beta p_D a^2 \text{ where } \beta = .059$$

$$\therefore M = .059 \times 150 \times 3.375^2 = 100.8 \text{ in. Lbs.}$$

$$\sigma = \frac{6M}{h^2} = \frac{6 \times 100.8}{.16^2} = 23,625 \text{ psi}$$

$$\text{M.S.} = \frac{33,000}{23,625} - 1 = .40$$

The above results indicate that it would not be possible to use a 100 psi pressure at 2000°F. In order to see the effect of temperature on allowable working pressure, see Figure 3.3.4.1.

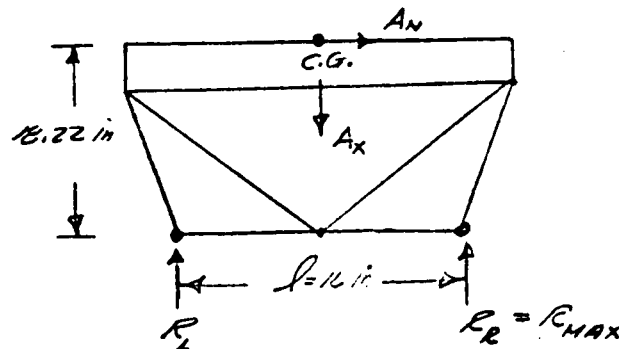
## Strut Analysis - Earth Orbit

### Strut Analysis

The strut is designed to support the maximum reentry inertial loads of the HSU, and will be checked for both compressive stresses and buckling. Where lateral g -loading is considered, an additional stress occurs in the strut due to the imposed moment. The HSU weight is 1571 lbs. and its C. G. is taken as 18.22 inches above the strut support ring on the aeroshell.

To find the worst strut load condition, it is necessary to consider the various critical load combinations and load orientations. The expression for the maximum reaction at the strut/aeroshell ring attachment when the lateral load occurs in the plane defined by the vehicle center line and one of the strut/aeroshell ring attachment points is

$$R_{\max} = \frac{(A_x)(1571)}{4} + \frac{(A_n)(1571)(18.22)}{L}$$



### Strut Analysis (Cont'd)

From the maximum reaction,  $R_{\max}$ , the maximum strut load can be found since there are two struts per reaction point and the strut true angle with the horizontal is 37.5 degrees.

$$F_s = \frac{R_{\max}}{2 \sin 37.5^\circ}$$

For the case of maximum lateral load (INT-21) the design loads are

$$A_x = 31.0 \times 1.25 = 38.75 - g$$

$$A_n = 4.6 \times 1.25 = 5.75 - g$$

Therefore  $R_{\max} = 25,506 \text{ lbs.}$

$$F_s = 20,947 \text{ lbs.}$$

Maximum axial load case

$$A_x = 38.1 \times 1.25 = 47.62 - g$$

$$A_n = 4.1 \times 1.25 = 5.12 - g$$

$$R_{\max} = 27,862 \text{ lbs.}$$

$$F_s = 22,883 \text{ lbs.}$$

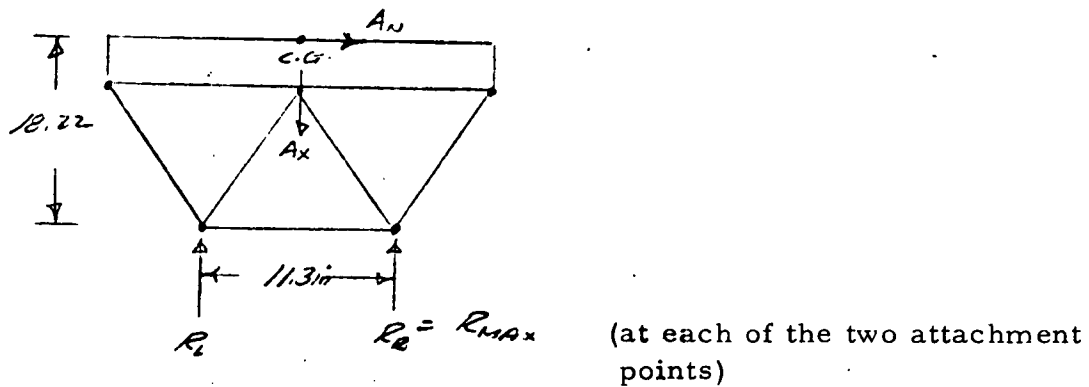
Maximum axial load (zero angle of attack)

$$A_x = 42.7 \times 1.25 = 53.38 - g$$

$$R_{\max} = 20,963 \text{ lbs. and } F_s = 17,217 \text{ lbs.}$$

### Strut Analysis (cont'd)

If the orientation of the lateral load is displaced angularly 45 degrees so that the lateral load is in the plane of the vehicle axis and one of the strut/plate attachments, the load diagram becomes



$$R_{\max} = \frac{A_x (1571)}{4} + \frac{A_n (1571) (18.22)}{(2) (11.3)}$$

For the two load case involving lateral -g's

	$R_{\max}$ , lbs.	$F_s$ , lbs.
Maximum lateral load	22,502	18,480
Maximum axial load	25,188	20,686

Since the maximum strut load will occur for one of the two orientations considered because of symmetry, it appears that the 22,883 lbs. calculated for the previous case is maximum.

### Strut Analysis (cont'd)

The maximum strut stress for a tubular cross section with 1.0 in. I. D. and .188 in. wall thickness (area = .48 in<sup>2</sup>) is

$$\sigma_s = \frac{22,883}{.48} = 47,673 \text{ psi}$$

The minimum yield strength of T-111 at 500°F is 53,000 psi, therefore, the margin of safety on stress is

$$\text{M.S.} = \frac{53,000}{47,673} - 1 = .11$$

For the reentry from orbit case where the design loads are  $A_x = 9.75\text{-g}$  and  $A_n = 0.5\text{-g}$ , the maximum strut stress, and margin of safety are:

$$F_s \text{ (orbit reentry)} = 3879 \text{ lbs.}$$

$$\sigma_{\text{max.}} = 3879 / .48 = 8081 \text{ psi}$$

$$\sigma_{\text{allow}} = 37,000 \text{ psi (T-111 at } 1900^\circ\text{F)}$$

$$\text{M.S.} = 3.58$$

### Buckling Criteria

The strut length is 20.9 inches and it is assumed that the struts are pinned at the upper end and built-in at their lower end where it attaches rigidly to the aeroshell ring.



### Strut Analysis (cont'd)

The critical buckling load is

$$P_{cr} = \frac{\pi^2 E I}{(.7l)^2}$$

$$\text{where } I = .0417 \text{ in.}^4$$

$$E = 25 \times 10^6 \text{ (T-111 at } 500^\circ\text{F)}$$

$$P_{cr} = \frac{\pi^2 (25 \times 10^6) (.0417)}{(.7 \times 20.9)^2} = 48,025 \text{ lbs.}$$

The maximum design load for buckling if a safety factor of 1.5 is used instead of 1.25 is 27,460 lbs. The resulting margin of safety on buckling is

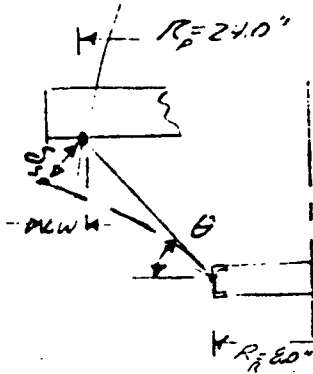
$$\text{M.S.} = \frac{48,025}{27,460} - 1 = .75$$

It is concluded that the reference strut design (1.0 in. I. D. and .188 in. wall) is adequate.

### Thermal Loads Due to Heat Source Plate Expansion and Effect on Reentry Loads

As the heat source temperature increases, it will expand radially, and since the mean temperature of the truss system is considerably lower, the struts will have to bend to accommodate the differential radial expansion.

## Strut Analysis(Cont'd)



INT-21 Abort HSU Temperature = 500°F

If the titanium ring on the aeroshell is assumed to be 100°F and the average strut temperature is 300°F.

The radial growth of the plate at the fitting based on an initial temperature equal to room temperature is

$$w_p = R \alpha \Delta T$$

where

R = Radius (24.0 inches)

$\alpha$  = coefficient of thermal expansion ( $4.1 \times 10^{-6}$  in/in.°F)

$\Delta T$  = temperature rise (500°F R. T. = 430°F)

Therefore,  $w_p = 24 \times 4.1 \times 10^{-6} \times 430 = .042$  inches

The unrestrained radial growth of the pinned end of the strut is a combination

of the ring attachment growth and strut growth projected in the radial plane of the fitting.

$$\begin{aligned} w \text{ (pinned end)} &= w_R + W_s = 8.0 \times .707 \times 5.0 \times 10^{-6} \times (100-70) \\ &\quad + [24 - (8.0 \times .707)] \times 3.1 \times 10^{-6} \times (300-70) \\ &= .0008 + .0131 \sim .014 \text{ in.} \end{aligned}$$

The radial thermal mismatch  $\Delta w$  is

$$\Delta w = .042 - .014 = .028 \text{ inches.}$$

### Strut Analysis (cont'd)

As shown by the above sketch, the interaction load at the pinned connection will cause the strut to bend about its fixed end an amount  $\delta_s$  which is equal to

$$\delta_s = \frac{\Delta W}{\sin \theta} = \frac{.028}{\sin 37.5} = .046 \text{ inches}$$

The end force perpendicular to the strut axis required to produce a deflection of .046 inches is given by

$$P = \frac{3 E I}{l^3} \times \delta_s$$

where  $l$ , strut length = 20.9

$$E, \text{ modulus of elasticity, } = 25 \times 10^6$$

$$I, \text{ moment of inertia, } = .042 \text{ in}^4$$

$$\text{Therefore } P = \frac{3 \times 25 \times 10^6 \times .042}{20.9^3} \times \delta_s = 16 \text{ lbs.}$$

During INT-21 abort reentry, this load and deflection will produce additional stress in the strut at the lower end.

The total stress becomes

$$\begin{aligned} \sigma_{\max}(\text{lower end}) &= \frac{22,883}{.48} + \frac{(22,883 \times .046)c}{I} + \frac{(16 \times 20.9)c}{I} \\ &= 47,673 + 12,531 + 3981 = 64,185 \text{ psi} \end{aligned}$$

The temperature at the lower end of the strut is 100°F and the allowable stress limit of the T-111 material is 80,000 psi. Although this would decrease for somewhat higher temperature so would the thermal mismatch resulting in lower stresses.

## Strut Analysis (cont'd)

### HSU Operating Temperature Case

The operating temperature of the HSU is assumed to be 1900°F. Thermal studies have indicated that the average strut temperature is 1200°F and the titanium ring temperature is 500°F. The radial thermal growth of the plate is then

$$w_p = 24 \times 4.4 \times 10^{-6} \times (1900 - 70) = .193 \text{ in.}$$

Note that a slightly higher  $\alpha = 4.4 \times 10^{-6}$  was used for

Cb-1Zr at 1900°F than the previous case.

The unrestrained radial growth for the pinned end of the strut is given as

$$\begin{aligned} w_s &= \frac{8}{.707} \times 5.0 \times 10^{-6} \times (500 - 70) + \left(24 - \frac{8}{.707}\right) 3.6 \times 10^{-6} \times (1200 - 70) \\ &= 0.24 \text{ in.} + .075 \text{ in.} = .098 \text{ in.} \end{aligned}$$

The mismatch is hence

$$\Delta w = .193 - .098 = .095 \text{ in.}$$

The strut end deflection,  $\delta_s$  is

$$\delta_s = \frac{.095}{.6088} = .156 \text{ in.}$$

The end load to produce this deflection

$$P = \frac{3EI}{L^3} \times \delta_s = 53.8 \text{ lbs.}$$

This causes a bending stress at the ring of

$$\sigma = \frac{(53.8 \times 20.9)c}{I} = \frac{1124.4 \times .5}{.042} = 13,386 \text{ psi}$$

During reentry from orbit, the maximum stress will occur at the ring and will consist of (1) compression stress from inertia load (2) a bending stress due to the compression load and thermal-induced deflection of .156 in. and (3) a bending stress produced by the thermal end load of 53.8 lbs.

$$\begin{aligned}\sigma_{\text{total}} &= \frac{3879}{.48} + \frac{(3879 \times .156)c}{I} + \frac{(53.8 \times 20.9)c}{I} \\ &= 8081 + 7204 + 13,386 = 28,671 \text{ psi}\end{aligned}$$

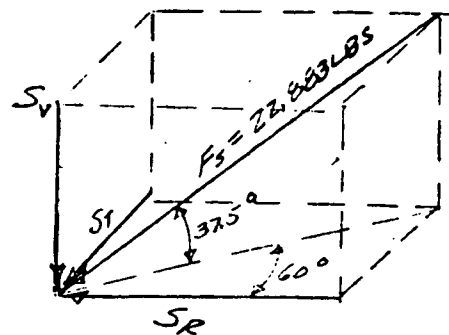
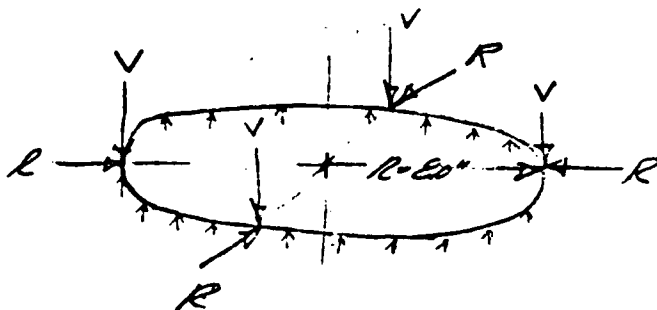
At the lower end, the temperature is 500°F and hence the allowable stress of T-111 is 53,000 psi. The margin of safety is

$$\text{M.S.} = \frac{53,000}{28,671} - 1 = .85$$

The results indicate that the reference strut is capable of supporting the HSU under the combined mechanical and thermal loads.

#### Strut Attachment Ring Analysis

The strut attachment ring on the aeroshell is fabricated from 6A L-4V titanium alloy. The ring must be capable of supporting the inertia loads of the HSU during reentry which are introduced at the four strut attachment points and distribute them into the aeroshell where they are reacted against by the aerodynamic pressure on the aeroshell surface. Because of the angular orientation of the struts, the ring must support both an axial load component, V, and a radial component, R, at each attachment point. These loads are found by resolving the intersecting strut loads as shown.



3-D STRUT LOAD  
DIAGRAM

### Strut Attachment Ring Analysis (cont'd)

Load components per strut for worst INT-21 case.

$$F_s = 22,883 \text{ Lbs.}$$

and

$$S_v = 22,883 \times \sin 37.5^\circ = 22,883 \times .6088 = 13,931 \text{ lbs.}$$

$$S_T = 22,883 \times \cos 37.5^\circ \cos 60^\circ = 15,722 \text{ lbs.}$$

$$S_R = 22,883 \times \cos 37.5^\circ \sin 60^\circ = 9,078 \text{ lbs.}$$

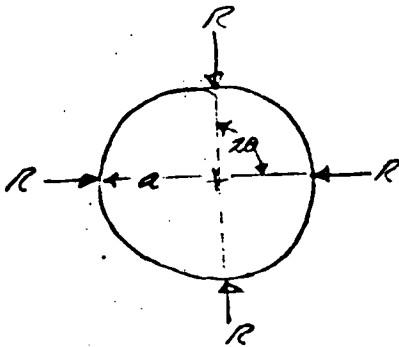
For intersecting struts the loads to the strut support ring become

$$V = 2 \times S_v = 27,862 \text{ lbs.}$$

$$R = 2 \times S_R = 18,156 \text{ lbs.}$$

The tangential loads,  $S_T$ , react against one another and cancel out.

### In-Plane Bending and Hoop Forces Due to Radial Loads



From Roark:

Midway between loads

$$\text{Max. } -M = \frac{1}{2} R a \left( \frac{1}{\sin \theta} - \frac{1}{\theta} \right)$$

$$= \frac{1}{2} R a \left( \frac{1}{.707} - \frac{4}{\pi} \right) = .0702 R a$$

$$F = \frac{1}{2} R \times \frac{1}{\sin \theta} = .707 R$$

For  $R = 18,156 \text{ lbs.}$  and  $a = 7.5 \text{ in.}$

$$M = .0702 \times 18,156 \times 7.5 = -9559 \text{ in. lbs.}$$

$$F = 12,836 \text{ lbs.}$$

Negative force means compression and negative moment denotes a direction which causes decrease in curvature (tension at O.D and compression at I. D.)

At each load

$$\text{Max. } + M = \frac{1}{2} R a \left( \frac{4}{\pi} - \cos \theta \right) = .137 R a = 18,648 \text{ in.lbs.}$$

$$F = \frac{1}{2} R = -9078 \text{ lbs.}$$

The forces for in-plane bending are most critical at the load points.

### Out of Plane Bending

At the load points, the out-of-plane bending moment  $M'$  for the ring is

$$M' = w a^2 \left( \frac{\sin \frac{\theta}{2} - \frac{\theta}{2} \cos \frac{\theta}{2}}{\sin \frac{\theta}{2}} \right)$$

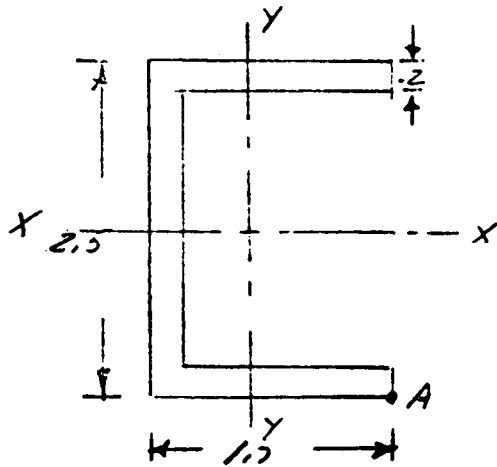
where the circumferential line load is

$$w = \frac{4 V}{2 a \pi} = \frac{2 V}{a \pi}$$

$$\begin{aligned} M' &= \frac{2 V a}{\pi} \left( 1 - \frac{\pi}{4} \right) = .138 V a \\ &= .138 \times 27,862 \times 7.5 = 28,749 \text{ in.lbs.} \end{aligned}$$

## Strut Attachment Ring Analysis (cont'd)

Find moments of inertia about principal cross-section axes



Find  $I_{yy}$  (in-plane bending)

	A	x	Ax	$Ax^2$	I
Web	.5	.1	.05	.0050	.0017
Flanges(2)	.6	.95	.57	.5415	.1125
Totals	1.1		.62	.5465	.1142

$$\bar{x} = \frac{.62}{1.1} = .5636$$

$$I_{yy} = (Ax^2 + I - A\bar{x}^2)$$

$$= .5465 + .1142 - 1.1 (.5636)^2 = .311 \text{ in.}^4$$

$I_{xx}$  (out-of-plane bending)

$$I_{xx} = 2 (1.5)(.2)(1.15) + \frac{2.5^3 \times .20}{12} = .794 + .260 = 1.05 \text{ in.}^4$$

$$\bar{y} = 1.25$$

Maximum combined stress occurs at point "A" on channel where stresses from both moments are additive.

$$\sigma_{\max} = \frac{18,648 \times 1.136}{.311} - \frac{9078}{1.1} + \frac{28,749 \times 1.25}{1.05}$$

$$= 68,116 - 8253 + 34,225 = 94,088 \text{ psi}$$

$$\sigma_{\text{allowable}} = 115,200 \text{ psi}$$

$$\text{M.S.} = \frac{115,200}{94,088} - 1 = .22$$

Radial deflection due to the radial kick loads is small

$$w = \frac{.0061 R a^3}{E I} = \frac{.0061 \times 18,156 \times 7.5^3}{16.4 \times 10^6 \times .311} = .009 \text{ in.}$$



## Aeroshell Design

The aeroshell is designed to withstand both stress and stability failures under peak reentry inertia and pressure loads. The INT-21 abort represents the critical design reentry environment with a peak stagnation pressure of 20.74 psi. The maximum structure temperature at peak pressure is assumed to be 350°F.

The aeroshell construction is an aluminum honeycomb, aluminum being selected since thermal studies indicated that the maximum operating temperature in the aeroshell is approximately 220°F<sup>\*</sup>, well within the capability of high-strength aluminum alloys such as 2024-T81. The procedure used in sizing the honeycomb is to first perform a membrane analysis to ensure facesheet gauges are adequate to support the membrane stresses, and then a buckling check to ensure adequate core thickness for shell stability under external pressure.

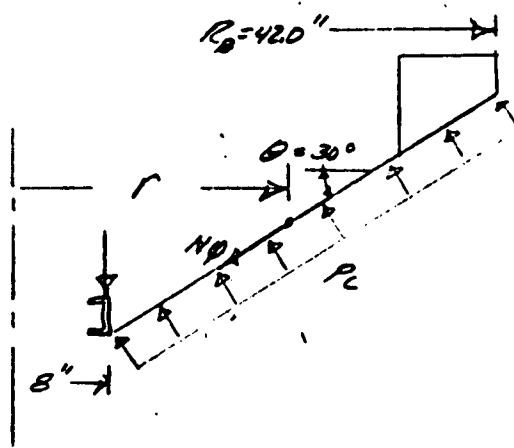
### Symmetrical Membrane Analysis

The design stagnation pressure is

$$P_D = 1.25 \times 20.74 = 25.92 \text{ psi}$$

Since large angles of attack ( $> 20^\circ$ ) persist at peak loading, the windward meridian of the  $60^\circ$  blunt cone could very well feel pressures close to the stagnation pressure level. For practical analysis, the cone pressure was taken as the stagnation pressure for the symmetrical case. Since the axial component of the aerodynamic pressure load on the cone is transmitted down the shell to the strut attachment ring where it is reacted primarily by the HSU inertia load, the membrane load distribution can be given as

\*HT424 Heat Tape is the bonding resin in the honeycomb fabrication.



$$\text{Meridian } N_{\phi} = \frac{P_c (R_B^2 - r^2)}{2 r \sin 30^\circ} = \frac{P_c (R_B^2 - r^2)}{r}$$

$$\text{Hoop } N_{\theta} = \frac{P_c r}{\sin 30^\circ} = 2 P_c r$$

Both  $N_{\phi}$  and  $N_{\theta}$  membrane forces were computed versus radius,  $r$ , for a  $P_c = 25.92$  psi and are presented in the Table below. Based on the Von Mises yield criteria for biaxial stress given by  $N_{\text{eff}}^2 = N_{\phi}^2 - N_{\phi}^2 N_{\theta} + N_{\theta}^2$  the required facesheet thicknesses are also presented. A conservative yield strength of 41,000 psi for 2024-T81 aluminum was used, which is the 350°F valve after long term exposure at around 300°F.

Radial Station, $r$	$N_{\phi}$ , Lbs/in	$N_{\theta}$ , Lbs/in.	$N_{\text{eff}}$ , Lbs/in	Required Facesheet Thk. ,in.
8	-415	5505	5723	.07
12	-622	3499	3848	.047
15	-777	2658	3120	.038
20	-1036	1766	2454	.03
25	-1295	1180	2144	.026
30	-1554	746	2033	.025
40	-2073	106	2127	.026

The membrane stress analysis indicates that for at least half the cone, the outer half which constitutes the major surface area and hence cone weight, a minimum facesheet thickness of .026 inches is adequate. Increased facesheet thicknesses are necessary closer to the strut support ring where the facesheet would normally be beefed-up anyway to take care of local bending effects. To establish the minimum core thickness needed to resist general shell buckling under an external pressure of 25, 92 psi., a minimum facesheet thickness of .026 inches was used. The expression for critical buckling pressure is given by

$$P_{cr} = 3.12 (1 - \mu^2)^{3/4} \frac{t_f E_f}{L} \left( \frac{t_c}{\rho_{ave}} \right)^{3/2}$$

Where  $E_f$  is modulus of elasticity of facesheet material.

$L$  is unsupported slant length of cone

$t_c$  is honeycomb core thickness

$\rho_{ave}$  is average radius of curvature of unsupported cone

For  $L = 36.95$  in.,  $\rho_{ave} = 48$  in.,  $t_f = .026$  in.,

$E = 9.8 \times 10^6$  and  $P_{cr} = 25, 92$  psi

The required core thk.,  $t_c = .51$  inches.

#### Asymmetrical Membrane Analysis

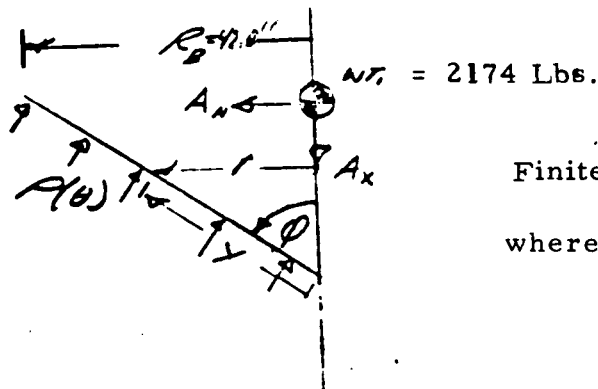
The asymmetrical pressure distribution on the aeroshell would result in higher forces at the windward meridian than the previous symmetrical analysis shows and therefore an asymmetrical analysis was performed. The circumferential pressure distribution was assumed to be given by:

$$P(\theta) = A + B \cos \theta$$

where  $\theta$  is measured from the windward meridian

### Aeroshell Analysis (cont'd)

In order to solve for the constants "A" and "B" the integrated pressure distribution on the aeroshell was equated to the reentry inertial loads. The effect of fence pressure loads was neglected which will result in somewhat conservative values for A and B



Finite surface element =  $r d\theta dy$

where

$$dy = \frac{dr}{\sin \phi}$$

### Equilibrium in Direction Normal to Vehicle Axis

The surface pressure load component of the element in the normal direction,

$$P_n = P_w \cos \phi \cos \theta$$

where  $P_w$  is surface pressure on windward meridian

Equate total pressure load acting in normal direction to normal inertia load.

$$2 \int_0^\pi \int_0^{R_B} (A + B \cos \theta) \cos \phi \cos \theta \frac{r d\theta}{\sin \phi} dr = 2174 \times 4.1 g$$

Integrating with respect to "r"

$$R_B^2 \cot \phi \int_0^\pi A \cos \theta + B \cos^2 \theta d\theta = 8913 \text{ Lbs.}$$

Integrating with respect to "θ" gives

$$.577 \pi R_B^2 B = 8913$$

$$\text{and } B = 2.79 \text{ psi}$$

### Equilibrium in Axial Direction

$$2 \int_0^\pi \int_0^{R_B} (A + B \cos \theta) r d\theta dr = 2174 \times A_x$$

## Aeroshell Analysis (cont'd)

Integrating:

$$R_B^2 A \pi = 2174 \times 38.1$$

and 
$$A = \frac{2174 \times 38.1}{\pi \times 42^2} = 14.95 \text{ psi}$$

Since unit values were used for  $A_x$  and  $A_n$  multiply  $A = 14.95$  and  $B = 2.79$  by 1.25

$$A(\text{ult.}) = 14.95 \times 1.25 = 18.69$$

$$B(\text{ult.}) = 2.79 \times 1.25 = 3.49$$

For the 60 degree blunt cone, therefore, the membrane forces for the windward meridian are given by

$$N_{\theta_w} = \frac{18.69 (R_B^2 - r^2)}{r} + (2.31) (3.49) \frac{\ell^3 - y^3}{3 y^2} - \frac{\ell^2 - y^2}{8y}$$

$$\text{where } \ell = \frac{R_B}{\sin \theta} = \frac{42.0}{.866} = 48.50$$

$$y = \frac{r}{.866}$$

$$N_{\theta_w} = \frac{(A+B) r}{\cos \theta} = \frac{22.18 r}{\cos \theta}$$

The membrane forces at the meridian, maximum for the aeroshell, are computed versus radius in the table below. So too, are the effective membrane force and minimum required facesheet thickness.

### Aeroshell Analysis (cont'd)

Radial Station, inches	$N_{\theta}$ , Lbs/in	$N_{\theta}$ , Lbs/in	$N_{eff}$ , lbs/in.	Minimum Facesheet Thk.
8	7287	-327	7456	.091
12	3930	-532	4221	.052
15	2772	-655	3151	.039
20	1760	-887	2334	.029
25	1088	-1109	1903	.023
30	683	-1330	1773	.022
40	92	-1774	1822	.022

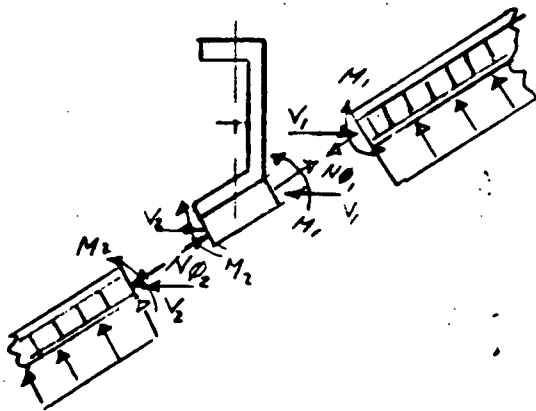
The asymmetrical membrane stress analysis results indicate that the facesheet thickness requirements close to the strut support ring are higher than previously calculated by symmetrical analysis. For the remaining cone, however, the symmetrical results are more critical, primarily because a conservative cone pressure of 25.92 psi, the stagnation pressure, was used.

Thermal studies, however, revealed that structural requirements for facesheet thickness did not provide sufficient thermal conductance to dissipate the heat energy from the heat source and a nominal facesheet of .05 inches was selected as the reference design. Local requirements at the strut support ring however are still governed by stress.

## Aeroshell Analysis (cont'd)

### Shell/Ring Interaction Analysis

A more detailed shell and ring stress analysis is performed since high bending and shear loads were anticipated at the ring to shell junction due to the concentrated application of the heat source unit inertia loads.



$V$  and  $M$  are shear and moment loads at cone and ring junction

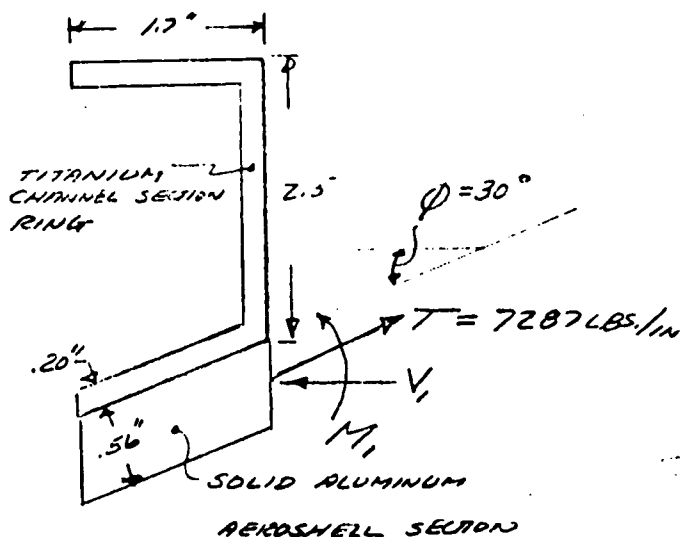
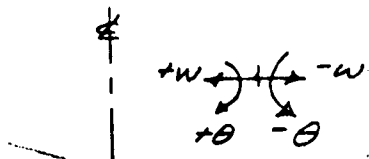
$V_2$  and  $M_2$  are shear and moment loads between nose section and ring.

To simplify the analysis the nose section is neglected since (1) the pressure-induced meridional load,  $N_{\theta_2}$ , from the nose section is insignificant compared to that of cone,  $N_{\theta}$  and (2) the H/C structure of the nose is also considerably more flexible than the cone because of its thinner facesheet thickness.

## Aeroshell Analysis (cont'd)

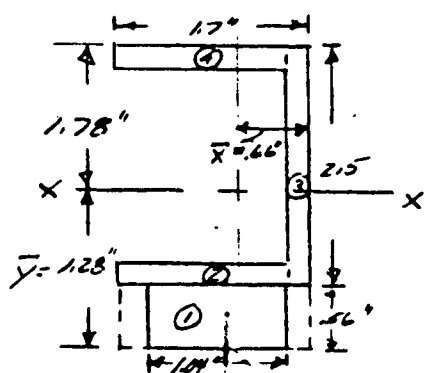
### Ring Deflection and Rotation

#### Sign Convention



maximum based on asymmetrical membrane analysis. Assuming this constant for full periphery is conservative.

Find  $I_{xx}$  and ring centroid of assumed shape shown



No.	A	y	Ay	Ay <sup>2</sup>	I
1	.5824	.28	.1630	.04566	.0152
2	.3000	.66	.1980	.13068	.0010
3	.5000	1.81	.905	1.63805	.2604
4	.3000	2.96	.888	2.62848	.0010
Total	1.6824		2.154	4.44287	.2776

$$\bar{y} = \frac{2.154}{1.6824} = 1.28$$

The segment of aluminum aeroshell to which the titanium ring is attached is reduced from 1.9" to 1.04" of equivalent titanium.



### Aeroshell Analysis (cont'd)

$$I_{xx} = \sum A_y^2 + \sum \bar{I} - A\bar{y}^2$$

$$= 4.443 + .278 - 2.756 = 1.964 \text{ in}^4$$

To locate centroid, also find  $\bar{x}$

$$\bar{x} = \frac{.500 (.1) + .5824 (.85) + .6 (.95)}{1.6824} = .66''.$$

$$R \text{ (radius of centroid)} = 7.34''$$

Ring rotation,  $\theta_R$

$$\theta_R = \frac{M_{\text{total}} R^2}{E I} = \frac{[(V_1 - T \cos \phi) (1.28 - .28) - M.] 7.34^2}{16.4 \times 10^6 \times 1.964}$$

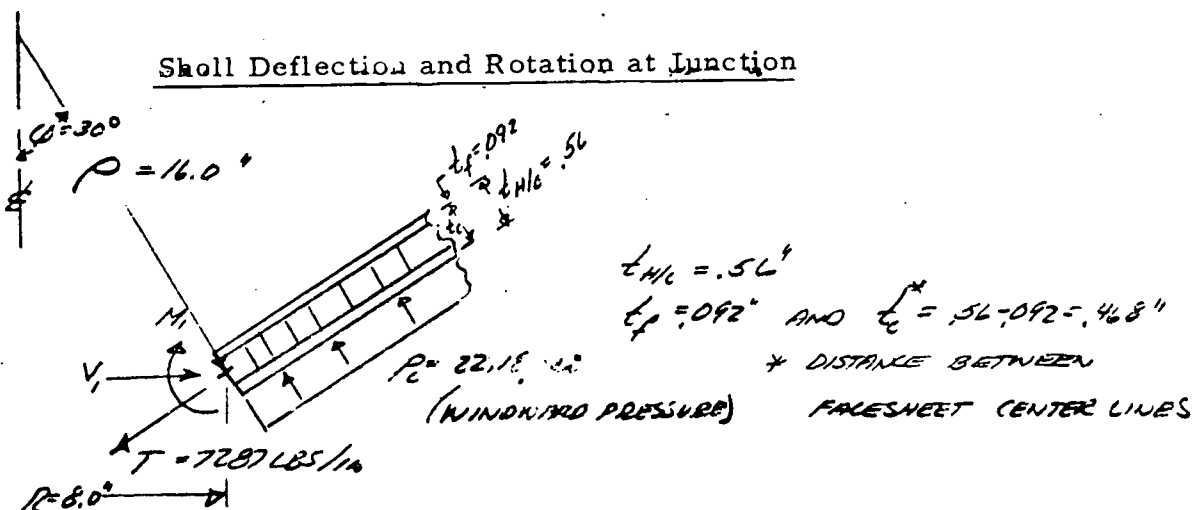
$$T \cos \phi = 7287 \times .866 = 6310$$

$$\theta_R = 1.67 V_1 - 10,539 - 1.67 M,$$

The  $10^6$  in denomination is dropped throughout these calculations.

Ring deflection,  $W_R$ , at junction with shell

$$\begin{aligned}
 W_R &= \left( \frac{V_1 - T \cos \phi}{A E} \right) R^2 + \theta_R (1.28-.28) \\
 &= 1.95 V_1 - 14229 + 1.674 - 10,539 - 1.67 M_1 = \\
 &3.62 V_1 - 24,768 - 1.67 M_1
 \end{aligned}$$



Treat honeycomb shell by finding equivalent monocoque shell having similar bending and axial rigidities. The properties of such a shell are given by

$$t_e = \sqrt{3} \times t_c = .81 \text{ inches}$$

$$E_e = \frac{2}{\sqrt{3}} \frac{t_f}{t_c} E_f = 2.27 \times 10^6 \text{ psi}$$

Shell deflection

$$w_s = \frac{-\sin \phi V_1}{2 \beta^3 D} + \frac{\sin \phi M_1}{2 \beta^2 D} + \frac{P_c \rho R}{t_e E_e} + \frac{\nu T R}{t_e E_e}$$

$$\beta^4 = \frac{3(1-\mu^2)}{\rho^2 t_e^2} \quad \text{or} \quad \beta = \frac{(3(1-\mu^2))^{1/4}}{(\rho t_e)^{1/2}} = \frac{1.284}{(12.96)^{1/2}} = .357$$

$$\beta^2 = .1275 \text{ and } \beta^3 = .0455$$

$$D = E_e T_e^3 / 12 (1-\mu^2) = .1105 \times 10^6$$

$$R = 8.0 \text{ inches}$$

Therefore

$$\begin{aligned} W_s &= - \frac{(.50)^2 V_1}{2 \times .0455 \times .1105} + \frac{.5 M_1}{2 \times .1275 \times .1105} + \frac{22.18 \times 16 \times 8}{.81 \times 2.27} + \frac{.3(7287) 8}{.81 \times 2.27} \\ &= -24.86 V_1 + 17.74 M_1 + 1544 + 9510 \\ &= -24.86 V_1 + 17.74 M_1 + 11054 \end{aligned}$$

Shell Rotation,  $\theta_s$ , is

$$\begin{aligned} \theta_s &= \frac{-\sin \phi V_1}{2 \beta^2 D} + \frac{1}{\beta D} M_1 + \frac{P_c \rho \cot \phi}{t_e E_e} + \frac{T \cot \phi}{t_e E_e} \\ &= - \frac{.5 V_1}{2 \times .1275 \times .1105} + \frac{M_1}{.357 \times .1105} + \frac{22.18 \times 16 \times 1.732}{.81 \times 2.27} \\ &\quad + \frac{7287 \times 1.732}{.81 \times 2.27} \\ &= -17.74 V_1 + 25.35 M_1 + 334 + 6863 \\ \theta_s &= -17.74 V_1 + 25.35 M_1 + 7197 \end{aligned}$$

## Aeroshell Analysis (cont'd)

Equate (1) ring and shell deflections

(2) ring and shell rotations

Deflection:

$$-24.86 V_1 + 17.74 M_1 + 11054 = 3.62 V_1 - 24,768 - 1.67 M_1$$

$$-28.46 V_1 + 19.41 M_1 = -35,822$$

Rotations:

$$-17.74 V_1 + 25.35 M_1 + 7197 = 1.67 V_1 - 10,539 - 1.67 M_1$$

$$-19.41 V_1 + 27.02 M_1 = -17,736$$

Find  $V_1$  and  $M_1$  by solving the equations simultaneously

$$-28.46 V_1 + 19.41 M_1 = -35,822$$

$$-19.41 V_1 + 27.02 M_1 = -17,736$$

First for Moment  $M_1$

$$-552.80 V_1 + 376.75 M_1 = -695,305$$

$$-552.80 V_1 + 769.53 M_1 = -505,121$$

---

$$392.78 M_1 = 190,184$$

$$M_1 = 484 \text{ in. Lbs/in.}$$

Then for Shear  $V_1$

$$-376.75 V_1 + 524.46 M_1 = -344,256$$

$$-769.53 V_1 + 524.46 M_1 = -967,910$$

---

$$392.8 V_1 = 623,654$$

$$V_1 = 1588 \text{ Lbs/in.}$$

Ring Stresses:

$$M_R (\text{total}) = (V - T \cos \phi) - M_1 = 1588 - 6310 - 484 = 5206 \text{ in-Lbs/in.}$$

$$Q (\text{total}) = -1588 + 6310 = 4722 \text{ Lbs/in.}$$

# Aeroshell Analysis (cont'd)

$$\begin{aligned}\sigma_{\text{ring (upper)}} &= - \frac{MR}{I/c} + \frac{QR}{A} \\ &= \frac{-5206 \times 7.34}{1.964/1.78} + \frac{4722 \times 7.34}{1.682} \\ &= -34,632 + 20,606 = -14,026 \text{ psi}\end{aligned}$$

$$\sigma_{\text{Ring(lower)}} = + \frac{5206 \times 7.34}{1.96/1.28} + 20,606 = 24,955 + 20,606 = 45,561 \text{ psi}$$

Since a portion of the aluminum shell was included as the ring, the maximum stress of 45,561 psi is compared to the 2024-T 81 aluminum allowable of 56,280 psi at 350°F. \*

$$\text{M. S.} = \frac{56,280}{45,561} - 1 = .23$$

Shell stress at junction (the shell is solid at .56 inch at the junction)

$$\begin{aligned}\text{Maximum Shell Stress} &= \frac{6M_1}{h^2} + \frac{T}{h} \\ &= \frac{6 \times 484}{.56^2} + \frac{7287}{.56} = 9260 + 13,012 = 22,272 \text{ psi} \\ \text{M. S.} &= \frac{56,280}{22,272} - 1 = 1.51\end{aligned}$$

Compute shell stress 2.0" from junction along meridian where the honeycomb actually begins

$$M_{\phi}(\beta x) = M_1 \phi(\beta x) - \frac{V_1 \sin \phi}{\beta} \int(\beta x)$$

$$\beta = \frac{[3(1-\nu^2)]^{1/4}}{(h)^{1/2}} = \frac{[3(1-.3^2)]^{1/4}}{(16 \times .56)^{1/2}} = .428$$

\*Allowable from MIL Handbook 5A "Metallic Materials and Elements for Aerospace Vehicle Structures".

## Aeroshell Analysis (cont'd)

For  $X = 2.0$  inches,  $\beta X = .856$

$\phi(\beta x) = .60$ ;  $\psi(\beta x) = .32$  (this represents the max. value for  $\psi$  and it will decrease for larger values of  $\beta x$ )

$$M\phi(\beta x = 2.0) = 484 \times .6 - \frac{1588}{.428} \times .5 \times .32 = 304 \text{ in-lb./in.}$$

Since total stress in the honeycomb is given by

$$\sigma_c = \frac{N\phi}{2 t_f} + \frac{6 M\phi}{t_f t_c}$$

The membrane force  $N\phi$  at this point must also be found. From previous membrane analysis

$$N\phi = \frac{A (R_B^2 - r^2)}{r} + 2.31 B \frac{l^3 - y^3}{3 y^2} - \frac{l^2 - y^2}{8 y}$$

Where  $A = 18.69 \text{ psi}$   $B = 3.49 \text{ psi}$

$$r = 8 + 2.0 (.866) = 9.73$$

$$y = 9.73 / .866 = 11.23$$

$$\begin{aligned} N\phi (r = 9.73'') &= \frac{18.69 (42^2 - 9.73^2)}{9.73} + 2.31(3.49) \left[ \frac{48.50^3 - 11.23^3}{3 \times 11.23^2} \right. \\ &\quad \left. - \frac{48.50^2 - 11.23^2}{8 \times 11.23} \right] \\ &= 3206 + 2199 = 5405 \text{ lbs./in.} \end{aligned}$$

Determine if  $t_f = .10''$  and  $t_c = .46''$  is adequate at this station

$$\sigma_c = \frac{5405}{2 \times .10} + \frac{6 \times 304}{.10 \times .46} = 27,025 + 39,656 = 66,677 \text{ psi} > 56,280 \text{ psi} \quad (\text{excessive stress})$$

If  $t_f$  is increased to .125,  $t_c$  becomes .435

$$\sigma_c = \frac{5405}{2 \times .125} + \frac{6 \times 304}{.125 \times .485} = 21,620 + 33,545 = 55,165 \text{ psi} \quad \text{O.K.}$$

### Aeroshell Analysis (cont'd)

The facesheet thickness and core thickness at  $r = 12.0''$  is .05 inches and .51 inches respectively. This represents a meridional distance away from the joint of 4.62 inches.

$$r = 12.0''$$

$$\rho = 24.0''$$

$$h = (\text{equivalent thick. based on bending rigidity}) = (t_f t_c)^{1/2} = .16$$

$$\text{Therefore } \beta = \frac{[3(1-\mu^2)]^{1/4}}{(\rho h)^{1/2}} = \frac{[3(1-\mu^2)]^{1/4}}{(24 \times .16)^{1/2}} = \frac{1.29}{1.96} = .658$$

$$B x = 4.62 \times .658 = 3.04$$

$$\phi(\beta x) = -0.042 \quad \int(\beta x) = .007$$

$$M \phi(\beta x = 3.04) = (-484)(-.042) = \frac{1588}{.658} \times .5 \times .007 =$$
$$-20.3 - 8.4 = 28.7 \text{ in. Lb/in.}$$

At  $r = 12.0''$   $N \phi = 3930$  Lbs/in. (windward meridian of asymmetrical model)

$$\sigma_{(total)} = \frac{N \phi}{2 \times t_f} + \frac{6M \phi}{t_f t_c} = \frac{3930}{2 \times .05} + \frac{6 \times 28.7}{.05 \times .51}$$

$$= 39,300 + 6753 = 46,053 \text{ psi} < 56,280 \text{ psi}$$

## DISTRIBUTION

### Addressee

### Mail Stop

NASA-Lewis Research Center  
21000 Brookpark Road  
Cleveland, Ohio 44135

Attn: 1.	H. Bloomfield	500-201
2.	G. M. Ault	3-13
3.	R. E. English	200-201
4.	H. O. Slone	500-201
5.	W. Wintucky	500-201
6.	R. R. Miller	500-202
7.	A. Valerino	500-201
8.	H. B. Block	500-202
9.	E. Maslowski	500-202
10.	D. Packe	500-201
11.	H. Schwartz	500-201
12.	R. Burns	500-201
13.	L. Shure	500-201
14.	R. Weltmann	6-2
15.	J. E. Dilley	500-309

NASA-Lewis, Space Power Facility  
Plum Brook Station  
Sandusky, Ohio 44870  
Attn: G. Prok

1441-1

U. S. Atomic Energy Commission  
SNS Division  
Washington, DC 20545

Attn: 1. R. Carpenter  
2. G. Newby  
3. H. Jaffe  
4. P. R. Miller  
5. G. Dix  
6. J. Powers  
7. M. Gaitanis  
8. L. Topper  
9. R. Kahler  
10. P. O'Riordan  
11. N. Goldenberg  
12. F. Schulman

2.

DISTRIBUTION (Cont'd)

<u>Addressee</u>	<u>Mail Stop</u>
NASA Headquarters 1512 H Street Washington, DC 20545 Attn: 1. T. B. Kerr 2. M. Shaw	RYN MF
NASA-Langley Research Center Hampton, Virginia 23365 Attn: 1. P. Bobbitt 2. R. Wells 3. R. Anderson	244 326 188
NASA-Ames Research Center Moffett Field, California 94035 Attn: 1. E. Katzen 2. V. Peterson 3. H. Stine 4. J. Vorreiter	229-1 229-1 229-2 229-2
NASA-Manned Spacecraft Center Houston, Texas 77058 Attn: 1. G. Rice 2. T. Redding	EG4 EP5
NASA-Marshall Space Flight Center Huntsville, Alabama 35812 Attn: 1. L. Brantley 2. G. Sieren	PD-DD-EP PD-SS
Aerospace Corporation P. O. Box 95085 Los Angeles, California 90045 Attn: H. Sampson	
AiResearch Manufacturing Company 9851 Sepulveda Boulevard Los Angeles, California 90009 Attn: M. Coombs	



3.

DISTRIBUTION (Cont'd)

Addressee

Mail Stop

Donald W. Douglas Labs  
2955 Geo. Washington Way  
Richland, Washington 99352  
Attn: J. Greenborg

General Electric Company  
Missile & Space Division  
P. O. Box 8661  
Philadelphia, Pennsylvania 19101  
Attn: B. Tharpe

Hittman Association  
P. O. Box 810  
Columbia, Maryland 21043  
Attn: T. Bustard

Lockheed Missile & Space Company  
P. O. Box 504  
Sunnyvale, California 94088  
Attn: H. Greenfield

McDonnell-Douglas Corporation  
5301 Bolsa Avenue  
Huntington Beach, California 92647  
Attn: R. Gervais

Monsanto Research Corporation  
Mound Laboratory  
Miamisburg, Ohio 45342  
Attn: R. Vallee

North American Rockwell  
Space Division  
2201 Bay Boulevard  
Seal Beach, California 90241  
Attn: A. Nussberger

Nus Corporation  
2351 Research Boulevard  
Rockville, Maryland 20850  
Attn: J. Coleman

DISTRIBUTION (Concl'd)AddresseeMail Stop

Sandia Corporation  
P. O. Box 5800  
Albuquerque, New Mexico 87115  
Attn: A. Clark

Teledyne Isotopes Inc.  
110 West Timonium Road  
Timonium, Maryland 21093  
Attn: P. Dick

TRW Systems  
Bldg. 01  
1 Space Park  
Redondo Beach, California 90278  
Attn: I. Jones

Westinghouse Astronuclear Laboratories  
P. O. Box 10864  
Pittsburgh, Pennsylvania 15236  
Attn: R. Lochbaum

Wright-Patterson Air Force Base  
Aero Prop Laboratory  
Dayton, Ohio 45433  
Attn: G. Sherman

AFAPL/PO